rijksuniversiteit
groningen

SEAGLE – Simulating EAGLE LEnses

Deciphering galaxy formation via strong lensing simulations

Proefschrift

ter verkrijging van de graad van doctor aan de
Rijksuniversiteit Groningen
op gezag van de
rector magnificus prof. dr. E. Sterken
en volgens besluit van het College voor Promoties.

De openbare verdediging zal plaatsvinden op

vrijdag 11 januari 2019 om 9:00 uur

door

Sampath Mukherjee

geboren op 26 juni 1990
te Serampore, West Bengalen, India

Promotores
Prof. dr. L. V. E. Koopmans
Prof. dr. J. Schaye

Co-promotor
Prof. dr. R. B. Metcalf

Beoordelingscommissie
Prof. dr. A. Helmi
Prof. dr. M. Vogelsberger
Prof. dr. P. Rosati

To the SEAGLE team

ISBN: 978-94-034-1308-2 (printed version)
ISBN: 978-94-034-1307-5 (electronic version)
Cover:
(Background) Strong lens created with SEAGLE pipeline using a spiral galaxy as the lens from EAGLE-Reference.
(Front) A collage of modified strong lenses systems from EAGLE model variations in the shape of 'SEAGLE'. Design- Sampath, Helmer and Nika.
Printed by: Gildeprint - The Netherlands

Contents

Chapter 1

Introduction

According to the cosmological principle, the Universe is homogeneous on large scales (Coles & Lucchin 2002). The observed Cosmic Microwave Background (CMB) radiation confirms this. But actually, the Universe around us is isotropic *only* on very large scales, of order 100s of Mpc or larger. On smaller scales, we find galaxies and superclusters of galaxies which have a mass density higher than the average density of the Universe. Therefore, we observe that the Universe exhibits a lot of structures on smaller scales. The existence of these cosmological structures gives us crucial information about the initial conditions of the origin of the universe, and about the underlying physical processes through which these structures have evolved.

1.1 Cosmological studies and galaxy formation

The physical process behind the formation of structure in the early Universe is one of the fundamental problems in cosmology. Our present approach to understand the structure-formation of the Universe, is based on the Λ Cold Dark Matter (ΛCDM) cosmology (Blumenthal et al. 1984; Riess et al. 1998; Carroll 2001; Spergel et al. 2003) in which the mass in the Universe is dominated by cold dark matter. Initially, the Universe was not perfectly homogeneous and isotropic and had some small, primordial

fluctuations in their density which were adiabatic quantum fluctuations in the gravitational potential in the early Universe that grew by the process of gravitational instability. In this process, regions, where the matter density is slightly higher than average, attract matter from their surrounding regions. Regions, where the matter density is below the average, will evolve to even lower densities. This instability grows and leads to the formation of galaxies which can subsequently merge to form bigger structures. This scenario is known as the hierarchical structure-formation scenario. The phases of the quantum fluctuations are random in origin and obey a Gaussian distribution. Therefore, the initial conditions for cosmic structure-formation are Gaussian random fields. Fluctuations exist on a variety of mass and length scales. The final structure-formation thus depends on the growth of these perturbations relative to each other. It is, therefore, necessary to look at the perturbations regarding their spectral distribution. The spectrum was suggested independently by Peebles & Yu (1970); Harrison (1970); Zeldovich (1972), and now is known as the Harrison-Zel'dovich or scale-invariant power spectrum. This spectrum is supported by inflationary models (Guth & Weinberg 1983; Guth & Sher 1983; Guth & Steinhardt 1984) and has the form:

$$P(k) = Ak^n \ , \tag{1.1}$$

where A is a normalization factor, k is the wave vector, and n is the spectral index. According to the theory of inflation, the Universe expanded by a factor $\sim 10^{26}$ during a short period of time. After inflation, these small density perturbations stretched to cosmological scales and created a plethora of structures that we see in the Universe. A small perturbation concerning a background density field is given by:

$$\delta(x) = \frac{\rho(x) - \rho_m}{\rho_m} \ , \tag{1.2}$$

where ρ_m is the mean matter density. These density perturbations collapse through gravitational instability.

To investigate the gravitational instability one needs to study the dynamics of a self-gravitating fluid. Assuming the Universe can be treated as a fluid, we require to solve the fluid equation. The equations of motion of a fluid in the Newtonian approximation, and for an expanding Universe, are:

$$\frac{\partial \delta}{\partial t} + \frac{1}{a}\nabla.[(1+\delta)v] = 0 \ , \tag{1.3}$$

$$\frac{\partial \delta}{\partial t} + \frac{1}{a}(v.\nabla)v + \frac{\dot{a}}{a}v = -\frac{1}{\rho a}\nabla p - \frac{1}{a}\nabla\phi \ , \tag{1.4}$$

$$\nabla^2\phi = 4\pi G\rho a^2\delta \ , \tag{1.5}$$

$$\partial h + \frac{\partial P}{\rho g} + \frac{\partial v^2}{2g} = 0 \ . \tag{1.6}$$

These are the continuity equation, the Euler equation, the Poisson equation and the Bernoulli equation (energy conservation), respectively. Deviations from homogeneity, at early stages, are small and the equations of motion can be solved analytically using linear perturbation theory. At some point, *linear theory* does not remain valid. Non-linear solutions are generally too complex to solve analytically, and one has to rely on other methods (numerical simulations) to study their evolution.

These structures collapsed into the cosmic web of sheets, filaments, and halos which we see around us today. The dark matter mainly provides the gravitational potential for these structures, and baryons are expected to fall into these potentials. Over the years after its development, the General Theory of Relativity (GTR) has been a great tool to study the gravitational evolution of the homogeneous and isotropic Universe. In general, the geometrical properties of space-time, described by a metric, needed to be constrained to carry out the study. The GTR does it for us.

The most general space-time metric based on the cosmological principle is represented by the Robertson-Walker metric (RW), which can be written as:

$$ds^2 = (cdt)^2 - a^2(t)\left[\frac{dr^2}{1-kr^2} + r^2(d\theta^2 + \sin^2(\theta)\, d\phi^2)\right] \ . \tag{1.7}$$

Here r, θ, and ϕ are the comoving coordinates, t is the proper time, $a(t)$ is the cosmological scale factor (expansion factor), and k is the curvature parameter with values +1, 0, or -1. The value of k leads to an open, flat

or closed Universe, respectively. Einstein's equations of general relativity relate the geometrical properties of space-time to an energy-momentum tensor describing the contents of the Universe. An ideal fluid approximation leads to the Friedmann equations (Coles & Lucchin 2002) which describe the evolution and expansion of the Universe. The Friedmann equations are :

$$\ddot{a} = -\frac{4}{3}\pi G\left(\rho + 3\frac{p}{c^2}\right)a \ , \tag{1.8}$$

$$\dot{a}^2 + Kc^2 = \frac{8}{3}\pi G\rho a^2 \ , \tag{1.9}$$

where G is the gravitational constant, ρ is the mass density, p is the pressure, and Λ is the cosmological constant. The scale factor $a(t)$ can be computed by solving the Friedman equations. Hubble (1929) discovered the expansion of the Universe, which is given by the Hubble law:

$$v = H(t)D \ , \tag{1.10}$$

where v is the recessional velocity of the source, D is the distance of the source from the observer and $H(t)$ is the Hubble parameter, given by $H(t) = \frac{\dot{a}}{a}$ and also called the expansion rate of the Universe. Its value at the present time is $H_0 \sim 71 \pm 2$ kms^{-1}Mpc^{-1} (Freedman et al. 2012). Similarly, the critical density of the Universe can be calculated as:

$$\rho_0 = \frac{3H_0^2}{8\pi G} \ . \tag{1.11}$$

The growth of structure depends on the contents of the Universe, which are baryons, dark matter, dark energy and radiation. In a ΛCDM cosmology, values of these parameters from Planck Collaboration 2014 are:

$$\Omega_b = \frac{\rho_b}{\rho_c} = 0.0482519, \ \Omega_m = \frac{\rho_m}{\rho_c} = 0.307, \ \Omega_\Lambda = \frac{\Lambda}{3H_0^2} = 0.6777 \ . \tag{1.12}$$

The content of the Universe is depicted in Figure 1.1. It can be noticed that 71.4% of the energy content of the Universe is dark energy, 24% is dark matter and 4.6% is baryonic matter. It was realized in the early 80s that most of the matter is not composed of baryons. Rather, a non-luminous source of gravitational potential was found to be necessary to explain optical rotation curves, known as the dark matter (Rubin & Ford 1970; Roberts & Rots 1973; Ostriker & Peebles 1973; Ostriker et al. 1974; Begeman 1989).

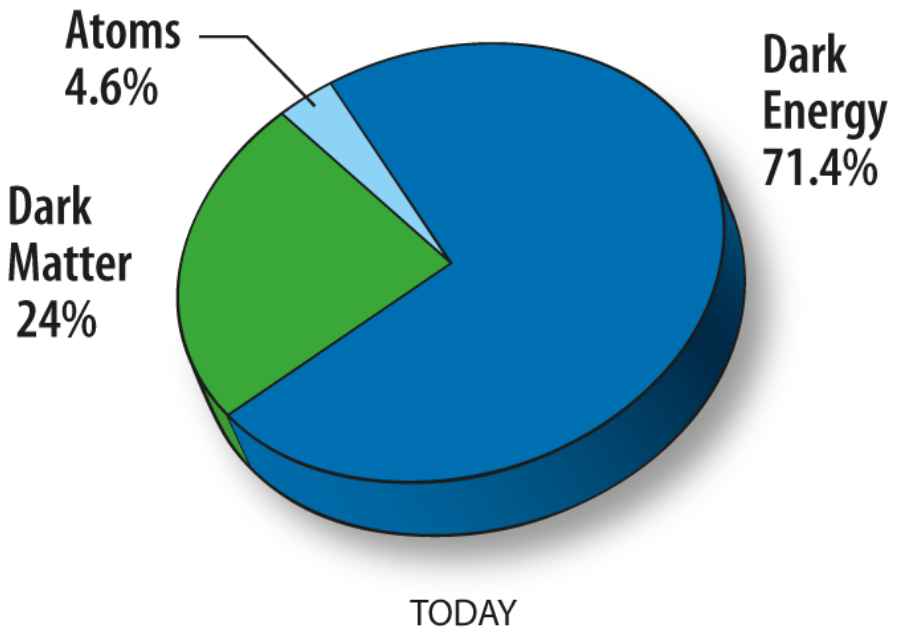

Figure 1.1: A pie plot showing the present composition of the Universe. Image credit: NASA.

1.2 Role of simulations – EAGLE

During the last few decades, there has been tremendous progress in our understanding of the cosmic structure and mechanisms of galaxy formations. Much of this understanding came from purely analytic arguments and insights. Calculations of the Cold Dark Matter (CDM) power spectrum (Peebles 1982; Blumenthal et al. 1984), Press and Schechter theory (Press & Schechter 1974), the statistics of peaks in Gaussian Random fields (Bardeen et al. 1986) and White and Rees galaxy formation model (White & Rees 1978) are a few seminal examples. But the purely analytical approach has its limitations in solving more complicated issues. Propelled by continuous improvements in numerical methods and computational capabilities, the future of structure formation and galaxy formation theory is going to be driven by cosmological simulations.

Cosmological simulations have been widely used for the interpretation of observations and the design of new observational campaigns and instruments. Simulations enable us to do numerical experiments which reveal valuable insights into our understanding of the physics of galaxy formation, even if sometimes the simulations fail to reproduce observations. Dark-matter only simulations were, for example, used to generate realistic models of the Universe. They have quantified the concentration-mass relationship, its scatter, and its evolution with time (Bullock et al. 2001; Wechsler et al. 2002; Zhao et al. 2009). But limited by its ability to predict the baryonic-physics soon they paved the way to hydrodynamic simulations. Initially most hydro-simulations could not reproduce galaxy mass functions (GMFs) with the correct shape and normalization. The galaxy morphologies were also incorrect, either too massive or too compact and the stars formed too early. Hence hydrodynamical simulations could not achieve a good overall agreement with the observed galaxies. In the absence of a successful hydrodynamical simulation to reproduce key observations, semi-analytic and halo-based models have become a preferred tool to perform comparisons between galaxy surveys and theoretical frameworks (Cooray & Sheth 2002; Baugh 2006). The flexibility, reliability and relatively modest computational expense of semi-analytic models gave many advantages over their hydrodynamic counterparts to explore and provide many key results e.g., the explanation of observational trends of galaxies within the context of the CDM framework, the creation of mock galaxy catalogues to investigate selection effects or to interpret the calculations of galaxy clustering into information regarding the dark matter distribution in the haloes of galaxies. Although computationally expensive, hydrodynamical simulations have important advantages over semi-analytic simulations. One of the main benefits is that hydrodynamical simulations evolve the dark matter and baryonic components self-consistently. That automatically includes the evolution and back-reaction of the baryons on the collision-less matter, both inside and outside of haloes (see Schaye et al. 2010, 2015). The higher resolution evolution of the baryonic component, provided by hydrodynamical simulations, also enables one to determine a more detailed model of galaxies and the intergalactic medium (IGM). Moreover, hydro-simulations even investigate the interface between the two, which is vital to understand the fuelling and feedback cycles of galaxies (Segers et al. 2016).

Hydrodynamic simulations, however, need to be calibrated to reproduce the correct stellar and black hole (BH) masses. Also, to predict the right amount of star-forming gas, there is a need to calibrate the subgrid model for star formation to the observed star formation law. This necessity is due to a lack of complete understanding of the physical events that operate at the sub-resolution limit and their interdependence with the physical processes operating at a much larger scales. Hence it is impossible to implement a subgrid model that is sufficiently realistic to retain full predictive power, yet much of the underlying gastrophysics need to be implemented via subgrid physics as high-performance computing resources limit us.

Even though hydrodynamical simulations cannot predict stellar masses or black-hole masses from the evolution itself and needs be calibrated, they can deliver crucial predictions for other observables that were not used to calibrate (see Schaye et al. 2015; Crain et al. 2015; Schaller et al. 2015a,b). To gain more insight and learn about the physics of galaxy formation it is an excellent experiment to vary the subgrid models and run multiple simulations (Schaye et al. 2010). It is particularly useful to use the same observables to calibrate multiple simulations run with different prescriptions. One of the primary motivation to use EAGLE in this thesis is because EAGLE comprises of simulation runs with several galaxy formation variations, including several that reproduce the $z \sim 0$ galaxy stellar mass function (GSMF) through different means (Crain et al. 2015). This variety of model gives insight into galaxy formation, making quantitative predictions for observables of the galaxy population. Also, these simulations can be explored to understand the fundamentals of physical processes and to make forecasts providing crucial information about gas accretion into galaxies, the size of galaxies, the origin of scatter in galaxy scaling relations, the potential effect of outflows on cosmology using gravitational lensing or the Lyα forest. Additionally, calibrated simulations can guide the interpretation and planning of observations providing more detailed information on both the galaxies and their gaseous environments. For a comprehensive study of the effects of baryons on the dark matter distribution and use of different numerical recipes of Smooth Particle Hydrodynamics (SPH) readers can consult Schaller (2015).

So the domain of cosmological numerical simulations ranges from providing more insight into large-scale structure formation, their isolated halo

properties such as shapes, kinematics and density profile, to subhalo mass functions and substructure etc. In light of all the existing hydro-simulations, we describe below the details of the EAGLE simulations used in this thesis.

1.3 Details of the EAGLE simulations

Evolution and Assembly of GaLaxies and their Environments (EAGLE; Schaye et al. 2015) is a suite of cosmological hydrodynamical simulations of a standard Λ Cold Dark Matter universe with volumes of 25 to 100 comoving Mpc (cMpc) on a side. The primary motivation of EAGLE was to reproduce the observables discussed in the above section using much-improved prescriptions for stellar and AGN feedback, then used in previous work with similar objectives.

To improve the realistic nature of the simulated galaxies, major improvement has been made in the implementation of efficient subgrid models for feedback from star formation that generates galactic winds more effectively. Also, at the high-mass end, a subgrid prescription for efficient feedback from active galactic nuclei (AGN) has been implemented. In the same line of thought, EAGLE's treatment of feedback from massive stars and AGN is improved such that the thermal energy injected into the gas does not need the cooling or decouple hydrodynamical forces to be turned off. So it allows winds to develop without predetermined speed or mass loading factors. But the feedback efficiencies cannot be predicted from first principles, so they are calibrate taking galaxy sizes into account to the present-day GSMF and the amplitude of the galaxy-central black hole mass relation. The observed GSMF is reproduced to 0.2 dex over the full resolved mass range, $10^8 < M_\star/\mathrm{M}_\odot < 10^{11}$. This level of agreement is unprecedented for hydrodynamical simulations and very close to that attained by semi-analytic models. Also unlike most previous work, there is no need for an ad hoc factor to boost the black hole Bondi–Hoyle accretion rates. Lastly, a local gas property dependent feedback is used to inject energy (and momentum) per unit stellar mass. The feedback is not affected by any non-local or non-baryonic properties (e.g. the dark matter velocity dispersion or halo mass).

EAGLE uses the observed present-day GSMF to calibrate the feedback efficiency. Two factors are responsible for using GSMF for calibration namely (a) GSMF is relatively well-constrained observationally and (b) it is a pre-condition to obtaining the correct GSMF (i.e., stellar mass–halo mass relation) when the cosmological initial conditions are known. Let us see more details of the simulation prescriptions and subgrid physics recipes of EAGLE.

1.3.1 Simulations and subgrid physics

EAGLE simulations use a modified SPH (Smoothed Particle Hydrodynamics) version of `GADGET 3` (Springel 2005). The major improvements have been done in the formulation of SPH, the time stepping and, the subgrid physics. EAGLE's subgrid physics is constructed on those used for OWLS (Schaye et al. 2010), in GIMIC (Crain et al. 2009) and COSMO-OWLS (Le Brun et al. 2014). The values of the cosmological parameters are $\Omega_\Lambda = 0.693$, $\Omega_\mathrm{b} = 0.0482519$, $\Omega_\mathrm{m} = 0.307$, $h = H_0/(100\ \mathrm{km\ s^{-1}\ Mpc^{-1}}) = 0.6777$ and $\sigma_8 = 0.8288$. These are taken from the Planck satellite data release (Planck Collaboration et al. 2014).

All the galaxies in Schaye et al. (2015) are identified in the simulations using a `Friends-Of-Friend` (`FoF`: Davis et al. 1985) halo finder combined with the `SUBFIND` algorithm (Springel et al. 2001; Dolag et al. 2009). Firstly, haloes subjected to a linking length 0.2 times the mean interparticle separation are found by running the `FoF` algorithm on the dark matter particles. Gas and star particles are assigned to the same `FoF` halo as their nearest dark matter particles. Secondly, substructure candidates are defined by `SUBFIND` that identifies over-dense patches within the `FoF` halo. These regions are bounded by saddle points in the mass density distribution. It is important to point out that `SUBFIND` uses all particle types within the `FoF` halo, but only dark-matter particles are accounted in `FoF`. Thirdly, particles that are isolated and are not bound gravitationally to the substructure are removed. These non-included substructures are referred to as subhaloes. Finally, subhaloes that are separated by < 3 pkpc in their stellar half-mass radius are merged. This final step removes very low mass subhaloes whose mass is dominated by a supermassive black or similar one particle-masses. However, these are very few in number. The lowest value of the gravitational potential for a particle in a subhalo for

each given FoF halo is defined as the central galaxy. All the remaining subhaloes (if any) are catalogued as satellite galaxies.

Having said this, due to the finite resolution of the simulations, many physical processes that operate on smaller can be modeled using (analytic) prescriptions (termed 'subgrid' physics). Below we briefly summarize the main features of different subgrid prescriptions used in EAGLE.

1.3.2 Reionization and radiative processes

A time-dependent, spatially uniform ionizing background, introduced in Haardt & Madau (2001), is implemented for mimicking the hydrogen reionization. Following the optical depth measurements from Planck Collaboration et al. (2014), this hydrogen reionization is administered at redshift $z = 11.5$. At higher redshifts net cooling rates are used for gas exposed to the CMB and the photo-dissociating background obtained by cutting the z = 9 Haardt & Madau (2001) spectrum above 1 Ryd. Radiative cooling and heating rates have been computed on each element-wise manner, with CLOUDY code, of Ferland et al. (1998). Total of 11 elements have been included, i.e. H, He, C, N, O, Ne, Mg, Si, S, Ca, and Fe.This element-by-element computation of rates not only accounts for variations in the metallicity, but also for variations in their relative abundances. It is performed by specifying cooling rates as a function of density, temperature and redshift assuming that the gas is optically thin. The radiative process is in ionisation equilibrium, and is exposed to the cosmic microwave background and a spatially uniform, temporally-evolving Haardt & Madau (2001) UV/X-ray background (Wiersma et al. 2009a). The UV/X-ray background is introduced instantaneously at $z = 11.5$. For each proton mass, 2 eV energy is injected instantaneously, during the epochs of reionisation for rapidly heating gas to $\sim 10^4$ K at $z = 11.5$. This is consistent with Planck constraints for HI reionisation. However, a Gaussian function centred about $z = 3.5$ with a width of $\sigma(z) = 0.5$ is used to distribute the energy injection for HeII. This setup simulates the thermal evolution of the intergalactic medium according to prescription introduced in Schaye et al. (2000). This choice has resulted in broad agreement with the thermal history of the intergalactic gas (Wiersma et al. 2009b).

1.3.3 Star formation

A stochastic Star formation is implemented, according to the pressure law scheme of Schaye & Dalla Vecchia (2008). However, a density threshold is given from Schaye (2004), depending on the metalliticity. This is performed assuming that the star-forming gas is self gravitating. This prescription of taking the starformation rate to depend on pressure is different to the usual way where dependence on density is employed. The observed Kennicutt-Schmidt star formation law (Kennicutt 1998):

$$\dot{\Sigma}_\star = A \left(\frac{\Sigma_{\rm g}}{1{\rm M}_\odot {\rm pc}^{-2}} \right)^n \ , \tag{1.13}$$

where $\Sigma_\star$ and $\Sigma_{\rm g}$ are the surface density density of stars and gas, respectively, can be expressed as a pressure law:

$$\dot{m}_\star = m_{\rm g} A \left(1{\rm M}_\odot pc^{-2}\right)^{-n} \left(\frac{\gamma}{G} f_{\rm g} P \right)^{(n-1)/2} \ , \tag{1.14}$$

where $\gamma = 5/3$ is the ratio of specific heats, $m_{\rm g}$ is the gas particle mass, P is the total pressure, G is the gravitational constant, and f_g is the mass fraction in gas. The advantages of this pressure law are: (a) observations specify the values of the free parameters of the star formation law, $A = 1.515 \times 10^{-4} {\rm M}_\odot {\rm yr}^{-1} {\rm kpc}^{-2}$ and $n = 1.4$, and (b) this implementation guarantees that the observed Kennicutt-Schmidt relation is reproduced for any equation of state which arises from any combination of $T_{\rm eos}$ and $\gamma_{\rm eos}$ applied to star-forming gas. Thus it needs no further recalibration which would have been necessary if volume density dependence have been used, making Kennicutt-Schmidt star formation law dependent on the thickness of the disc and thus on the equation of state. The value of n has been increased to 2.0 for $n_{\rm H} > 10^3 {\rm cm}^{-3}$ due to steepening at high densities (Genzel et al. 2010).

Star formation occurs only in cold ($T << 10^4$K), dense gas. But it requires a density threshold, $n_{\rm H}^{\star}$. In EAGLE the metallicity-dependent star formation threshold proposed in equation 19 and 24 of Schaye (2004) has been adopted, which was implemented in the OWLS simulation (Schaye et al. 2010) SFTHRESHZ:

$$n_{\rm H}^{\star}(Z) = 10^{-1} cm^{-3} \left(\frac{Z}{0.002}\right)^{-0.64} , \tag{1.15}$$

where Z is the gas metallicity (i.e. the fraction of the gas mass in elements heavier than helium).

1.3.4 Stellar evolution and mass loss

The implementation of stellar evolution and mass loss is based on prescription described in Wiersma et al. (2009b). Star particles are treated as simple stellar populations (SSPs) with an IMF of the form proposed by Chabrier (2003), spanning the range 0.1 -100 $M_{\odot}$. At each time step and for individual stellar particle, those stellar masses reaching the end of the main sequence phase have been identified using metallicity-dependent lifetimes (Portinari et al. 1998). The mass of each element that is lost through winds from AGB stars, winds from massive stars, and type II SNe are computed using the fraction of the initial particle mass reaching this evolutionary stage and the particle that initial elemental abundances and nucleosynthetic yields (Marigo et al. 2011; Portinari et al. 1998). Eleven elements are tracked individually. Type Ia SNe mass and energy losses are also computed. Here it is assumed that the rate of type Ia SNe per unit stellar mass is specified by an empirically-motivated exponential delay function. The mass lost by star particles is distributed among neighbouring particles using SPH kernal but mass of gas particles are set to constant initial value,$m_{\rm g}$.

1.3.5 Energy feedback

Stellar winds, radiation, and SNe facilitates the injection of energy and momentum from stars into the ISM. However, cosmological simulations, presently does not have the resolution necessary to model these outflows

from feedback injected on the scales of individual star clusters. The simplest model of energy feedback by thermal heating, is to distribute the stellar energy produced at each time-step to a number of its neighbouring hydrodynamic resolution elements. Dalla Vecchia & Schaye (2012) argued that the distribution of the feedback energy, $\sim 10^{51}$ erg per 100 $M_{\odot}$, over too much mass may be a more fundamental issue.

This results in a very low increment in temperature which is far smaller than in reality. Eventually resulting into a much shallower pressure gradients due to the heating. Thus subgrid models are needed to generate galactic wind in large-volume cosmological simulations.Three types of prescriptions are generally implemented: (a) injecting energy in kinetic form (Navarro & White 1993; Springel & Hernquist 2003; Dalla Vecchia & Schaye 2008; Dubois & Teyssier 2008) often in combination with temporarily disabling hydrodynamical forces acting on wind particles (Springel & Hernquist 2003; Okamoto et al. 2005; Oppenheimer & Davé 2006), (b) temporarily turning off radiative cooling (Gerritsen & Icke 1997; Stinson et al. 2006), and (c) explicit decoupling different thermal phases (Marri & White 2003; Scannapieco et al. 2012; Keller et al. 2014)

A stochastic thermal feedback scheme introduced in Dalla Vecchia & Schaye (2012) is implemented in EAGLE. In this scheme a specified value of the temperature increment, $\triangle T_{\rm SF}$, elements are used. This implementation fixes the quantity of energy injected per feedback event. The fraction of the energy budget available for feedback determines the probability that a resolution element neighbouring a young star particle is heated. Using the nomenclature introduced by Dalla Vecchia & Schaye (2012), this fraction is referred to as $f_{\rm th}$. The convention that $f_{\rm th} = 1$ equates to an expectation value of the injected energy of $1.736 \times 10^{49}{\rm erg M}_{\odot}^{-1}(8.73 \times 10^{15}{\rm erg\ g}^{-1})$ of stellar mass formed. This equates to the energy available from type II SNe resulting from a Chabrier IMF. This above calculation assumes that 10^{51} erg is liberated per SN, and that 6 - 100 $M_{\odot}$ stars are the progenitors of type II SNe.

Durier & Dalla Vecchia (2012) compared the sound crossing and cooling time scales. They showed that in the limit of long cooling time, implementations of thermal and kinetic feedback converge to similar solutions. For heated resolution elements, Dalla Vecchia & Schaye (2012) derived an estimate for the maximum gas density at which their stochastic heating

scheme can be efficient (their equation 18),

$$n_{\mathrm{H,t_c}} \sim 10 cm^{-3} \left(\frac{T}{10^{7.5}K}\right)^{3/2} \left(\frac{m_{\mathrm{g}}}{10^{6}\mathrm{M}_{\odot}}\right) \ , \tag{1.16}$$

where $T > \triangle T_{\mathrm{SF}}$ is the post-heating temperature.

For a constant f_{th}, the probability that a star particle triggers a heating event is inversely proportional to $\triangle T_{\mathrm{SF}}$. Using the above energy budget, Dalla Vecchia & Schaye (2012) gave an analytic expression [equation 8 therein] for the expectation value of the number of resolution elements heated by a star particle as:

$$\langle N_{\mathrm{heat}} \rangle \approx 1.3 f_{\mathrm{th}} \left(\frac{\triangle T_{SF}}{10^{7.5}K}\right)^{-1} \ . \tag{1.17}$$

1.3.6 AGN feedback and black holes

AGN feedback and growth of BHs forms an important ingredient of the EAGLE simulations. AGN feedback is essential as it shapes the gas profiles of their host haloes by quenching the star formation in massive galaxies. Two recipes are used to implement AGN feedback and BH growth, namely (i) a prescription introduced by Springel et al. (2005) and modified by Booth & Schaye (2009) and Rosas-Guevara et al. (2015) by seeding galaxies with central BHs and for following their growth via mergers and gas accretion in which accretion of stars and dark matter have been neglected, and (ii) a prescription described by Booth & Schaye (2009) for coupling the radiated energy, liberated by BH growth, injected to the ISM. Every halo $> 10^{10} M_{\odot}/h$ that does not already contain a BH, are seeded with BHs (Springel et al. 2005). FoF algorithm with linking length $b = 0.2$ on the dark matter distribution are used to find the halos.

The highest density gas particle gets transformed into a collisionless BH particle, whenever a seed id required. The converted BH inherits the particle-mass with a subgrid BH mass of $m_{\mathrm{BH}} = 10^{5}\mathrm{M}_{\odot}/\mathrm{h}$. This is smaller than the initial gas particle mass by a factor of 12.30. All calculations for gravitational interactions are computed using the particle mass, but for BH properties m_{BH} is used.

Gas accretion onto black holes

The gas accretion rate, $\dot{m}_{\rm accr}$, is specified by the minimum of the Eddington rate as:

$$\dot{m}_{\rm Edd} = \frac{4\pi G m_{\rm BH} m_{\rm p}}{\epsilon_{\rm r}\sigma_{\rm T} c} \ , \tag{1.18}$$

and

$$\dot{m}_{\rm accr} = \min\left(\dot{m}_{\rm Bondi}[(c_{\rm s}/V_\phi)^3/C_{\rm visc}], \dot{m}_{\rm Bondi}\right) \ , \tag{1.19}$$

where $m_{\rm p}$ is the proton mass, σ_T the Thomson cross section, c the speed of light, ϵ_r is the radiative efficiency of the accretion $\dot{m}_{Bondi}$ is the Bondi & Hoyle (1944) rate applicable to spherically symmetric accretion by:

$$\dot{m}_{\rm Bondi} = \frac{4\pi G^2 m_{\rm BH}^2 \rho}{(c_{\rm s}^2 + v^2)^{3/2}} \ . \tag{1.20}$$

Here v is the relative velocity of the BH and the gas, V_ϕ is the circulation speed of the gas around the BH computed using equation 16 of **?** and C_{visc} is a free parameter related to the viscosity of a notional subgrid accretion disc. The growth of the BH is specified by:

$$\dot{m}_{\rm BH} = (1-\epsilon_{\rm r})\dot{m}_{\rm accr} \ . \tag{1.21}$$

A radiative efficiency of $\epsilon_{\rm r} = 0.1$ has been assumed. The factor $(c_{\rm s}/V_\phi)^3/C_{\rm visc}$ multiplied with Bondi rate is same as the ratio of the Bondi and viscous time scales (Rosas-Guevara et al. 2015). This prescription for gas accretion differs in two aspects from the previous work: (1) the Bondi rate is not multiplied by an ad-hoc factor, α (Springel et al. 2005 used $\alpha = 100$ and Schaye et al. 2010, OWLS, and Rosas-Guevara et al. (2015) used a density dependent factor which asymptoted to unity below the star formation threshold). In EAGLE it was not required to boost the Bondi-Hoyle rate for the BH growth to become self regulated. So the number of free parameters were reduced by eleminating α. (2) Heuristic correction of Rosas-Guevara et al. (2015) has been used to account for the lower accretion rate for gas with more angular momentum.

One of the major improvement in EAGLE is done in AGN feedback. AGN feedback prescription in EAGLE adopts a single mode of thermal energy

injection implemented stochastically, similar to energy feedback from star formation. The energy injection rate is $\epsilon_{\rm f}\epsilon_{\rm r}\dot{m}_{\rm accr}c^2$, where $\epsilon_{\rm f}$ is the fraction of the radiated energy that couples to the ISM. The value of $\epsilon_{\rm f}$ must be chosen by calibrating to observations as it only affects the masses of BHs (Booth & Schaye 2009), making it vary inversely with $\epsilon_{\rm f}$, and it has little effect on the stellar mass of galaxies (provided its value is non-zero). Ensuring that the normalisation of the observed relation between BH mass and stellar mass get reproduced at $z = 0$, the parameter $\epsilon_{\rm f}$ can be calibrated.

OWLS adopted an efficiency of $\epsilon_{\rm f} = 0.15$, which is also a suitable choice at the higher resolution of EAGLE (see Schaye et al. 2015). Therefore, as feedback to the local ISM, a fraction $\epsilon_{\rm f}\epsilon_{\rm r} = 0.015$ of the accreted rest mass energy is coupled. A reservoir of feedback energy, $E_{\rm BH}$ is held by each BH. After each time step $\triangle t$, an energy $\epsilon_{\rm f}\epsilon_{\rm r}\dot{m}_{\rm accr}c^2 \triangle t$ is added to the reservoir. Once a sufficient energy is stored a in the BH to heat at least one fluid element of mass $m_{\rm g}$, it stochastically heats its SPH neighbours by a temperature increase of $\triangle T_{\rm AGN}$. The heating probability for individual SPH neighbour is:

$$P = \frac{E_{\rm BH}}{\triangle \epsilon_{\rm AGN} N_{\rm ngb} < m_{\rm g} >} \tag{1.22}$$

where $N_{\rm ngb}$ is the number of gas neighbours of the BH , $\triangle T_{\rm AGN}$ (the parameter $\triangle T_{\rm AGN}$ is converted into $\triangle \epsilon_{\rm AGN}$ assuming a fully ionised gas of primordial composition), $\triangle \epsilon_{\rm AGN}$ is the change in internal energy per unit mass corresponding to the temperature increment, and $< m_{\rm g} >$ is their mean mass. The most important parameter for the AGN feedback is $\triangle T_{\rm AGN}$. Larger values can make the individual feedback more energetic as well as intermittent.

1.3.7 Galaxy stellar mass fraction (GSMF)

Since the efficiency of the stellar feedback and the BH accretion were calibrated to broadly match the observed $z \sim 0$ GSMF subjected to the constrain that the galaxy sizes must also be reasonable, we need to see if EAGLE actually could produce better GSMF or even one which is comparable with the previous existing simulations.

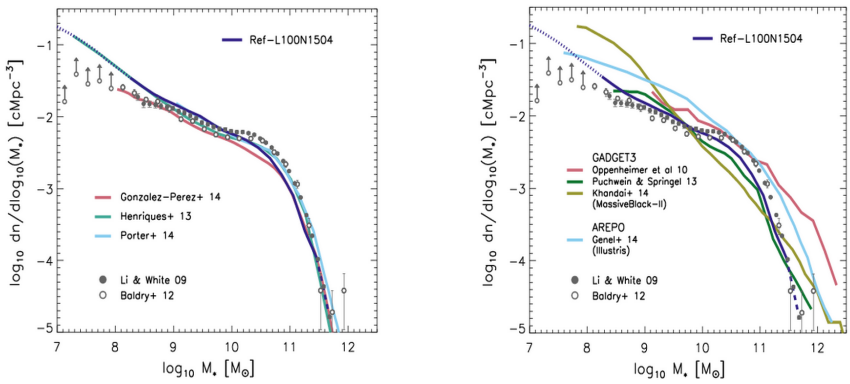

(a) (b)

Figure 1.2: Comparisons of the GSMF from EAGLE's Ref-L100N1504 with semi-analytic models (left panel) and with large hydrodynamical (right panel) simulations. Reproduced from Schaye et al. 2015

Figure 1.2 is a comparison of GSMF from EAGLE simulations with semi analytic and hydrodynamical simulations. The semi analytical models used for comparison are of Gonzalez-Perez et al. (2014), Henriques et al. (2013), and Porter et al. (2014). The large hydrodynamical simulations have been taken are of Oppenheimer et al. (2010), Puchwein & Springel (2013), the Illustris simulation (Vogelsberger et al. 2014, data taken from Genel et al. 2014), and the MassiveBlack-II simulation (Khandai et al. 2015). All models are for a Chabrier IMF. While comparing with Gonzalez-Perez et al. (2014) and Khandai et al. (2015), they have been converted from Kennicutt and Salpeter IMFs respectively to Chabrier IMF. The EAGLE curve is dotted when galaxies contain fewer than 100 stellar particles and dashed when there are fewer than 10 galaxies per stellar mass bin. Except for Oppenheimer et al. (2010), all simulations include AGN feedback. Apart from MassiveBlack-II, all models were calibrated to data. The Galform semi-analytic model of Gonzalez-Perez et al. (2014) was calibrated to fit the K-band galaxy luminosity function. The agreement with the data is relatively good for both EAGLE and the semi-analytic models, but when compared to other hydrodynamical simulations, EAGLE fits the data substantially better than them. Figures 1.2 and 1.3 have been reproduced from Schaye et al. 2015.

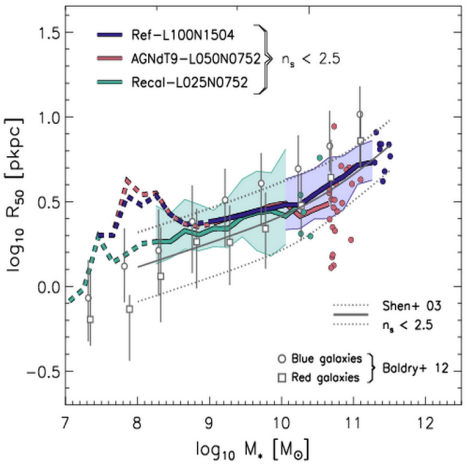

Figure 1.3: The galaxy stellar mass function at $z = 0.1$ for the EAGLE simulations Ref-L100N1504 (blue), AGNdT9-L050N0752 (red), and Recal-L025N0752 (green-blue). Reproduced from Schaye et al. 2015.

1.3.8 Limitations of EAGLE

EAGLE has achieved overall impressive agreement between different observable in the observations. Also, EAGLE results are consistent with other recent, cosmological hydrodynamical simulations (e.g. Vogelsberger et al. 2014). But there are some limitations of EAGLE that we should keep in mind. EAGLE have not attempted to model several of the small scale physical processes that are important for the formation and evolution of galaxies. For example, EAGLE does not include a cold interstellar gas phase, magnetohydrodynamics, cosmic rays, radiation transport, conduction, or non-equilibrium chemistry. Moreover, EAGLE does not distinguish between different forms of energy feedback from star formation and different forms of AGN feedback. These limitations are mainly due to resolution effect. These shortcomings can only be lifted if several orders of magnitude increase in the numerical resolution are achieved. It will take some time and improvements in technology/software or both for simulations of representative volumes to attain the desired resolution that is required to model the cold ISM. Until then we need to

rely on simulations of individual objects for better understanding of the small scale physical processes.

1.4 Gravitational lensing

In previous section we saw that the matter distribution is homogeneous and isotropic on large scales ($\sim$ 100 Mpc) but on small scales ($\sim$ 1-10 kpc), the universe is rather extremely clumpy and not at all smooth. This indicates a hierarchical structuring based on increasing larger structures. The deviations from smooth mass distribution causes a deviation from the large scale curvature of space-time. So they will distort the background emission from galaxies, quasars, CMB etc when the electromagnetic waves propagate through their gravitational field. This gravitational deflection of light is termed as *Gravitational Lensing*. The effects of these density perturbations can be large or small depending on their masses. Even before general relativity came into existence, John Mitchell in 1784 and Johann von Soldner in 1804 proposed the possibility of light being bent by mass. Later with Einstein's general relativity it was proved mathematically that mass bends space time hence effects the light passing nearby it. The effect of gravitational lensing was studied by Einstein himself (1912) and verified during a solar eclipse (1919). Galaxy-galaxy strong lensing was predicted by Zwicky in 1937 (Zwicky 1937). But only after a long 42 years wait, the first strong gravitational lens system, Q0957+561, was discovered by Walsh et al. (1979). It was a two image system of a quasar at source redshift of $z_s = 1.39$ having 6 arcsec image separation and lensed by a complex galaxy/cluster system at lens redshift $z_l = 0.36$. Now with the improvements of telescopes and new scientific selection techniques a large sample ($\sim$ 600) strong lenses have been found and studied in the last two decades. This led to the development of an active research field with Gravitational lensing technique.

According to the strength of the distortions, historically there are three distinct regimes in gravitational lensing. Each has their own unique way of measurement and astrophysical applications:

- **Strong Lensing:** The foreground mass distribution is generally a large massive object (e.g., a galaxy, a galaxy group or a cluster of galaxies) and is responsible for strong distortions creating multiple images of a single background source (e.g., another galaxy) thus

naming this effect as *Strong Lensing*. This is commonly used to provide strong constraints on the lens mass distribution (e.g., Treu & Koopmans 2004; Treu et al. 2006; Gavazzi et al. 2007; Koopmans & Treu 2003; Koopmans et al. 2006, 2009). Also when light travels through different parts of gravitational potential of the lensing mass distribution, they traverse along different paths before reaching the observer. This introduces a time delay between the lens images. The time delays are inversely proportional to the Hubble parameter H_0. Thus the measurements of the time delays between lens images via strong lensing is used to constrain H_0(Refsdal 1964, H0LiCOW project: Suyu et al. 2017).

- **Weak Lensing:** The mass distribution of a galaxy, a galaxy cluster or any massive line of sight object produce a relatively small distortion and are singly imaged. These distortions are hard to identify in individual sources and can only be measured statistically. So they are referred to as *Weak Lensing*. One can determine the average distortion of many background sources as a function of their position in sky and reconstruct the mass distribution. Weak lensing is thus generously used in constraining galaxy cluster mass profiles (Meneghetti et al. 2003, 2010, 2011; van den Bosch et al. 2013; More et al. 2013; Cacciato et al. 2013), galaxies (Harnois-Déraps et al. 2012; Giocoli et al. 2014; Li et al. 2016), and groups of galaxies (e.g., Hoekstra et al. 1999; Li et al. 2016). Also from a single cluster lens having many piecewise arcs (called 'arclets') spanning different redshifts one can obtain a relation between angular diameter distances and redshifts of those objects. This interdependence is a function of cosmological parameters. So weak lensing is also used in obtaining robust measurements of cosmological parameters (Bernardeau et al. 1997; Meneghetti et al. 2011; Giocoli et al. 2016, 2018).

- **Microlensing:** When the multiplicity of images loses its importance but still, there can be deflection of lights of typically ≤ 1 mas we enter the regime of *Microlensing*. In microlensing low mass compact objects (e.g, stars) acts as a lens. The main use of microlensing has been to detect dark matter dominated compact objects and study their mass function. The high-redshift quasars due to their compact ($\lesssim 10^{16}$cm) optical regions are always microlensed by compact objects (Hawkins 1996). However, microlensing has found relevance in the detailed

study of the stellar atmosphere of a lensed star and their accretion discs (Vernardos 2018), the structure of AGNs (Kochanek et al. 2007; Stalevski et al. 2012), dark matter substructure (Metcalf & Madau 2001; Schechter & Wambsganss 2002; Bate et al. 2011) and planetary systems (Mao & Paczynski 1991; Rattenbury et al. 2017; Han et al. 2017).

1.4.1 The lens equation

The phenomenon of gravitational lensing is depicted in Figure 1.4 where a mass concentration at a distance $D_{\rm d}$ deflects the light rays from a source at a distance $D_{\rm s}$. The magnitude and direction of the bending of light is described by the deflection angle $\hat{\alpha}$. From the geometrical picture of gravitational lensing it is clear from the similar triangles and the small-angle approximation ($\sin\hat{\alpha} \approx \hat{\alpha} \approx \tan\hat{\alpha}$):

$$\frac{\Big(\boldsymbol{\eta} + D_{\rm ds}\ \hat{\boldsymbol{\alpha}}(\boldsymbol{\xi})\Big)}{D_{\rm s}} = \frac{\boldsymbol{\xi}}{D_{\rm d}}\ , \tag{1.23}$$

where $D_{\rm s}, D_{\rm d}, D_{\rm ds}$ are angular diameter distances as shown in Fig.3.1. The above geometrical identity can be rewritten as:

$$\boldsymbol{\eta} = \frac{D_{\rm s}}{D_{\rm d}}\ \boldsymbol{\xi} - D_{\rm ds}\ \hat{\boldsymbol{\alpha}}(\boldsymbol{\xi})\ . \tag{1.24}$$

Using the angular coordinates defined by $\boldsymbol{\eta} = D_{\rm s}\boldsymbol{\beta}$ and $\boldsymbol{\xi} = D_{\rm d}\boldsymbol{\theta}$ we can write the equation as:

$$\boldsymbol{\beta} = \boldsymbol{\theta} - \frac{D_{\rm ds}}{D_{\rm s}}\ \hat{\boldsymbol{\alpha}}(D_{\rm d}\boldsymbol{\theta}) = \boldsymbol{\theta} - \boldsymbol{\alpha}\ , \tag{1.25}$$

where we have introduced the scaled deflection angle $\boldsymbol{\alpha} = \frac{D_{\rm ds}}{D_{\rm s}}\ \hat{\boldsymbol{\alpha}}(D_{\rm d}\boldsymbol{\theta})$.

The above equation is called the lens equation. So, a source with true angular position $\boldsymbol{\beta}$ will be seen by an observer at angular positions $\boldsymbol{\theta}$ which may have different values giving rise to multiple images of a single source.

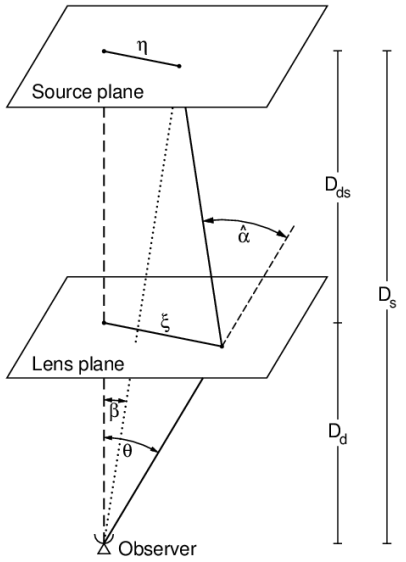

Figure 1.4: The geometry of gravitational lensing

The scaled deflection angle can be written in terms of the surface mass density as follows:

$$\boldsymbol{\alpha}(\theta) = \frac{1}{\pi} \int_{R^2} d^2\theta' \ \kappa(\boldsymbol{\theta}') \ \frac{\boldsymbol{\theta} - \boldsymbol{\theta}'}{|\boldsymbol{\theta} - \boldsymbol{\theta}'|^2} \ , \tag{1.26}$$

where the *convergence* or dimensionless surface mass density is defined as:

$$\kappa(\boldsymbol{\theta}) = \frac{\Sigma(D_{\rm d}\boldsymbol{\theta})}{\Sigma_{\rm cr}} \qquad ; \qquad \Sigma_{\rm cr} = \frac{c^2}{4\pi G} \frac{D_{\rm s}}{D_{\rm d} \ D_{\rm ds}} \ . \tag{1.27}$$

Here the *critical surface mass density* $\Sigma_{\rm cr}$ gives us a limit of strong or weak lensing. If $\kappa \geq 1$ or $\Sigma \geq \Sigma_{\rm cr}$ we can get multiple images for a single source.
Now using the mathematical identity $\nabla \ln|\boldsymbol{\theta}| \equiv \boldsymbol{\theta}/|\boldsymbol{\theta}|^2$ we can write the scaled deflection angle as a gradient of a scalar potential:

$$\boldsymbol{\alpha} = \nabla\psi \ , \tag{1.28}$$

where the lensing deflection potential is defined as:

$$\psi(\boldsymbol{\theta}) = \frac{1}{\pi} \int_{R^2} d^2\theta' \ \kappa(\boldsymbol{\theta}') \ln|\boldsymbol{\theta} - \boldsymbol{\theta}'|. \tag{1.29}$$

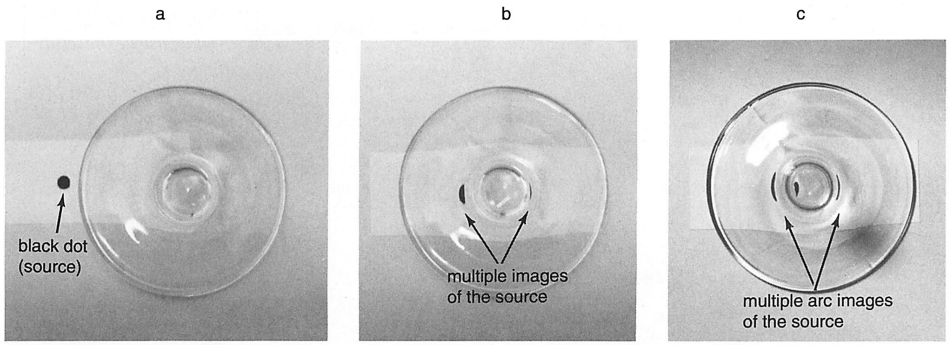

Figure 1.5: The phenomenon of gravitational lensing visualized using a wine glass bottom (lens). (a) The source (black dot) is not in the line of sight of the lens, (b) multiple images are produced when the source within the lens potential and (c) arcs and ring like structure when the source and the lens are almost collinear.

Also, we may write the Poisson's equation in two dimensions by using the identity $\nabla^2 \ln|\boldsymbol{\theta}| \equiv 2\pi\delta(\boldsymbol{\theta})$ where $\delta(\boldsymbol{\theta})$ denotes Dirac delta function:

$$\nabla^2\psi = 2\kappa \ . \tag{1.30}$$

In gravitational lensing, the shapes of the images differ from the shapes of the sources due to the differential deflection of light bundles. If there is no other source or sink of emission or absorption of photons then Liouville's theorem implies that lensing conserves surface brightness or specific intensity. So, if $I^{(s)}[\beta]$ is the surface brightness distribution at source plane, then the observed surface brightness distribution at the lens plane is:

$$I(\boldsymbol{\theta}) = I^{(s)}[\boldsymbol{\beta}(\boldsymbol{\theta})] \ . \tag{1.31}$$

The distortion of infinitesimally small images can be described by the Jacobian matrix:

$$A(\boldsymbol{\theta}) = \frac{\partial\boldsymbol{\beta}}{\partial\boldsymbol{\theta}} = \left(\delta_{\rm ij} - \frac{\partial^2\psi(\boldsymbol{\theta})}{\partial\theta_{\rm i}\partial\theta_{\rm j}}\right) = \begin{pmatrix} 1-\kappa-\gamma_1 & -\gamma_2 \\ -\gamma_2 & 1-\kappa+\gamma_1 \end{pmatrix} \ , \tag{1.32}$$

where we have introduced the complex *shear* $\gamma = \gamma_1 + i\gamma_2 = |\gamma|e^{2i\phi}$ with components:

$$\gamma_1 = \frac{1}{2}(\psi_{,11} - \psi_{,22}), \qquad \gamma_2 = \psi_{,12} \ . \tag{1.33}$$

If θ_0 is a point within an image in the image plane corresponding to a point β_0 in the source plane, we can write:

$$I(\theta) = I^{(s)}[\boldsymbol{\beta_o} + A(\boldsymbol{\theta_o}) \cdot (\boldsymbol{\theta} - \boldsymbol{\theta_o})] \ . \tag{1.34}$$

which tells us that images of circular sources are ellipses where the ratios of semi-axes of the image to the radius of the source are given by $(1-\kappa\pm|\gamma|)^{-1}$. The magnification matrix M is the inverse of the Jacobian A:

$$M(\boldsymbol{\theta}) = A^{-1} \ . \tag{1.35}$$

The magnification $|\mu(\boldsymbol{\theta_o})|$ is defined as the ratio of the fluxes observed from the image and from the unlensed source. This is given by the ratio of the integrals over $I(\boldsymbol{\theta})$ and $I^{(s)}(\boldsymbol{\beta})$ which is the same as the determinant of magnification tensor:

$$\mu = \det\ M = \frac{1}{\det\ A} = \frac{1}{(1-\kappa)^2 - |\gamma|^2} \ . \tag{1.36}$$

For a point source, the total magnification is the sum over magnifications over all its images:

$$\mu_p(\beta) = \sum_i\ |\mu(\theta_i)| \ . \tag{1.37}$$

The magnification of a real source with finite extent is then given by weighted mean of μ_p over the extended source:

$$\mu = \frac{\int d^2\beta\ I^{(s)}(\beta)\ \mu_p(\beta)}{\int d^2\beta\ I^{(s)}(\beta)} \ . \tag{1.38}$$

Critical curves are closed smooth curves on the lens plane for which $det\ A(\theta) = 0$. So, magnification $\mu = 1/detA$ diverges for an image on the critical curve. If we map these critical curves on the source plane via lens equation, we get caustics. Caustics may not necessarily be smooth and can have cusps. Critical curves and caustics are very important to understand the lens mapping qualitatively because of the following reasons:

- The magnification $\mu = \frac{1}{\det A}$ diverges for an image on a critical curve. But all astronomical sources are finite and their magnifications are also finite which makes infinite magnification unphysical. For a hypothetical source of vanishing extent, the magnification would

Image type	Lens*	Source**	Image separation	First discovery
Multiply imaged	IG & GG	CG/Q	$\sim$ 1 arcsec	Walsh et al. 1979
Giant arcs	GC or GG	EG	$\sim$ 10-20 arcsec	Lynds & Petrosian 1986
Einstein ring	IG	IG	$\sim$ 0.33-5 arcsec	Hewitt et al. 1988

*IG- Isolated Galaxy, GG- Galaxy Group, GC- Galaxy Cluster
** CG- Compact Galaxy, EG-Extended Galaxy, Q- Quasar

Table 1.1: The types of different lens systems discovered observationally and their lens and source types.

be finite as then wave optics prevails over geometric optics and the resulting diffraction pattern predicts finite though very high magnification.

- The number of images a source plane produces depends on its location relative to the caustic curves.
- Critical curves are smooth but caustics does not need to be always smooth.

1.5 Applications of strong gravitational lensing

Before discussing the applications of strong gravitational lensing let us briefly summaries the properties of lensing which finds so many applications to astrophysical studies.

Lensed images of background source(s) are the most impressive and striking manifestation of gravitational lensing. Generally, the lensed image can be (a) multiply imaged quasars, (b) giant arcs and (c) Einstein rings. In Table 1.1 we give an overview of the types of astronomical object that can be a lens(es) or source(s) in the above three kinds of lensed images and their first observational discoveries.

Two fundamental properties of strong lensing are: (a) the surface brightness of the lensed source is conserved (direct result of Liouville's theorem) and (b) magnification of the lensed image(s) compared with the observed source. Magnification again has two main contributors: (a) an isotropic stretching that depends on the local lens surface mass density and (b) an anisotropic distortion caused by shear. Mentioned in the previous section, the time

delays are also very important. Time delay is comprised of two delays: (i) *geometrical delay*, the deflected photons traverse an increased path length compared with the undeflected light path, i.e. due to the change in geometry of space-time, and (ii) *Shapiro delay* as photons travel a longer path in the curved space-time generated by a deep potential well compared to a flat space-time.

Let us now look at the astrophysical applications of gravitational lens systems. We have subdivided the applications based on the object of analysis i.e. (a) the lens and the source.

1.5.1 The Lens

Lensing is a pure geometrical effect that only involves gravity and is independent of both the dynamical state and luminous or dark nature of the matter present in the lens. Thus gravitational lensing is the most robust powerful technique to measure with a precision of less than a percentage error, the amount and distribution of mass content in galaxies and galaxy clusters.

Strong lensing measurements with known redshifts of the source and the lens, together with the fluxes, and relative positions of the lensed images make it possible for the observer to obtain information about (i) the total mass of the lens within the Einstein radius and (ii) the mass distribution properties, such as the symmetry of the potential (ellipticity, and position angle), core radius, and slope of the radial density profile according to a given cosmological model. These measurements provide crucial insight into structure formation and evolution studies:

- calculating the density profile of massive lensing galaxies at $z \gtrsim 0.1$, and the formation and evolution mechanisms of these lens systems (e.g., Koopmans et al. 2006; Auger et al. 2010b,a; Sonnenfeld et al. 2013a,b; Mukherjee et al. 2018).
- substructure detection in the dark matter halos of lens galaxies (e.g., Mao & Schneider 1998; Metcalf & Madau 2001; Dalal & Kochanek 2002; Koopmans & Treu 2003; McKean et al. 2007; Vegetti & Koopmans 2009; Vegetti et al. 2014).

1.5.2 The Source

Strong Gravitational lenses are natural telescopes due to the magnification that they introduce in the observed images. The increase in size and the conservation of surface brightness results in an increase of the observed flux with respect to the unlensed source. This magnification event of strong gravitational lenses increases the detectability of faint sources which otherwise would be below the detection limit of current instruments. On the other hand, lensed images that are resolved will benefit from the high resolution provided by the lensing magnification, which can be used to study the structure of high-redshift sources with a level of detail that would otherwise not be possible. There have been many astrophysical applications of the magnification provided by gravitational lenses. I have summarized most important of them here:

(A) **Morphology and internal dynamical properties:** High redshift sources have been extensively studied for details of their internal structure with strong lensing when they get lensed by galaxies and galaxy clusters into giant arcs or Einstein rings (Swinbank et al. 2003, 2006; Nesvadba et al. 2006; Swinbank et al. 2007; Coppin et al. 2007; Marshall et al. 2007; Stark et al. 2008; Brewer & Lewis 2008; Riechers et al. 2008; Swinbank et al. 2009; Yuan et al. 2017).

(B) **Lyα emitting galaxies:** Deep imaging and spectroscopic observations of galaxy clusters are important to search for Lyα emitting galaxies. Lensing magnification enhances the S/N ratio for these sourced and makes it possible to derive constraints on the possible contribution of low luminosity star forming galaxies to cosmic reionization (Ellis et al. 2001; Santos et al. 2004; Kneib et al. 2004; Egami et al. 2005; Richard et al. 2006; Stark et al. 2007; Richard et al. 2008; Willis et al. 2008; Livermore et al. 2012; Grillo & Fynbo 2014; Caminha et al. 2016; Croft et al. 2018).

(C) **Studying the physical properties:** Star formation rates (SFRs), metallicities, dynamical masses, velocity dispersions, and spectral energy distributions of intrinsically faint sources lensed by galaxies and galaxy clusters have been extensively studied through photometric and spectroscopic observations of them (e.g., Rigby et al. 2008; Siana et al. 2008; Finkelstein

et al. 2009; Hainline et al. 2009; Siana et al. 2009; Quider et al. 2009; Rigby et al. 2017; Johnson et al. 2017a,b).

1.5.3 Cosmological studies

Apart from these aforementioned applications strong lensing measurements are also applied for the determination of the Hubble parameter. As mentioned previously the time delays are utilized to put constraints on H_0 value. Time delay is proportional to the angular diameter distance to the lensed object, it is inversely proportional to H_0, which means that multiply imaged systems can be used to constrain H_0 (Refsdal 1964). This approach is advantageous over the traditional distance-ladder methods as it does not rely on local distance indicators and it provides a measurement of H_0 at cosmological distances, unlike distance ladder methods that are locally confined and therefore can suffer from larger fractional deviations from the Hubble flow.

Recently an international collaboration launched the H0LiCOW project (H0 Lenses in COSMOGRAIL's Wellspring, Suyu et al. 2017; Sluse et al. 2017; Rusu et al. 2017; Wong et al. 2017; Bonvin et al. 2017; Ding et al. 2017a,b; Tihhonova et al. 2018) a program that aims to measure H_0 with <3.5% uncertainty from five lens systems (B1608+656, RXJ1131–1231, HE 0435–1223, WFI2033–4723 and HE 1104–1805). The H0LiCOW project provided robust constraint on the value of H_0 and crucial insight on the systematics. H0LiCOW program established gravitational lens time delays as an independent and robust probe of cosmology. In future H0LiCOW is expected to determine H_0 to 1% from the numerous timedelay lens systems that are expected to be discovered in ongoing and future surveys.

1.6 SLACS, SL2S, and BELLS

In the field of strong gravitational lensing, the Sloan Lens ACS Survey (SLACS; Bolton et al. 2006; Koopmans et al. 2006; Bolton et al. 2008a,c; Koopmans et al. 2009; Auger et al. 2010b,a; Shu et al. 2015, 2017) is the most successful survey till date with most homogeneous sample

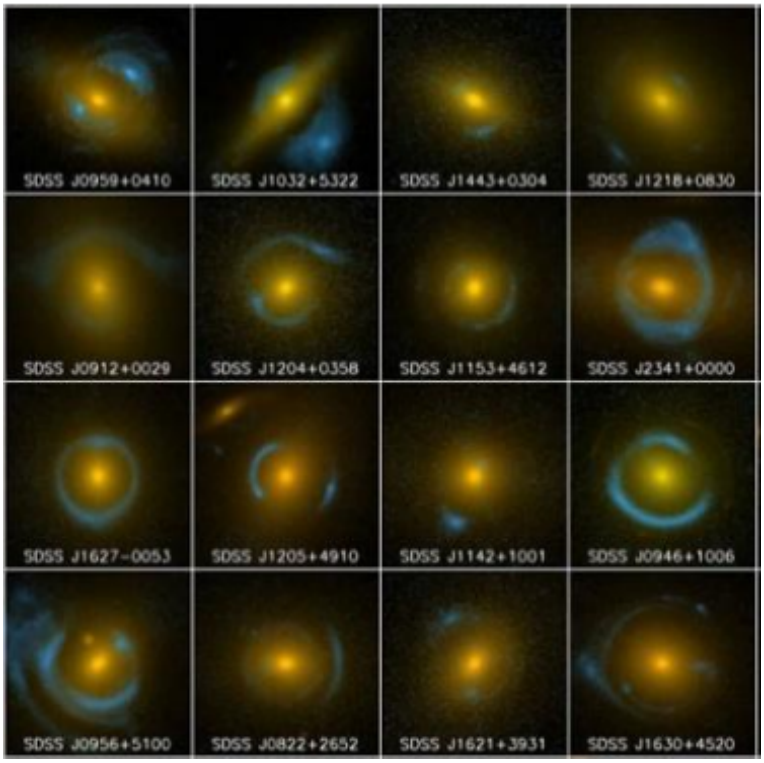

Figure 1.6: A sub-sample of SLACS lenses from Bolton et al. (2006). All the lenses in SLACS are selected from spectroscopy and hence they are dominated by luminous red lensing galaxies and large population of arc and ring systems.

(around hundred confirmed strong lens systems) of optical lenses. SLACS is a HST snapshot imaging survey, where lens candidates were selected spectroscopically from SDSS (Bolton et al. 2006). Hence the SLACS sample was primarily a lens-selected sample. With more than a hundred confirmed strong lenses, SLACS is currently the largest and most complete early-type lens survey. The SLACS candidates were selected to select Luminous Red Galaxies (LRGs) with faint star-forming background sources, generally with irregular morphology. The approximate mean Einstein radius is 1.2 arcsec (Koopmans et al. 2006; Auger et al. 2010b) with background galaxies having a typical scale length of about 0.2 arcsec (Koopmans et al. 2006). In later SLACS papers the sources were modeled with Sérsic profiles (Newton et al. 2011).

SL2S (Cabanac et al. 2007) is a survey dedicated to find and study galaxy-scale and group-scale strong gravitational lenses in the Canada France Hawaii Telescope Legacy Survey (CFHTLS). The galaxy-scale SL2S lenses are found by searching the 170 square degrees of the CFHTLS with the automated software `RingFinder` (Gavazzi et al. 2014) looking for tangentially elongated blue arcs and rings around red galaxies. The lens candidates undergo a visual inspection and the most promising systems are followed up with HST and spectroscopy. For details, one can consult Gavazzi et al. (2012).

The BOSS Emission-Line Lens Survey (BELLS; Brownstein et al. 2012) used the same methodology as SLACS to select the strong lenses, but they used Baryon Oscillation Spectroscopic Survey (BOSS; Eisenstein et al. 2011) spectra. BELLS discovered a sample of strong galaxy-galaxy lenses at substantially higher redshift that is of comparable size and homogeneity to that of SLACS at lower redshift. BELLS is also comparable in stellar mass to the SLACS lens galaxies. Both the BELLS and SLACS samples are complete in both spectroscopic lens and source galaxy redshifts.

SL2S differs from SLACS and BELLS in the way lenses are found. While in SL2S lenses are identified in wide-field imaging data, SLACS and BELLS lenses were selected by searching for spectroscopic signatures coming from two objects at different redshifts in the same line of sight in the Sloan Digital Sky Survey (SDSS) spectra. These two different techniques lead to differences in the population of lenses in the respective samples. Due to the relatively small fiber used in SDSS spectroscopic observations (1.5″ in

radius), the SLACS spectroscopic survey tends to limit the search to lenses with equivalent or smaller Einstein radii, where light of both the arcs from the lensed source and the deflector are captured within the fiber. SL2S however finds a larger number of lenses with Einstein radii greater than $1''$, because they are more clearly resolved in ground-based images. BELLS have used the same methodology as SLACS to select the strong lenses, so they do not provide additional information on selection effect (Brownstein et al. 2012).

Figure 1.6 shows a subset of SLACS lenses (Bolton et al. 2006). The morphologies are largely being arc and ring systems.

1.7 GLAMER: the ray-tracing code

GLAMER is a ray-tracing code for the simulation of gravitational lenses. It uses an Adaptive Mesh Refinement (AMR) tool in selecting the rays to dart, based on the requirements of the source size, location and surface brightness distribution or to find critical curves and caustics. There are also a range of source types to choose from: (i) circular with uniform brightness, (ii) source with analytic surface brightness distribution, (iii) pixellized surface brightness, and (iv) a number of mixed type sources having same or different redshift. It also allows for a variety of lenses: (i) analytic halos & galaxies, (ii) N-body particles (gas, dark matter and stars), and (iii) Smooth Shear fields.

The GLAMER codes are interlinked C++ scripts written in an object-oriented manner such that the user is facilitated with a great flexibility for defining the characteristics of the lenses and sources. There are a number of options allowed which are described above. Rays originate from the observer to the source plane such that the deflection, convergence, and shear are calculated. The mass distribution on each plane can be represented in several different ways. A surface density map can be given in FITS format. This option is useful for representing the output of N-body simulations and semi-analytic methods for constructing galaxies and galaxy clusters such as MOKA (Giocoli et al. 2012). The haloes described in the above section, can have a variety of mass profiles Navarro-Frenk-White (NFW) (Navarro et al. 1996, 1997), non-singular isothermal sphere (NSIE), powerlaw, Hernquist (1990), point mass, etc.

The code allows us to use any combination of these representations. For example one can use NFW profile for DM haloes, NSIE for baryonic galaxy, mass-map for mass outside of halos and the stars as point masses at the same time. So the code allows the user a large number of options, in a relatively user friendly way, in choosing for the characteristics of their lenses and the sources thus making the code powerful as well as flexible. The contributions (e.g., deflection angles, shear etc) of the halos to the lensing quantities are calculated using a modified tree algorithm described in Barnes & Hut (1989). Finally, the mass on a plane can be represented by simulation particles with an adaptive smoothing in which case the lensing quantities are calculated by a tree algorithm. Once the lens has been constructed, rays are shot back to the source plane given a uniform grid on the image plane. This initial gridding can be used to make shear or magnification map with uniform resolution if that is desired. The code finds the critical curves and caustics and increases their resolution to the desired level. The ray shootings are parallelized with POSIX threads which increases its speed of functioning.

1.7.1 Ray tracing mechanism

GLAMER, like any ray-tracing code performs two main tasks. One is to calculate the deflection angle and the other is to find and map the images. A standard gravitational lens system consisting of one source plane and one image plane where the lens acts on the image plane and maps an apparent angular position $\vec{x}$ to the angular position $\vec{y}$ on the source plane according to the *lens equation*:

$$\vec{y}(\vec{x}) = \vec{x} - \vec{\alpha}(\vec{x}) \; . \tag{1.39}$$

The function $\vec{\alpha}$ is the *deflection angle*, which for the purpose of this method characterises the lens completely. For our work we restrict ourselves to a single lens plane. For more complicated case of multiple lens planes readers can see the companion paper (Petkova et al. 2014). For a single lens plane, the coordinates can be related to points on the sky by:

$$\mathbf{x} = \mathcal{D}_l \boldsymbol{\theta} \quad , \quad \mathbf{y} = \mathcal{D}_l \boldsymbol{\beta} \tag{1.40}$$

where $\mathcal{D}_l$ is a reference distance which will usually be taken to be the angular size distance to the lens in the case of a single lens-plane. The deflection angle, $\boldsymbol{\alpha}(\mathbf{x})$, (which has units of length in this form) can be related to the true deflection angle in the path of a light-ray, $\tilde{\boldsymbol{\alpha}}(\mathbf{x})$, if the lens consists of a single plane by:

$$\boldsymbol{\alpha}(\mathbf{x}) = \frac{\mathcal{D}_l \mathcal{D}_{ls}}{\mathcal{D}_s}\, \tilde{\boldsymbol{\alpha}}(\mathbf{x}) \tag{1.41}$$

where $\mathcal{D}_s$ is the angular size distance to the source and $\mathcal{D}_{ls}$ is the angular size distance between the lens and the source. One more quantity very useful for our work is the critical surface density defined as:

$$\Sigma_{\rm crit} \equiv \frac{c^2}{4\pi G} \frac{\mathcal{D}_s}{\mathcal{D}_l \mathcal{D}_{ls}} \tag{1.42}$$

where G is Newton's constant and c is the speed of light.

The lensing equation (1.39) relates points on the lens–plane, $\mathbf{x}$, to points on the source–plane, $\mathbf{y}$. deflection angle $\boldsymbol{\alpha}(\mathbf{x})$ and the derivatives of the lens equation need to be calculated. By tradition the derivatives are grouped into the convergence, $\kappa(\mathbf{x})$, two components of shear, $\boldsymbol{\gamma}(\mathbf{x})$ and time delay, $\delta t(\mathbf{x})$, which are defined as:

$$\boldsymbol{\alpha}(\mathbf{x}) = \boldsymbol{\nabla}\psi(\mathbf{x}) \,, \tag{1.43}$$

$$\kappa(\mathbf{x}) = \frac{1}{2}\mathrm{tr}\left[\frac{\partial \boldsymbol{\alpha}}{\partial \mathbf{x}}\right] = \frac{\Sigma(\mathbf{x})}{\Sigma_{\rm crit}} \,, \tag{1.44}$$

$$\gamma_1(\mathbf{x}) = \frac{1}{2}\left[\frac{\partial \alpha_1}{\partial x_1} - \frac{\partial \alpha_2}{\partial x_2}\right] \,, \tag{1.45}$$

$$\gamma_2(\mathbf{x}) = \frac{\partial \alpha_2}{\partial x_1} = \frac{\partial \alpha_1}{\partial x_2} \,, \tag{1.46}$$

$$\delta t(\mathbf{x}) = \frac{1}{2}\left|\boldsymbol{\alpha}(\mathbf{x})\right|^2 - \psi(\mathbf{x}) \,, \tag{1.47}$$

where the second equality in (1.44) and (1.47) are only valid when assuming a single, thin lens plane. From the Poisson equation the potential is calculated as:

$$\nabla^2\psi(\mathbf{x}) = 2\,\kappa(\mathbf{x}). \tag{1.48}$$

The magnification of a point is $\mu(\mathbf{x}) = \left[(1-\kappa)^2 - |\boldsymbol{\gamma}|^2\right]^{-1}$. Quantities (1.43) through (1.47) are the lensing quantities that need to be calculated.

However, when calculating the images of finite sized sources only the deflection angle (1.43) is sufficient.

For all the work in this thesis, GLAMER reads in mass maps and use them as lens planes. In this case, it uses the Fast Fourier Transform (FFT) approach to find the lensing quantities. In FFT based deflection solver, the surface density is interpolated onto a regular, 2D grid. The lensing quantities can then be found by FFT through their connection to the lensing potential, (1.43) through (1.48). This method has the advantage of being fast scaling as $N \log N$ and not N^2 as in the case of a direct summation. In all other cases GLAMER adopts a tree deflection solver very similar to tree force solvers commonly used for N-body simulations (Barnes & Hut 1989).

A source's position and shape is chosen and its images needs to be obtained. The number, size and shape of images are completely unknown and images can be highly elongated or much smaller than others. For finding the images of point sources, GLAMER minimizes $|\mathbf{y}(\mathbf{x}) - \mathbf{y}_{\rm source}|$ with respect to $\mathbf{x}$ where $\mathbf{y}_{\rm source}$ is the source position. GLAMER adopts an adaptive mesh refinement (AMR) scheme where the points on the source plane are linked to their image points and vice versa. The source and image points are sorted into separate kd-trees so that they can be quickly searched for nearest neighbors and neighbor points within a fixed distance. Points can be continuously added to them as the grid is refined.

A telescoping source strategy is implemented to find the images. First an initial coarse grid is put down with grid spacing $\Delta_{\rm init}$. The source size is first set to $\Delta y_{\rm source} = \Delta_{\rm init}/\sqrt{\mu_{\rm min}}$ where $\mu_{\rm min}$ is the absolute value of the magnification of the smallest image that one is required to find. For non circular sources, $\Delta y_{\rm source}$ represents the largest linear dimension of the source. All the points within source are found. If any of these points have a grid size larger than $\Delta y_{\rm source}\sqrt{\mu_{\rm min}}/3$ it is refined. A grid cell is always refined by dividing it into nine subcells and thus reducing the grid spacing by 1/3. After the refinements the source size is reduced by 1/3 and the process is repeated. This is done until the desired source size is reached at which point a more complex refinement scheme is adopted.

After the target source size is attained in the telescoping stage, the code separates individual images by a neighbors-of-neighbors algorithm on the image points. The points on the inner and outer borders of each image are also found. The code goes through repeated grid refinements until a

termination criterion is met. In each refinement, only the grid points within the image or its outer border with the largest grid size are refined. First a uniform grid refinement all cells within the image and outer border is done which ensures that each detected image has at least 50 points in it.

1.7.2 Advantages of GLAMER

The main advantage of GLAMER lies in the fact that it reads in mass maps and uses them as lens planes using a FFT approach to find the lensing quantities. For calculating all other lensing quantities, GLAMER adopts a tree deflection solver very similar to tree force solvers commonly used for N-body simulations (Barnes & Hut 1989) thereby greatly reducing and overcoming the problem of the resolution of the lensing calculation being limited to the grid size on which the FFT is performed. Moreover GLAMER is the only existing code which is flexible enough to simulate many different types of lensing data include weak lensing on large scales from cosmological simulations, weak and strong lensing by galaxy clusters, galaxy–galaxy lensing, galaxy–quasar lensing, lensing by substructures in the lenses or somewhere along the line of sight and microlensing by stars in a lens galaxy.

1.8 LENSED: the modeling code

LENSED is a publicly available code which performs parametric modelling of strong lenses by taking advantage of the massively parallel ray-tracing kernel on a graphics processing unit (Tessore et al. 2016) to perform all necessary calculations. Combining these accurate and fast forward simulations with the Nested-Sampling Bayesian analysis, `MULTINEST` (Feroz & Hobson 2008; Feroz et al. 2009, 2013), allows the simultaneous optimization of tens of non-linear parameters of the selected model (e.g. lens and source) and the full posterior probability distribution for the mass distribution and the background source on a multicore machine. The setup of the physical system, priors, input files including images, masks, PSFs, and noise maps can be done using a single configuration file. The code reports statistically well-justified errors, including degeneracies, for the lens model parameters.

LENSED is characterised by its user-friendliness in setting up and handling the lens systems. This includes easy importation of images, PSFs and masks. It also has a great flexibility in modification of models. Users are able to easily create any model they choose and use the code to constrain its parameters, simultaneous fitting of sources and lenses.

1.8.1 Lens modeling

LENSED provides an implementation of the forward reconstruction method of lenses and sources from strong lensing observations where the algorithm is built around a massively parallel ray-tracing kernel that performs fast calculations on a modern graphics processing unit (GPU).

LENSED starts with an image of observed pixel values d_i and their observational variance s_i^2. Variance is generated from the data when not provided. Mask is implemented if provided otherwise it begins to build a model of the lens and sources, parametrised by a number of parameters ξ with prior probabilities $P(\xi)$. For a set of parameters ξ from the prior $P(\xi)$ it calculates the expected luminosities L_i using:

$$L_i = \int_{P_i} I(\vec{x})\, d\vec{x} \tag{1.49}$$

where $I(\vec{x})$ is the total surface brightness over the pixel area P_i. Then it calculates the likelihood $P(d \mid \xi)$ of the model using:

$$P(d_i \mid L_i) = \frac{1}{\sqrt{2\pi\, s_i^2}} \exp\left\{ -\frac{1}{2} \frac{(d_i - L_i)^2}{s_i^2} \right\} , \tag{1.50}$$

and

$$P(d \mid L) = \prod_{i=1}^{m} P(d_i \mid L_i) \, . \tag{1.51}$$

where the variance s_i^2 is fixed, d is the observing data. From (1.50) to (1.51) it is assumed that the pixels are independent. Next the posterior probability $P(\xi \mid d)$ is calculated using the likelihood $P(d \mid \xi)$ and prior $P(\xi)$. A number of set of parameters are picked and above discussed steps are repeated until the parameter space is sufficiently sampled.

The pixel luminosities (1.49) are integrated numerically via a weighted sum as:

$$L_i = \int_{P_i} I(\vec{x})\, d\vec{x} \approx \sum_{k=1}^{N} w_k\, I(\vec{x}_k)\ , \tag{1.52}$$

with weights w_k and abscissae $\vec{x}_k \in P_i$ prescribed by the Cartesian square of a classical seven-point Gauß–Kronrod quadrature rule (Patterson 1968).

Classic MCMC method have limitations to explore posterior distribution due to the high dimensionality of typical models and the usually strong correlations between individual model parameters. LENSED uses the `MULTINEST` library (Feroz & Hobson 2008; Feroz et al. 2009, 2013), which is an implementation and extension of the Nested Sampling algorithm that is well suited for working with the $10 < n < 50$ parameters, multiple modes, and correlations that typically arise in strong lensing reconstructions.

MultiNest requires the logarithm of the likelihood:

$$\log P(d \mid \xi) = \sum_{i=1}^{m} -\frac{1}{2} \left\{ \frac{(d_i - L_i)^2}{s_i^2} + \log(2\pi s_i^2) \right\}\ . \tag{1.53}$$

Since the observational variance s_i^2 is fixed, one can use:

$$\mathrm{loglike}(d \mid \xi) = -\frac{1}{2} \sum_{i=1}^{m} w_i\, (d_i - L_i)^2\ , \tag{1.54}$$

to perform the required calculations, where $w_i = 1/s_i^2$ are the weights. The second term from (1.53) which amounts to an overall normalisation that has no bearing on the results was dropped. The sum in (1.54) amounts to the usual χ^2 term, which summaries the ability of the given parameter values ξ to reconstruct the observed data. For more details one can consult Tessore et al. (2016).

1.9 Thesis motivation

The properties of early-type galaxies in the local universe obey several empirical scaling laws. But the challenge for galaxy formation models is to understand the origin of several empirical scaling laws such as the correlations between velocity dispersion and stellar ages and chemical composition (Bender et al. 1992; Burstein et al. 1992), and the correlation between velocity dispersion, effective radius, effective surface brightness known as the Fundamental Plane (Djorgovski & Davis 1987; Dressler et al. 1987) and the small scatter of the nearly-isothermal central density profiles (e.g., Rusin & Kochanek 2005; Rusin et al. 2003a; Koopmans et al. 2006, 2009) of early-type galaxies. The difficulty in understanding comes from the homogeneity of the scaling laws which is hard to explain without detailed knowledge of feedback in the hierarchical merging scenario. Treu et al. (2006) tried to tentatively quantify the degree of homogeneity of the early-type galaxies by measuring the ratio between stellar velocity dispersion and velocity dispersion of the singular isothermal ellipsoid (SIE) mass model that best fits the geometry of the multiple images, using the results of the lens models (Koopmans et al. 2006). However, there are many details of this homogeneity that remain unresolved, including an explanation for the tilt of the Fundamental Plane with respect to the virial plane and for the scatter,or finite thickness, orthogonal to the plane. Bolton et al. (2008b) have used lensing and stellar velocity dispersion to show that the dynamical mass scales with the lensing (i.e., total) mass of early-type galaxies, suggesting that non-homology is unlikely to cause the observed tilt. Dynamical and stellar population modeling combined together has predicted that more massive early-type galaxies have higher dark matter fractions (Padmanabhan et al. 2004; Auger et al. 2009; Barnabè et al. 2015; Spiniello et al. 2014) that could explain most of the tilt (Tortora et al. 2009). These models depend on assumptions about the initial mass function (IMF) and do not readily explain how the luminous bulge and a dark matter halo might produce an isothermal total mass density profile.

Strong gravitational lensing provides a complementary approach (Kochanek 1991) and a powerful observational test of these theoretical predictions for mass structures at $z \sim 1$, especially combining it with stellar kinematic data (Treu & Koopmans 2004; Sand et al. 2004; Koopmans et al. 2006). The Sloan Lens ACS Survey (SLACS, Bolton et al. 2006; Koopmans et al. 2006; Bolton et al. 2008a,c; Koopmans et al. 2009; Auger et al. 2010b,a;

Shu et al. 2015, 2017) has made this type of modeling feasible for the first time for a large and uniformly selected data-set. But these models have not been compared in detail to high resolution simulations. So scaling relations of early-type lens galaxies are still unclear. Lensing analysis has been used to demonstrate the presence of dark matter around early-type galaxies and, in some systems, to provide evidence for **isothermal** (i.e., $\rho_{tot} \propto r^{-2}$) mass density profiles equivalent to the flat rotation curves observed for spiral galaxies (Kochanek 1995; Rusin & Ma 2001; Ma 2003; Rusin et al. 2003a,b; Cohn et al. 2001; Muñoz et al. 2001; Winn et al. 2003; Wucknitz et al. 2004; Rusin & Kochanek 2005; Koopmans et al. 2006, 2009). However, the mass-profile and mass-sheet degeneracy often prevent a truly accurate determination of the logarithmic density slope at the Einstein radius (Wucknitz 2002; Falco et al. 1985). Recent studies (Vegetti & Koopmans 2009; Vegetti et al. 2014) gave considerable information of cold dark matter substructure at $z \sim 0.2$ and provided constraints on substructure mass functions form strong gravitational lensing point of view.

In this thesis, I intend to give more insight into the understanding of the galaxy formation mechanism by comparing simulated strongly lensed galaxies with observationally confirmed, strong lens systems from SLACS (Auger et al. 2010b,a), SL2S (Sonnenfeld et al. 2013a,b) and BELLS (Brownstein et al. 2012). Using a very high resolution hydrodynamic simulations, EAGLE (described in more details in chapter 4), I plan to create an ensemble of early type galaxies that mimics selected SLACS strong lenses. This will be done for a range of galaxy formations scenarios (Crain et al. 2015).

This thesis aims to address the issues of mass measurement and test the models (discussed in section 2.1) against IMF variations of EAGLE simulations. This work involving simulations of strong gravitational lensed galaxies from EAGLE (Schaye et al. 2015) having different sub-grid models (Crain et al. 2015) with IMF variations, is expected to explore the effect of IMF on mass distributions more critically than before. Viewing galaxies from random line of sight will provide a statistical solution to the aforesaid problems. We will compare the results obtained by putting similar constraints on EAGLE simulations and if possible fine tune them to get tighter upper and lower bounds of the constraints.

Based on the limited amount of information available so far, no significant difference has been found between the structural properties (e.g. Treu & Koopmans 2004) of lens and non-lens galaxies. Although there have been some attempts to analyze the radial distribution of substructures and satellite galaxies using hydrodynamic simulations (Macciò et al. 2005) and give statistics of gravitationally lensed arcs in galaxy clusters for constraining cosmological models (Meneghetti et al. 2003), but no such notable attempts of probing the galaxy formation mechanism have been done from strong lensing point of view using high resolution hydrodynamic simulations. Previous studies have been mostly involved dark matter only simulations with much coarser resolutions than EAGLE. This thesis attempts to provide valuable insight to the problems of differentiating structural properties of lens and non lens galaxies with EAGLE (Schaye et al. 2015; Crain et al. 2015) from strong gravitational lensing's view point.

The reasons for tilting of the Fundamental plane, which is thought to be related to a varying mass-to-light ratio, can be tested for various inner and outer density profiles corresponding to different variations in sub-grid physics. EAGLE simulations (Schaye et al. 2015) with more realistic star formation and AGN feedback process implemented thermally so that pressure gradient results in outflow without any ad hock imposition, are best suited to explore the issues of underlying principal of scaling laws in much more details than any other previous studies.

1.9.1 Outline

Here I give a chapter-wise outline of the thesis. I start by giving details of the entire theoretical framework and then give descriptions about the strong lensing analysis with their results.

Chapter 2
This chapter introduces the *SEAGLE* (i.e. Simulating EAGLE LEnses) pipeline in details. We briefly summarize the details of Evolution and Assembly of GaLaxies and their Environments (EAGLE) simulation and analysis pipeline together with the first set of results from the analysis of early-type galaxies. The details of the methodology that identifies and extracts an ensemble of simulated lens galaxies and creates mock lenses using the `GLAMER` ray-tracing lensing code are presented in this chapter. The simulated strong lenses are strikingly similar to those observed in the SLACS and SL2S surveys after including observational effects such as the Point-Spread-Function (PSF), pixelization and noise levels. The simulated lenses are subsequently modeled using the code `LENSED` and the results are compared with SLACS and SL2S observations.

Chapter 3, 4
These chapters explore the global properties of EAGLE lensing galaxies from 9 different galaxy formation scenarios testing the effect of different baryonic physics. In Chapter 3 the total mass density slopes, ellipticities and position angles are calculated for massive galaxies. This is followed by Chapter 4 where the focus is on determining the dark matter fractions for EAGLE galaxies that were analysed previously in Chapter 3.

Chapter 5
This chapter describes the role of IMF in lensing observables. Here I used a suite of cosmological, hydrodynamical simulations that self-consistently vary the IMF on a per-particle basis as a function of the ISM pressure from which star particles are born. These simulations, which adopt respectively a bottom-heavy and a top-heavy IMF, use the EAGLE model for galaxy formation and thus providing an excellent baseline for comparing different

observations with either a constant IMF.

Chapter 6
Finally, I summarize our most significant results and our main conclusions drawn from them. I also outline a few possible realistic future works based on the research carried out in this Thesis.

References

Auger, M. W., Treu, T., Bolton, A. S., et al. 2009, ApJ, 705, 1099
Auger, M. W., Treu, T., Bolton, A. S., et al. 2010a, ApJ, 724, 511
Auger, M. W., Treu, T., Gavazzi, R., et al. 2010b, ApJL, 721, L163
Bardeen, J. M., Bond, J. R., Kaiser, N., & Szalay, A. S. 1986, ApJ, 304, 15
Barnabè, M., Spiniello, C., & Koopmans, L. V. E. 2015, in IAU Symposium, Vol. 309, Galaxies in 3D across the Universe, ed. B. L. Ziegler, F. Combes, H. Dannerbauer, & M. Verdugo, 77–80
Barnes, J. E. & Hut, P. 1989, ApJS, 70, 389
Bate, N. F., Floyd, D. J. E., Webster, R. L., & Wyithe, J. S. B. 2011, ApJ, 731, 71
Baugh, C. M. 2006, Reports on Progress in Physics, 69, 3101
Begeman, K. G. 1989, A&A, 223, 47
Bender, R., Burstein, D., & Faber, S. M. 1992, ApJ, 399, 462
Bernardeau, F., van Waerbeke, L., & Mellier, Y. 1997, A&A, 322, 1
Blumenthal, G. R., Faber, S. M., Primack, J. R., & Rees, M. J. 1984, Nature, 311, 517
Bolton, A. S., Burles, S., Koopmans, L. V. E., et al. 2008a, ApJ, 682, 964
Bolton, A. S., Burles, S., Koopmans, L. V. E., et al. 2008b, ApJ, 682, 964
Bolton, A. S., Burles, S., Koopmans, L. V. E., Treu, T., & Moustakas, L. A. 2006, ApJ, 638, 703
Bolton, A. S., Treu, T., Koopmans, L. V. E., et al. 2008c, ApJ, 684, 248
Bondi, H. & Hoyle, F. 1944, MNRAS, 104, 273
Bonvin, V., Courbin, F., Suyu, S. H., et al. 2017, MNRAS, 465, 4914
Booth, C. M. & Schaye, J. 2009, MNRAS, 398, 53
Brewer, B. J. & Lewis, G. F. 2008, MNRAS, 390, 39
Brownstein, J. R., Bolton, A. S., Schlegel, D. J., et al. 2012, ApJ, 744, 41
Bullock, J. S., Kolatt, T. S., Sigad, Y., et al. 2001, MNRAS, 321, 559
Burstein, D., Haynes, M. P., & Faber, S. M. 1992, Nature, 356, 114
Cabanac, R. A., Alard, C., Dantel-Fort, M., et al. 2007, A&A, 461, 813
Cacciato, M., van den Bosch, F. C., More, S., Mo, H., & Yang, X. 2013, MNRAS, 430, 767
Caminha, G. B., Karman, W., Rosati, P., et al. 2016, A&A, 595, A100
Carroll, S. M. 2001, Living Reviews in Relativity, 4, 1
Chabrier, G. 2003, PASP, 115, 763
Cohn, J. D., Kochanek, C. S., McLeod, B. A., & Keeton, C. R. 2001, ApJ, 554, 1216

Coles, P. & Lucchin, F. 2002, Cosmology: The Origin and Evolution of Cosmic Structure, Second Edition, 512
Cooray, A. & Sheth, R. 2002, Physics Reports, 372, 1
Coppin, K. E. K., Swinbank, A. M., Neri, R., et al. 2007, ApJ, 665, 936
Crain, R. A., Schaye, J., Bower, R. G., et al. 2015, MNRAS, 450, 1937
Crain, R. A., Theuns, T., Dalla Vecchia, C., et al. 2009, MNRAS, 399, 1773
Croft, R. A. C., Romeo, A., & Metcalf, R. B. 2018, MNRAS, 477, 1814
Dalal, N. & Kochanek, C. S. 2002, ApJ, 572, 25
Dalla Vecchia, C. & Schaye, J. 2008, MNRAS, 387, 1431
Dalla Vecchia, C. & Schaye, J. 2012, MNRAS, 426, 140
Davis, M., Efstathiou, G., Frenk, C. S., & White, S. D. M. 1985, ApJ, 292, 371
Ding, X., Liao, K., Treu, T., et al. 2017a, MNRAS, 465, 4634
Ding, X., Treu, T., Suyu, S. H., et al. 2017b, MNRAS, 472, 90
Djorgovski, S. & Davis, M. 1987, ApJ, 313, 59
Dolag, K., Borgani, S., Murante, G., & Springel, V. 2009, MNRAS, 399, 497
Dressler, A., Lynden-Bell, D., Burstein, D., et al. 1987, ApJ, 313, 42
Dubois, Y. & Teyssier, R. 2008, A&A, 482, L13
Durier, F. & Dalla Vecchia, C. 2012, MNRAS, 419, 465
Egami, E., Kneib, J.-P., Rieke, G. H., et al. 2005, ApJL, 618, L5
Eisenstein, D. J., Weinberg, D. H., Agol, E., et al. 2011, AJ, 142, 72
Ellis, R., Santos, M. R., Kneib, J.-P., & Kuijken, K. 2001, ApJL, 560, L119
Falco, E. E., Gorenstein, M. V., & Shapiro, I. I. 1985, ApJL, 289, L1
Ferland, G. J., Korista, K. T., Verner, D. A., et al. 1998, PASP, 110, 761
Feroz, F. & Hobson, M. P. 2008, MNRAS, 384, 449
Feroz, F., Hobson, M. P., & Bridges, M. 2009, MNRAS, 398, 1601
Feroz, F., Hobson, M. P., Cameron, E., & Pettitt, A. N. 2013, ArXiv e-prints
Finkelstein, S. L., Rhoads, J. E., Malhotra, S., & Grogin, N. 2009, ApJ, 691, 465
Freedman, W. L., Madore, B. F., Scowcroft, V., et al. 2012, ApJ, 758, 24
Gavazzi, R., Marshall, P. J., Treu, T., & Sonnenfeld, A. 2014, ApJ, 785, 144
Gavazzi, R., Treu, T., Marshall, P. J., Brault, F., & Ruff, A. 2012, ApJ, 761, 170
Gavazzi, R., Treu, T., Rhodes, J. D., et al. 2007, ApJ, 667, 176
Genel, S., Vogelsberger, M., Springel, V., et al. 2014, MNRAS, 445, 175

Genzel, R., Tacconi, L. J., Gracia-Carpio, J., et al. 2010, MNRAS, 407, 2091
Gerritsen, J. P. E. & Icke, V. 1997, A&A, 325, 972
Giocoli, C., Baldi, M., & Moscardini, L. 2018, ArXiv e-prints
Giocoli, C., Jullo, E., Metcalf, R. B., et al. 2016, MNRAS, 461, 209
Giocoli, C., Meneghetti, M., Metcalf, R. B., Ettori, S., & Moscardini, L. 2014, MNRAS, 440, 1899
Giocoli, C., Tormen, G., & Sheth, R. K. 2012, MNRAS, 422, 185
Gonzalez-Perez, V., Lacey, C. G., Baugh, C. M., et al. 2014, MNRAS, 439, 264
Grillo, C. & Fynbo, J. P. U. 2014, MNRAS, 439, L100
Guth, A. H. & Sher, M. 1983, Nature, 302, 505
Guth, A. H. & Steinhardt, P. J. 1984, Scientific American, 250, 116
Guth, A. H. & Weinberg, E. J. 1983, Nuclear Physics B, 212, 321
Haardt, F. & Madau, P. 2001, in Clusters of Galaxies and the High Redshift Universe Observed in X-rays, ed. D. M. Neumann & J. T. V. Tran
Hainline, K. N., Shapley, A. E., Kornei, K. A., et al. 2009, ApJ, 701, 52
Han, C., Udalski, A., Gould, A., et al. 2017, AJ, 154, 223
Harnois-Déraps, J., Vafaei, S., & Van Waerbeke, L. 2012, MNRAS, 426, 1262
Harrison, E. R. 1970, Physical Review D, 1, 2726
Hawkins, M. R. S. 1996, MNRAS, 278, 787
Henriques, B. M. B., White, S. D. M., Thomas, P. A., et al. 2013, MNRAS, 431, 3373
Hernquist, L. 1990, ApJ, 356, 359
Hewitt, J. N., Turner, E. L., Schneider, D. P., Burke, B. F., & Langston, G. I. 1988, Nature, 333, 537
Hoekstra, H., Franx, M., & Kuijken, K. 1999, ArXiv Astrophysics e-prints
Hubble, E. 1929, Proceedings of the National Academy of Science, 15, 168
Johnson, T. L., Rigby, J. R., Sharon, K., et al. 2017a, ApJL, 843, L21
Johnson, T. L., Sharon, K., Gladders, M. D., et al. 2017b, ApJ, 843, 78
Keller, B. W., Wadsley, J., Benincasa, S. M., & Couchman, H. M. P. 2014, MNRAS, 442, 3013
Kennicutt, Jr., R. C. 1998, ARA&A, 36, 189
Khandai, N., Di Matteo, T., Croft, R., et al. 2015, MNRAS, 450, 1349
Kneib, J.-P., Ellis, R. S., Santos, M. R., & Richard, J. 2004, ApJ, 607, 697
Kochanek, C. S. 1991, ApJ, 382, 58
Kochanek, C. S. 1995, ApJ, 445, 559

Kochanek, C. S., Dai, X., Morgan, C., Morgan, N., & Poindexter, G., S. C. 2007, in Astronomical Society of the Pacific Conference Series, Vol. 371, Statistical Challenges in Modern Astronomy IV, ed. G. J. Babu & E. D. Feigelson, 43
Koopmans, L. V. E., Bolton, A., Treu, T., et al. 2009, ApJL, 703, L51
Koopmans, L. V. E. & Treu, T. 2003, ApJ, 583, 606
Koopmans, L. V. E., Treu, T., Bolton, A. S., Burles, S., & Moustakas, L. A. 2006, ApJ, 649, 599
Le Brun, A. M. C., McCarthy, I. G., Schaye, J., & Ponman, T. J. 2014, Monthly Notices of the Royal Astronomical Society, 441, 1270
Li, N., Gladders, M. D., Rangel, E. M., et al. 2016, ApJ, 828, 54
Livermore, R. C., Jones, T., Richard, J., et al. 2012, Monthly Notices of the Royal Astronomical Society, 427, 688
Lynds, R. & Petrosian, V. 1986, in BAAS, Vol. 18, Bulletin of the American Astronomical Society, 1014
Ma, C.-P. 2003, ApJL, 584, L1
Macciò, A. V., Governato, F., & Horellou, C. 2005, MNRAS, 359, 941
Mao, S. & Paczynski, B. 1991, ApJL, 374, L37
Mao, S. & Schneider, P. 1998, MNRAS, 295, 587
Marigo, P., Bressan, A., Girardi, L., et al. 2011, in Astronomical Society of the Pacific Conference Series, Vol. 445, Why Galaxies Care about AGB Stars II: Shining Examples and Common Inhabitants, ed. F. Kerschbaum, T. Lebzelter, & R. F. Wing, 431
Marri, S. & White, S. D. M. 2003, MNRAS, 345, 561
Marshall, P. J., Treu, T., Melbourne, J., et al. 2007, ApJ, 671, 1196
McKean, J. P., Koopmans, L. V. E., Flack, C. E., et al. 2007, MNRAS, 378, 109
Meneghetti, M., Bartelmann, M., & Moscardini, L. 2003, MNRAS, 340, 105
Meneghetti, M., Fedeli, C., Zitrin, A., et al. 2011, A&A, 530, A17
Meneghetti, M., Rasia, E., Merten, J., et al. 2010, A&A, 514, A93
Metcalf, R. B. & Madau, P. 2001, ApJ, 563, 9
More, S., van den Bosch, F. C., Cacciato, M., et al. 2013, MNRAS, 430, 747
Muñoz, J. A., Kochanek, C. S., & Keeton, C. R. 2001, ApJ, 558, 657
Mukherjee, S., Koopmans, L. V. E., Metcalf, R. B., et al. 2018, MNRAS, 479, 4108
Navarro, J. F., Frenk, C. S., & White, S. D. M. 1996, ApJ, 462, 563

Navarro, J. F., Frenk, C. S., & White, S. D. M. 1997, ApJ, 490, 493
Navarro, J. F. & White, S. D. M. 1993, MNRAS, 265, 271
Nesvadba, N. P. H., Lehnert, M. D., Eisenhauer, F., et al. 2006, ApJ, 650, 693
Newton, E. R., Marshall, P. J., Treu, T., et al. 2011, ApJ, 734, 104
Okamoto, T., Eke, V. R., Frenk, C. S., & Jenkins, A. 2005, MNRAS, 363, 1299
Oppenheimer, B. D. & Davé, R. 2006, MNRAS, 373, 1265
Oppenheimer, B. D., Davé, R., Kereš, D., et al. 2010, MNRAS, 406, 2325
Ostriker, J. P. & Peebles, P. J. E. 1973, ApJ, 186, 467
Ostriker, J. P., Peebles, P. J. E., & Yahil, A. 1974, ApJL, 193, L1
Padmanabhan, N., Seljak, U., Strauss, M. A., et al. 2004, New Astronomy, 9, 329
Patterson, T. N. L. 1968, Mathematics of Computation, 22, 847
Peebles, P. J. E. 1982, ApJL, 263, L1
Peebles, P. J. E. & Yu, J. T. 1970, ApJ, 162, 815
Petkova, M., Metcalf, R. B., & Giocoli, C. 2014, MNRAS, 445, 1954
Planck Collaboration, Ade, P. A. R., Aghanim, N., et al. 2014, A&A, 571, A16
Porter, L. A., Somerville, R. S., Primack, J. R., & Johansson, P. H. 2014, MNRAS, 444, 942
Portinari, L., Chiosi, C., & Bressan, A. 1998, A&A, 334, 505
Press, W. H. & Schechter, P. 1974, ApJ, 187, 425
Puchwein, E. & Springel, V. 2013, MNRAS, 428, 2966
Quider, A. M., Pettini, M., Shapley, A. E., & Steidel, C. C. 2009, MNRAS, 398, 1263
Rattenbury, N. J., Bennett, D. P., Sumi, T., et al. 2017, MNRAS, 466, 2710
Refsdal, S. 1964, MNRAS, 128, 307
Richard, J., Pelló, R., Schaerer, D., Le Borgne, J.-F., & Kneib, J.-P. 2006, A&A, 456, 861
Richard, J., Stark, D. P., Ellis, R. S., et al. 2008, ApJ, 685, 705
Riechers, D. A., Walter, F., Carilli, C. L., Bertoldi, F., & Momjian, E. 2008, ApJL, 686, L9
Riess, A. G., Filippenko, A. V., Challis, P., et al. 1998, AJ, 116, 1009
Rigby, J. R., Johnson, T. L., Sharon, K., et al. 2017, ApJ, 843, 79
Rigby, J. R., Marcillac, D., Egami, E., et al. 2008, ApJ, 675, 262
Roberts, M. S. & Rots, A. H. 1973, A&A, 26, 483

Rosas-Guevara, Y. M., Bower, R. G., Schaye, J., et al. 2015, MNRAS, 454, 1038
Rubin, V. C. & Ford, Jr., W. K. 1970, ApJ, 159, 379
Rusin, D. & Kochanek, C. S. 2005, ApJ, 623, 666
Rusin, D., Kochanek, C. S., Falco, E. E., et al. 2003a, ApJ, 587, 143
Rusin, D., Kochanek, C. S., & Keeton, C. R. 2003b, ApJ, 595, 29
Rusin, D. & Ma, C.-P. 2001, ApJL, 549, L33
Rusu, C. E., Fassnacht, C. D., Sluse, D., et al. 2017, MNRAS, 467, 4220
Sand, D. J., Treu, T., Smith, G. P., & Ellis, R. S. 2004, ApJ, 604, 88
Santos, N. C., Israelian, G., & Mayor, M. 2004, A&A, 415, 1153
Scannapieco, C., Wadepuhl, M., Parry, O. H., et al. 2012, MNRAS, 423, 1726
Schaller, M. 2015, PhD thesis, Durham University, UK
Schaller, M., Frenk, C. S., Bower, R. G., et al. 2015a, MNRAS, 451, 1247
Schaller, M., Frenk, C. S., Bower, R. G., et al. 2015b, MNRAS, 452, 343
Schaye, J. 2004, ApJ, 609, 667
Schaye, J., Crain, R. A., Bower, R. G., et al. 2015, MNRAS, 446, 521
Schaye, J. & Dalla Vecchia, C. 2008, MNRAS, 383, 1210
Schaye, J., Dalla Vecchia, C., Booth, C. M., et al. 2010, MNRAS, 402, 1536
Schaye, J., Theuns, T., Rauch, M., Efstathiou, G., & Sargent, W. L. W. 2000, MNRAS, 318, 817
Schechter, P. L. & Wambsganss, J. 2002, ApJ, 580, 685
Segers, M. C., Schaye, J., Bower, R. G., et al. 2016, MNRAS, 461, L102
Shu, Y., Bolton, A. S., Brownstein, J. R., et al. 2015, ApJ, 803, 71
Shu, Y., Brownstein, J. R., Bolton, A. S., et al. 2017, ArXiv e-prints
Siana, B., Smail, I., Swinbank, A. M., et al. 2009, ApJ, 698, 1273
Siana, B., Teplitz, H. I., Chary, R.-R., Colbert, J., & Frayer, D. T. 2008, ApJ, 689, 59
Sluse, D., Sonnenfeld, A., Rumbaugh, N., et al. 2017, MNRAS, 470, 4838
Sonnenfeld, A., Gavazzi, R., Suyu, S. H., Treu, T., & Marshall, P. J. 2013a, ApJ, 777, 97
Sonnenfeld, A., Treu, T., Gavazzi, R., et al. 2013b, ApJ, 777, 98
Spergel, D. N., Verde, L., Peiris, H. V., et al. 2003, ApJS, 148, 175
Spiniello, C., Trager, S., Koopmans, L. V. E., & Conroy, C. 2014, MNRAS, 438, 1483
Springel, V. 2005, MNRAS, 364, 1105
Springel, V. & Hernquist, L. 2003, MNRAS, 339, 289
Springel, V., White, S. D. M., Jenkins, A., et al. 2005, Nature, 435, 629

Springel, V., Yoshida, N., & White, S. D. M. 2001, New Astronomy, 6, 79
Stalevski, M., Jovanović, P., Popović, L. Č., & Baes, M. 2012, MNRAS, 425, 1576
Stark, D. P., Ellis, R. S., Richard, J., et al. 2007, ApJ, 663, 10
Stark, D. P., Swinbank, A. M., Ellis, R. S., et al. 2008, Nature, 455, 775
Stinson, G., Seth, A., Katz, N., et al. 2006, MNRAS, 373, 1074
Suyu, S. H., Bonvin, V., Courbin, F., et al. 2017, MNRAS, 468, 2590
Swinbank, A. M., Bower, R. G., Smith, G. P., et al. 2007, MNRAS, 376, 479
Swinbank, A. M., Chapman, S. C., Smail, I., et al. 2006, MNRAS, 371, 465
Swinbank, A. M., Smith, J., Bower, R. G., et al. 2003, ApJ, 598, 162
Swinbank, A. M., Webb, T. M., Richard, J., et al. 2009, MNRAS, 400, 1121
Tessore, N., Bellagamba, F., & Metcalf, R. B. 2016, MNRAS, 463, 3115
Tihhonova, O., Courbin, F., Harvey, D., et al. 2018, MNRAS, 477, 5657
Tortora, C., Napolitano, N. R., Romanowsky, A. J., Capaccioli, M., & Covone, G. 2009, MNRAS, 396, 1132
Treu, T., Koopmans, L. V., Bolton, A. S., Burles, S., & Moustakas, L. A. 2006, ApJ, 640, 662
Treu, T. & Koopmans, L. V. E. 2004, ApJ, 611, 739
van den Bosch, F. C., More, S., Cacciato, M., Mo, H., & Yang, X. 2013, MNRAS, 430, 725
Vegetti, S. & Koopmans, L. V. E. 2009, MNRAS, 392, 945
Vegetti, S., Koopmans, L. V. E., Auger, M. W., Treu, T., & Bolton, A. S. 2014, MNRAS, 442, 2017
Vernardos, G. 2018, MNRAS
Vogelsberger, M., Genel, S., Springel, V., et al. 2014, MNRAS, 444, 1518
Walsh, D., Carswell, R. F., & Weymann, R. J. 1979, Nature, 279, 381
Wechsler, R. H., Bullock, J. S., Primack, J. R., Kravtsov, A. V., & Dekel, A. 2002, ApJ, 568, 52
White, S. D. M. & Rees, M. J. 1978, MNRAS, 183, 341
Wiersma, R. P. C., Schaye, J., & Smith, B. D. 2009a, MNRAS, 393, 99
Wiersma, R. P. C., Schaye, J., Theuns, T., Dalla Vecchia, C., & Tornatore, L. 2009b, MNRAS, 399, 574
Willis, J. P., Courbin, F., Kneib, J.-P., & Minniti, D. 2008, MNRAS, 384, 1039
Winn, J. N., Rusin, D., & Kochanek, C. S. 2003, ApJ, 587, 80
Wong, K. C., Suyu, S. H., Auger, M. W., et al. 2017, Monthly Notices Of The Royal Astronomical Society, 465, 19. 4895

Wucknitz, O. 2002, MNRAS, 332, 951
Wucknitz, O., Biggs, A. D., & Browne, I. W. A. 2004, MNRAS, 349, 14
Yuan, T., Richard, J., Gupta, A., et al. 2017, ApJ, 850, 61
Zeldovich, Y. B. 1972, MNRAS, 160, 1P
Zhao, D. H., Jing, Y. P., Mo, H. J., & Börner, G. 2009, ApJ, 707, 354
Zwicky, F. 1937, ApJ, 86, 217

Chapter 2

A novel pipeline for Simulating EAGLE LEnses

Based on

SEAGLE – I: A pipeline for simulating and modeling strong lenses from cosmological hydrodynamic simulations,

Sampath Mukherjee, Léon V. E. Koopmans, R. Benton Metcalf, Nicolas Tessore, Crescenzo Tortora, Matthieu Schaller, Joop Schaye, Robert A. Crain, Giorgos Vernardos, Fabio Bellagamba, Tom Theuns

MNRAS, 2018, 479, 4108

Abstract

In this chapter we introduce the *SEAGLE* (i.e. Simulating EAGLE LEnses) program, that approaches the study of galaxy formation through strong gravitational lensing, using a suite of high-resolution hydrodynamic simulations, Evolution and Assembly of GaLaxies and their Environments (EAGLE) project. Here we introduce the simulation and analysis pipeline and present the first set of results from our analysis of early-type galaxies. We identify and extract an ensemble of simulated lens galaxies and use the `GLAMER` ray-tracing lensing code to create mock lenses similar to those observed in the SLACS and SL2S surveys, using a range of source parameters and galaxy orientations, including observational effects such as the Point-Spread-Function (PSF), pixelization and noise levels, representative of single-orbit observations with the Hubble Space Telescope (HST) using the ACS-F814W filter. We subsequently model these mock lenses using the code `LENSED`, treating them in the same way as observed lenses. We also estimate the mass model parameters directly from the projected surface mass density of the simulated galaxy, using an identical mass model family. We perform a three-way comparison of all the measured quantities with real lenses. The average total density slope of EAGLE lenses, $t = 2.26$ (0.25 rms) to be higher than SL2S, $t = 2.16$ or SLACS, $t = 2.08$. We find a very strong correlation between the external shear (γ) and the complex ellipticity (ϵ), with $\gamma \sim \epsilon/4$. This correlation indicates a degeneracy in the lens mass modeling. A dispersion is also seen between lens modeling and direct fitting results, indicating systematical biases.

2.1 Introduction

Massive early-type galaxies (ETGs) are expected to form during the later stages in the hierarchical formation process (Blumenthal et al. 1984; Frenk et al. 1985). ETGs in the local universe follow a number of well-known relations or correlations between their velocity dispersion, stellar age, chemical composition (Bender et al. 1992, 1993), and exhibit a small scatter around the nearly-isothermal central density profiles (e.g., Rusin et al. 2003a,b; Rusin & Kochanek 2005; Koopmans et al. 2006, 2009). Galaxy formation models are only now beginning to address the origin of these empirical scaling relations accounting for the physical processes that play a role in their formation. There are various possibilities for their formation, for example via monolithic collapse (Eggen 1965; Searle & Zinn 1978), mergers of lower-mass (disk) galaxies (Toomre & Toomre 1972; Schweizer 1982), satellite accretion (Searle & Zinn 1978), and hierarchical merging (White & Rees 1978; Fall 1983). Various environmentally dependent evolutionary processes such as stripping (Gunn & Gott 1972), cannibalism (Ostriker & Hausman 1977), stretching (Barnes & Hernquist 1992), harassment (Moore et al. 1998), strangulation (Balogh & Morris 2000), squelching (Tully et al. 2002) and splash-back (Fukugita & Peebles 2006) have been proposed to explain the formation-mechanisms of early-type galaxies. The explicit study of their structure (Navarro et al. 1996; Moore et al. 1998), formation and subsequent evolution provides a powerful test of the (dis)agreement between observations and the ΛCDM paradigm.

Loeb & Peebles (2003) suggest that the inner regions might behave as dynamical attractors, whose phase-space density is nearly invariant under the accretion of collisionless matter (Gao et al. 2004; Kazantzidis et al. 2006). In this scenario, one might expect less structural evolution of the inner regions of massive early-type galaxies at $z < 1$, compared to models in which most gas had not yet turned into stars before the mass assembly of their inner regions took place. Hence, one way to study the formation scenario of massive elliptical galaxies is to quantify the evolution of the mass distribution in their inner regions in the redshift range $0 < z < 1$.

Over the last few decades, tremendous progress has been made in our understanding of cosmic structure and galaxy formations mechanisms. This is in part due to (semi) analytic galaxy-formation theory giving us detailed calculations of the Cold Dark Matter (CDM) power spectrum (Peebles 1982;

Blumenthal et al. 1984), Press-Schechter theory (Press & Schechter 1974), the statistics of peaks in Gaussian Random fields (Bardeen et al. 1986) and galaxy formation models (White & Rees 1978). Analytical approaches have their limitations though in addressing more complicated physical processes. In the absence of precise analytical methods for computing for example the non-linear dark matter power spectrum, the properties of dark matter substructure, etc., full-scale numerical simulations are the only method available. Semi-numerical models have also been employed, building on numerical simulations. The combined results of these semi-analytical and numerical simulations have provided valuable insight into the study of galaxy formation over the last two decades (Frenk et al. 1999; Springel et al. 2005a,b, 2006; Springel 2010; Schaye et al. 2010; Vogelsberger et al. 2012, 2014; Schaye et al. 2015).

Strong gravitational lensing due to ETG provides a robust observational test of a number of theoretical predictions for galaxies at $z \leq 1$, especially when it is being combined with stellar kinematic data (Treu & Koopmans 2004; Sand et al. 2004; Koopmans et al. 2006). Employing the results of the lens models (Koopmans et al. 2006), some studies (Treu et al. 2006) quantified the degree of homogeneity in the inner density profiles of the early-type galaxies, suggesting close to isothermal density profiles on average, but with a scatter. Many questions however remain unanswered. To study strong-lensing ETGs in more detail, the Sloan Lens ACS Survey (SLACS, Bolton et al. 2006; Treu et al. 2006; Koopmans et al. 2006; Gavazzi et al. 2007; Bolton et al. 2008; Gavazzi et al. 2008; Treu et al. 2009; Auger et al. 2009, 2010b,a; Newton et al. 2011; Shu et al. 2015, 2017) and the Strong Lensing Legacy Survey (SL2S, Ruff et al. 2011; Gavazzi et al. 2012; Sonnenfeld et al. 2013a,b, 2015) have provided relatively uniform samples. The lens models from these surveys, however, have not yet been compared in detail to high resolution numerical simulations. An exception is Bellagamba et al. (2017) who found a significantly shallower slope for the dark matter alone by preforming a detailed study of one lens.

In this chapter, we present a new lens-galaxy simulation and analysis pipeline using the EAGLE simulations (Schaye et al. 2015; Crain et al. 2015) and compare the results from mock lens projections to those of SLACS and SL2S. We introduce an automatic prescription that creates, models, and analyzes simulated lenses. We introduce a weighing scheme necessary to reduce the selection bias and statistically compare the simulated lenses with

observations. We also probe the systematic errors and biases arising from the different line of sight projections and environmental effects. We find that using a simplex parameter estimator, we can quite robustly obtain the key lensing observables e.g., the Einstein radius, and mass density slope etc. We put-forward the concept of a 2D-complex space involving axis ratio and position angle in order to disentangle the degeneracy among them.

The chapter is structured as follows. In Section 2.2 the EAGLE galaxy formation simulations and the relevant codes that are use in this work are summarized. Section 2.3 describes the simulation and analysis pipeline that we have constructed. Lens modeling details are explained in Section 2.4. The results of my mock-lens analyses are described in Section 2.5. We compare our mock-lens samples and their properties with observations in Section 2.6 and conclude with a summary in Section 2.7. Throughout the chapter EAGLE simulations that assume a Chabrier stellar Initial Mass Function (IMF, Chabrier 2003) has been used. The values of the cosmological parameters are $\Omega_\Lambda = 0.693$, $\Omega_\mathrm{b} = 0.0482519$, $\Omega_\mathrm{m} = 0.307$, $h = H_0/(100\ \mathrm{km\ s^{-1}\ Mpc^{-1}}) = 0.6777$ and $\sigma_8 = 0.8288$. These are taken from the Planck satellite data release (Planck Collaboration et al. 2014), again in agreement with the EAGLE simulations.

Name	L (cMpc)	N	$m_{\rm g}$ ($M_\odot$)	$m_{\rm DM}$ ($M_\odot$)	$\epsilon_{\rm com}$ (ckpc)	$\epsilon_{\rm prop}$ (pkpc)
L025N0376	25	376^3	1.81×10^6	9.70×10^6	2.66	0.70
L025N0752	25	752^3	2.26×10^5	1.21×10^6	1.33	0.35
L050N0752	50	752^3	1.81×10^6	9.70×10^6	2.66	0.70
L100N1504	100	1504^3	1.81×10^6	9.70×10^6	2.66	0.70

Table 2.1: The main EAGLE simulations. From left to right: simulation name suffix; comoving box size; number of Dark Matter (DM) particles (initially an equal number of baryonic particles are present); initial baryonic particle mass; DM particle mass; comoving Plummer-equivalent gravitational softening length; maximum proper softening length (reproduced from Schaye et al. 2015). Throughout the chapter proper kpc is used synonyously with kpc unless otherwise mentioned.

2.2 Numerical Codes

In this section we briefly describe the simulations, numerical codes, and tools that are used in this work. Here we describe the EAGLE hydrodynamical simulations from which we select lens galaxies (Section 2.2.1), the `GLAMER` ray-tracing code to simulate mock lenses for various lens orientations and sources (Section 2.2.2), and the `LENSED` lens-modeling code used to infer mass-model parameters (Section 2.2.3).

2.2.1 Galaxy-Formation Simulations from EAGLE

Evolution and Assembly of GaLaxies and their Environment (EAGLE)[1] is a suite of hydrodynamical simulations of the formation of galaxies and supermassive black holes in a ΛCDM universe (Schaye et al. 2015; Crain et al. 2015; McAlpine et al. 2016). EAGLE simulations are carried out using the modified N-Body Tree-PM (Particle Mesh) SPH (Smoothed Particle Hydrodynamics) code `GADGET 3` (Springel et al. 2005b). The resulting galaxies are in good agreement with observations of the star formation rate, passive fraction, Tully-Fischer relation, total stellar luminosity of galaxy cluster and colors (Schaye et al. 2015; Trayford et al. 2015), the evolution of the galaxy stellar mass function and sizes (Furlong et al. 2015a,b), rotation curves (Schaller et al. 2015b) and the α-enhancement of ETGs (Segers et al.

[1] `http://icc.dur.ac.uk/Eagle/`

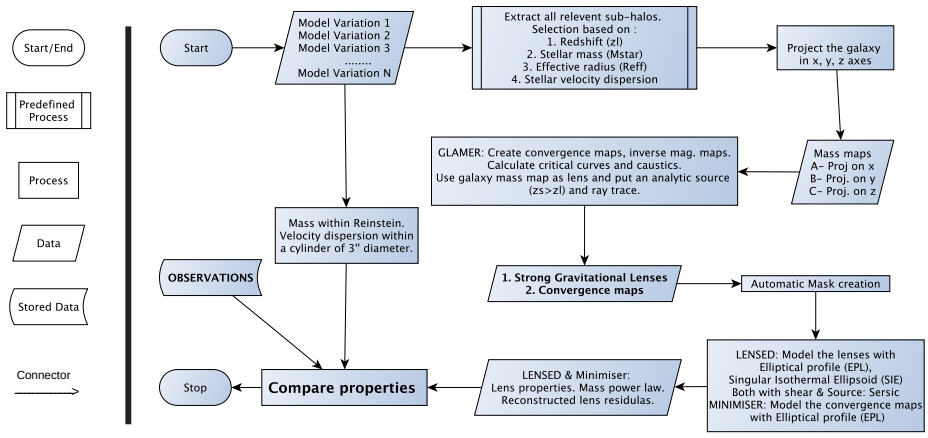

Figure 2.1: The SEAGLE flow chart showing that the convergence mass maps – simulated using GLAMER and galaxies extracted from EAGLE – are analyzed via two different channels, i.e. via the modeling of the simulated lensed images, and via direct fitting of the same (lens) mass model to the convergence mass map. The two resulting parameter sets are compared to each other and to the corresponding observables coming from the SLACS and SL2S surveys.

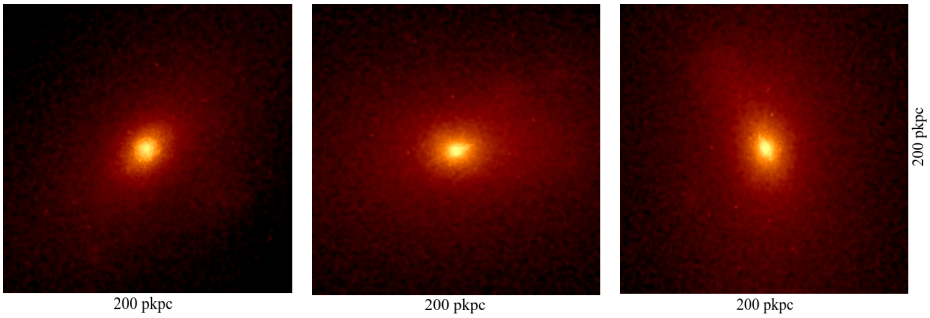

Figure 2.2: An example of mass maps of a typical ETG of stellar mass $=1.9 \times 10^{11}$ $M_{\odot}$ at $z = 0.271$, extracted from the Reference (L050N0752) EAGLE simulation and the box-size is 200 pkpc. Frame [left] is the visualization of projected mass map of the galaxy having axis ratio, q ≈ 0.76 when the line of sight is rotated by (90, 0, 0) deg i.e., 90 deg rotation in x axes with respect to the center of the simulation box. Frame [middle] displays the galaxy having q ≈ 0.72 when our focus has been rotated by (0, 90, 0) deg i.e., 90 deg rotation in y axes. Frame [right] displays the galaxy with q ≈ 0.69 when the rotation angle is (0, 0, 90) degrees in z axes.

2016).

The subgrid physics employed in EAGLE is based on that developed for OWLS (Schaye et al. 2010) and used also in `GIMIC` (Crain et al. 2009) and cosmo-OWLS (Le Brun et al. 2014). The modifications to the SPH implementation together are known as 'Anarchy' (Schaller et al. 2015a). EAGLE galaxies are defined as gravitationally bound sub-halos identified by the `subfind` algorithm (Springel et al. 2001; Dolag et al. 2009). The gravitational softening is summarized in Table 2.1.

In this analysis we have chosen to use the `Reference` model having L050N0752 (see Table2.1 and Schaye et al. 2015; Crain et al. 2015) to ensure that we have a coherent sample of galaxies that have been formed from an identical set of initial conditions subjected to different physical models when comparing results between different model variations of EAGLE (Crain et al. 2015) in forthcoming works. For detailed descriptions on the various galaxy-formation prescriptions and sub-grid physics we refer to Schaye et al. (2015) and Crain et al. (2015).

2.2.2 Strong Lens Simulations with GLAMER

GLAMER[2] is a ray-tracing code for the simulation of gravitational lenses (Metcalf & Petkova 2014; Petkova et al. 2014). The deflection angles, shear, and other relevant properties are calculated using a modified tree algorithm described in Barnes & Hut (1989). It uses Adaptive Mesh Refinement (AMR) in ray-casting, based on the requirements of the source size, location and surface brightness distribution and to find critical curves and caustics. Ray paths are determined from the observer to the source plane through multi-plane deflection, convergence, and shear calculations. GLAMER allows for a wide variety of source types and the mass distribution on each lens plane can be represented in several different ways, for example via a surface density map in FITS format. The resulting lensed images are subsequently convolved with a point spread function (PSF) and appropriate noise levels can be added. For further details one can consult GLAMER I & II papers (Metcalf & Petkova 2014; Petkova et al. 2014).

In this analysis, a single lens plane has been used for representing the convergence of galaxies extracted from EAGLE, because the maximum box size ($< 100\,\mathrm{Mpc}$) is still small compared to the cosmological distances involved. This can be expanded to multiple lens planes for much larger boxes. We also assume an elliptical Sérsic profile for the sources with varying parameters, placed inside the diamond caustic to generate preferentially highly magnified systems, similar to those found in the SLACS and SL2S surveys. All of these choices can be varied in the pipeline if desired.

2.2.3 Gravitational Lens Modeling with LENSED

LENSED[3] is a publicly available code which performs parametric modeling of strong lenses by taking advantage of the massively parallel ray-tracing kernel on a graphics processing unit (Tessore et al. 2016) to perform all necessary calculations. Combining these accurate and fast forward simulations with the Nested-Sampling Bayesian analysis, MULTINEST (Feroz & Hobson 2008; Feroz et al. 2009, 2013), allows the simultaneous optimization of tens

[2] http://glenco.github.io/glamer/
[3] http://glenco.github.io/lensed/

of non-linear parameters of the selected model (e.g. lens and source) and the full posterior probability distribution for the mass distribution and the background source in typically 10 minutes on a multi-core machine. The setup of the physical system, priors, input files including images, masks, PSFs and noise maps can be done using a single configuration file. The code reports statistically well-justified errors, including degeneracies, for the lens model parameters i.e., the full posterior reconstruction, and also simultaneous fitting of sources and lenses. `LENSED` has been well tested on SLACS lenses. For details see Tessore et al. (2016) and Bellagamba et al. (2017).

Galaxy Selection		
Observable	Value	Comments
$M_\star$	$\geq 1.76 \times 10^{10} M_\odot$	Stellar mass lower threshold. Taken from Auger et al. (2010b)
σ	> 120 km/sec	Stellar Velocity dispersions are kept lower than SLACS
R_{50}	> 1 kpc	Half mass projected radius
Lens Candidates		
Object-properties	Value	Comments
Sim. used	Reference (L050N0752)	50 cMpc box is best for comparing with other scenarios
Orientation	x, y and z axis	Projected surface density maps are made along each axis
Redshift	$z_l = 0.271$	Consistent with SLACS' mean lens-redshift of 0.3
No. of galaxies	252	Total number of galaxies satisfying our selection criteria
No. of projected galaxies	756	Total number of galaxies after projection on 3 axes
Source Properties		
Parameters	Value	Comments
Source Type	Sérsic	Consistent with analyzed SLACS lenses (Newton et al. 2011)
Brightness	23 apparent mag.	〃
Size ($R_{\rm eff}$)	0.2 arcsec	〃
Axis ratio (q_s)	0.6	〃
Sérsic Index	1	〃
Redshift	z_s=0.6	〃
Position	Random within caustics	Producing more rings and arcs lens systems, consistent with SLACS
Instrumental Settings		
Parameters	Value	Comments
PSF	Gaussian, FWHM=0.1 arcsec	-
Noise	HST ACS-F814W, 2400 sec	-
Image Properties		
Map used	Properties	Value
Surface density	(a) Size	512×512 pixels
	(b) Units	kpc
κ, Inv. mag. map and Lens	(a) Size	161×161 pixels
	(b) Units	degrees (converted from arcsec)

Table 2.2: The summary of the current SEAGLE pipeline settings.

2.3 Pipeline

In this section we describe the SEAGLE (Simulating EAGLE LEnses) pipeline in more details. Here we describe the selection criteria of the lens candidates from EAGLE (Section 2.3.1), the lens galaxy extraction technique (Section 2.3.2), the line-of-sight projection effects on the shape of lens galaxies (Section 2.3.3), the method to create mock lens systems with `GLAMER` (Section 2.3.4), the automatic mask creation process (Section 2.3.5), and details of the final lens sample used in this work (Section 2.3.6). The simulation and analysis pipeline is shown in Figure 2.1.

In this work extraction of galaxies is done at one particular redshift and the resulting mass distribution is projected along one of the three principal axes of the simulation box. A Sersic (1968) source is then placed at a random source position within the diamond caustics at a higher redshift as experimented with `GLAMER`. The PSF and noise are similar to those for a single orbit HST ACS-F814W observations to make the mock lenses appear similar to observed SLACS lenses. The resulting lenses are subsequently modeled and analyzed by comparing their ensemble properties with those from SLACS and SL2S. We note that most of the above choices can be easily modified.

2.3.1 Lens-Galaxy Selection

The next generation of lens surveys (for example with *Euclid* (Laureijs et al. 2011)) are expected to increase the number of lenses by orders of magnitude, in particular finding lower mass and smaller image separation lenses. This will increase the parameter space of strong lenses in terms of their mass, stellar velocity dispersion and other observables considerably. The selection criteria for extracting galaxies from EAGLE, however, are based on parameters obtained from currently confirmed strong lenses due to ETGs, in particular from SLACS. Keeping this restriction in mind, we explore a volume-limited sample of lens galaxies with observables (e.g. stellar mass) in the range of ETGs from SLACS (Auger et al. 2009, 2010b,a) and SL2S (Sonnenfeld et al. 2013a,b). The SLACS sample consists of a wide ranges of photometric and spectroscopic measurements using HST

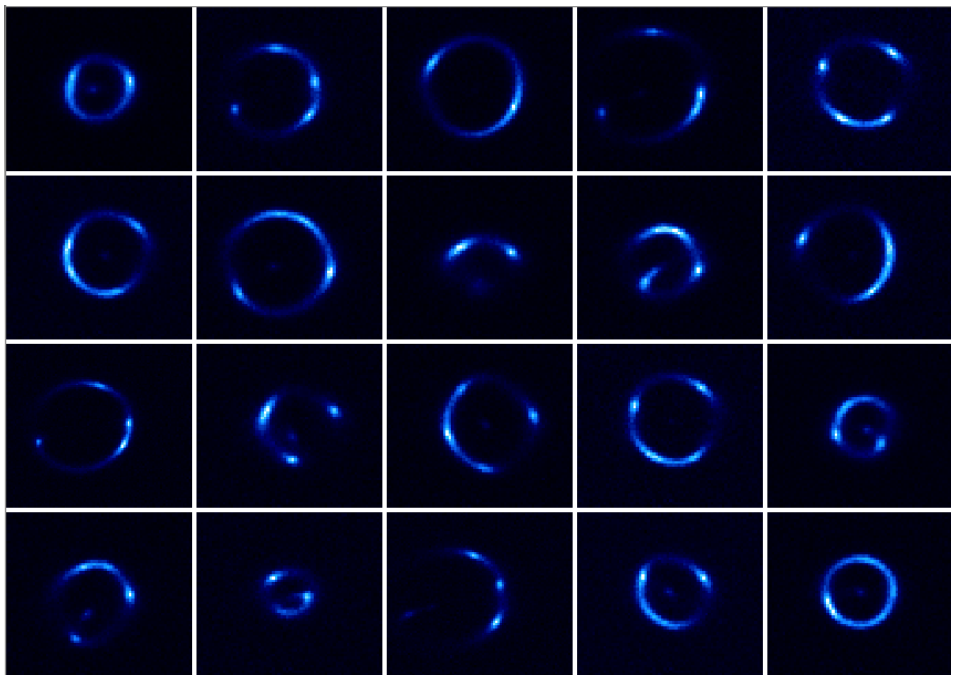

Figure 2.3: A subset of strong lenses from EAGLE (Reference model) 50 cMpc, $z_l = 0.271$. Even some of the rare SLACS lenses has been mimicked very well via our pipeline. The sub kpc fluctuations however cannot be simulated with a simple Sérsic source object. But that is not necessary for having a statistical sample of simulated SLACS like lenses. We have not put the lensing galaxy in the foreground so there is no contamination of the light from the foreground ETG.

and SDSS and inferred data products, which include for example, the parameters inferred from lens modeling and stellar-population analysis (Auger et al. 2010a). The parameter space of SLACS broadly overlaps with SL2S lenses, which makes it useful to compare properties of simulated lenses with both samples.

The initial selection is based on lens redshift (z_l) and stellar mass ($M_\star$) in accordance with Auger et al. (2010b), where the lens redshift range is $0.1 \leq z_{\rm lens} \leq 0.3$ and the stellar mass threshold is $M_\star \geq 1.76 \times 10^{10}$ $M_\odot$. No upper limit is set. The stellar velocity dispersion (σ) and half mass radii (R_{50}), which is a proxy for effective radii ($R_{\rm eff}$) in observations, are only used to clip outliers e.g., due to halo stars, mergers and other contaminations arising from stray particles in the simulations. Table 2.2 summarizes the details of our selection criteria.

It is difficult to implement an automated recipe for the lens modeling for galaxies with stellar masses, $M_\star < 10^{11}$ $M_\odot$. This is due to the resolution effect of the particles during projection, which creates prominent but artificial images in the central regions of the lenses after ray tracing, which are not seen in real lens galaxies. In order to implement an automated lens modeling scheme with `LENSED` we therefore further restrict ourselves to galaxies with $M_\star > 10^{11}$ $M_\odot$ (calculated within a cylinder of $1.5''$ in radius, consistent with SLACS) which produce extended arcs and rings (see Figure 2.3). These are far less affected by any resolution effect and are still within the upper mass range of SLACS and SL2S lenses. To down-weight lower-mass galaxies in the volume limited set of EAGLE lenses in comparisons to SLACS or SL2S, in Section 2.6.2 we introduce a weighting scheme based on their lensing cross-section, that compensates for the observational selection biases and allows for a more accurate comparison between the simulations and the observations. We ignore the magnification bias, which we assume to vary more slowly with galaxy mass unlike the cross section.

2.3.2 Galaxy/Halo Extraction

To extract a galaxy from the EAGLE snapshots I use the `Friends-Of-Friend (FoF)` catalogs. We use the stellar mass catalog from the snapshots and particle data at the desired redshift of the currently used `Reference`

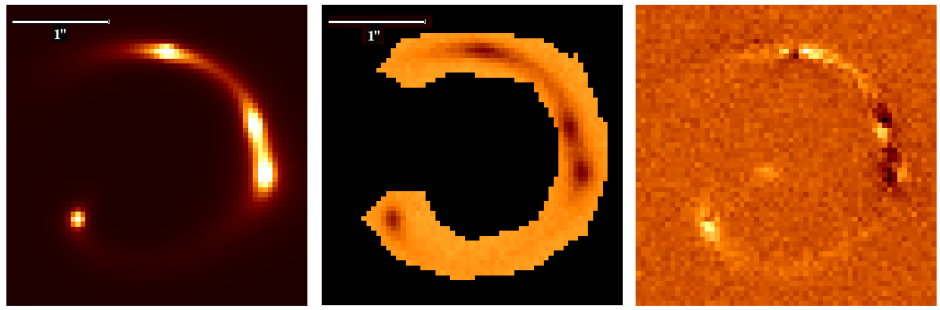

Figure 2.4: The left panel shows an example of a simulated lens with noise and PSF (see Table 2.2 for details). The middle panel shows the reconstructed image of the lens inside the mask, using `LENSED`. The right panel shows the unnormalized residual image of the data minus the model. The peak brightness of simulated lens and residuals are 1.30 and 0.37, respectively.

simulation (i.e., L050N0752). The choice of aperture is important given its direct effect on the stellar mass calculation for massive and extended galaxies with $M_* > 10^{11} M_\odot$ (see Schaye et al. 2015). Given that most lens-galaxies have half-mass radii of 5-10 kpc, we choose a 10-kpc aperture to select the closest analogues to observed lenses from the simulations. We select all sub-halo indices that match our selection criteria, and reject any galaxy having half-light radii < 1 kpc in the EAGLE catalogs (these objects are misidentified galaxies and lie far from the Fundamental Plane). This aperture size avoids inclusion of spurious stellar mass which would be discounted in the modeling of observed lens galaxies using e.g. a smooth Sérsic profile. Eagle catalogs have `GroupNumber` and `SubGroupNumber` which are numbers assigned to `FoF` group and subgroup respectively. They are numbered according to their decreasing masses. That means subgroup 0 of a `FoF` group corresponds to the most massive subgroup within the group. We read the `GroupNumber` and `SubGroupNumber` using the same indices to recover the `FoF` Group ID and `Subfind` subgroup ID and subsequently select all their particles and obtain their meta-data from the simulations, using the group IDs. Galaxy selection and outlier rejection are currently fully automated in the pipeline and the criteria can be altered if necessary.

2.3.3 Line-of-sight Projection

Once the catalogs of dark-matter, stellar, gas and black hole particles of a galaxy have been extracted from the simulations, we allow for any arbitrary spatial rotation. We rotate particle position vectors around the center of the lens galaxy. Although this does not lead to an independent lens galaxy, it does allow for some testing of the effects of orientation on the inference of the galaxy properties.

Figure 2.2 shows how the projected shape of a galaxy changes when viewing it from three different angles. In this work we use each galaxy three times, projected along each of the three principle axes of the simulation box. In the future works we use these to assess systematics due to projection of the main galaxy halo and line-of-sight effects in the nearby environment of the lens (i.e. inside the box). The particles are then converted into projected mass maps after smoothing of the particles with the same SPH kernel as used in the simulation (for details see appendix A of Trayford et al. 2017).

We also simultaneously calculate the surface density profiles of the matter distribution for each projected mass map. The surface densities for individual particle types (DM, stars and gas) and a total mass profile are calculated separately. Figure 2.5 shows a typical example for an ETG's mass profiles. The effect of the resolution of the simulation inside $\sim$1 kpc is clearly visible.

The resolution of the simulation plays a role in the core of the galaxy, where we hit the resolution limit. 2-3 times the gravitational softening length, which is independent of the density, away from the core its effect no longer plays a crucial role. So we mask the central pixels in the lensed images. In subsection 2.3.5 we describe this in details.

2.3.4 Mock Lens-System Creation

The surface density maps are created on grids of 512×512 pixels (Table 2.2), in units of solar mass per pixel, and form the input to `GLAMER`. The width (100 pkpc) and pixel scale (0.2 pkpc) of the grid ensure the surface density map and corresponding convergence map are well-resolved in the relevant regions (see Tagore et al. 2018), down to the softening length and consistent with SLACS resolution of 0.05 arcsec (at z=0.271, SLACS

resolution corresponds to ≈ 0.2 pkpc). We then choose a lens and source redshifts for `GLAMER` to convert these mass maps into convergence maps. For each mass map, the critical curves and caustics are calculated to determine where a source has to be placed in order to create multiple lensed images. In this work we use an elliptical Sérsic brightness profile of the source with index $n = 1$. Its apparent magnitude is constant at 23 in the HST-ACS F814W filter (AB system) and its redshift is $z_{\rm s} = 0.6$. The other parameters are its effective radius of 0.2 arcsec, a position angle $\phi_s = 0\,$deg and a constant axis ratio q_s=0.6. Given that source and galaxy position angles are uncorrelated, this fixed position angle of the source does not reduce generality. The source is placed randomly inside the diamond caustics of the lens. The pixel scale is 0.05 arcsec, and the PSF and noise correspond to an HST-ACS-F814W exposure of typically 2400 s. The resulting images have a size of 161 $\times$ 161 pixels of 8.0 arcsec. The above parameter values are currently fixed for each lens, but are typical for the sample space of SLACS lenses (Koopmans et al. 2006; Newton et al. 2011; Bandara et al. 2013). Since our goal is to assess global properties of the lenses, the precise choice of the source model (which is an exponential disk here; Sérsic with n=1) is currently of secondary importance. The images are exported in standard fits-file format. Table 2.4 lists all parameter values. We like to point out that in this work, only arcs and rings lenses are simulated. We do not simulate any two lensed image system i.e. lensed system having two bright image surface brightness. Since the number counts of two-image system in SLACS is $6/84 \sim 7\%$ (Auger et al. 2010b) and $3/56 \sim 6\%$ in SL2S (Sonnenfeld et al. 2013a) are very low and no evidence of the lens properties being a function of lens geometry is reported (Auger et al. 2010a; Sonnenfeld et al. 2013b), so we assume non inclusion of the two image lenses are highly unlikely to bias the overall statistics.

In addition to the simulated lenses, we store convergence maps and inverse magnitude maps of each lens galaxy. The brightness distribution of the lensing galaxy is not added to the lensed image grid. Here we assume that subtraction of the surface brightness distribution of the lens galaxy can be done to sufficient accuracy that it does not affect the analysis in the current paper. Hence we assume little covariance between the source and lens brightness distributions. Experience with high-resolution HST-quality data of lenses in the I-band confirms this, although this assumption might not hold for lower-resolution ground based data.

2.3.5 Mask Creation

The strong lens systems created using `GLAMER` are modeled similarly to a real lens system. Masks are generated automatically in order to enable direct comparison with the lens models to the region around the lensed images. We do this for each lens by convolving the noisy lensed images with a Gaussian with a FWHM of 0.25 arcsec to reduce the noise and smear the images to a slightly larger footprint. We then set a surface brightness threshold for the mask being a factor of typically 2.5–5 below the original noise. Pixels above the threshold are set to one and all others to zero. The mask then traces the surface brightness of the lensed images well below the noise level. We set the threshold values such that the mask bounds the significant surface brightness pixels but leaves a padding area that is largely noise example, middle panel of Figure 2.4. The central 7×7 pixels are also masked to remove any artificially bright central images as a result of the finite size of the SPH kernel and limited resolution. The final mask is used in the modeling and minimizer fitting in the following steps.

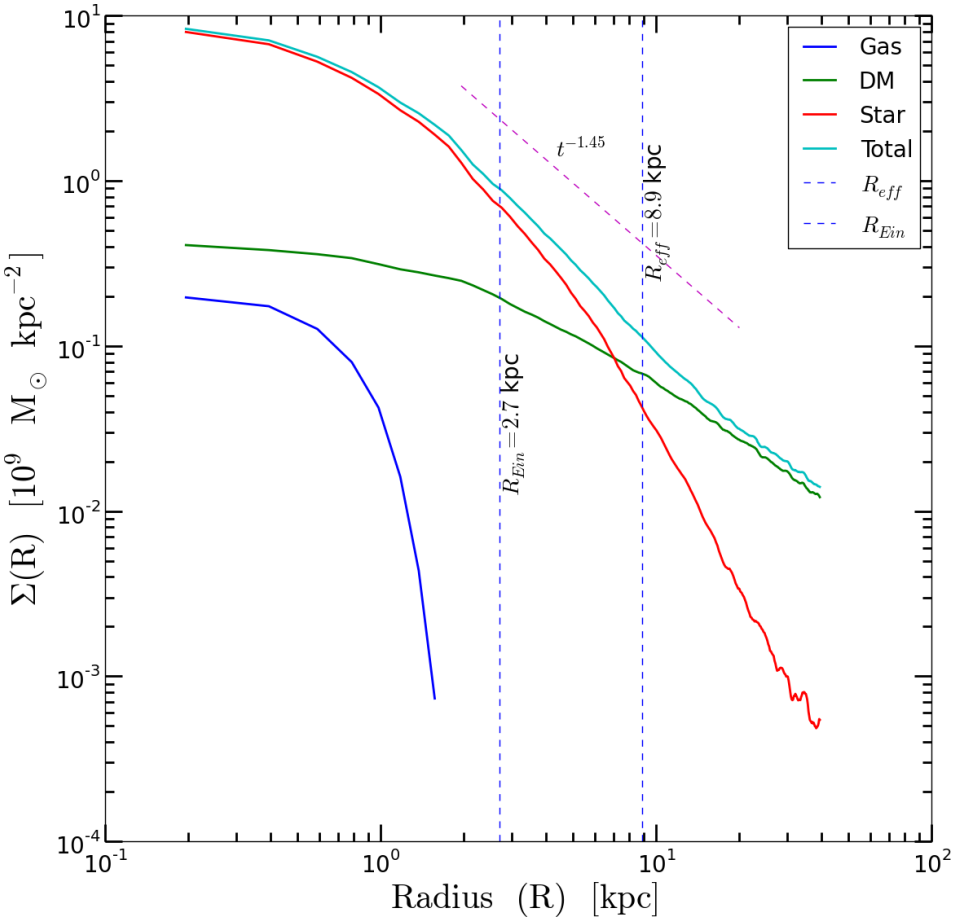

Figure 2.5: Surface density profiles of DM, stars, gas and the total mass of a typical ETG from EAGLE. The effective radius of the galaxy and the slope of best fitted mass model profile along with Einstein radius, as obtained from lens modeling, are also indicated.

Table 2.3: The prior settings used in the lens-modeling with **EPL + shear** mass model in LENSED.

Priors used in LENSED*						
Elliptical Power Law (EPL) + Shear						
Parameter	Prior type**	Prior range				Description
		μ	σ	min	max	
$x_{\rm L}$	norm	80.0	5.0	-	-	Lens position: x coordinate
$y_{\rm L}$	norm	80.0	5.0	-	-	Lens position: y coordinate
$r_{\rm L}$	unif	-	-	5.0	70.0	Einstein radius in pixel units
$t_{\rm L}$	norm	1.1	0.1	-	-	Surface mass density slope
$q_{\rm L}$	unif	-	-	0.2	0.99	Lens axis ratio
$\phi_{\rm L}$	unif	-	-	0.0	180.0	Lens position angle in degrees, wrapped around
$\gamma_{1{\rm L}}$	norm	0.0	0.01	-	-	Shear vector
$\gamma_{2{\rm L}}$	norm	0.0	0.01	-	-	Shear vector
$x_{\rm S}$	norm	80.0	30.0	-	-	Source position: x coordinate
$y_{\rm S}$	norm	80.0	30.0	-	-	Source position: y coordinate
$r_{\rm S}$	unif	-	-	0.1	10.0	Source size in pixel units
$mag_{\rm S}$	unif	-	-	-5.0	0.0	Source magnitude, adjusted with the background magnitude$^{\#}$
$n_{\rm S}$	norm	1.0	0.1	-	-	Sérsic index
$q_{\rm S}$	norm	0.5	0.1	-	-	Source axis ratio
$\phi_{\rm S}$	unif	-	-	0.0	180.0	Source position angle in degrees, wrapped around

$\star$ All values are in pixels except q, γ, $t_{\rm L}$, $mag_{\rm S}$, $n_{\rm S}$, and ϕ. $\star\star$ norm = Gaussian (with mean μ and standard dev. σ), unif = Uniform
$\#$ Source's real magnitude = Background magnitude - mag_s, where background magnitude is flux due to background in mag/arcsec^2

Table 2.4: The prior settings used in the lens-modeling with **SIE + shear** mass model in `LENSED`.

Priors used in `LENSED`*						
Singular Isothermal Ellipsoid (SIE) + Shear						
Parameter	Prior type**	Prior range				Description
		μ	σ	min	max	
$x_{\rm L}$	norm	80.0	5.0	-	-	Lens position: x coordinate
$y_{\rm L}$	norm	80.0	5.0	-	-	Lens position: y coordinate
$r_{\rm L}$	unif	-	-	5.0	70.0	Einstein radius in pixel units
$q_{\rm L}$	unif	-	-	0.2	0.99	Lens axis ratio
$\phi_{\rm L}$	unif	-	-	0.0	180.0	Lens position angle in degrees, wrapped around
$\gamma_{1\rm L}$	unif	-	-	-0.1	0.1	Shear vector
$\gamma_{2\rm L}$	unif	-	-	-0.1	0.1	Shear vector
$x_{\rm S}$	norm	80.0	30.0	-	-	Source position: x coordinate
$y_{\rm S}$	norm	80.0	30.0	-	-	Source position: y coordinate
$r_{\rm S}$	unif	-	-	0.1	10.0	Source size in pixel units
$mag_{\rm S}$	unif	-	-	-5.0	0.0	Source magnitude, adjusted with the background magnitude$^{\#}$
$n_{\rm S}$	unif	-	-	0.5	2.0	Sérsic index
$q_{\rm S}$	unif	-	-	0.2	0.99	Source axis ratio
$\phi_{\rm S}$	unif	-	-	0.0	180.0	Source position angle in degrees, wrapped around

$\star$ All values are in pixels except q, γ, $t_{\rm L}$, $mag_{\rm S}$, $n_{\rm S}$, and ϕ. $\star\star$ norm = Gaussian (with mean μ and standard dev. σ), unif = Uniform
$\#$ Source's real magnitude = Background magnitude - mag_s, where background magnitude is flux due to background in mag/arcsec^2

Table 2.5: The sample of EAGLE lenses used.

SEAGLE-I lenses			
Tag	No. of Galaxies	Proj. galaxies	Comments
A	252	756	Total number of galaxies satisfying all the selection criteria mentioned in Table 2.2
B	48	144	Total number of galaxies satisfying all the selection criteria and having $M_\star > 10^{11}$ $M_\odot$
C	48	48	Number of modeled galaxies having $M_\star > 10^{11}$ $M_\odot$ using one orientation
D	11	11	Number of modeled galaxies having $M_\star < 10^{11}$ $M_\odot$ for test purposes

2.3.6 The Lens Samples

In this subsection I summarize the pilot sample selected for this paper. Out of the 252 initially selected galaxies (Table 2.5), 48 have $M_\star > 10^{11}M_\odot$. The projected stellar masses are calculated within a cylinder of $3''$ diameter (see Auger et al. 2010a) to keep the comparison consistent with SLACS (see Figure 2.1). From the remaining galaxies having $M_\star < 10^{11}M_\odot$, we randomly select 11 galaxies motivated to test the performance of the pipeline. I perform lens-modeling on these two sets of samples. Given the pilot nature of the sample when comparing properties (e.g., total density slope) with observations we restrict to galaxies having $M_\star > 10^{11}M_\odot$, also most reliable and least affected by SPH smoothing. To limit computation effort, we also currently only use one of the projected mass maps. The selected lenses cover nearly one dex in stellar mass of the SLACS, but because of the limited volume of the simulations, they are poorly represented when approaching very massive ETGs. Finally we apply the end-to-end pipeline on the sample and analyze the results in this work. The result is that 34 out of 48 lenses having substantial arcs or Einstein rings (see Figure 2.3), converged to optimized solutions. 14 lenses having smaller arcs and more complex structure failed to converge to any reasonable solution in lens-modeling. Table 2.5 summarizes the sample selection.

The reason for our current down selection of the total sample is mainly due to the complexity in the implementation of automated lens-modeling with `LENSED`. All the resulting mass maps, inverse magnification maps, convergence maps, the simulated lenses and model-fitting results are stored in a MySQL[4] database, which has been widely used in astronomy (Lemson & Springel 2006).

[4] `http://www.mysql.com/products/community/`

2.4 Lens-System Modeling

Once we have created all the inputs to simulate mock lens systems including observational effect and masks, I model each lens system with `LENSED` (Tessore et al. 2016) using either an Elliptic Power Law (EPL; Tessore & Metcalf 2015) or a Singular Isothermal Ellipsoid (SIE; Kormann et al. 1994) mass model, including external shear. A total of 14 and 15 parameters are sampled for the SIE and EPL models, respectively, and posterior distributions of all lens and source parameters are created via the MCMC method Nested Sampling.

2.4.1 Mass Models

Various observational studies find that the EPL mass model (including the SIE) in general provides a good approximation of the mass model of massive galaxy-scale strong gravitational lenses (Koopmans et al. 2006, 2009; Treu & Koopmans 2004; Newton et al. 2011). As a first step we therefore model the lenses as a SIE plus external shear with the prior settings tabulated in Table 2.4. The dimensionless surface mass density of the SIE model is given by

$$\kappa(R) = \frac{b}{2R}, \tag{2.1}$$

where b is approximately the Einstein ring radius and R is the elliptical radius defined by

$$R = \sqrt{qx^2 + y^2/q}, \tag{2.2}$$

where q is the axis ratio (short over long axis length)and x, y are cartesian coordinates of the model. Similarly we model and analyze the lenses with an EPL mass model plus external shear, whose convergence is given by

$$\kappa(R) = \frac{(2 - t_L)}{2} \left(\frac{b}{R}\right)^{t_L} \quad , \tag{2.3}$$

where $0 < t_L < 2$ is the the power-law density slope of the mass model and the other parameters are the same as for the SIE model. This profile can arise from a three-dimensional mass distribution, given by

$$\rho(r) \propto r^{-t} \tag{2.4}$$

where $t = t_L + 1$.

The EPL model allows us to (statistically) compare the ensemble of density slopes of the simulated lenses with those from SLACS and SL2S. We note that many of the SLACS density slopes were obtained from a combined lensing and dynamics analysis, not just from lensing. The same model also allows for a comparison with the convergence model fitting in Section 2.4.4.

2.4.2 Nested Sampling and Priors

We compare our models to the simulations using a Bayesian approach and sample the posterior via Nested Sampling (NS; Skilling 2006; Feroz & Hobson 2008; Feroz et al. 2013). NS is a modified Markov Chain Monte Carlo (MCMC) method that carries out the integral over the posterior probability distribution function (PDF) resulting in a value of the marginalized posterior, i.e. the evidence. As a by-product it also provides a first-order sampling of the posterior. The posteriors are used to estimate the maximum a posteriori (MAP) lens parameter values, their uncertainties, as well as potential degeneracies (see Tessore et al. 2016 for more details). The lens modeling is performed semi-automatically with 200 live points, where the initial values of priors are kept such that effectively all of the lens and source parameter spaces are covered (see Table 2.4). The parameter space is sometimes degenerate with multiple extrema, making a straightforward sampling difficult. To avoid any catastrophic failures in the reconstructed source or lens parameters, the analysis of the mock lenses was performed by trying a range of well-motivated priors without affecting the end result too much. A combination of rather uninformative Gaussian and uniform priors was found to be optimal in our modeling analysis. The details of the prior settings can be found in Table 2.4. In the EPL case we used tighter priors on n_s and q_s to avoid degeneracies that would slow the convergence. All NS chains are analyzed through `GetDist`[5]. I get posterior distributions, corner plots and also marginalized plots for each individual source and lens parameters. I tested for a range of priors for the density slopes and shear (the two main parameters of the analysis) and found that our choice of priors improves convergence and reduces the computation time. Hence we

[5] `http://getdist.readthedocs.io/en/latest/`

use the prior in Table 2.4 to speed up convergence, but they have little to no impact on the final solution. See Appendix 2.A.2 for details.

2.4.3 Choice of Source Model

The source parameters are observationally motivated (Bolton et al. 2008; Newton et al. 2011) and can in principle be varied between sources. Our main goal in this paper is to infer global properties of the lensing galaxies, and the precise choice of the source model is currently of secondary importance (see Section 2.3.4). So even-though some of the SLACS and SL2S sources show irregular morphologies, we expect a change in the source model not to bias the result especially since the systematic errors far outweigh random errors. Tessore et al. (2016) for example performed rigorous testing to demonstrate that the choice of source model does not bias the lens-modeling (see Section 4.4 of Tessore et al. 2016). They reported only a minor variance for the lens modeling parameters. We tested with a sub-sample of our pilot lenses and note sometimes an increase in the computational time for some but no change in the distribution of the parameters (see Appendix 2.A.2). Hence in the current paper we have decided not to change the source model parameters between lenses.

2.4.4 Convergence-Map Modeling

We also fit the EPL model in Equation 2.3 directly to the convergence map of the galaxy inside the same mask that was used for the lens modeling, using the Nelder-Mead (NM) simplex method (Nelder & Mead 1965) including some annealing to help convergence. We do this in order to compare the resulting lens-model parameters, as discussed in Section 2.4, with those from the actual mass model of the simulated galaxy. Even the resulting parameters from this 'direct' fit are still a limited representation of the true mass distribution, which can be more complex than an EPL mass model. Comparing the two, however, allows us to assess the reliability of the lensing results and the variance between the two parameter sets.

We use an unweighted least square penalty function. We take the parameter values that minimize the penalty function from a set of ten different optimization runs with random initial parameter values, each having a

maximum of 150 iterations. Most solutions agree well, with some outliers due to local minima. We choose the solution with the lowest penalty from this set, in general leading to a robust solution. This step of analysis in the pipeline is important for a number of reasons: (1) we obtain a fairly robust estimate of the main observables of the lensing galaxies such as the Einstein radius, axis ratio, position angle, and density slope, (2) we can make a direct comparison with the modeled output for each individual lenses, (3) the residuals obtained via this analysis could also be used for power-spectrum analysis.

2.5 Comparing the Results from Lens and Convergence Mass Models

The two independent mass-model analyses i.e. via lens modeling and via direct convergence-map fitting, provide a consistency check and assessment of systematic errors on the simulated lenses when compared with observations (Marshall et al. 2007). We compare the results from both model fits using an identical family of mass models. To compare their ensemble properties, however, a weighting scheme is needed that mimics the selection effects in observed samples. These selection biases can be rather complex (Dobler et al. 2008) but in this work we use the lens cross-section based on stellar mass. We ignore the magnification bias which is expected to change slowly with stellar mass for the most massive lens galaxies that has been studied.

Below we discuss the results from the comparison between the two sets of parameters, in particular the complex ellipticity, its correlation with external shear, and the Einstein radius. We have used the SIE model results when comparing with observations' ellipticity and position angle which is consistent with the model used in SLACS and SL2S. For comparison of density slopes we have used EPL modeling results which are also consistent with the mass density slope model used in SLACS and SL2S.

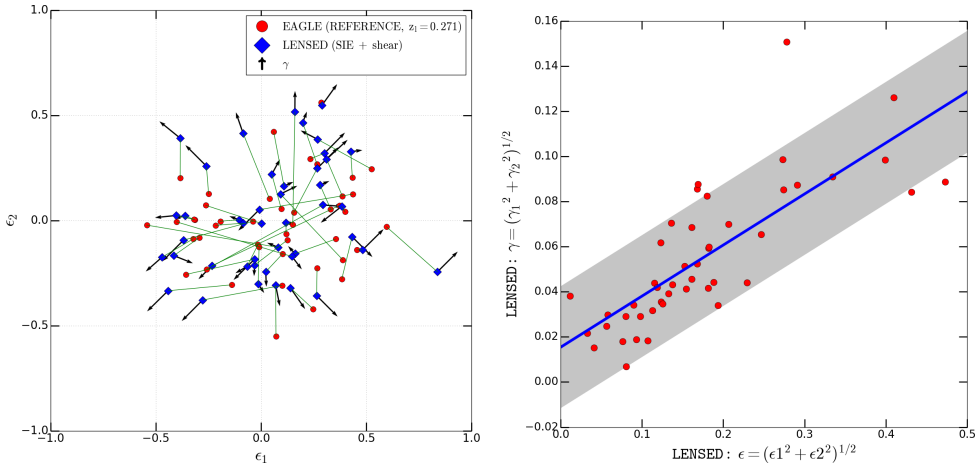

Figure 2.6: Left panel: The complex ellipticity (see eq. 2.6) of the SIE lens models (eq. 2.1) from `LENSED` (blue diamonds) and from a direct fit to the convergence mass maps (red filled circles). The green line represents the line joining the two ϵ measurement ($\overline{\epsilon_L \epsilon_K}$), from lens-modeling and direct fitting. The shear vector (γ) tends to point radially outwards in this plot, so the ellipticity is degenerate with the shear. It is most likely to cause differences in the ellipticity in the direction of the shear which causes the true lens mass model to deviate from the assumed mass models. Right panel: Complex ellipticity versus shear suggests a strong correlation among them. The shaded region shows the 1σ (=0.027) interval. Here samples C and D (see Table 2.5) have been used.

2.5.1 Complex Ellipticity

The position angle of the lens mass model has an ambiguity of $\pm\pi$ due to its point symmetry. In addition, when the lens is nearly round ($q \to 1$), the position angle becomes ill-defined. In order to disentangle this degeneracy we use a complex ellipticity representation which connects both ϕ and q.

To accomplish this, we use the complex ellipticity defined as:

$$\epsilon = \frac{(1-q)}{(1+q)} e^{+2i\phi} \ , \tag{2.5}$$

or in vector notation:

$$(\epsilon_1, \epsilon_2)^{\mathrm{T}} = \frac{(1-q)}{(1+q)} (\cos(2\phi), \sin(2\phi))^{\mathrm{T}} \ . \tag{2.6}$$

In this representation rounder lenses will have a smaller values of ϵ, regardless of the value of ϕ. For smaller values of q, the absolute value of ϵ increases and ϕ should be better determined. The agreement between two models depends on the distance in this ϵ-space, $|\epsilon_{\mathrm{model\ 1}} - \epsilon_{\mathrm{model\ 2}}|$.

We present the model values of ϵ from both the lensing and direct fitting to the convergence maps in Figure 2.6. The shear vectors from the lens model are also indicated. Calculating $\Delta\epsilon_1 = \epsilon_{1,\mathrm{L}} - \epsilon_{1,\kappa}$ and $\Delta\epsilon_2 = \epsilon_{2,\mathrm{L}} - \epsilon_{2,\kappa}$, where 'L' suffix refers to `LENSED` results and 'κ' suffix refers to results from convergence map fitting, we find standard deviations of 0.24 and 0.17 for $\Delta\epsilon_1$ and $\Delta\epsilon_2$ respectively. The errors on the standard deviation are 0.1 and 0.07, respectively, hence the differences in the two directions are not significant. The scatter is significant though. We conclude that for lower stellar mass lenses ($\mathrm{M}_\star < 10^{11}\mathrm{M}_\odot$) a significant difference can exist between the inference of the complex ellipticity from the convergence map and that from lens modeling. This might be regarded as a systematic error or bias in lens modeling which is hard to overcome. Below I investigate its cause in a little more detail.

2.5.2 Shear versus Ellipticity

For the majority of the lens systems there is good agreement between the values of the complex ellipticity from both analyses (Figure 2.6, for errors

see subsection 2.5.1), but some systems suffer from a significant mismatch. Some previous studies have associated the differences in alignment and ellipticity to the presence of external shear (complex γ), given by:

$$\gamma = \gamma_1 + \mathrm{i}\gamma_2 \, . \tag{2.7}$$

They also indicated a pronounced degeneracy between ellipticity and external shear (Bandara et al. 2013; Tessore et al. 2016). We find that the majority of the systems with large differences in the complex ellipticity between the lens and convergence modeling have external shears that have a preferred angle (Figure 2.7) to the vector joining the two ϵ measurement, $\overline{\epsilon_{\mathrm{L}}\epsilon_{\mathrm{K}}}$. This correlation in ellipticity and shear angles suggests that the 'external' shear is in fact 'internal' and is possibly caused by the mass distribution of the lens galaxy and not by external galaxies. In the latter case no strong correlation between shear and ellipticity angles would be expected. Hence, contrary to Bandara et al. (2013), who suggested that there may not be a direct correlation between q and γ, we find a correlation between γ and ϵ values of our simulated lenses (Figure 2.6), being:

$$\gamma = 0.226\epsilon + 0.015 \tag{2.8}$$

Also we compute the angle (φ) between the shear vector and the line joining the complex ellipticities, ϵ_{L} and ϵ_{K}, obtained from lens modeling and convergence ellipticity fitting respectively. Figure 2.7 illustrates the normalized distribution of angle φ in degrees. It reaches peak at $\sim 135\,\mathrm{deg}$ implying that the shear components γ_1 and γ_2 appear orthogonal to ϵ_1 and ϵ_2 respectively. But the standard deviation in the distribution is ~ 50 deg which also suggests that orthogonal orientations of the shear vector have considerable scatter.

Based on this strong correlation and the apparent alignment or orthogonality between shear and ellipticity, we conclude that much of the difference in ellipticity inferred from lens models and direct fitting to the convergence maps is the result of an internal shear causing a bias in the lens models. This shear is therefore not caused by the external galaxies, but more likely by a difference between the assumed mass model (SIE) and the true mass model. Its difference is likely compensated for by the shear used in lens modeling. A first order deviation could be boxy or diskines of the galaxy.

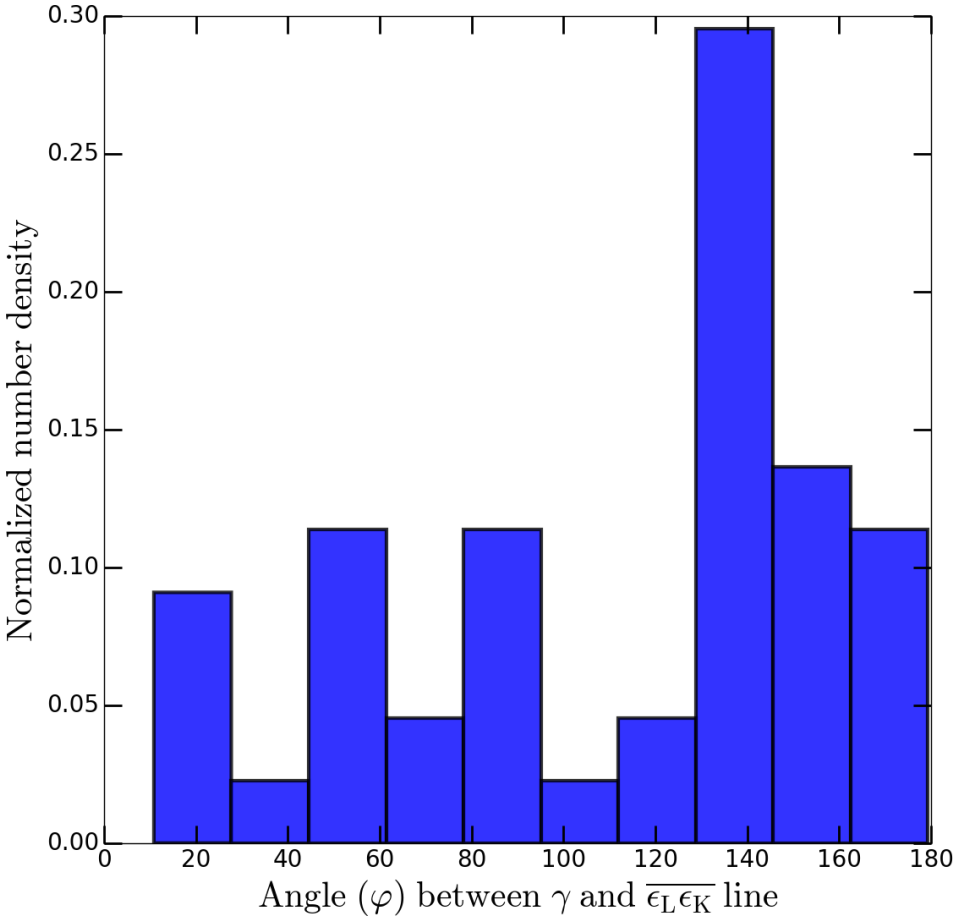

Figure 2.7: The normalized number density histogram of the angle (φ) between the shear vector (γ) and the $\overline{\epsilon_{\rm L}\epsilon_{\rm K}}$ line.

2.5.3 Einstein Radius

Another comparison between the two models is that between the inferred Einstein radii. We have to be careful here though since the lens model that we use is a singular mass model whereas the convergence is affected by the SPH kernel and therefore has a small (0.7 kpc) core that might affect a direct comparison. Figure 2.8 shows the comparison of the Einstein radii obtained from the convergence and the lens modeling. The values obtained from the two independent analyses agree reasonably well and without an appreciable bias, but there is a large $\sim$20% scatter (shaded region) from the one-to-one line. We rejected four data points which have a difference of more than $0.5''$ as critical failures that can heavily bias the standard deviation. From individual inspection of the first, we find that the Einstein radii from the lens models seem more reliable than from the convergence fitting, possibly due to the central core affecting a direct fit.

2.5.4 Density Profile

Finally we describe the comparison of surface density slopes inferred via convergence fitting, t_{NM} and `LENSED`, t_{LENSED} respectively. In Figure 2.9, we show a normalized number density histogram of ratio of the mass density slopes analyzed from both the processes. We find a mean ratio of 0.91 for t_{NM}/t_{LENSED}, with a standard deviation of 0.17. Eventhough the mean suggest a one-to-one correlation between the mass density slopes obtained from lens modeling and convergence fitting, from Figure 2.9 we can also see a tail suggesting that some differences are still present in them. These differences can be attributed to the different methodologies used in direct fitting and lens modeling. The lens modeling fits the density profile (more precisely that of the potential) near the lensed images, whereas the direct fit is mostly fitting the higher density regions inside the mask. The overall agreement however is encouraging, suggesting that lensing does not provide strongly biased density slopes.

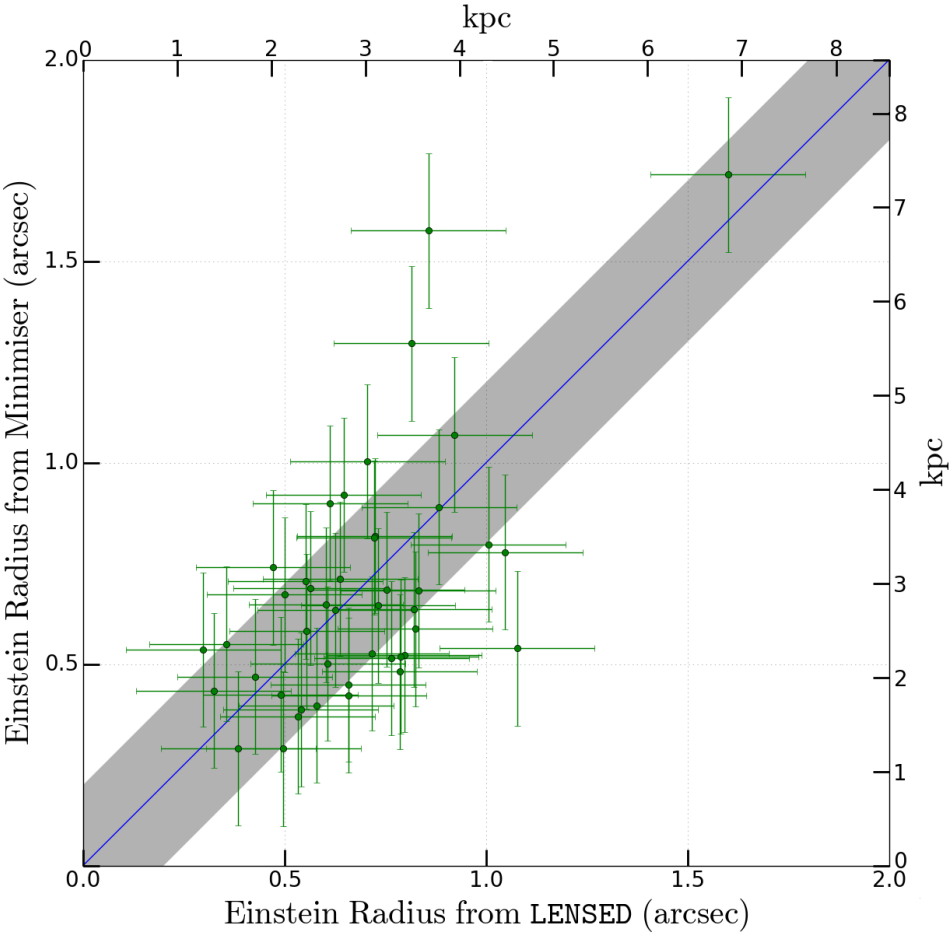

Figure 2.8: Comparison between the values of the Einstein radius R_{Eins} inferred from SIE lens modeling and convergence fitting. The blue line is the one-to-one correspondence. The scatter is given by the gray shaded region. The error-bars are the same 0.2 value of the scatter. Here samples C and D (see Table 2.5) have been used.

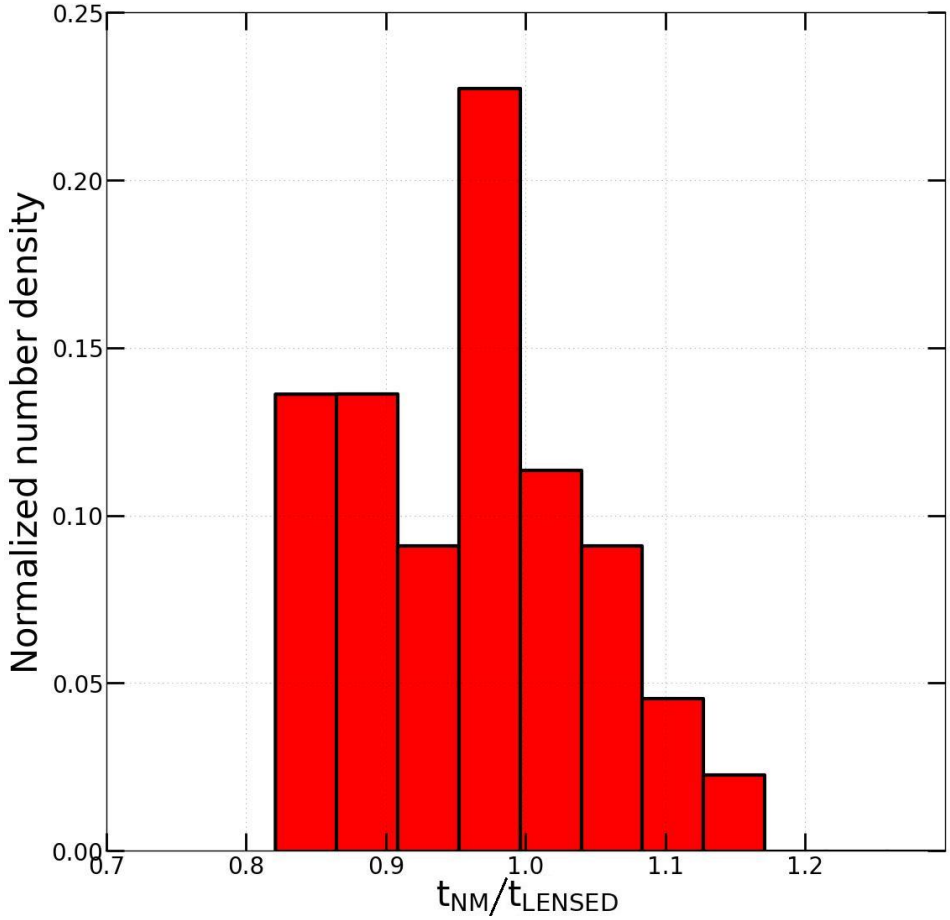

Figure 2.9: Comparison between the values of the mass density slope obtained from `LENSED`, t_{LENSED}, and convergence fitting, t_{NM}. Here samples C and D (see Table 2.5) have been used.

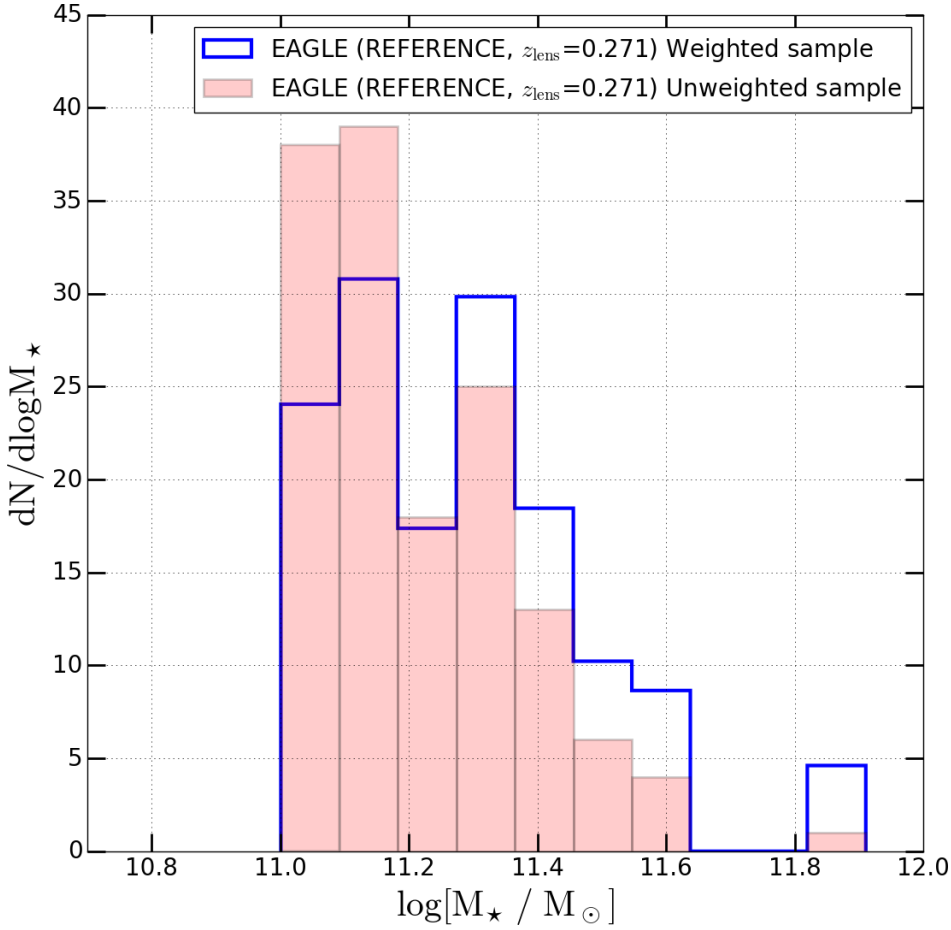

Figure 2.10: The mass function of galaxies having stellar masses $M_\star > 10^{11} M_\odot$, including and excluding the weighting scheme based on stellar mass as discussed in the text. Here sample B has been used.

2.6 Comparisons with SLACS and SL2S

Having studied how well lens-model parameters agree with direct fitting of the same surface density model to the simulations, and having assessed their level of systematic and/or random differences, in this section we do a first-order comparison between EAGLE lenses from the Reference model with those from SLACS and SL2S. In the latter cases we make a correction for the lensing cross-section inferred from their stellar masses (see Section 2.6.2). We concentrate on lenses with a stellar mass exceeding $10^{11}\,\mathrm{M}_{\odot}$, which we believe are currently most reliably represented in the EAGLE simulations, based on the assessments in the previous section.

2.6.1 SLACS & SL2S

SLACS is a HST snapshot imaging survey, where lens candidates were selected spectroscopically from SDSS (Bolton et al. 2006). With more than a hundred confirmed strong lens systems, SLACS is currently the largest and most complete early-type lens survey. The SLACS candidates were selected to yield bright lenses i.e. massive ETGs, in particular Luminous Red Galaxies (LRGs) with faint star-forming background sources, generally with irregular morphology. Hence the SLACS sample was primarily a lens-selected sample. The approximate mean Einstein radius is 1.2 arcsec (Koopmans et al. 2006; Auger et al. 2010b) with background galaxies having a typical scale length of about 0.2 arcsec (Koopmans et al. 2006). In later SLACS papers the sources were modeled with Sérsic profiles (Newton et al. 2011).

SL2S (Cabanac et al. 2007) is a survey dedicated to find and study galaxy-scale and group-scale strong gravitational lenses in the Canada France Hawaii Telescope Legacy Survey (CFHTLS). The galaxy-scale SL2S lenses are found by searching the 170 square degrees of the CFHTLS with the automated software `RingFinder` (Gavazzi et al. 2014) looking for tangentially elongated blue arcs and rings around red galaxies. The lens candidates undergo a visual inspection and the most promising systems are followed up with HST and spectroscopy. For details one can consult Gavazzi et al. (2012).

SL2S differs from SLACS in the way lenses are found. While in SL2S lenses are identified in wide-field imaging data, SLACS lenses were selected by searching for spectroscopic signatures coming from two objects at different redshifts in the same line of sight in the Sloan Digital Sky Survey (SDSS) spectra. These two different techniques lead to differences in the population of lenses in the respective samples. Due to the relatively small fiber used in SDSS spectroscopic observations ($1.5''$ in radius), the SLACS spectroscopic survey tends to limit the search to lenses with equivalent or smaller Einstein radii, where light of both the arcs from the lensed source and the deflector are captured within the fiber. SL2S however finds a larger number of lenses with Einstein radii greater than $1''$, because they are more clearly resolved in ground-based images.

Figure 2.3 shows a subset of simulated lens systems closely mimicking SLACS lenses (Bolton et al. 2006) in morphology and largely being arc and ring systems. Small-scale structure in the lensed images is lacking, because we are using a Sérsic source rather than the more complex (star-forming) real systems. We do not aim to reproduce small-scale features in the source because we only compare global properties such as Einstein radii, axis ratios, density slopes and position angles between SLACS and SL2S and the recovery of these quantities should not strongly depend on the fine-scale structure of the source.

2.6.2 Lens Selection Bias

The statistical comparison of a sample of volume and mass-selected lenses systems from simulations with observations is difficult due to selection biases as well as the often small simulation volumes compared to the volumes probed by lens surveys. The sample properties are for example affected by a lens cross-section that is mass dependent and a magnification bias which are different for different surveys. Because a precise analysis is beyond the scope of this paper, we only correct for the largest of these effects, being the lens cross-section. We assume that the magnification bias does not vary strongly with galaxy mass, which is a reasonable assumption if the source is small compared to the lens cross-section and if the properties of the lens mass model (besides mass) such as its flattening also do not depend strongly on mass. In most surveys that are dominated by $M_\star$ early-type galaxies, these are reasonable assumptions.

The lensing cross-section for the EPL model that we assume (generally close to the SIE), is proportional to the square of the Einstein radius, which in turn is proportional to the stellar mass, assuming the Faber-Jackson relation (Faber & Jackson 1976) and a constant mass-to-light ratio. The latter is a direct observable in both the simulations and observations. We therefore define our weighting scheme (Figure 2.10) per lens simply as

$$W(M) \equiv \left(\frac{M_\star}{\langle M_\star \rangle} \right), \tag{2.9}$$

with $\langle M_\star \rangle$ being the average of the sample. This scheme is used to re-weigh each strong lens when comparing distributions of parameters between observed lenses (i.e. SLACS and SL2S) and simulated lenses. Because most of the lenses are drawn from the exponential tail of the mass function, even such a rather strong (linear) reweighing has only a limited impact on the tilt of the distribution functions. Figure 2.10 shows that although massive ellipticals are rarer than low stellar mass galaxies, more massive ellipticals are more likely to be observed in a lens-survey because of their larger lensing cross-section.

Now we compare the properties of simulated EAGLE lenses with SLACS and SL2S. In this paper we restrict ourselves to $M_\star > 10^{11}$ $M_\odot$. Table 2.5 summarizes the number of galaxies, lenses and projected mass maps. I compare the number density versus stellar mass, the mass density slope and then compare ellipticity and position angle in complex space that I mentioned in section 2.5.1.

2.6.3 Stellar Masses

In Figure 2.11 we compare the simulated and observed stellar mass functions of the lens samples. Although not perfect, given the small-number statistics of the samples, the distributions show that the re-weighting scheme results in a distribution of EAGLE lenses similar to that of SLACS and SL2S. Although a significant number of EAGLE lenses are within the stellar mass range $10^{11.0-11.2}$ $M_\odot$ which are not common in SLACS and SL2S, we can still compare them considering that the simulation box covers only a fraction of the real universe and sample variance is thus very large.

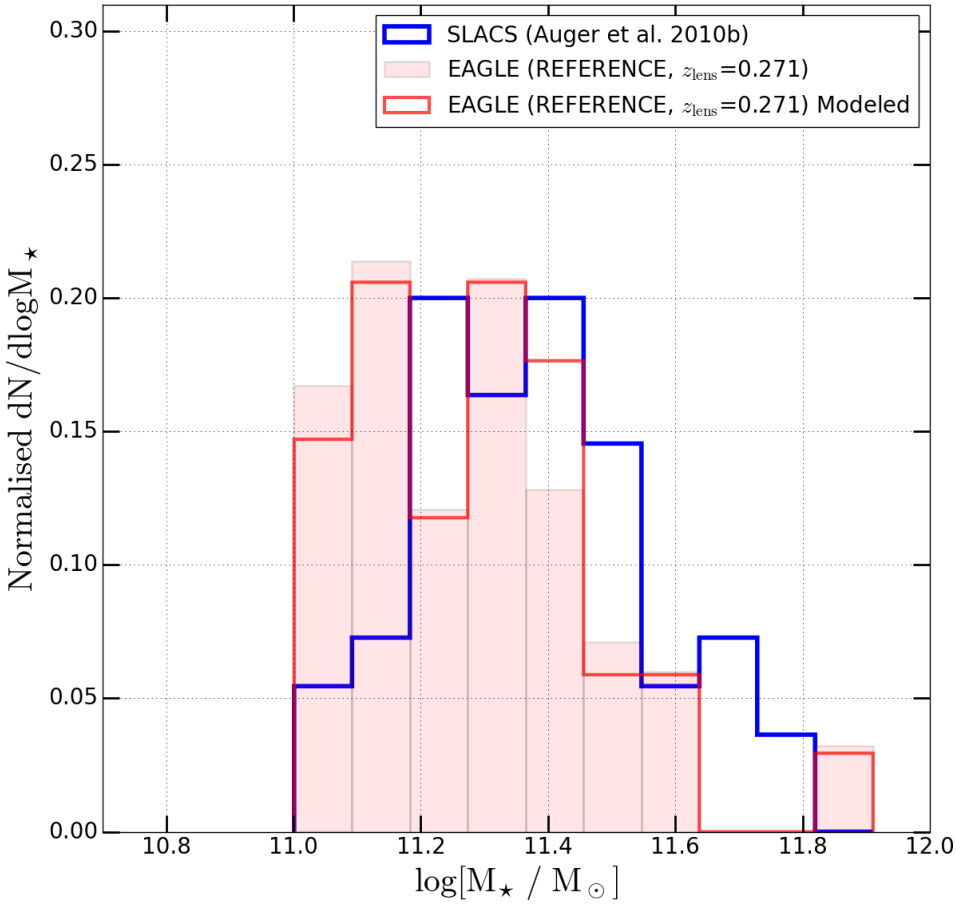

Figure 2.11: –continue–

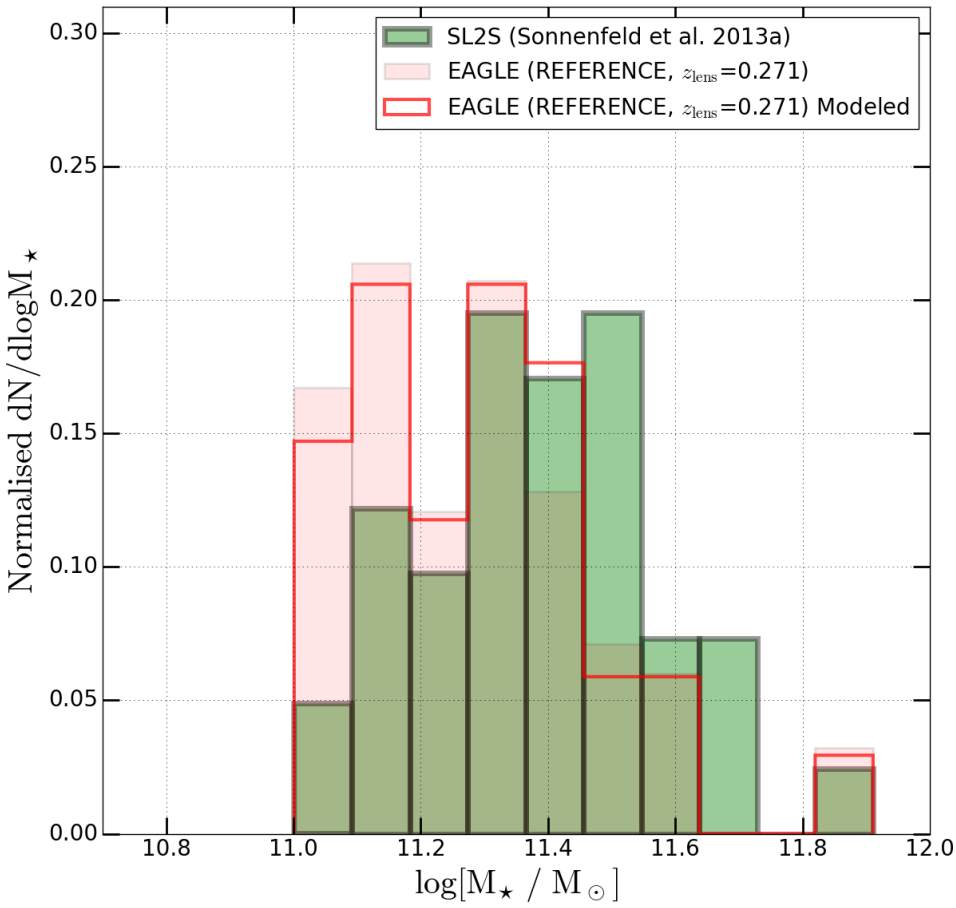

Figure 2.11: Comparison of the EAGLE lenses (total sample and modeled sample) with SLACS and SL2S lenses having stellar masses $M_\star > 10^{11}$ $M_\odot$.

2.6.4 Density Slopes

To compare the density slopes, t (see eq. 2.4) of the simulated lenses with their SLACS and SL2S counterparts, we have binned them into two mass ranges and one overlapping mass range: $10^{11.0-11.5}\mathrm{M}_{\odot}$, $10^{11.5-12.0}\mathrm{M}_{\odot}$ and $10^{11.0-12.0}\mathrm{M}_{\odot}$. Figure 2.12 shows the (normalized) histograms of the density slope. We find a mean value of density slope of 2.26, which quite similar, although slightly higher than SLACS with 2.08 and SL2S with 2.16. This can be explained by several SLACS lenses having much more shallower slopes ($\approx$1.6) especially in the $10^{11.5-12.0}$ $\mathrm{M}_{\odot}$ stellar mass range and SL2S lenses are highly concentrated around density slope $\approx$2.10 in all the three mass-bins which makes the mean value of SLACS and SL2S density slope lower than that of EAGLE. This slight difference (although within rms limits) can be attributed to the subgrid physics, feedback mechanisms used in this simulation run and/or due to systematics. These aspects will be tested in the forthcoming paper in this series.

The mean slope is also consistent with other studies where the mass density slopes are determined from the central dynamics of local galaxies (Dutton & Treu 2014; Tortora et al. 2014) and recent simulations (Remus et al. 2017; Xu et al. 2017). In these simulations, however, the slopes were calculated directly from the particle distributions whereas here we use lens modeling and convergence fitting. In Table 5 I have summarized the mean, root mean square (RMS), median and the 68% confidence interval for the three stellar mass bins.

2.6.5 Complex Ellipticity

Finally, we compare the complex ellipticity from lens modeling of EAGLE lenses (Section 2.5.1) and SLACS. We do not use SL2S results since we do not have direct access to these mass model parameters. Figure 2.13 shows the SLACS lenses in black dots and EAGLE lenses in a similar way as in figure 2.6. The gray shaded region shows the domain of SLACS obtained from Bolton et al. (2008). We find broad agreement between them for 33 out of 45 modeled EAGLE lenses. SLACS lenses are concentrated around the origin of the plot but still some of them suffer from the $q-\phi$ degeneracy (or "conspiracy"). 12 out of 45 modeled EAGLE lenses are completely outside of the shaded region (Figure 2.13).

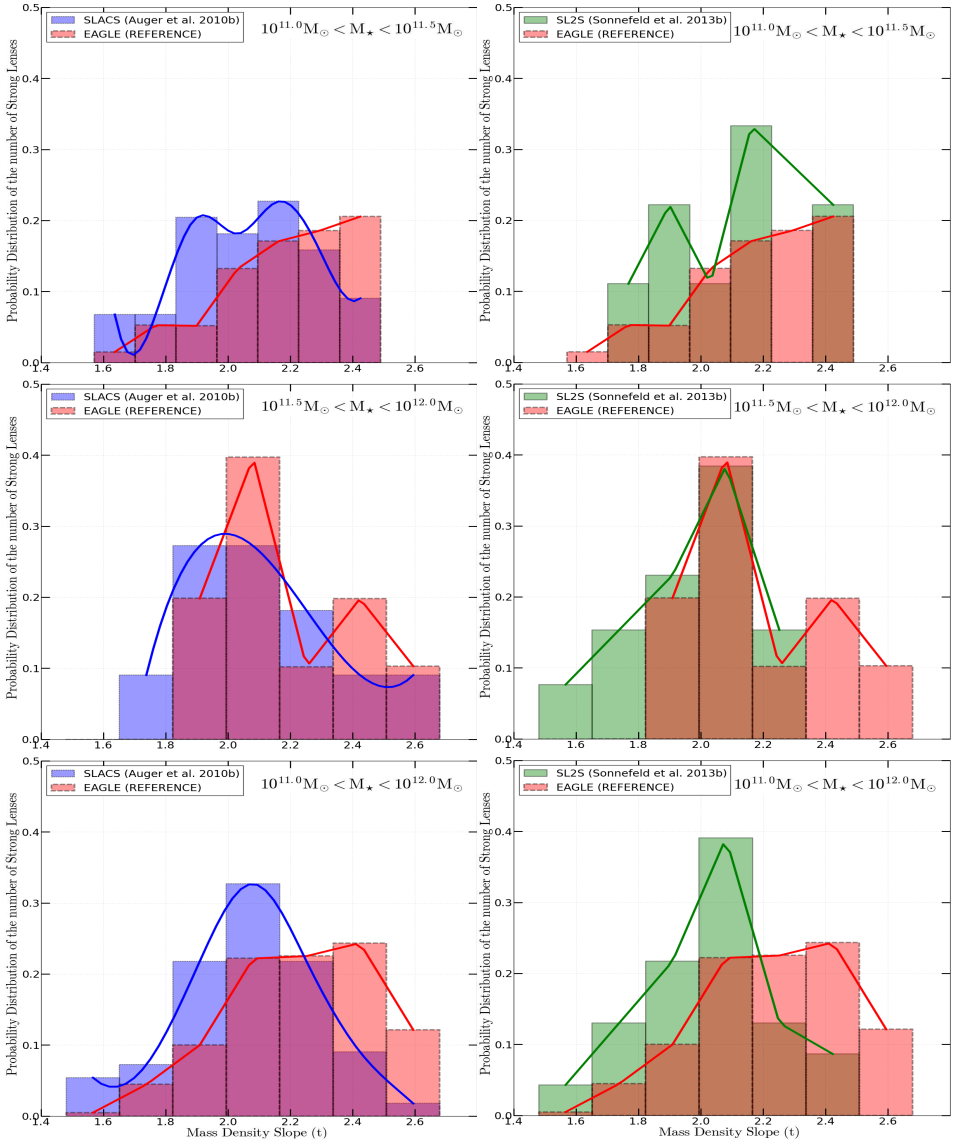

Figure 2.12: The probability distributions of the mass density slope (t, see eq. 2.4) for selected lenses of Reference scenario at $z_l = 0.271$ in three stellar mass-bins of $10^{11.0-11.5}$ $M_\odot$, $10^{11.5-12.0}$ $M_\odot$ and $10^{11.0-12.0}$ $M_\odot$. They are compared to SLACS and SL2S samples. The distributions for EAGLE lenses have been weighted using Equation 2.9. We have created a homogeneous and statistically representative sample of simulated mock strong lens systems mimicking observational surveys of SLACS and SL2S.

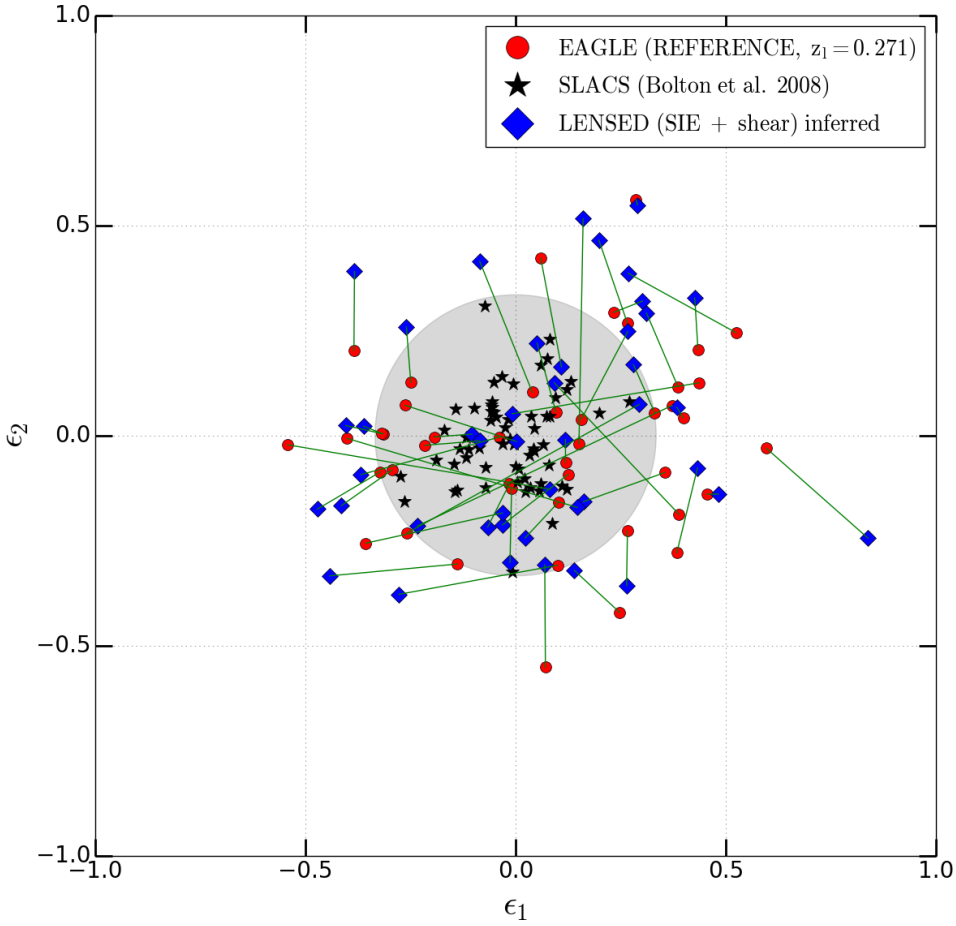

Figure 2.13: -continue-

Table 2.6: The mean, rms, median and 68% confidence limits of mass density slopes, t (see eq. 2.4) of the simulated lenses.

$\log M_\star$ ($M_\odot$)	Mean	RMS	Median	68% CL
$11.0 - 11.5$	2.26	0.26	2.26	1.49-3.03
$11.5 - 12.0$	2.28	0.21	2.23	1.46-3.00
$11.0 - 12.0$	2.26	0.25	2.26	1.49-3.03

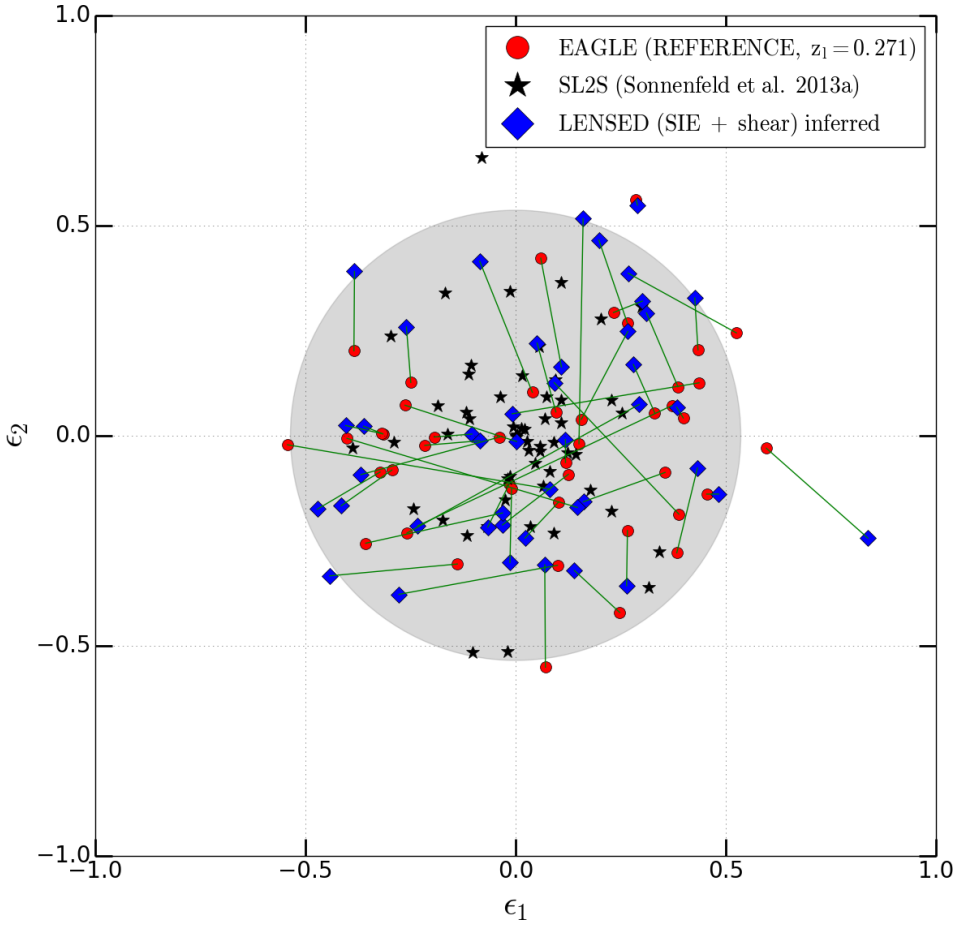

Figure 2.13: Comparison of the axis ratio and position angle of the EAGLE lenses (total modeled sample) with SLACS. The shaded region shows the domain of the SLACS lenses. 12 out of 45 EAGLE lenses fall completely outside of the SLACS range.

2.7 Discussions and Summary

In this chapter I have presented an end-to-end strong-lens simulation and modeling pipeline, allowing us to assess the (dis)agreement between mass-model parameters (e.g. density slope, complex ellipticity) inferred from lens modeling and from direct fitting to the simulations, using the same mass-model family. In the current implementation (called "SEAGLE"), we use the EAGLE (Reference-L050N0752) hydrodynamical galaxy simulations (Schaye et al. 2015; Crain et al. 2015), the `GLAMER` ray-tracing package (Metcalf & Petkova 2014; Petkova et al. 2014), the `LENSED` lens-modeling code (Tessore et al. 2016), and model all lenses as power-law elliptical mass models or singular isothermal ellipsoid mass models with external shear.

When making a stellar mass cut in EAGLE at $> 10^{11}\mathrm{M}_{\odot}$ and after re-weighting the EAGLE stellar mass function $\mathrm{dN/dM}_{\star}$ by a simple estimator of the lens cross-section (Figure 2.10), we find that the simulated lenses have a broadly similar stellar mass function to SLACS and SL2S. Their visual appearance is also strikingly similar (see Figure 2.3). This motivates us to compare these observed lens samples to the simulated lens systems.

In more detail, the conclusions from this work can be briefly summarized as follows:

(1) When comparing the results from lens modeling and direct fitting of the mass surface density of lenses in the simulations, we find a correlation between the external shear (γ) and the complex ellipticity (ϵ), with $\gamma \sim \epsilon/4$ (Figure 2.6). This correlation indicates a degeneracy in the mass model, where the shear compensates for a mismatch between the model and the real mass distribution. This is supported by the fact that the shear and complex ellipticity angles are correlated (Figure 2.7). This could be related to a disky or boxy mass model, ill described by the elliptical model in the direct fit, but affecting the lensed images.

(2) The Einstein radii of the lens models and direct fits broadly match, i.e. within a 20% scatter (Figure 2.8). We attribute this surprisingly large scatter due to the fact that lens modeling really only fits the density profile (more precisely that of the potential) near the lensed images, whereas the direct fit is mostly fitting the higher density regions inside the mask, which might lead to a larger scatter when inferring the Einstein radius. We see

no significant bias however and believe that the scatter is largely coming from the convergence fits.

(3) From the EAGLE Reference model we find that the mass density slope of galaxies inferred from lens-modeling ($t_{\rm LENSED}$) and direct fitting ($t_{\rm NM}$) generally agree well with the ratio, t_{NM}/t_{LENSED}, having a mean of 0.91 and standard deviation of 0.17 (Figure 2.9).

(4) The lens modeling yields a mean density slope of $t = 2.26$ (an SIE has $t = 2$). Direct fitting, though, shows that this slope has a typical rms of 0.15 with that from lensing, setting a limit to the level to which the density slope can be determined (at least in these simulations). The average total density slope is higher than for SL2S, $t = 2.16$ or SLACS, $t = 2.08$ (Figure 2.12). This slight difference within rms can be due to the feedback mechanisms and sub-grid physics adopted in simulations, and also due to systematics.

(5) The complex ellipticity of EAGLE and SLACS lenses shows that three quarters of the modeled EAGLE lenses agree quite well with the distribution of SLACS lenses which is shown by the shaded region (Figure 2.13). Ten out of 12 of the more elliptical simulated lenses have stellar mass $< 10^{11}{\rm M}_{\odot}$. Although a degeneracy exists between q and ϕ but for massive ETGs in EAGLE we find broad agreement with SLACS lenses.

In this work I have presented a pipeline to create and model simulated realistic mock strong lenses and a pilot comparison between EAGLE lenses and SLACS and SL2S lenses. Even though previous work (e.g. Xu et al. 2012) have simulated lenses and tested lensing degeneracies, we have extended those studies by incorporating the aspects of lens modeling and by comparing the inputs to quantify systematic effects in lens modeling. Moreover this work also aims at a full automation of simulated lens creation, modeling and comparison with observation which will be needed when future surveys starts discovering 1000s of strong lenses. In the future, we will use the SEAGLE pipeline to analyze various galaxy formation scenarios of EAGLE, and compare them to observations in order to disentangle various aspects of galaxy formation mechanisms.

Acknowledgements

SM, LVEK, CT and GV are supported through an NWO-VICI grant (project number 639.043.308). SM thanks SURFSARA network in Amsterdam. SM thanks Saikat Chatterjee, Dorota Bayer, Cristiana Spingola, Hannah Stacey and Carlo Enrico Petrillo for useful feedback on the representation of the paper. NT acknowledges support from the European Research Council in the form of a Consolidator Grant with number 681431. MS is supported by VENI grant 639.041.749. JS is supported by VICI grant 639.043.409. RAC is a Royal Society University Research Fellow. FB thanks the support from the grants ASI n.I/023/12/0 "Attività relative alla fase B2/C per la missione Euclid" and PRIN MIUR 2015 "Cosmology and Fundamental Physics: Illuminating the Dark Universe with Euclid". This work used the DiRAC Data Centric system at Durham University, operated by the Institute for Computational Cosmology on behalf of the STFC DiRAC HPC Facility (www.dirac.ac.uk). This equipment was funded by BIS National E-infrastructure capital grant ST/K00042X/1, STFC capital grant ST/H008519/1, and STFC DiRAC Operations grant ST/K003267/1 and Durham University. DiRAC is part of the National E-Infrastructure. This work was supported by the Netherlands Organisation for Scientific Research (NWO), through VICI grant 639.043.409.

References

Auger, M. W., Treu, T., Bolton, A. S., et al. 2009, ApJ, 705, 1099
Auger, M. W., Treu, T., Bolton, A. S., et al. 2010a, ApJ, 724, 511
Auger, M. W., Treu, T., Gavazzi, R., et al. 2010b, ApJL, 721, L163
Balogh, M. L. & Morris, S. L. 2000, MNRAS, 318, 703
Bandara, K., Crampton, D., Peng, C., & Simard, L. 2013, ApJ, 777, 1
Bardeen, J. M., Bond, J. R., Kaiser, N., & Szalay, A. S. 1986, ApJ, 304, 15
Barnes, J. E. & Hernquist, L. 1992, ARA&A, 30, 705
Barnes, J. E. & Hut, P. 1989, ApJS, 70, 389
Bellagamba, F., Tessore, N., & Metcalf, R. B. 2017, MNRAS, 464, 4823
Bender, R., Burstein, D., & Faber, S. M. 1992, ApJ, 399, 462
Bender, R., Burstein, D., & Faber, S. M. 1993, ApJ, 411, 153
Blumenthal, G. R., Faber, S. M., Primack, J. R., & Rees, M. J. 1984, Nature, 311, 517
Bolton, A. S., Burles, S., Koopmans, L. V. E., et al. 2008, ApJ, 682, 964
Bolton, A. S., Burles, S., Koopmans, L. V. E., Treu, T., & Moustakas, L. A. 2006, ApJ, 638, 703
Cabanac, R. A., Alard, C., Dantel-Fort, M., et al. 2007, A&A, 461, 813
Chabrier, G. 2003, PASP, 115, 763
Crain, R. A., Schaye, J., Bower, R. G., et al. 2015, MNRAS, 450, 1937
Crain, R. A., Theuns, T., Dalla Vecchia, C., et al. 2009, MNRAS, 399, 1773
Dobler, G., Keeton, C. R., Bolton, A. S., & Burles, S. 2008, ApJ, 685, 57
Dolag, K., Borgani, S., Murante, G., & Springel, V. 2009, MNRAS, 399, 497
Dutton, A. A. & Treu, T. 2014, MNRAS, 438, 3594
Eggen, O. J. 1965, ARA&A, 3, 235
Faber, S. M. & Jackson, R. E. 1976, ApJ, 204, 668
Fall, S. M. 1983, in IAU Symposium, Vol. 100, Internal Kinematics and Dynamics of Galaxies, ed. E. Athanassoula, 391–398
Feroz, F. & Hobson, M. P. 2008, MNRAS, 384, 449
Feroz, F., Hobson, M. P., & Bridges, M. 2009, MNRAS, 398, 1601
Feroz, F., Hobson, M. P., Cameron, E., & Pettitt, A. N. 2013, ArXiv e-prints
Frenk, C. S., White, S. D. M., Bode, P., et al. 1999, ApJ, 525, 554
Frenk, C. S., White, S. D. M., Efstathiou, G., & Davis, M. 1985, Nature, 317, 595
Fukugita, M. & Peebles, P. J. E. 2006, ApJ, 639, 590

Furlong, M., Bower, R. G., Crain, R. A., et al. 2015a, ArXiv e-prints
Furlong, M., Bower, R. G., Theuns, T., et al. 2015b, MNRAS, 450, 4486
Gao, L., White, S. D. M., Jenkins, A., Stoehr, F., & Springel, V. 2004, MNRAS, 355, 819
Gavazzi, R., Marshall, P. J., Treu, T., & Sonnenfeld, A. 2014, ApJ, 785, 144
Gavazzi, R., Treu, T., Koopmans, L. V. E., et al. 2008, ApJ, 677, 1046
Gavazzi, R., Treu, T., Marshall, P. J., Brault, F., & Ruff, A. 2012, ApJ, 761, 170
Gavazzi, R., Treu, T., Rhodes, J. D., et al. 2007, ApJ, 667, 176
Gunn, J. E. & Gott, III, J. R. 1972, ApJ, 176, 1
Kazantzidis, S., Zentner, A. R., & Kravtsov, A. V. 2006, ApJ, 641, 647
Koopmans, L. V. E., Bolton, A., Treu, T., et al. 2009, ApJL, 703, L51
Koopmans, L. V. E., Treu, T., Bolton, A. S., Burles, S., & Moustakas, L. A. 2006, ApJ, 649, 599
Kormann, R., Schneider, P., & Bartelmann, M. 1994, A&A, 284, 285
Laureijs, R., Amiaux, J., Arduini, S., et al. 2011, ArXiv e-prints
Le Brun, A. M. C., McCarthy, I. G., Schaye, J., & Ponman, T. J. 2014, Monthly Notices of the Royal Astronomical Society, 441, 1270
Lemson, G. & Springel, V. 2006, in Astronomical Society of the Pacific Conference Series, Vol. 351, Astronomical Data Analysis Software and Systems XV, ed. C. Gabriel, C. Arviset, D. Ponz, & S. Enrique, 212
Loeb, A. & Peebles, P. J. E. 2003, ApJ, 589, 29
Marshall, P. J., Treu, T., Melbourne, J., et al. 2007, ApJ, 671, 1196
McAlpine, S., Helly, J. C., Schaller, M., et al. 2016, Astronomy and Computing, 15, 72
Metcalf, R. B. & Petkova, M. 2014, MNRAS, 445, 1942
Moore, B., Ghigna, S., Governato, F., et al. 1998, in Astronomical Society of the Pacific Conference Series, Vol. 136, Galactic Halos, ed. D. Zaritsky, 426
Navarro, J. F., Frenk, C. S., & White, S. D. M. 1996, ApJ, 462, 563
Nelder, J. A. & Mead, R. 1965, The Computer Journal, 7, 308
Newton, E. R., Marshall, P. J., Treu, T., et al. 2011, ApJ, 734, 104
Ostriker, J. P. & Hausman, M. A. 1977, ApJL, 217, L125
Peebles, P. J. E. 1982, ApJL, 263, L1
Petkova, M., Metcalf, R. B., & Giocoli, C. 2014, MNRAS, 445, 1954
Planck Collaboration, Ade, P. A. R., Aghanim, N., et al. 2014, A&A, 571, A16

Press, W. H. & Schechter, P. 1974, ApJ, 187, 425
Remus, R.-S., Dolag, K., Naab, T., et al. 2017, MNRAS, 464, 3742
Ruff, A. J., Gavazzi, R., Marshall, P. J., et al. 2011, ApJ, 727, 96
Rusin, D. & Kochanek, C. S. 2005, ApJ, 623, 666
Rusin, D., Kochanek, C. S., Falco, E. E., et al. 2003a, ApJ, 587, 143
Rusin, D., Kochanek, C. S., & Keeton, C. R. 2003b, ApJ, 595, 29
Sand, D. J., Treu, T., Smith, G. P., & Ellis, R. S. 2004, ApJ, 604, 88
Schaller, M., Dalla Vecchia, C., Schaye, J., et al. 2015a, MNRAS, 454, 2277
Schaller, M., Frenk, C. S., Bower, R. G., et al. 2015b, MNRAS, 451, 1247
Schaye, J., Crain, R. A., Bower, R. G., et al. 2015, MNRAS, 446, 521
Schaye, J., Dalla Vecchia, C., Booth, C. M., et al. 2010, MNRAS, 402, 1536
Schweizer, F. 1982, ApJ, 252, 455
Searle, L. & Zinn, R. 1978, ApJ, 225, 357
Segers, M. C., Schaye, J., Bower, R. G., et al. 2016, MNRAS, 461, L102
Sersic, J. L. 1968, Atlas de galaxias australes
Shu, Y., Bolton, A. S., Brownstein, J. R., et al. 2015, ApJ, 803, 71
Shu, Y., Brownstein, J. R., Bolton, A. S., et al. 2017, ArXiv e-prints
Skilling, J. 2006, Bayesian Anal., 1, 833
Sonnenfeld, A., Gavazzi, R., Suyu, S. H., Treu, T., & Marshall, P. J. 2013a, ApJ, 777, 97
Sonnenfeld, A., Treu, T., Gavazzi, R., et al. 2013b, ApJ, 777, 98
Sonnenfeld, A., Treu, T., Marshall, P. J., et al. 2015, ApJ, 800, 94
Springel, V. 2010, MNRAS, 401, 791
Springel, V., Di Matteo, T., & Hernquist, L. 2005a, MNRAS, 361, 776
Springel, V., Frenk, C. S., & White, S. D. M. 2006, Nature, 440, 1137
Springel, V., White, S. D. M., Jenkins, A., et al. 2005b, Nature, 435, 629
Springel, V., Yoshida, N., & White, S. D. M. 2001, New Astronomy, 6, 79
Tagore, A. S., Barnes, D. J., Jackson, N., et al. 2018, MNRAS, 474, 3403
Tessore, N., Bellagamba, F., & Metcalf, R. B. 2016, MNRAS, 463, 3115
Tessore, N. & Metcalf, R. B. 2015, A&A, 580, A79
Toomre, A. & Toomre, J. 1972, ApJ, 178, 623
Tortora, C., La Barbera, F., Napolitano, N. R., et al. 2014, MNRAS, 445, 115
Trayford, J. W., Camps, P., Theuns, T., et al. 2017, MNRAS, 470, 771
Trayford, J. W., Theuns, T., Bower, R. G., et al. 2015, MNRAS, 452, 2879
Treu, T., Gavazzi, R., Gorecki, A., et al. 2009, ApJ, 690, 670
Treu, T., Koopmans, L. V., Bolton, A. S., Burles, S., & Moustakas, L. A. 2006, ApJ, 640, 662

Treu, T. & Koopmans, L. V. E. 2004, ApJ, 611, 739
Tully, R. B., Somerville, R. S., Trentham, N., & Verheijen, M. A. W. 2002, ApJ, 569, 573
Vogelsberger, M., Genel, S., Springel, V., et al. 2014, MNRAS, 444, 1518
Vogelsberger, M., Sijacki, D., Kereš, D., Springel, V., & Hernquist, L. 2012, MNRAS, 425, 3024
White, S. D. M. & Rees, M. J. 1978, MNRAS, 183, 341
Xu, D., Springel, V., Sluse, D., et al. 2017, MNRAS, 469, 1824
Xu, D. D., Mao, S., Cooper, A. P., et al. 2012, MNRAS, 421, 2553

Appendix 2.A

2.A.1 Cores in Simulations and masking

Here I show how the spatial resolution affects the inner (< 1 kpc) region of EAGLE galaxies. We used two simulation boxes of EAGLE-Reference run i.e., L050N0752 and L025N0752 (the latter with higher resolution). In Figure 2.14 I plot the surface mass density vs the radius for an example galaxy (after projection and lens creation). We can see that the slopes flatten at their respective softening lengths (represented by $\epsilon_{\rm prop}$, as in Table 1). The radius where the two density profiles start to converge, is well inside the Einstein radii of this galaxies.

However, the effect of smoothing in the central region does not bias the strong lensing analysis, since we mask out the inner 7×7 pixels, which correspond to 1.4×1.4 kpc. Masking is a standard practice in observational analysis, too, where strong lenses are analysed after masking out the lensing galaxy. In order to not bias the results from simulation and to make an unbiased comparison with direct fitting results we perform this masking operation in our simulated galaxies (see Section 3). This aspect is very important as the cores can skew the density slopes obtained directly from simulations, if the mask is not used.

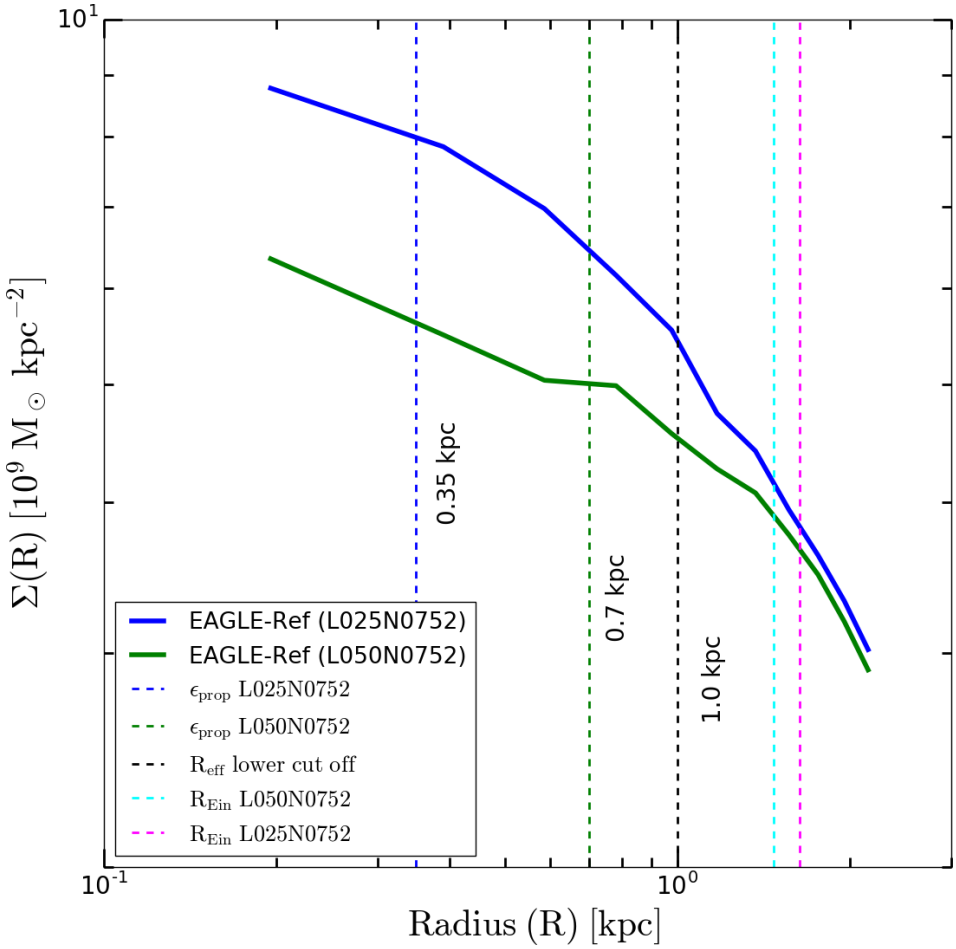

Figure 2.14: Comparison of the surface mass density profile of two example ETGs extracted from the EAGLE-Reference runs L050N0752 and L025N0752 having similar stellar masses ($M_\star \sim 10^{10.6}\ M_\odot$). The effect of the smoothing kernel can be visualized when the slope flattens at their respective softening lengths.

Table 2.7: Comparison of the modeled density slopes and shear having different prior settings in `LENSED` and using different source sizes. We note that the differences are minor and much smaller than the spread between systems or their typical errors ($t_{\rm L}$ is $\pm$ 0.05 and $\gamma_{1,2}$ is $\pm$ 0.001).

	EPL-Gaussian			EPL-Uniform		
Prior on t_L	μ=1.1, σ=0.1			0 – 2		
Prior on γ_1 γ_2	μ=0.0, σ=0.01			-0.1 – 0.1		
Source	$t_{\rm L}$	γ_1	γ_2	$t_{\rm L}$	γ_1	γ_2
†Sérsic, $R_{\rm eff} = 0.2$	1.06	-0.040	0.021	1.05	-0.041	0.021
†Sérsic, $R_{\rm eff} = 0.3$	1.08	-0.038	0.020	1.05	-0.039	0.021
†Sérsic, $R_{\rm eff} = 0.4$	1.06	-0.036	0.020	1.04	-0.040	0.021

† All other Source parameters have been kept same as Table 2.4

2.A.2 Effect of source sizes and prior types

I have used a sub sample of our simulated lenses to asses the impact of source sizes and different prior settings. There lensing galaxies having $\rm M_\star > 10^{11} M_\odot$ projected along 3 axes have been used. So lens-modeling results from a total of 9 lenses have been presented here.

In Table 2.7 I summarize the effect of different source sizes and prior types on the mean results of modeled density mass slope ($t_{\rm L}$) and shear components (γ_1 and γ_2). We used two different families of prior settings: Gaussian and uniform. The values of the priors (the mean μ and standard deviation σ for gaussian priors and *minimum* and *maximum* of the range of values for uniform priors) are tabulated in Table 2.7. We find that there is no substantial effect of the priors on the final result. In this work we used the Gaussian priors on $t_{\rm L}$ since the computational time is decreased by 30-40% with respect to using uniform priors.

Also to note that there is no significant improvement in the final results using more spatially extended sources. This is expected since with $R_{\rm eff}$=0.2 arcsec (typical SLACS source size; see Newton et al. 2011) for an HST-ACS filter, the S/N is already sufficient to constrain lens parameters.

Chapter 3

Impact of subgrid physics on total mass density slope

Based on

SEAGLE–II: The impact of feedback in galaxy formation on the mass-size relation and the total density profile of massive early-type strong lens galaxies,

Sampath Mukherjee, Léon V. E. Koopmans, R. Benton Metcalf, Crescenzo Tortora, Matthieu Schaller, Joop Schaye, Georgios Vernardos, Fabio Bellagamba

To be submitted to MNRAS

Abstract

We use ten different galaxy formation scenarios from the EAGLE – a suite of ΛCDM hydrodynamical simulations – to assess the impact of feedback mechanisms in galaxy formation and compare these to observed strong lenses. To compare observations with simulations, we create strong lenses with the appropriate resolution and noise level, and model them with an elliptical power-law mass model to constrain their total mass density slope. We also obtain the mass-size relation of the simulated lens-galaxy sample. We find significant variations in their total mass density slope calculated at their Einstein radii and projected stellar mass-size relation, when compared to observed strong lens galaxies, mainly due to different implementations of stellar and AGN feedback. Models with either too weak or too strong stellar and/or AGN feedback fail to explain the distribution of observed mass-density slopes, with the counter-intuitive trend that increasing feedback steepens of the mass density slope around the Einstein radius (3-10 kpc). On the other hand, models with constant stellar feedback, or AGN feedback with a higher duty cycle but milder temperature increases of their surrounding gas, produce strong lenses with total mass density slopes close to isothermal (i.e. $-d\log(\rho)/d\log(r) \approx 2.0$) and slope distributions statistically agreeing with observed strong lens galaxies in SLACS and BELLS. Agreement is only slightly worse with the more heterogeneous SL2S lens galaxy sample. Strong lenses in simulations thus appear to favor models with weaker AGN feedback to obtain agreement with lens observables.

3.1 Introduction

Large-scale numerical simulations have established the Cold Dark Matter (CDM) paradigm as a viable framework for galaxy formation (e.g. Davis et al. 1985; Frenk et al. 1988). The CDM model predicts that galaxies form in dark matter halos having a Navarro-Frenk-White (NFW) density profile (Navarro et al. 1996, 1997) and predict the abundance and distribution of substructures within these halos (Springel 2010; Gao et al. 2004). The non-linearity of galaxy formation (Peebles & Yu 1970; Peebles 1974), assembly and evolution (White & Rees 1978; Loeb & Peebles 2003), however, complicates a full description of galaxy formation on small (several kpc) scales and the central regions of CDM halos can also be strongly modified by baryonic matter and their associated physical processes. Baryons settle into the centers of density concentrations due to dissipation thereby modifying the inner DM slopes (Duffy et al. 2010; Sonnenfeld et al. 2012; Grillo 2012; Remus et al. 2013; Cappellari et al. 2013; Tortora et al. 2014; Pontzen & Governato 2014). Because a complete analytic theory of baryonic physics is lacking, the use of hydrodynamic simulations including many physical processes (e.g. Schaye et al. 2010; Vogelsberger et al. 2014; Schaye et al. 2015; Dubois et al. 2016; Hopkins et al. 2016) has emerged as the dominant tool to study the complex non-linear interactions taking place during galaxy formation. State-of-the art hydrodynamical simulations with improved stellar and AGN feedback, for example, can reproduce the cosmic star formation history of the Universe Pearce et al. 2001; Springel & Hernquist 2003), the galaxy stellar mass function (Oppenheimer et al. 2010; Puchwein & Springel 2013), as well as their environment (Crain et al. 2009). Hydro-simulations work only above certain mass and spatial resolutions, however, and physical processes on smaller scales are implemented via analytic prescriptions known as 'sub-grid physics'. The impact of varying sub-grid physics prescriptions on large representative populations of stellar systems was first addressed in the 'OverWhelmingly Large Simulations' project (OWLS; Schaye et al. 2010), a suite of over fifty large cosmological hydrodynamical simulations with varying sub-grid physics. Calibration of sub-grid prescriptions to reproduce limited number of observables has been explored extensively (Vogelsberger et al. 2014; Schaye et al. 2015; Crain et al. 2015; McCarthy et al. 2017), showing that their exact parameterizations are very important to understand the

mechanism of galaxy formation and the effects of baryons on shaping CDM halos.

Strong gravitational lensing is one of the most robust and powerful techniques to measure the total mass and its distribution in galaxies on kpc scales (Kochanek 1991; Koopmans et al. 2006), allowing their inner structure and evolution over cosmic time to be studied in great detail (Treu et al. 2006, 2009; Koopmans et al. 2006, 2009; Dutton & Treu 2014), independently of the nature of the matter or its dynamical state. In particular, the study of the mass density profile of massive lensing galaxies at $z > 0.1$ can trace their formation and evolution mechanisms (Barnabè et al. 2009, 2011). The last two decades saw major progress in observational studies of strong lensing thanks to surveys such as the Lenses Structure and Dynamics survey (LSD; Treu & Koopmans 2004), the Sloan Lens ACS Survey (SLACS; Bolton et al. 2006; Koopmans et al. 2006; Bolton et al. 2008a,c; Koopmans et al. 2009; Auger et al. 2010b,a; Shu et al. 2015, 2017), the Strong Lensing Legacy Survey (SL2S; Cabanac et al. 2007; Ruff et al. 2011; Gavazzi et al. 2012; Sonnenfeld et al. 2013a,b, 2015) and the BOSS Emission-Line Lens Survey (BELLS; Brownstein et al. 2012). Future or ongoing surveys such as with Euclid (Laureijs et al. 2011) and with the Large Synoptic Survey Telescope (LSST; Ivezić et al. 2008), as well as the Kilo Degree Survey (KiDS; de Jong et al. 2015) and the Dark Energy Survey (DES; The Dark Energy Survey Collaboration 2005), are expected to increase the number of known strong lenses by several orders of magnitude (Petrillo et al. 2017; Metcalf et al. 2018) and revolutionize strong lensing studies.

Although there have been simulation studies of strong lensing focusing on the study of the mass-size relations, the total density slope and other observables (Remus et al. 2017; Peirani et al. 2017; Xu et al. 2017), the impact of varying sub-grid physics (in particular baryonic feedback) on lensing statistics, their mass density slopes and stellar masses and sizes have not been studied comprehensively (Duffy et al. 2010; Peirani et al. 2018). Duffy et al. (2010) in particular analyzed the impact of baryon physics on dark matter structure at redshift of z=2. But because most of the strong lenses are found in the redshift range $0<z<0.5$, an more extensive analysis is necessary at lower redshift. To remedy this, Mukherjee et al. (2018a) (hereafter M18), introduced the `SEAGLE` pipeline to systematically study galaxy formation via simulated strong lenses.

SEAGLE (M18; Mukherjee et al. 2018b,c) aims to investigate and possibly disentangle galaxy formation and evolution mechanisms by comparing strong lens early-type galaxies (ETGs) from hydrodynamic simulations with those observed, analyzing them as similarly as is possible (although this is not always exactly possible).

In the current study, we make use of the Evolution and Assembly of GaLaxies and their Environments (EAGLE) simulations (Schaye et al. 2015; Crain et al. 2015; McAlpine et al. 2016) – a suite of state-of-the-art hydrodynamical simulations – to create, model and analyze simulated strong lens-galaxies and compare them with observations. We extend the work of M18. Throughout this study, we use ten selected galaxy formation scenarios (i.e. having different sub-grid physics prescriptions; Schaye et al. 2015; Crain et al. 2015), the GLAMER ray-tracing package (Metcalf & Petkova 2014; Petkova et al. 2014), and the LENSED lens-modeling code (Tessore et al. 2016). We preselect potential strong lenses based on their cataloged stellar masses and create projected mass maps for three different orientations. We calculate the half-mass radius from the simulated mass maps. We create mock lenses by ray tracing through the mass maps, placing an analytic Sersic (1968) source, at a higher redshift, having observationally motivated parameters. We ignore line-of-sight effects, which for massive ETGs is expected to be a decent assumption (see e.g., Koopmans et al. 2006). We use a single-orbit HST-ACS F814W noise level and PSF to more closely mimic strong lenses found in SLACS and BELLS observations (Auger et al. 2010b; Bolton et al. 2012a).

Throughout this work, we also discuss possible observational systematics (e.g. differences in model-fitting methodologies, differences in filters/bands of the observational surveys, possible lens selection biases, etc.) as well as resolution effects in the simulations, that might affect their comparison. The key aim of this study, however, is to illustrate the effects of the sub-grid physics parametrization adopted by the EAGLE reference model, and the strong sensitivity of a number of strong lens observables to the variation of the key sub-grid physics. In future work, we will also analyze other properties such as the dark matter fractions and stellar Initial Mass Function (IMF).

The paper is structured as follows. In Section 3.2, we summarize the EAGLE galaxy formation simulations and the relevant codes that are used

in this paper. Section 3.3 describes the simulation and analysis pipeline. The mass models used in this work are described in Section 3.4. We give a brief description of the strong lensing observations in Section 3.5. We compare mock lens samples with observations in Section 3.6, in terms of their mass-size relations and the total matter density slopes. The implications of our results are discussed and summarized in Section 3.7. Throughout the paper we use EAGLE simulations that assume a Chabrier stellar Initial Mass Function (IMF, Chabrier 2003) and compare these observables derived under the same IMF assumption. The values of the cosmological parameters are $\Omega_\Lambda = 0.693$, $\Omega_\mathrm{b} = 0.0482519$, $\Omega_\mathrm{m} = 0.307$, $h = H_0/(100\ \mathrm{km\ s^{-1}\ Mpc^{-1}}) = 0.6777$ and $\sigma_8 = 0.8288$. These are taken from the Planck satellite data release (Planck Collaboration et al. 2014).

3.2 EAGLE Simulations

In this section we describe the EAGLE simulations used in this study. In Section 3.2.1, we broadly describe the types of model-variations that have been chosen and in Section 3.2.2, we describe the simulation setup and the sub-grid physics recipes that are used in those model variations. Section 3.2.3 describes the calibrated simulations and reference models variation are summarized in Section 3.2.4. The details presented here are kept concise, yet informative, to make this paper self-contained.

3.2.1 EAGLE model variations

The simulations explored in this paper are taken from Crain et al. (2015) plus the 100cMpc-Reference run from Schaye et al. (2015). Crain et al. (2015) divided the simulations into two categories. The first comprises four simulations *calibrated* to yield the $z = 0.1$ galaxy stellar mass function (GSMF) and central black hole (BH) masses as function of galaxy stellar mass. The second category comprises simulations that each vary a single sub-grid physics parameter with respect to the reference model but without considering whether they match the GSMF (i.e. they are not calibrated). In the calibrated simulations, the models differ in terms of their adopted efficiency of feedback associated with star formation, and how this efficiency depends upon the local environment. In the Reference variation

simulations, the sensitivity of the resulting galaxies to these variations are assessed. We note that similar variations have previously been done in the OWLS project (Schaye et al. 2010). The general conclusion from previous work has been that the properties of simulated galaxies are most sensitive to the efficiency of baryonic feedback (see e.g., Schaye et al. 2010; Scannapieco et al. 2012; Haas et al. 2013a,b; Vogelsberger et al. 2013) . This has motivated us to focus in this study largely on the effect of baryonic feedback on lensing observables, in particular on the total mass density profile in the inner regions of massive early-type galaxies (∼5 kpc) which is not part of the calibration process.

3.2.2 Subgrid physics

Physical processes on scales smaller than the resolution of the EAGLE simulations are incorporated via analytic prescriptions. In EAGLE, radiative cooling and heating rates have been computed for eleven chemical elements by interpolating tables generated with the `CLOUDY` (version 07.02) code of Ferland et al. (1998). The calculations of rates account for variations in metallicity and for variations in the relative abundances of individual elements. The cooling rates are specified as a function of density, temperature and redshift, assuming that the gas is optically thin, in ionization equilibrium, and is exposed to the cosmic microwave background and an instantaneous, spatially uniform, temporally-evolving (Haardt & Madau 2001) UV/X-ray background (Wiersma et al. 2009a). Star formation has been implemented stochastically, based on the pressure law scheme of Schaye & Dalla Vecchia (2008), but with the metallicity-dependent density threshold of Schaye (2004) under the assumption that the star-forming gas is self gravitating. A density threshold for star formation, $n_{\rm H}^{\star}$, was imposed because star formation occurs only in cold ($T \ll 10^4$K), dense gas. Because the transition from a warm, neutral phase to a cold, molecular only occurs at lower densities and pressures in more metal-rich (and hence dust-rich) gas, the metallicity-dependent star formation threshold proposed by Schaye (see equations 19 and 24 of Schaye 2004) was adopted:

$$n_{\rm H}^{\star}(Z) = \min\left[0.1\,{\rm cm}^3\left(\frac{\rm Z}{0.002}\right)^{-0.64}, 10\,{\rm cm}^3\right], \tag{3.1}$$

where Z is the gas metallicity. Every star particle constitutes a stellar population with a fixed Chabrier (2003) IMF. The mass-to-light (M/L) ratio includes all the stellar remnants. The implementation of stellar evolution and mass loss is based on the prescription described in Wiersma et al. (2009b). Stars inject energy and momentum into the ISM. The energy produced at each time step by a star particle is distributed to a number of its neighboring hydrodynamic resolution elements, supplementing their internal energy. The simulations adopt the stochastic thermal feedback scheme of Dalla Vecchia & Schaye (2012), in which the temperature increment, $\triangle T_{\rm SF}$, of heated resolution elements is specified. The fraction of the energy budget that is available for feedback determines the probability that a resolution element neighboring a young star particle is heated. This fraction is referred to as $f_{\rm th}$ (Dalla Vecchia & Schaye 2012). According to the convention, $f_{\rm th} = 1$ equates to an expectation value of the injected energy of 1.736×10^{49}erg $\mathrm{M}_{\odot}^{-1}$ of stellar mass formed. Lastly, AGN feedback is implemented via a single mode, where energy is injected thermally and stochastically, analogous to energy feedback from star formation. The efficiency of the stellar feedback and the BH accretion were calibrated to broadly match the observed local ($z \approx 0$) GSMF, subject to the constraint that galaxy sizes must be in agreement with observations.

Identifier	Side length [cMpc]	N	$\gamma_{\rm eos}$	$n_{\rm H}^{\star}$ [cm^{-3}]	$f_{\rm th}$-scaling	$f_{\rm th,max}$	$f_{\rm th,min}$	$n_{\rm H,0}$ [cm^{-3}]	$n_{\rm n}$	$C_{\rm visc}/2\pi$	$\Delta T_{\rm AGN}$ $\log_{10}$ [K]
Calibrated models											
FBconst	50	752	4/3	Eq. 3.1	–	1.0	1.0	–	–	10^3	8.5
FBσ	50	752	4/3	Eq. 3.1	$\sigma^2_{\rm DM}$	3.0	0.3	–	–	10^2	8.5
FBZ	50	752	4/3	Eq. 3.1	Z	3.0	0.3	–	–	10^2	8.5
Ref (FBZρ)	50	752	4/3	Eq. 3.1	Z, ρ	3.0	0.3	0.67	$2/\ln 10$	10^0	8.5
Ref-100 (FBZρ)	100	1504	4/3	Eq. 3.1	Z, ρ	3.0	0.3	0.67	$2/\ln 10$	10^0	8.5
Reference-variations											
ViscLo	50	752	4/3	Eq. 3.1	Z, ρ	3.0	0.3	0.67	$2/\ln 10$	$\mathbf{10^2}$	8.5
ViscHi	50	752	4/3	Eq. 3.1	Z, ρ	3.0	0.3	0.67	$2/\ln 10$	$\mathbf{10^{-2}}$	8.5
AGNdT8	50	752	4/3	Eq. 3.1	Z, ρ	3.0	0.3	0.67	$2/\ln 10$	10^0	**8.0**
AGNdT9	50	752	4/3	Eq. 3.1	Z, ρ	3.0	0.3	0.67	$2/\ln 10$	10^0	**9.0**
NOAGN	50	752	4/3	Eq. 3.1	Z, ρ	3.0	0.3	0.67	$2/\ln 10$	10^0	–

Table 3.1: A summary of the subgrid parameters of the EAGLE simulations used in this work. Columns are: the side length of the volume (L) and the particle number per species (i.e. gas, DM) per dimension (N), the power law slope of the polytropic equation of state ($\gamma_{\rm eos}$), the star formation density threshold ($n_{\rm H}^{\star}$), the scaling variable of the efficiency of star formation feedback ($f_{\rm th}$), the asymptotic maximum and minimum values of $f_{\rm th}$, the Ref model's density term denominator ($n_{\rm H,0}$) and exponent ($n_{\rm n}$) from equation, the subgrid accretion disc viscosity parameter ($C_{\rm visc}$) from equation, and the temperature increment of stochastic AGN heating ($\Delta T_{\rm AGN}$). The upper section shows the four calibrated models that reproduce the $z = 0.1$ GSMF, and the lower section features Reference-variation simulation where a single-parameter has been changed. The varied parameter are in bold. All models also adopt $n_{\rm Z} = 2/\ln 10$ with the exceptions of FBσ, for which the parameter $n_{\rm Z}$ is replaced by $n_{\rm T}$ with the same numerical value (see equation 3.3), and FBconst, for which the parameter is inapplicable. Partially reproduced from Crain et al. (2015).

3.2.3 Calibrated simulations

The choice of sub-grid routines and the adjustment of their parameters can result in substantial alterations of the simulation outcomes. Schaye et al. (2015) established that the appropriate methodology for cosmological simulations is to calibrate the parameters of sub-grid routines with a small number of key observations, in order that simulations reproduce those representative observables, and then compare properties (between simulations and observations) those quantities that are not considered during the calibration. The total mass density slopes is one of those. The results thus obtained can reasonably be considered being a consequence of the implemented astrophysics. Below we briefly describe the calibrated simulations of Crain et al. (2015) that are also used in this paper. Table 3.1 provides a concise overview of all the important parameters and a brief description of the four calibrated EAGLE simulations.

FBConst

This is the simplest feedback model where a fixed amount of energy per unit stellar mass is injected into the ISM, independently of the local conditions. This value corresponds to the total energy liberated by type-II SNae, i.e. $f_{\rm th} = 1$.

FBσ

This model prescribes feedback based on to local conditions, inferred from neighboring DM particles. The efficiency, $f_{\rm th}$, is calibrated as a function of $\sigma^2_{\rm DM}$. The latter is the square of the 3-dimensional velocity dispersion of the DM particles within the smoothing kernel of a star particle at the instant it is born. It represents a proxy for the characteristic virial scale of environment of the star particle, with corresponding temperature

$$T_{\rm DM} = \frac{\mu m_{\rm p} \sigma^2_{\rm DM}}{3k} \simeq (4 \times 10^5 \text{ K}) \mu \left(\frac{\sigma_{\rm DM}}{100 \,\text{kms}^{-1}} \right)^2 . \tag{3.2}$$

For simplicity, it is assumed that the mean molecular weight of a fully ionized gas has a primordial composition at all times, $\mu = 0.591$. The

adopted functional form of $f_{\rm th}$ is a logistic (sigmoid) function,

$$f_{\rm th} = f_{\rm th,min} + \frac{f_{\rm th,max} - f_{\rm th,min}}{1 + \left(\frac{T_{\rm DM}}{10^5\ {\rm K}}\right)^{n_{\rm T}}}\ . \tag{3.3}$$

The function asymptotically tends to $f_{\rm th,max}$ and $f_{\rm th,min}$ in the limits $T_{\rm DM} \ll 10^5$K and $T_{\rm DM} \gg 10^5$K, respectively, and varies smoothly between these limits above and below $T_{\rm DM} = 10^5\ K$ (or $\sigma_{\rm DM} \simeq 65$ km/s). The parameter $n_{\rm T} > 0$ controls how rapidly $f_{\rm th}$ transitions as the dark matter 'temperature' scale deviates from 10^5 K.

FBZ

This model make the radiative losses, $f_{\rm th}$, a function of the metallicity of the ISM. Energy losses associated with star formation feedback are likely to be more significant when the metallicity is sufficient for cooling from metal lines to dominate over the cooling contribution from H and He. For temperatures $10^5\,K < T < 10^7\,K$, characteristic of outflowing gas in the simulations, the transition is expected to occur at $Z \sim 0.1Z_{\odot}$ (Wiersma et al. 2009a). This phenomenon can be represented by the same functional form as equation 3.3, replacing ($T_{\rm DM}$,$n_{\rm T}$,10^5 K) with (Z,$n_{\rm Z}$,$0.1Z_{\odot}$) to obtain,

$$f_{\rm th} = f_{\rm th,min} + \frac{f_{\rm th,max} - f_{\rm th,min}}{1 + \left(\frac{Z}{0.1Z_{\odot}}\right)^{n_Z}}\ , \tag{3.4}$$

where $Z_{\odot} = 0.0127$ is the solar metallicity and $n_{\rm Z} = n_{\rm T} = 2/\ln 10$.

Galaxy Selection				
Observable	Value	Name		Comments
$M_\star$	$\geq 1.76 \times 10^{10} M_\odot$	Stellar mass threshold		Taken from Auger et al. (2010b)
σ	> 120 km/sec	Stellar velocity dispersions		Kept lower than SLACS
R_{50}	> 1 kpc	Projected half-mass radius		
Lens Candidates				
	$M_\star$ threshold for follow-up works	$M_\star$ threshold for this work		
Simulation	$\geq 1.76 \times 10^{10} M_\odot$	$>10^{11}$ $M_\odot$	Projection	Comments
Reference-100cMpc	-	67	201	100 cMpc box.
Reference-50 (FBZρ)	252	25	75	50 cMpcbox
FBconst	279	22	66	〃
FBσ	259	22	66	〃
FBZ	312	19	57	〃
ViscLo	289	29	87	〃
ViscHi	188	14	42	〃
AGNdT8	276	27	81	〃
AGNdT9	194	8	24	〃
NOAGN	312	37	111	〃
Object-properties	Value	Type		Comments
Orientation	3	x, y, z		Projected surface density maps
Redshift	$z_l = 0.271$	-		Consistent with SLACS' mean lens-redshift of 0.3
Source Properties				
Parameters	Value	Unit		Comments
Source Type	Sérsic	-		Consistent with SLACS lenses (Newton et al. 2011)
Brightness	23	apparent mag.		〃
Size ($R_{\rm eff}$)	0.2	arcsec		〃
Axis ratio (q_s)	0.6	-		〃
Sérsic Index	1	-		〃
Redshift	z_s=0.6	-		〃
Position	Random	Within caustics		Producing rings and arcs lens systems consistent with SLACS

Table 1 : —– contd—–

Instrumental Settings		
Parameters	Value	Comments
PSF	Gaussian, FWHM=0.1 arcsec	-
Noise	HST ACS-F814W, 2400 sec	-
Image Properties		
Map used	Properties	Value
Surface density	(a) Size	512×512 pixels
	(b) Units	kpc
κ, Inv. mag. map and Lens	(a) Size	161×161 pixels
	(b) Units	degrees (converted from arcsec)

Table 3.2: The summary of the simulation settings and output products.

Reference (FB$Z\rho$)

The feedback associated with FBσ and FBZ is numerically inefficient because a significant fraction of the star particles form at densities greater than $n_{\mathrm{H,t_c}}$, the resolution-dependent critical density above which feedback energy is quickly radiated away (Dalla Vecchia & Schaye 2012). These spurious energy losses can be partly compensated when a density dependence is introduced in the expression for f_{th}:

$$f_{\mathrm{th}} = f_{\mathrm{th,min}} + \frac{f_{\mathrm{th,max}} - f_{\mathrm{th,min}}}{1 + \left(\frac{Z}{0.1Z_{\odot}}\right)^{n_Z} \left(\frac{n_{\mathrm{H,birth}}}{n_{\mathrm{H},0}}\right)^{-n_n}} , \tag{3.5}$$

where $n_{\mathrm{H,birth}}$ is the density of a gas particle at the instant that it is converted into a star particle. The feedback efficiency therefore increases with density at a fixed metallicity, whilst respecting the original asymptotic values. Such a density dependence may have a physical basis, because the star formation law and hence the feedback energy injection rate per unit volume, has a supra-linear dependence on surface density, which may result in smaller radiative losses at higher densities. In this work we use both the 50 and 100 cMpc boxes of the Reference model. The 100 cMpc box has a much larger number of massive galaxies for comparison to strong lens observations, whereas we use the Reference-50 boxes to compare with other model variations.

3.2.4 Variations of the reference model

Schaye et al. (2015) demonstrated that it is possible to calibrate the Reference model satisfactorily to reproduce the GSMF and the observed sizes of galaxies at $z = 0.1$. However, it remains important to quantify the sensitivity of this model to variations of its key sub-grid parameters. Hence, Crain et al. (2015) conducted a series of simulations (listed in the lower section of Table 1) for which the value of a single parameter was varied from that adopted in the Reference model. Here we briefly summarize five Reference-variation models that are used in this work. There are five more Reference-model variations available, but those have a smaller box size (25 cMpc) that provide insufficient numbers of high-mass galaxies for comparsions to observed strong lens galaxies.

ViscLo and ViscHi

The parameter $C_{\rm visc}$ governs both the angular momentum scale at which gas accretion onto black holes switches from the relatively inefficient viscosity-limited regime to the Bondi-limited regime (with both cases being subject to the Eddington limit), as well as the rate at which gas transits through the accretion disc when the viscosity-limited regime applies. A *lower* value of the viscosity parameter $C_{\rm visc}$, corresponding to a higher sub-grid viscosity, leads to an earlier onset of the dominance of AGN feedback, and a larger energy injection rate when in the viscosity-limited regime. The viscosity parameter could be important in the baryon conversion efficiency and in the halo mass scale at which the peak baryon conversion occurs. Lower (higher) values for the viscosity increases (decreases) both of them. However, we note that Bower et al. (2017) showed that the transition from slow to fast black hole growth, which leads to the quenching of star formation, occurs when the halo is sufficiently massive to make stellar feedback inefficient, and depends only very weakly on $C_{\rm visc}$.

AGNdT8 and AGNdT9

Schaye et al. (2015) have examined the role of the AGN heating temperature in EAGLE by adopting $\Delta T_{\rm AGN} = 10^{8.5}$Kand 10^9K. They concluded that a higher heating temperature, which yields more energetic although less frequent AGN feedback episodes, appears necessary to reproduce the gas fractions and X-ray luminosities of galaxy groups. Le Brun et al. (2014) also concluded that a higher heating temperature yields more efficient AGN feedback. We analyze two Reference-model variation simulations with $\Delta T_{\rm AGN} = 10^8$K (AGNdT8) and $\Delta T_{\rm AGN} = 10^9$K (AGNdT9), besides the Reference model itself which adopted $\Delta T_{\rm AGN} = 10^{8.5} K$. The heating events (less frequent but more energetic) associated with a higher heating temperature are more effective at regulating star formation in massive galaxies. The peak baryon conversion efficiency is higher (lower) in the AGNdT8 (AGNdT9) model, with respect to the Reference model. The reduced efficiency of AGN feedback, when a lower heating temperature is adopted, leads to the formation of more compact galaxies, because gas can more easily accrete into the centers of galaxies and form stars.

NOAGN

The final model that we consider has no AGN feedback and is the most extreme EAGLE model variation for massive galaxies. It appears unrealistic because it because the lack of AGN feedback is expected to dramatically increase the baryon concentration in the inner region of galaxies, producing overly massive and concentrated galaxies. The reason that this variation is included is to clearly demonstrate the effect of absence of AGN activity. All other parameters are kept the same as in the Reference run.

3.3 Creating Mock Lens Data

We describe the `SEAGLE` (Simulating EAGLE LEnses) pipeline in more detail in this section. We briefly describe the selection criteria of the (lens) galaxies from EAGLE, the extraction technique of the galaxy from the simulations, the impact of the projection on the lens galaxy convergence map (Section 3.3.1), ray-tracing with `GLAMER` to create mock lensed images (Section 3.3.2), and finally the automatic process to create masks around the lensed images (Section 3.3.3) that are used in the lens modeling. The flow diagram shown in Figure 1 of M18 describes the `SEAGLE` pipeline and the resulting data products. The reader is referred to M18 for more details on the pipeline.

3.3.1 Galaxy selection and post-processing

The initial down-selection of (lens) galaxies is based on the broad lens redshift (z_l) and stellar mass ($\mathrm{M}_\star$) range from SLACS. Auger et al. (2010b) find a lens redshift range of $0.075 < z_\mathrm{lens} < 0.513$ and a lower limit on the total stellar mass lower limit of $\mathrm{M}_\star \geq 1.76 \times 10^{10}\ \mathrm{M}_\odot$. The luminosities and effective radii of SLACS lens galaxies are based on a deVaucouleur profile fit to the galaxy brightness distribution as observed with HST. We choose their I-band filter value, assuming it is closest to the bulk of the stellar mass. The former are turned into stellar masses assuming either a Chabrier or Salpeter stellar IMF. We use the former in this paper to remain consistent with EAGLE. We also use a lower limit on both the line-of-sight stellar velocity dispersion ($\sigma > 120\ \mathrm{km\,s^{-1}}$) inside a aperture of 10 kpc and the half stellar

mass radius ($R_{50} > 1$ kpc) from the EAGLE snapshot catalogs to avoid blatant outliers e.g., due to halo stars, mergers and other contaminations arising from stray particles in the simulations. Table 3.2 summarizes these initial selection criteria. We select all sub-halo indices that match these selection criteria and extract all their particles from the snap-shot. We do this for a single redshift in the middle of the SLACS redshift range, i.e. $z_l = 0.271$[1]. Although this neglects the effect evolution in the simulated sample, this redshift sits roughly in the middle of the bulk of the redshifts of the combined set of SLACS, BELLS and SL2S lenses. For more details on the galaxy extraction we refer to Section 3.2 of M18. We finally rotate the particle position vectors in several direction around the center of the lens galaxy. Although this does not lead to an independent lens galaxy, it does allow for some testing of the effects of orientation on the inference of the galaxy properties. In the current paper, each galaxy is projected along its three principle axes. The particles are subsequently converted into projected surface density maps, after smoothing of the particles with the same SPH kernel as used in the simulation (see appendix A of Trayford et al. 2017). For each galaxy, we separately calculate the surface density maps for the individual particle types (DM, stars and gas), as well as their total surface density map. Stellar remnants are included in the star particles.

3.3.2 Creating mock lens systems

The surface density maps are created in units of solar masses per pixel on grids of 512 × 512 pixels (Table 3.2). They form the input to the ray-tracing lensing code `GLAMER` (Metcalf & Petkova 2014; Petkova et al. 2014). The size (100 pkpc) and pixel scale (∼0.2 pkpc) of the grid ensure that the surface density map and the corresponding convergence map are well resolved in the inner regions of the galaxy (see Tagore et al. 2018), down to the simulation softening length, and are consistent with the SLACS pixel scale of 0.05 arcsec at z=0.271, corresponding to ∼0.2 pkpc. We

[1] We reiterate, as in M18, that the lens redshift is fixed at z=0.271 for all mock lenses, despite having a range of observed lens redshifts. This redshift is intermediate between that of SLACS at somewhat lower redshifts and SL2S plus BELLS at somewhat higher redshifts. Choosing a separate box for all lenses, to account for the minor effect of evolution, is computationally not feasible. We expect the effect of evolution to be small around this redshift (Furlong et al. 2015b,a) and to be smaller than the observed scatter in the inferred quantities.

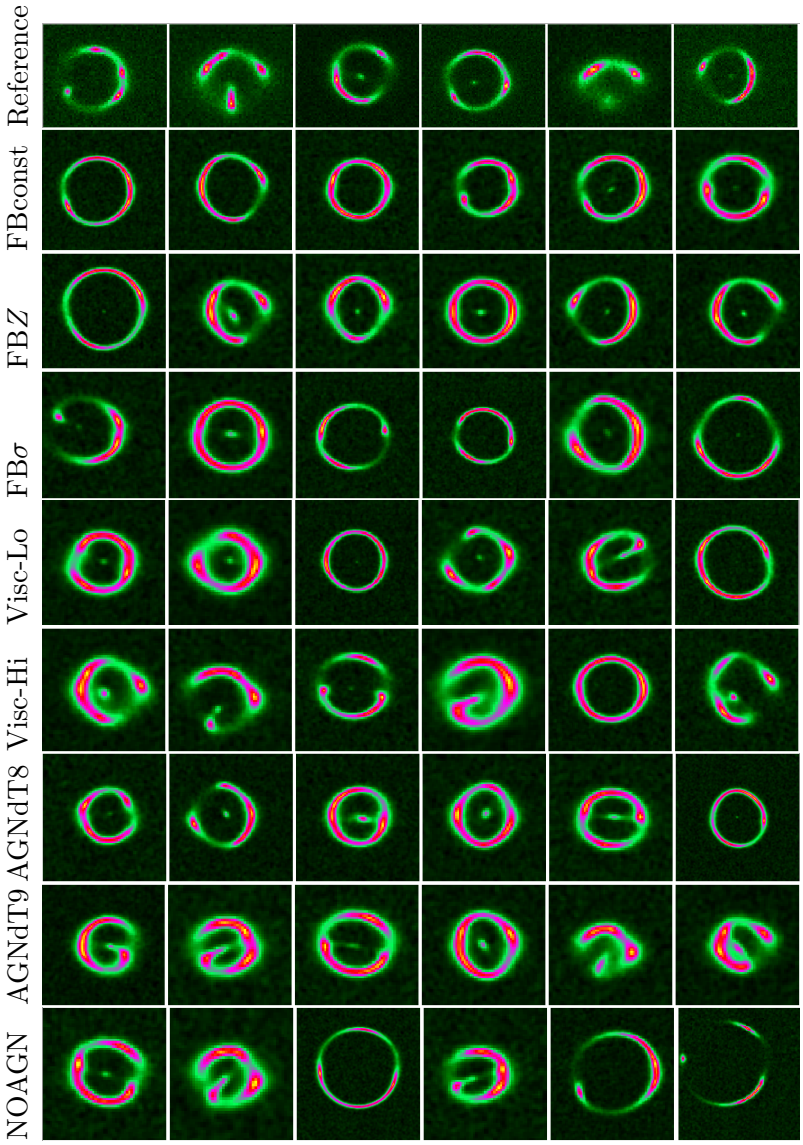

Figure 3.1: Mosaic of a randomly selected sub-sample of six strong lenses from each of the nine EAGLE model variations ($z_l = 0.271$, $z_s = 0.6$). Their morphologies (for a source randomly placed inside the diamond caustic) covers that of quads, rings and arcs, and visually resemble SLACS lenses remarkably well.

also need to choose a source redshift for GLAMER to convert these mass maps into convergence maps, by dividing the surface density maps by the critical surface density which is set by the lens and source redshifts (Meylan et al. 2006). We choose a fixed redshift of $z_{\rm s} = 0.6$, typical for SLACS lenses[2] To described the source, we use an elliptical Sérsic brightness profile with an index $n = 1$, apparent magnitude = 23 in the HST-ACS F814W filter (AB system), an effective radius of 0.2 arcsec, a position angle $\phi_s = 0$ deg and a constant axis ratio q_s=0.6. Given that source and galaxy position angles are uncorrelated, the fixed position angle of the source does not reduce generality. For each convergence map, the critical curves and caustics are calculated, using GLAMER, to determine where a source has to be placed in order to create multiple lensed images. The source is then placed randomly inside the diamond caustics of the lens to maximize the number of arc and ring-like systems in the simulations (this roughly mimics the large magnification bias in the observations). The pixel scale of the grid – representing the lensed images – is set to 0.05 arcsec with the PSF and noise corresponding to an HST-ACS F814W exposure of typically 2400 s. As shown in M18, the choice of the source parameters has negligible influence on the quantities of interest in this analysis. The final resulting images have sizes of 161 × 161 pixels of 8.0 arcsec side length. The images are exported in standard fits-file format. All parameter values are again listed in Table 3.2 and motivated mostly by the range of values inferred from SLACS lenses (e.g. Koopmans et al. 2006; Newton et al. 2011; Bandara et al. 2013).

3.3.3 Mask creation

To mask large areas in the image of noisy pixels and include only regions around the lensed images in the lens modeling, we automatically create a mask for each lens system. We convolve the noisy lensed images with a Gaussian with a FWHM of 0.25 arcsec to reduce the noise by about a factor of ∼5 and to smear the images to a slightly larger footprint. We then set a surface brightness threshold typically 2.5–5 times below the original noise level. This threshold defines the edge of the mask and faithfully traces the

[2]Similar to the lens redshift, we choose a fixed source redshift to reduce computational overhead, although this restriction cab be let go in the future. The dependence of the Einstein radius on source redshift is weak, however, increasing by $< 20\%$ from $z_s = 0.6$ to 1.0. Since all quantities in this work are determined inside fractions of the effective radius, the impact of choice of the source redshift is very small.

lensed images below the noise and sufficiently extends outside the lensed images to include some noise-dominated pixels in the original image (see e.g. Figure 4 in M18). The central 7×7 pixels of images (i.e. centered on where the lens galaxy is) are also masked, very similar to real lenses. This removes any artificially bright central images that are purely the result of a too low central convergence due to the small, but still finite, size of the SPH kernel. Whereas in real lenses the central surface density in general is extremely high (i.e. leading to large gradients in the potential), thereby de-magnifying the central lensed image, in the mock lenses it leads to a too bright central image. To avoid a bias in the lens model, we mask this central region. This artificial core however has little impact on the outer images near the Einstein radius. The resulting mask is used in all subsequent modeling and only image data inside the mask are used in the lens modeling.

3.4 Modeling of the Lens Sample

In this section we describe the selection of the final mock lens sample (Section 3.4.1), and the subsequent gravitational lens modeling and convergence-map fitting, i.e. the modeling of the surface mass density as directly obtained from the simulations (Section 3.4.2).

3.4.1 The lens sample

Implementing an automated recipe for the lens modeling of galaxies with stellar masses $M_\star < 10^{11}$ $M_\odot$ has proven extremely difficult due to the finite resolution effect of the particles during projection causing an artificial 'core' in inner density profile, which in turn creates prominent but artificial images in the central regions of the lenses during ray tracing. These artificial images are not observed in real lens systems and are particularly pronounced in lower-mass galaxies that are more affected by the finite resolution of the simulations. As in M18, we therefore restrict ourselves further to galaxies with total stellar masses $M_\star > 10^{11}$ $M_\odot$. These galaxies are far less affected by any resolution effects and still significantly overlap with the mass range of SLACS and SL2S lenses. Of these massive galaxies, ∼80% are central galaxies (the most massive subhalo of a given halo) and ∼20% are satellites

(subhalos other than the main subhalo) in the 100 cMpc box. For the 50 cMpc boxes they are mostly (>90%) central galaxies. Table 3.2 summarizes the selection of this restricted and more massive sub-sample, used for all comparisons with observed lenses in this work.

3.4.2 Gravitational lens modeling

Having created the mock lens systems, we model each lens system with `LENSED` (Tessore et al. 2016; Bellagamba et al. 2017) using either an Elliptic Power Law (EPL; Tessore & Metcalf 2015) or a Singular Isothermal Ellipsoid (SIE; Kormann et al. 1994) mass model, including external shear. We use the corresponding mask, noise level and PSF for each system. A total of 14 or 15 parameters are sampled using an Nested Sampling MCMC method for the SIE or EPL models, respectively. The EPL mass model (which includes the SIE) has provided a good approximation of the mass model of massive galaxy-scale strong gravitational lenses in various observational studies (Treu & Koopmans 2004; Koopmans et al. 2006, 2009; Newton et al. 2011). As a first step we therefore model the lenses as a SIE plus external shear with the prior settings tabulated in Table 3 of M18. This keeps the power-slaw density slope fixed. The dimensionless surface mass density of the SIE model is given by

$$\kappa(R) = \frac{b}{2R}, \tag{3.6}$$

where b is approximately the Einstein ring radius (formally only for q=1) and R is the elliptical radius defined by $R = \sqrt{qx^2 + y^2/q}$, where q is the axis ratio (short over long axis) and x, y are Cartesian coordinates of the model. The lens is allowed to change in position angle and mass centroid as well. Similarly, we model and analyze the lenses with an EPL mass model, whose convergence is given by

$$\kappa(R) = \frac{(2 - t_L)}{2} \left(\frac{b}{R}\right)^{t_L}, \tag{3.7}$$

where $0 < t_L < 2$ is the power-law surface mass density slope and the other parameters are the same as for the SIE model. This profile can arise from an oblate three-dimensional density distribution, with $\rho(r) \propto r^{-t}$, where $t = t_L + 1$. Both models also include an external shear. Statistically one can

compare the ensemble of density slopes of the simulated lenses with those from SLACS, BELSS and SL2S via the EPL model. We note though that many of the SLACS density slopes were obtained from a combined lensing and dynamics analysis, rather than only from lensing (Koopmans et al. 2009; Auger et al. 2010a). We assume here that there is no significant bias between the lensing and lensing plus dynamics analyses. The same model also allows for a direct comparison with the convergence map fitting, which we do not further discuss in this work but was extensively studied in M18. As in the creation of the mock lenses, we use a Sérsic profile to model the source. Even though some of the SLACS, BELSS and SL2S sources show irregular morphologies, our main objective is to infer the global properties of the lensing galaxies, and the precise choice of the source model does not bias the lens parameters for different (and inexact) source models (see Section 4.4 of Tessore et al. 2016). An additional test was carried out in M18, where we found no change in the distribution of the model parameters when changing the source model parameters between lens systems (see Appendix A of M18). The priors used in the lens and source modeling are listed in in Table 3 in M18, being a combination of Gaussian and uniform priors. The priors were chosen such that the convergence of lens modeling parameters occurs faster in the Nested Sampling Optimization and leads to minimal biases. We note that the priors are generally much wider than the inferred errors, hence they mostly guide the convergence rather than impact the error budget.

3.5 Observations

Here we summarize the strong lensing observational surveys that we use to compare with our results. In Section 3.5.1 we describe briefly the observations. Section 3.5.2 describes the weighting scheme that is used to compare simulated lens ensemble properties with observation. We note that in our comparison between simulated and observed lenses, we show all of the SLACS lens galaxies for visual purposes, even lower mass ones which are limited in number, but only quantitatively compare these galaxies with simulated galaxies for the restricted range $M_\star > 10^{11}\ M_\odot$.

3.5.1 SLACS, SL2S and BELLS

SLACS is a survey where lens candidates were selected spectroscopically from SDSS (Bolton et al. 2006). SLACS has identified more than a hundred confirmed strong lens systems, with HST follow-up. The SLACS galaxies are massive ETGs, specifically Luminous Red Galaxies (LRGs) with star-forming background sources emitting strong emission lines. The advantage of the SLACS survey is that for all lenses spectroscopic lens and source galaxy redshifts are available. The mean Einstein radius is 1.2 arcsec (Koopmans et al. 2006; Auger et al. 2010b) with background galaxies having a typical size of about 0.2 arcsec (Koopmans et al. 2006; Newton et al. 2011) and typically being at $z_{\rm s} \approx 0.6$. Although being the largest complete strong lens sample, SLACS has a relatively limited lens redshift range with the bulk of the lenses in the range of $z_{\rm l} \approx 0.1 - 0.3$. SL2S (Cabanac et al. 2007) was dedicated to find and study galaxy-scale and group-scale strong gravitational lenses in the Canada France Hawaii Telescope Legacy Survey (CFHTLS), providing a larger sample of strong lenses at higher redshift. SL2S lenses were found by searching 170 square degrees of the sky with the automated software `RingFinder` (Gavazzi et al. 2014), searching for tangentially elongated blue arcs and rings around red galaxies. The most promising systems were followed up with HST and spectroscopy (Gavazzi et al. 2012). Even though SL2S lenses combined with SLACS provided evidence of structural evolution (Ruff et al. 2011), the SL2S sample is limited by a lack of source-galaxy redshifts for a considerable number of systems. BELLS (Brownstein et al. 2012) used the same methodology as SLACS to select the strong lenses, but they used Baryon Oscillation Spectroscopic Survey (BOSS; Eisenstein et al. 2011) spectra. BELLS discovered a sample of strong galaxy-galaxy lenses, at somewhat higher redshifts, that is of comparable size and homogeneity to that of SLACS at lower redshift. BELLS is also comparable in stellar mass to the SLACS lens galaxies. Both the BELLS and SLACS samples are complete in their spectroscopic lens and source galaxy redshifts. Bolton et al. (2012b) has reported evidence for mild evolution in the mass density slope between BELLS and SLACS. We ignore this in the sample of mock lenses and compare observations with simulations only at $z = 0.271$, in the middle between the two samples, as discussed earlier.

3.5.2 Lens selection bias

Differences in lens-galaxy selection and follow-up can lead to differences in the population of lenses in the SLACS, BELLS and SL2S samples. For example, due to the relatively small fiber opening used in SDSS spectroscopic observations (1.5″ radius), the SLACS spectroscopic survey typically limits the search to lenses with an equivalent or smaller Einstein radii (although larger lenses could be found if one of the lensed images is inside the fiber and bright enough), and finite source effects play a role as well. SL2S on the other hand can select lenses directly from images and over a larger Einstein radius range, i.e. mass scale, typically yielding Einstein radii greater than 1″, because they are less well resolved in ground-based images. These selection effects are extremely hard to quantify though (see e.g., Dobler et al. 2008, for SLACS). Observational selection biases often hinder a proper comparison between simulations and lens surveys, strong lensing being no exception. In this work, we assume that lens selection biases are dominated by the lens-galaxy mass and correlate sub-dominantly with the lens and source redshifts, and with the lens-galaxy mass density profile and ellipticity. This is a decent assumption if the lens mass models are close to isothermal (i.,e, the caustics are shape invariance as function of redshifts sand only scale in cross-section) and the source size is small compared to the Einstein radius (Dobler et al. 2008). Massive elliptical also do not vary strongly in their ellipticity. The observed lens sample properties are then mainly affected by the lensing cross-section, which is mass dependent, and by the magnification bias, which can be different between surveys. A precise analysis is very difficult to implement and beyond the scope of this paper. We therefore take an empirical approach and only correct for the lens cross-section and we assume that the magnification bias does not correlate with galaxy mass[3]. The lensing cross-section for the EPL model that we assume (generally close to the SIE), is proportional to the square of the Einstein radius, which in turn is proportional to the stellar mass, assuming the Faber-Jackson relation (Faber & Jackson 1976) and a constant mass-to-light ratio. The latter is a direct observable in both the simulations and observations.

[3]This holds exactly for SIE models if the source is a point source and the galaxy mass model (i.e. ellipticity for the SIE) does not vary with galaxy mass.

We then define our weighting scheme per lens as

$$W(M_\star) \equiv \left(\frac{M_\star}{\langle M_\star \rangle} \right)^\alpha , \tag{3.8}$$

with $\langle M_\star \rangle$ being the average stellar mass of the galaxies in the sample and $\alpha = 1$. We re-weigh each simulated strong lens (which we assume to be volume limited) when comparing distributions (i.e. histograms) of the mass-density slopes between observed lenses from SLACS, BELLS, SL2S and simulated lenses. Hence a weight W_i for simulated lens i implies it counts as W_i galaxies (note that the weights are non-integers). Most of the lenses are massive systems, and in general drawn from the exponential tail of the mass function. Hence re-weighing should have a limited impact on the massive end of the distribution functions, but it does affect strong the low-mass end. We test a few values for $\alpha = 0.5, 1.0, 1.5$ to show that the weighing scheme does not affect the conclusions and are only to mimic the observation selection bias of the lenses depending on their stellar mass. Other options for re-weighing the lens galaxies, to account for their lens cross-section, are by using either their Einstein radius or their stellar velocity dispersions, which we have not done in this work and leave for future improvements in the analysis when we study the redshift evolution of these lenses. Currently, we do not reweigh the mass-size relations, which are compared to SLACS and also statistically constrained via the KS test.

3.6 Results

In this section we compare the simulated EAGLE lenses with those from SLACS, BELLS and SL2S, in terms of their surface mass density profile. Even though SL2S and BELLS lenses are typically at somewhat higher redshifts, we compare the simulated lenses at z_l=0.271 assuming limited ETG evolution within the redshift range $0<z<1$, as discussed earlier. This assumption is reasonable as it was pointed out by both Sonnenfeld et al. (2013b) and Koopmans et al. (2006), that the total mass density slopes (which are close to isothermal) do not strongly evolve with time in observed ETG lenses (although see Bolton et al. 2012a). We compare the mass-size relation in Section 3.6.1, and the total density slopes in Section 3.6.2. Table 3.2 summarizes the number of galaxies, lenses and projected mass maps.

3.6.1 The Mass-Size Relation

Observationally the stellar mass (or luminosity more precisely) of an ETG correlates with its size (Shen et al. 2003; Baldry et al. 2012). Similarly, in simulations the stellar masses of galaxies correlates with their sizes (Furlong et al. 2015a). Previously, Sales et al. (2010) explored different feedback models in OWLS (Schaye et al. 2010) and found large variations in the abundance and structural properties of bright galaxies at $z = 2$. They showed that models with inefficient or no feedback lead to the formation of overly massive and compact galaxies with a large fraction (upwards of 50 per cent) of all available baryons (gas, stars, and stellar remnants) being retained in each halo. Increasing the efficiency of stellar or AGN feedback reduces the baryonic mass fraction fraction and increases the size of the simulated galaxies.

To assess whether a similar relation holds for the mock lenses at $z_\mathrm{l} = 0.271$, we define the effective radius (R_eff) as the stellar projected half-mass radius in the simulations, hence assuming a constant mass-to-light ratio. As demonstrated by Remus et al. (2013, 2017), this might lead to a slight overestimation of the actual size of the galaxy compared to observations (e.g. in the case of SLACS the effective radius is derived from a deVaucouleur fit to the galaxy brightness distribution), but we ignore this minor effect rather than fit a profile to the projected stellar mass for all simulated galaxies. We assume a constant Chabrier IMF for both the observed and simulated galaxies.

Figure 3.2 shows the mass-size relations for the nine selected EAGLE model variations, overlaid on SLACS. We find that the Reference model (REF) yields somewhat larger effective radii compared to similarly massive SLACS galaxies. On the other hand, the models FBconst, FBσ and FBZ, which were calibrated on the GSMF, all have similar effective radii as SLACS, except for two outliers around the lowest stellar mass end and above the relation that have unusually large effective radii[4]. Due to the relatively low efficiency of stellar feedback in the FBconst, FBσ, FBZ models and the absence of AGN feedback in the NOAGN model, stars tend to form somewhat nearer to the center of the galaxy (see Crain et al. 2015).

[4]We note that each mock lens is shown three times (once for each principle-axis orientation), as discussed earlier, and hence the number of independent outliers is very small.

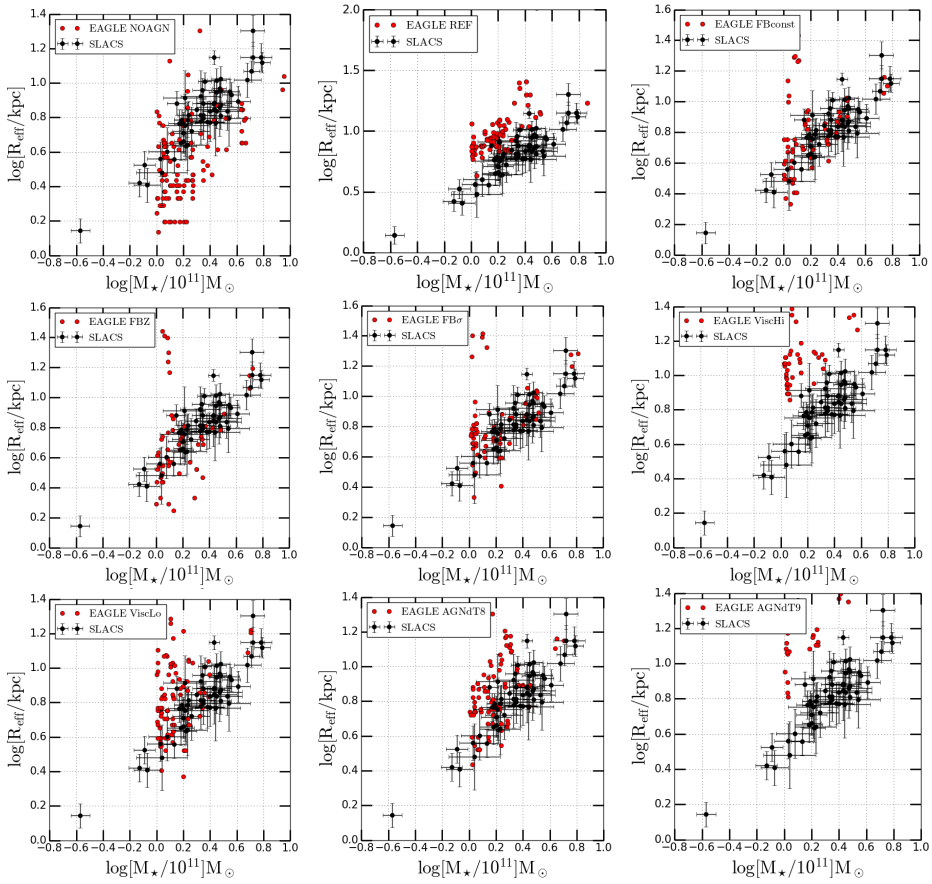

Figure 3.2: The mass-size relation at z_l=0.271 for EAGLE model variations from simulations with a box-size of 50 cMpc, as compared to the mass-size relation of SLACS lens galaxies.

The NOAGN model, on the other hand, leads to much more compact galaxies, with many systems even straddling the resolution limit of the simulations. This trend can be attributed to the nature of the stellar and AGN feedback mechanisms incorporated in those four model variations. The galaxies from the AGN model variations (AGNdT8 and AGNdT9) both have larger effective radii than the NOAGN model. When $\Delta T = 10^8$K about half of the galaxies are more compact in size, in good agreement with SLACS, whereas for $\Delta T = 10^9$K (AGNdT9) hardly any galaxy matches the observations. The higher temperature in the AGNdT9 model leads to more effective AGN feedback keeping gas away from the center and increasing the size of the galaxy. For comparison, the Reference model assumes $\Delta T = 10^{8.5}$K, explaining its halfway position between AGNdT8 and AGNdT9. The viscosity parameter on the other hand affects the amplitude of the baryonic conversion efficiency. A low viscosity (ViscLo), i.e a high viscosity parameter, lowers the baryonic conversion efficiency thereby delaying the onset of AGN feedback and allowing gas to settle closer to the galaxy center before star formation. The ViscLo model has the opposite effect, increasing the size of the galaxy.

Overall, we conclude that simulated galaxies from EAGLE better match the mass-size relation of SLACS lens galaxies when there is moderately low AGN activity or stellar feedback driving the galaxy formation, with only a mild impact from variations in the type of stellar feedback model. This trend is consistent with previous studies (Remus et al. 2017; Figure 1 in Peirani et al. 2018). Changes in the viscosity have strong impact, mostly by indirectly affecting AGN feedback.

3.6.2 The total mass density slope

Keeping the mass-size results discussed in the the previous section in mind, in this section we assess whether the same galaxy-formation models that (visually) reproduce the mass-size relation of SLACS lens galaxies also reproduce their mass density slopes, which is not an observable used in the calibration of the EAGLE simulations. We use the EPL surface mass density profile to model the simulated strong lenses with `LENSED`, closely mimicking real lens observations (see Section 3.4 for details). This allows for a more unbiased and systematic comparison with strong lens observations.

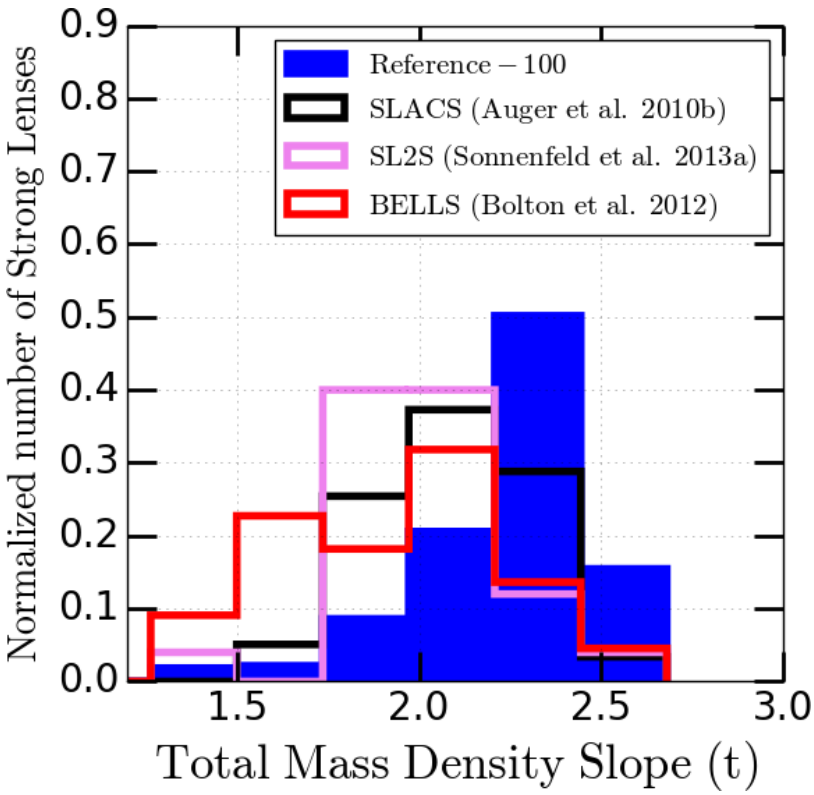

Figure 3.3: Histograms of the total mass density slopes (i.e. $t = 1 - \log(\Sigma)/\log(R)$; $\Sigma(R)$ being the surface mass density of the lens galaxies) of galaxies from the EAGLE model variation Reference-100 cMpc at z_l=0.271 (having $M_\star > 10^{11}\mathrm{M}_\odot$), compared to those from SLACS, BELLS and SL2S. The mean density slope from the simulations is 2.10 and the median value is 2.31. The EAGLE distributions have been obtained from lens modeling with the code `LENSED`, similar in setup to the observations (see text) and have been re-weighted by a proxy of their lens cross-section to correct for the larger lens selection bias. The total mass density slopes of observations are taken from Auger et al. (2010a) for SLACS, Sonnenfeld et al. (2013b) for SL2S and Bolton et al. (2012a) for BELLS. For SLACS and BELLS, the density slopes are derived from a combination of lensing and stellar-kinematic constraints.

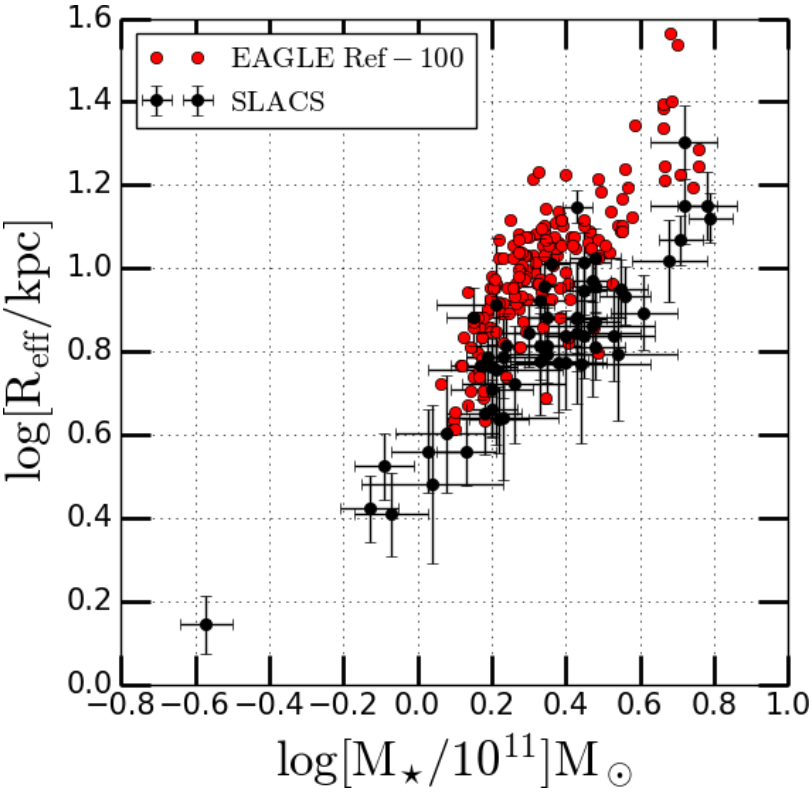

Figure 3.4: The mass-size relation from the same simulation compared with SLACS. A comparative study of all the total mass density slopes (from the 50cMpc boxes) for all other simulations is presented in Figure 3.5.

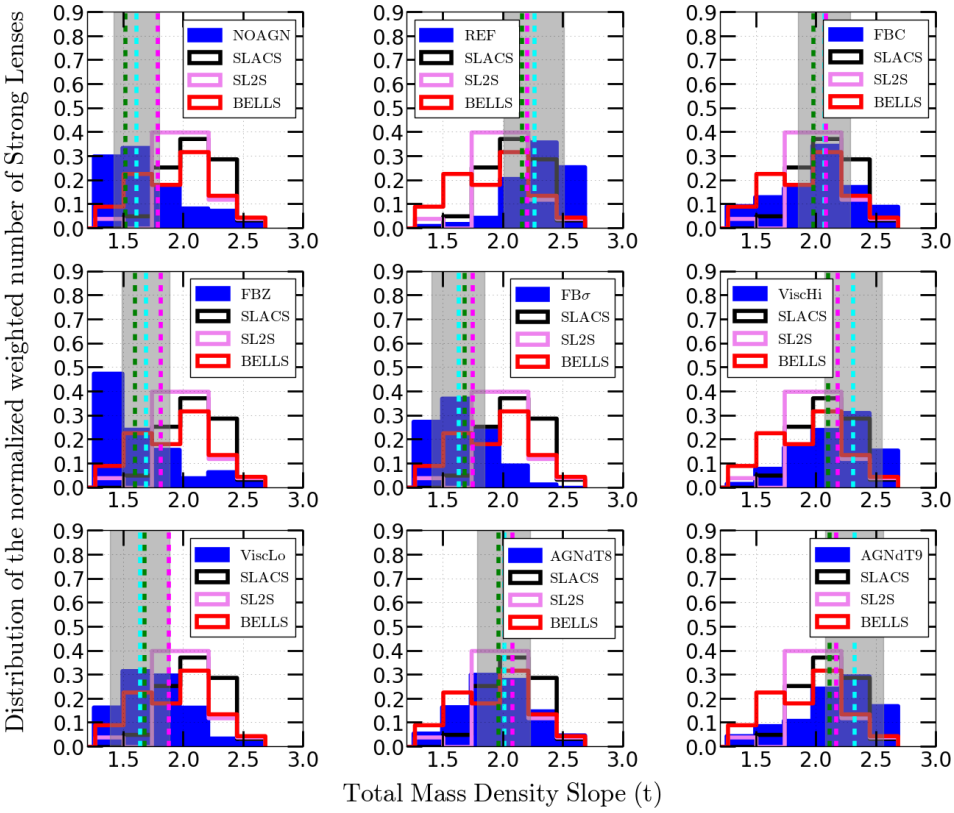

Figure 3.5: Histograms of the total mass density slopes (i.e. $t = 1 - \log(\Sigma)/\log(R)$; $\Sigma(R)$ being the surface mass density of the lens galaxies) of galaxies from EAGLE model variations (having $M_\star > 10^{11}\mathrm{M}_\odot$) compared to those from SLACS, BELLS and SL2S. The EAGLE distributions have been obtained from lens modeling with the code `LENSED`, similar in setup to the observations (see text) and have been re-weighted by a proxy of their lens cross-section to correct for the larger lens selection bias. Also the effect of different values of α, see equation 3.8, are shown in colored vertical dashed lines. α=0.5 (green), α=1.0 (cyan) and α=1.5 (magenta). The shaded region shows the respective $\pm$ rms range centered on median value (for α=1.0) for each scenario. The total mass density slopes of observations are taken from Auger et al. (2010a) for SLACS, Sonnenfeld et al. (2013b) for SL2S and Bolton et al. (2012a) for BELLS. For SLACS and BELLS, the density slopes are derived from a combination of lensing and stellar-kinematic constraints.

Calibrated simulations

As a first check, we confirm that the lens galaxies from the Reference-100 cMpc model show a similar distribution in density slopes as presented in M18 where the smaller 50 cMpc box was used. The latter has a much smaller number of massive galaxies. We confirm that EAGLE galaxies from the Reference model tend to have slightly steeper density slopes than SLACS, BELLS and SL2S (see left panel in Figure 3.4 and also Figure 12 in M18).

In Figure 3.5 the density slopes for all EAGLE model variations are shown for the smaller 50 cMpc boxes. Visually, the FBconst model appears to yield galaxies most similar to SLACS with the total mass density profile being close very to isothermal. This can be attributed to their less efficient stellar feedback, which yields a mass profile more shallow than the Reference model. The FBZ and FBσ models have more dark matter in the center of the galaxy, compared to the FBconst and Reference model, leading to a more shallow total density slope in their central regions. Hence, whereas the FBZ and FBσ models visually reproduce the mass-size relation of SLACS rather well, they fail to reproduce their mass density slopes. We find the rather counterintuitive trend that when feedback efficiency increases from the FBZ, FBσ, FBconst to Reference models, the average total mass density slope steepens as well. We will see that AGN feedback shows the same trend and discuss the cause in the next section.

Reference-model variations

There is a clear dependency of the total mass density slope on AGN feedback. As the stochastic temperature increment in AGN models increases from $\Delta T = 10^8$K (AGNdT8) via $\Delta T = 10^{8.5}$K (Reference) to $\Delta T = 10^9$K (AGNdT9) the total density slope steepens. Generally, we would expect the opposite, since stronger AGN activity (i.e. temperature increments) should move or keep gas particles away from the galaxy center, preventing star formation. As mentioned in Le Brun et al. (2014), more energetic heating events associated with a higher heating temperature, even-though less frequent, are more effective at regulating star formation in massive galaxies. Crain et al. (2015) also pointed out that the peak baryon conversion efficiency decreases with increasing AGN temperature.

The reduced efficiency of AGN feedback thus, counter-intuitively, manifests itself in a steeper total mass density slope. A similar trend is found when the Viscosity parameter is increased, which directly impacts AGN feedback as discussed earlier. This trend is consistent with previous simulation studies (e.g. Remus et al. 2017; Xu et al. 2017). In short, the AGNdT8 model with weaker AGN feedback (compared to the Reference model) produces lensing galaxies that are closer to isothermal and in better agreement with the results from SLACS, BELLS and SL2S lens galaxies. Table 3.3 summarizes the mean, median and standard deviation of the density slopes for all EAGLE model variations used in this work.

Potential systematics

There could be several effects that play a role in the comparison between observations and simulations. We describe three of these below.

Evolution of the density profile: The inclusion of baryons results in differences in the total density profiles that depend on the efficiency of the radiative cooling and feedback. In a previous study using five model variations from OWLS (Schaye et al. 2010) and also DM-only simulations, Duffy et al. (2010) probed the mass density slope at z=2 and compared with SLACS lenses (Figure 3 therein). They found that AGN feedback, or extremely efficient feedback from massive stars, is necessary to match observed stellar-mass fractions in groups and clusters. This contrasts with the results in this work, where we find that weaker feedback leads to better agreement with SLACS, BELLS and SL2S observations. Our analysis is carried out at a redshift of $z = 0.271$, however, closer in redshift to where these lens galaxies are observed and is consistent with the results of several other simulation studies (Xu et al. 2017; Remus et al. 2017). As pointed out in the latter two works, there could be a significant steepening of the total mass density slope in the simulations at higher redshifts which might affect the density-slope analysis. Even though Koopmans et al. (2006) have shown that there is no strong evidence for evolution in the total mass density slope in SLACS with redshift, this only holds for the redshift range of $0.1 \lesssim z \lesssim 0.3$ where the bulk SLACS lenses are found. Evolution might exist as we move to higher redshifts (Bolton et al. 2012a; Sonnenfeld et al. 2013b). Moreover, the galaxies analyzed in Duffy et al. (2010) are less massive than

those used in our analysis, mostly due to the significant difference in the redshifts of both the analysis.

Simulation resolution bias: Duffy et al. (2010) found that resolution of the simulations can strongly affect the region where the mass density slope is measured. Their density slope measurement, however, was typically done around an Einstein radius of $\sim$ 3 kpc, only just above the resolution limit in the highest-resolution OWLS run at $z = 2$. Similarly, Schaller et al. (2015) showed that below a radius of roughly $\sim$ 2-3 kpc, the matter density slopes due to the resolution is increasingly less reliable. This is not directly due to the softening length, but rather due to the radius enclosing a certain number of particles needed for the circular velocity to converge to within $\sim$10% (i.e. the convergence radius) and the enclosed mass to within $\sim$20%. At radii smaller than the convergence radius, the mass profile become increasingly less reliable and typically displays a too shallow density profiles. The impact of baryons, especially a large number of stars dominating the potential in these regions, also becomes more uncertain. In our work, however, we analyze galaxies at much a lower redshift and at a much higher resolution, similar to Xu et al. (2017) and Remus et al. (2017) (i.e. to Illustris and Magneticum, respectively). In these lower-redshift and higher-resolution simulations, massive galaxies have a larger Einstein radius, in the range of 3-10 kpc, well above the resolution limit and also above the convergence radius in the simulations. We therefore think that convergence only plays a minor role in the current EAGLE simulations around the Einstein radius of massive early types galaxies with $M_\star > 10^{11}\,\mathrm{M}_\odot$.

Observational biases: Dobler et al. (2008) found that the most significant instrumental selection effect is the finite size of the spectroscopic fiber which selects against large separation lenses and results in a non-monotonic dependence of the rogue line probability (defined as the probability that a given luminous red galaxy (LGR) has a rogue [O II] line in its spectrum) on velocity dispersion. The situation is further complicated by the effects of atmospheric seeing which can add flux into the fiber from images outside or remove flux from the fiber from images inside. Dobler et al. (2008) also reported that the lensing probability has a fairly weak dependence on the size of the source (see also appendix of M18). Hence, whereas it clear that lens galaxies are mass selected and biased to higher mass galaxies, some of

$\log M_\star/M_\odot = 11.0 - 12.0$											
	Mass density slope (t)			Mass density slope KS test						Mass-size KS test	
Simulation	Mean	RMS	Median	SLACS		SL2S		BELLS		SLACS	
				D-value	p-value	D-value	p-value	D-value	p-value	D-value	p-value
Ref-100	2.10	0.26	2.31	0.26	0.53e-2	0.43	0.46e-3	0.42	0.17e-2	0.44	0.57e-2
Ref-50	2.26	0.25	2.26	0.35	0.15e-5	0.51	0.27e-5	0.48	0.59e-5	0.41	**0.29**
FBconst	2.00	0.22	2.07	0.15	**0.39**	0.36	0.005	0.17	**0.63**	0.47	**0.15**
FBσ	1.64	0.22	1.63	0.76	1.25e-26	0.77	4.44e-13	0.99	2.52e-19	0.48	**0.11**
FBZ	1.62	0.20	1.69	0.82	5.08e-27	0.84	2.23e-14	0.63	1.24e-7	0.53	0.02
ViscLo	1.67	0.25	1.64	0.68	1.2e-22	0.65	0.9e-10	0.46	0.001	0.52	0.002
ViscHi	2.10	0.24	2.31	0.17	**0.09**	0.22	**0.15**	0.21	**0.26**	0.77	1.95e-7
AGNdT8	1.96	0.22	2.01	0.38	**0.12**	0.36	0.003	0.21	**0.26**	0.44	**0.24**
AGNdT9	2.21	0.24	2.32	0.23	0.01	0.24	0.10	0.22	**0.23**	0.82	1.17e-5
NOAGN	1.70	0.19	1.52	0.78	5.06e-20	0.78	1.38e-11	0.51	0.11e-3	0.58	5.12e-6

Table 3.3: The mean, standard deviation and median values of mass density slopes, t, of the simulated lenses in different galaxy formation models. The K-S results for the mass density slopes (1D) and mass-size relation (2D) are also listed when compared to SLACS, SL2S and BELLS. P-values exceeding 0.05 are shown in bold.

the most massive lenses might not have been found in SLACS due to the above-mentioned effects. These massive systems, to begin with, are already rare and their absence would not bias the bulk of the lens population which peaks around $M_\star = 10^{11.35} M_\odot$ (Auger et al. 2010a). As was shown by (Bolton et al. 2008b), SLACS lens galaxies also appear in all observational aspects similar to their LRG parent population, suggesting that they are not a biased LRG sub-sample.

3.6.3 Kolmogorov-Smirnov Statistics

Even though we find qualitatively and visually quite similar distributions between some of the model variations (i.e., FBC, AGNdT8) and observations, we have not quantified this (dis)agreement. The Kolmogorov–Smirnov (KS) test (Kolmogorov 1933) is a nonparametric test of the equality of continuous, one-dimensional probability distributions that can be used to compare a sample with a reference probability distribution, or be used to compare two samples. KS tests have been extensively used in astronomy (Peacock 1983; Fasano & Franceschini 1987; Press et al. 2007). The KS statistics (D-value) quantifies the maximum probability difference between the cumulative probability distribution functions of two samples. A KS test also yields a p-value, being the probability that two distributions are in fact drawn from the same underlying distribution and are dissimilar

at the current level (D) or larger, by pure random chance. Hence smaller p-values imply a larger dissimilarity and a smaller probability this is purely by coincidence. In this work, we use the standard 1D KS test to compare the mass density slopes and wee use the 2D KS test of Peacock (1983) to compare the mass-size relations. Table 3.3 summarizes the KS D- and p-values by comparing the results from the EAGLE model variations with those of SLACS, BELLS and SL2S, respectively.

We indeed find that the FBconst, AGNdT8 and ViscHi models which visually also appeared most consistent with the observations, also have consistently high p-values (we assume a lower limit of acceptance of $p > 0.05$). When we combine our analysis with the p-values from 2D KS test for mass-size relation, we find that only the FBconst and AGndT8 model variations remain viable. The Reference model, even though displaying similarity to observations from SLACS in its mass-size relation, performs poorly in the mass density slope KS test. In addition, we can clearly rule out the NOAGN, ViscLo, FBZ and FBσ model variations in producing the observed strong lenses distributions in slope, mass and size. This confirms our earlier visual inspection.

3.7 Summary and Conclusions

In this paper we have systematically explored the impact of different galaxy formation processes used in the EAGLE hydrodynamical simulations – in particular stellar and AGN feedback – on strong lens observables in massive early-type galaxies with $M_\star > 10^{11} M_\odot$. Simulations of various mock-lens ensembles with the `SEAGLE` pipeline (M18) allow us to quantify in particular the (dis)agreement between the total mass density slopes around Einstein radius and the stellar mass-size relation between these mock lens ensembles and observations from the SLACS, BELLS and SL2S lens surveys. We compared these observables with the outcome of a range of EAGLE model variations, varying stellar & AGN feedback and viscosity parameters (Schaye et al. 2015; Crain et al. 2015).

Here we briefly summarize our methodology once again. We select potential strong lenses based on cataloged stellar mass and created projected mass maps at three different orientations. We create mock lenses by ray tracing

through the mass maps, placing an analytic Sersic (1968) source, at a higher redshift, having observationally motivated parameters. We add realistic HST noise and PSF to mimic strong lenses found in observations. We calculate the projected half-mass radius for each individual mass maps. We also model these lenses with elliptic power-law model (EPL) and obtain their mass density slopes around their respective Einstein radius. Their strikingly similar visual appearance (see Figure 3.1) and similar stellar mass function to SLACS, SL2S and BELLS, motivates us to compare these observed lens samples to the simulated lens systems. This allows us to compare our findings with observations. We also make sure that our findings are not biased from any systematics or resolution effects.

We draw the following main conclusions:

(1) The stellar mass-size relations and total mass density slopes of strong lensing galaxies from SLACS, BELLS and SL2S agree best with EAGLE galaxy formation models that have weak or mild AGN activity or constant stellar feedback. In particular, the AGN model with a moderate temperate increments during active periods, $\Delta T = 10^8$K (AGNdT8), shows excellent agreement with the observations. Models with no or high-temperature increments agree considerably less well in statistical KS tests. Similarly, the stellar-feedback model with a constant super-nova energy injection per unit stellar mass in to the surrounding medium (i.e. FBC) also shows excellent agreement with the observations.

(2) Models where the energy injection per unit stellar mass formed depends either on metalicity or local environment perform less well. Models with a high viscosity also do well to reproduce the total mass density slopes of observed lens galaxies, but perform poorly in reproducing the mass-size relation. The EAGLE Reference model (the benchmark model) also does not perform well, most likely due to a too efficient AGN feedback model.

(3) Quantitatively, we find that if the simulated lensed images are modeled using an elliptical power law (EPL) profile plus external shear that the median total mass density slope of galaxies from the AGNdT8 and FBC models, that have the highest p-values in the KS tests, are t=2.01 and t=2.07, respectively, in good agreement with the observations. Galaxies in

the EAGLE Reference model, however, tend to have a steeper median total mass density slope (t=2.31) than observed lens galaxies (i.e. t =2.08 for SLACS, t=2.11 for BELLS and t=2.18 for SL2S), although it agrees with the results from other analyses (e.g. Remus et al. 2017; Xu et al. 2017).

Overall we conclude that more efficient feedback in galaxy formation models yields steeper total mass density slopes at radius of 3-10 kpc and that strong lens galaxies appear most consistent with galaxy formation models with some what more limited feedback. Our findings are consistent with the work by Remus et al. (2017) and Peirani et al. (2018) using different simulations

However, they seemingly contradict Duffy et al. (2010) that looked at inner density slopes in the OWLS models. We believe these differences are due to the fact that their mass density slope was obtained at a higher redshift (z=2) and for lower mass galaxies. Also, they did not create simulated lenses and model them with an EPL model, as in this work, which might lead to some additional biases. Also, our results prefer galaxy-formation models that seem to have been ruled out in Crain et al. (2015) after comparison with non-lensing observations, and Furlong et al. (2015a) found that the Reference model agrees well in the mass-size relation when compared to non-lensing galaxies. These seemingly opposing conclusions could be due to either differences in the precise methodologies adopted in our strong-lensing and their non-lensing studies, or additional observational selection biases in the galaxy samples. We stress again that SLACS lens galaxies are not different than the parent population of non-lens galaxies from which they were drawn (Treu et al. 2006; Bolton et al. 2008b).

Overall, we have demonstrated that observables of strong lens galaxies, in particular their total mass density profiles in the inner 3-10 kpc radial range, are very sensitive to galaxy-formation feedback models. Whereas in this paper we have concentrated on the mass-size and mass density slopes, in several forthcoming papers, we will investigate the inner mass regions in more detail in particular focusing on the effects of the dark matter distribution and the stellar IMF, and their degeneracies with the stellar mass distribution.

Acknowledgements

We thank the anonymous referee for her/his insightful comments and constructive suggestions which improved this work to its present form. SM, LVEK, CT and GV are supported through an NWO-VICI grant (project number 639.043.308). SM thanks SURFSARA network in Amsterdam. MS is supported by VENI grant 639.041.749. JS is supported by VICI grant 639.043.409. FB thanks the support from the grants ASI n.I/023/12/0 "Attività relative alla fase B2/C per la missione Euclid" and PRIN MIUR 2015 "Cosmology and Fundamental Physics: Illuminating the Dark Universe with Euclid". This work used the DiRAC Data Centric system at Durham University, operated by the Institute for Computational Cosmology on behalf of the STFC DiRAC HPC Facility (www.dirac.ac.uk). This equipment was funded by BIS National E-infrastructure capital grant ST/K00042X/1, STFC capital grant ST/H008519/1, and STFC DiRAC Operations grant ST/K003267/1 and Durham University. DiRAC is part of the National E-Infrastructure. This work was supported by the Netherlands Organisation for Scientific Research (NWO), through VICI grant 639.043.409.

References

Auger, M. W., Treu, T., Bolton, A. S., et al. 2010a, ApJ, 724, 511
Auger, M. W., Treu, T., Gavazzi, R., et al. 2010b, ApJL, 721, L163
Baldry, I. K., Driver, S. P., Loveday, J., et al. 2012, MNRAS, 421, 621
Bandara, K., Crampton, D., Peng, C., & Simard, L. 2013, ApJ, 777, 1
Barnabè, M., Czoske, O., Koopmans, L. V. E., Treu, T., & Bolton, A. S. 2011, MNRAS, 415, 2215
Barnabè, M., Czoske, O., Koopmans, L. V. E., et al. 2009, MNRAS, 399, 21
Bellagamba, F., Tessore, N., & Metcalf, R. B. 2017, MNRAS, 464, 4823
Bolton, A. S., Brownstein, J. R., Kochanek, C. S., et al. 2012a, ApJ, 757, 82
Bolton, A. S., Brownstein, J. R., Kochanek, C. S., et al. 2012b, ApJ, 757, 82
Bolton, A. S., Burles, S., Koopmans, L. V. E., et al. 2008a, ApJ, 682, 964
Bolton, A. S., Burles, S., Koopmans, L. V. E., et al. 2008b, ApJ, 682, 964
Bolton, A. S., Burles, S., Koopmans, L. V. E., Treu, T., & Moustakas, L. A. 2006, ApJ, 638, 703
Bolton, A. S., Treu, T., Koopmans, L. V. E., et al. 2008c, ApJ, 684, 248
Bower, R. G., Schaye, J., Frenk, C. S., et al. 2017, MNRAS, 465, 32
Brownstein, J. R., Bolton, A. S., Schlegel, D. J., et al. 2012, ApJ, 744, 41
Cabanac, R. A., Alard, C., Dantel-Fort, M., et al. 2007, A&A, 461, 813
Cappellari, M., Scott, N., Alatalo, K., et al. 2013, MNRAS, 432, 1709
Chabrier, G. 2003, PASP, 115, 763
Crain, R. A., Schaye, J., Bower, R. G., et al. 2015, MNRAS, 450, 1937
Crain, R. A., Theuns, T., Dalla Vecchia, C., et al. 2009, MNRAS, 399, 1773
Dalla Vecchia, C. & Schaye, J. 2012, MNRAS, 426, 140
Davis, M., Efstathiou, G., Frenk, C. S., & White, S. D. M. 1985, ApJ, 292, 371
de Jong, J. T. A., Verdoes Kleijn, G. A., Boxhoorn, D. R., et al. 2015, A&A, 582, A62
Dobler, G., Keeton, C. R., Bolton, A. S., & Burles, S. 2008, ApJ, 685, 57
Dubois, Y., Peirani, S., Pichon, C., et al. 2016, MNRAS, 463, 3948
Duffy, A. R., Schaye, J., Kay, S. T., et al. 2010, MNRAS, 405, 2161
Dutton, A. A. & Treu, T. 2014, MNRAS, 438, 3594
Eisenstein, D. J., Weinberg, D. H., Agol, E., et al. 2011, AJ, 142, 72
Faber, S. M. & Jackson, R. E. 1976, ApJ, 204, 668

Fasano, G. & Franceschini, A. 1987, Monthly Notices of the Royal Astronomical Society, 225, 155
Ferland, G. J., Korista, K. T., Verner, D. A., et al. 1998, PASP, 110, 761
Frenk, C. S., White, S. D. M., Davis, M., & Efstathiou, G. 1988, ApJ, 327, 507
Furlong, M., Bower, R. G., Crain, R. A., et al. 2015a, ArXiv e-prints
Furlong, M., Bower, R. G., Theuns, T., et al. 2015b, MNRAS, 450, 4486
Gao, L., White, S. D. M., Jenkins, A., Stoehr, F., & Springel, V. 2004, MNRAS, 355, 819
Gavazzi, R., Marshall, P. J., Treu, T., & Sonnenfeld, A. 2014, ApJ, 785, 144
Gavazzi, R., Treu, T., Marshall, P. J., Brault, F., & Ruff, A. 2012, ApJ, 761, 170
Grillo, C. 2012, ApJL, 747, L15
Haardt, F. & Madau, P. 2001, in Clusters of Galaxies and the High Redshift Universe Observed in X-rays, ed. D. M. Neumann & J. T. V. Tran
Haas, M. R., Schaye, J., Booth, C. M., et al. 2013a, MNRAS, 435, 2931
Haas, M. R., Schaye, J., Booth, C. M., et al. 2013b, MNRAS, 435, 2955
Hopkins, P. F., Torrey, P., Faucher-Giguère, C.-A., Quataert, E., & Murray, N. 2016, MNRAS, 458, 816
Ivezić, Ž., Kahn, S. M., Tyson, J. A., et al. 2008, ArXiv e-prints
Kochanek, C. S. 1991, ApJ, 382, 58
Kolmogorov, A. N. 1933, Giornale dell'Istituto Italiano degli Attuari, 4, 83
Koopmans, L. V. E., Bolton, A., Treu, T., et al. 2009, ApJL, 703, L51
Koopmans, L. V. E., Treu, T., Bolton, A. S., Burles, S., & Moustakas, L. A. 2006, ApJ, 649, 599
Kormann, R., Schneider, P., & Bartelmann, M. 1994, A&A, 284, 285
Laureijs, R., Amiaux, J., Arduini, S., et al. 2011, ArXiv e-prints
Le Brun, A. M. C., McCarthy, I. G., Schaye, J., & Ponman, T. J. 2014, Monthly Notices of the Royal Astronomical Society, 441, 1270
Loeb, A. & Peebles, P. J. E. 2003, ApJ, 589, 29
McAlpine, S., Helly, J. C., Schaller, M., et al. 2016, Astronomy and Computing, 15, 72
McCarthy, I. G., Schaye, J., Bird, S., & Le Brun, A. M. C. 2017, MNRAS, 465, 2936
Metcalf, R. B., Meneghetti, M., Avestruz, C., et al. 2018, ArXiv e-prints
Metcalf, R. B. & Petkova, M. 2014, MNRAS, 445, 1942

Meylan, G., Jetzer, P., North, P., et al., eds. 2006, Gravitational Lensing: Strong, Weak and Micro
Mukherjee, S., Koopmans, L. V. E., Metcalf, R. B., et al. 2018a, ArXiv e-prints
Mukherjee, S., Koopmans, L. V. E., Metcalf, R. B., et al. 2018b, ArXiv e-prints
Mukherjee, S., Koopmans, L. V. E., Metcalf, R. B., et al. 2018c, ArXiv e-prints
Navarro, J. F., Frenk, C. S., & White, S. D. M. 1996, ApJ, 462, 563
Navarro, J. F., Frenk, C. S., & White, S. D. M. 1997, ApJ, 490, 493
Newton, E. R., Marshall, P. J., Treu, T., et al. 2011, ApJ, 734, 104
Oppenheimer, B. D., Davé, R., Kereš, D., et al. 2010, MNRAS, 406, 2325
Peacock, J. A. 1983, Monthly Notices of the Royal Astronomical Society, 202, 615
Pearce, F. R., Jenkins, A., Frenk, C. S., et al. 2001, MNRAS, 326, 649
Peebles, P. J. E. 1974, ApJL, 189, L51
Peebles, P. J. E. & Yu, J. T. 1970, ApJ, 162, 815
Peirani, S., Dubois, Y., Volonteri, M., et al. 2017, MNRAS, 472, 2153
Peirani, S., Sonnenfeld, A., Gavazzi, R., et al. 2018, ArXiv e-prints
Petkova, M., Metcalf, R. B., & Giocoli, C. 2014, MNRAS, 445, 1954
Petrillo, C. E., Tortora, C., Chatterjee, S., et al. 2017, MNRAS, 472, 1129
Planck Collaboration, Ade, P. A. R., Aghanim, N., et al. 2014, A&A, 571, A16
Pontzen, A. & Governato, F. 2014, Nature, 506, 171
Press, W. H., Teukolsky, S. A., Vetterling, W. T., & Flannery, B. P. 2007, Numerical Recipes 3rd Edition: The Art of Scientific Computing, 3rd edn. (New York, NY, USA: Cambridge University Press)
Puchwein, E. & Springel, V. 2013, MNRAS, 428, 2966
Remus, R.-S., Burkert, A., Dolag, K., et al. 2013, ApJ, 766, 71
Remus, R.-S., Dolag, K., Naab, T., et al. 2017, MNRAS, 464, 3742
Ruff, A. J., Gavazzi, R., Marshall, P. J., et al. 2011, ApJ, 727, 96
Sales, L. V., Navarro, J. F., Schaye, J., et al. 2010, MNRAS, 409, 1541
Scannapieco, C., Wadepuhl, M., Parry, O. H., et al. 2012, MNRAS, 423, 1726
Schaller, M., Frenk, C. S., Bower, R. G., et al. 2015, MNRAS, 452, 343
Schaye, J. 2004, ApJ, 609, 667
Schaye, J., Crain, R. A., Bower, R. G., et al. 2015, MNRAS, 446, 521
Schaye, J. & Dalla Vecchia, C. 2008, MNRAS, 383, 1210

Schaye, J., Dalla Vecchia, C., Booth, C. M., et al. 2010, MNRAS, 402, 1536
Sersic, J. L. 1968, Atlas de galaxias australes
Shen, S., Mo, H. J., White, S. D. M., et al. 2003, MNRAS, 343, 978
Shu, Y., Bolton, A. S., Brownstein, J. R., et al. 2015, ApJ, 803, 71
Shu, Y., Brownstein, J. R., Bolton, A. S., et al. 2017, ArXiv e-prints
Sonnenfeld, A., Gavazzi, R., Suyu, S. H., Treu, T., & Marshall, P. J. 2013a, ApJ, 777, 97
Sonnenfeld, A., Treu, T., Gavazzi, R., et al. 2012, ApJ, 752, 163
Sonnenfeld, A., Treu, T., Gavazzi, R., et al. 2013b, ApJ, 777, 98
Sonnenfeld, A., Treu, T., Marshall, P. J., et al. 2015, ApJ, 800, 94
Springel, V. 2010, MNRAS, 401, 791
Springel, V. & Hernquist, L. 2003, MNRAS, 339, 289
Tagore, A. S., Barnes, D. J., Jackson, N., et al. 2018, MNRAS, 474, 3403
Tessore, N., Bellagamba, F., & Metcalf, R. B. 2016, MNRAS, 463, 3115
Tessore, N. & Metcalf, R. B. 2015, A&A, 580, A79
The Dark Energy Survey Collaboration. 2005, ArXiv Astrophysics e-prints
Tortora, C., La Barbera, F., Napolitano, N. R., et al. 2014, MNRAS, 445, 115
Trayford, J. W., Camps, P., Theuns, T., et al. 2017, MNRAS, 470, 771
Treu, T., Gavazzi, R., Gorecki, A., et al. 2009, ApJ, 690, 670
Treu, T., Koopmans, L. V., Bolton, A. S., Burles, S., & Moustakas, L. A. 2006, ApJ, 640, 662
Treu, T. & Koopmans, L. V. E. 2004, ApJ, 611, 739
Vogelsberger, M., Genel, S., Sijacki, D., et al. 2013, MNRAS, 436, 3031
Vogelsberger, M., Genel, S., Springel, V., et al. 2014, MNRAS, 444, 1518
White, S. D. M. & Rees, M. J. 1978, MNRAS, 183, 341
Wiersma, R. P. C., Schaye, J., & Smith, B. D. 2009a, MNRAS, 393, 99
Wiersma, R. P. C., Schaye, J., Theuns, T., Dalla Vecchia, C., & Tornatore, L. 2009b, MNRAS, 399, 574
Xu, D., Springel, V., Sluse, D., et al. 2017, MNRAS, 469, 1824

Chapter 4

Inner dark matter fractions of early type galaxies in EAGLE model variations

——— **Based on**
SEAGLE–III: The observed and simulated dark matter fractions in the central regions of early-type lens galaxies,

Sampath Mukherjee, Léon V. E. Koopmans, Crescenzo Tortora, R. Benton Metcalf, Joop Schaye, Matthieu Schaller, Giorgos Vernardos, Fabio Bellagamba, ———

To be submitted in MNRAS

Abstract

The central dark matter fraction of galaxies is a strong function of feedback during galaxy formation. In this chapter, we analyze the central dark matter fraction of early-type galaxies (ETG) in hydrodynamical simulations from EAGLE in comparison with strong lens galaxies from SLACS, as well as galaxies from the SPIDER survey. Although we find overall good agreement between the dark matter fractions inside one effective radius from simulated and observed galaxies, we see a large discrepancy between observations and simulations inside half of an effective radius, with considerably higher inferred dark matter fractions (by factors 2–3) in strong lens galaxies. Whereas stronger feedback in the simulations increases both the effective radius and the dark-matter fraction for a given stellar mass of the galaxy, it increases the disagreement with SLACS lens galaxies. A slightly better agreement between the dark matter fractions within one effective radius and mass-size relation with non-lensing ETGs with SPIDER galaxies shows that some systematical differences are still present in strong lensing and non-lensing observations. Although finite resolution in the simulations and aperture effects in the simulations and observations might account for some of this discrepancy with strong lensing observations, it could also indicate a yet unaccounted for dependency of the properties of ETGs on stellar and AGN feedback and the assumed stellar initial mass function (IMF), or that the dark matter profiles inside $R_{\rm eff}$ are different between simulated and observed massive galaxies.

4.1 Introduction

The study of massive early-type galaxies (ETGs) has been a significant topic of interest in galaxy evolution and cosmology studies. They are believed to be the end product of hierarchal galaxy merging (Toomre & Toomre 1972; White & Frenk 1991; Cole et al. 2000). They are metal-rich, gas-poor and star formation happens in their early formation phase (Thomas et al. 2005; Fontanot et al. 2009). Many essential but open problems remain in the study of massive galaxy evolution, e.g., quantifying the role of mergers in their evolution (van Dokkum et al. 1999; Khochfar & Burkert 2003) and the mechanism responsible for their size-evolution (Daddi et al. 2005; Zirm et al. 2007). The lack of precise mass measurements, limited by uncertainties in the stellar initial mass function (IMF) (Conroy et al. 2009), the deficit of easily interpretable dynamical tracers and the effect of orbital-anisotropy degeneracies on dynamical modelling methods (Cappellari et al. 2006) are some of the reasons for the enduring lack of a full understanding of their internal dark-matter and baryonic mass structure and evolution with cosmic time.

Despite the limitations of various estimators, various authors (e.g. Cappellari et al. 2006; Tortora et al. 2009, 2010) have examined the inner structure of ETGs. The estimations of luminous and dark-matter distributions have proved to be very important to address still-open questions in galaxy formation and evolution (Napolitano et al. 2010; Tortora et al. 2012; Lovell et al. 2018; Tortora et al. 2018). For example, the tilt in the fundamental plane is now thought to be due to an increasing central dark matter fraction as a function of the total stellar mass of the galaxy (e.g. Auger et al. 2010a; Napolitano et al. 2010). These studies, however, still assume a constant stellar Initial Mass Function (IMF) or stellar mass-to-light (M/L) ratio, which itself is under heavy debate (e.g. Conroy 2013)

Strong gravitational lensing provides robust measurements of the total mass within the Einstein radius of strong lens galaxies (Treu & Koopmans 2004; Treu et al. 2006; Koopmans et al. 2006, 2009) and of their dark and luminous matter content. Observational surveys, such as the Lenses Structure and Dynamics Survey (LSD; Treu & Koopmans 2004), the Sloan Lens ACS Survey (SLACS; Bolton et al. 2006; Koopmans et al. 2006; Bolton et al. 2008a,b; Koopmans et al. 2009; Auger et al. 2010b,a; Shu et al. 2015, 2017), the Strong Lensing Legacy Survey (SL2S; Cabanac et al. 2007; Ruff et al.

2011; Gavazzi et al. 2012; Sonnenfeld et al. 2013a,b, 2015) and the BOSS Emission-Line Lens Survey (BELLS; Brownstein et al. 2012), have provided direct and precise measurements of the total mass distributions within the interior of the lens ETGS, including the luminous and dark components. Moreover, when combined with stellar dynamics, strong lensing can break degeneracies such as the mass-anisotropy, bulge-halo and IMF-Dark-Matter degeneracy which are otherwise hard to disentangle (Koopmans & Treu 2003; Koopmans et al. 2009; Auger et al. 2010a; Tortora et al. 2010; Barnabè et al. 2011; Spiniello et al. 2014).

Besides these observational constraints, numerical galaxy-formation simulations have become important to constrain the process of baryonic evolution in galaxies (e.g. Duffy et al. 2010; Sales et al. 2010; Pontzen & Governato 2014; Schaller et al. 2015a,b; Remus et al. 2017; Xu et al. 2017; Peirani et al. 2017, 2018) and to guide and interpret trends seen in the observations. To properly compare numerical simulations with observations of strong lens galaxies, we recently started a systematic comparison between relatively well-selected lens-galaxy samples and state-of-the-art galaxy-formation simulations (Mukherjee et al. 2018a).

In this chapter, we extend that pilot study of the single 'Reference' galaxy-formation model in EAGLE, to the study of nine galaxy-formation scenarios selected from a wider suite of EAGLE simulations (Schaye et al. 2015; Crain et al. 2015). We complement the work of Mukherjee et al. (2018b) by performing a more detailed comparison between their central dark-matter fractions, inferred at two different radii (one and one-half effective radius) from simulations and observations. The principal goals of this study are to illustrate the similarities between numerical simulations and strong-lensing and non-lensing observations, as well as some significant discrepancies that remain unexplained. Besides strong lens observations, we also compare the simulations to optical and near-infrared (NIR) observations of ETGs from the Spheroid's Panchromatic Investigation in Different Environmental Regimes survey (SPIDER; La Barbera et al. 2010b,a,c; Tortora et al. 2012) in order to assess potential systematics between galaxy samples that have been selected in two distinct ways (e.g., lens galaxies are large mass-selected).

The chapter is structured as follows: in Section 4.2 we summarize the EAGLE galaxy formation simulations and the relevant codes that we

use in our analyses. Section 4.3 describes the methodology used to calculate $f_{\rm DM}$. In Section 4.4 we discuss the dark-matter fractions obtained from simulations and compare them with SLACS and SPIDER galaxies and also with other simulations (i.e., Illustris and IllustrisTNG). The implications of our results on galaxy formation are discussed and summarized in Section 4.5. Throughout the chapter we use EAGLE simulations that assume a Chabrier (2003) stellar IMF. The values of the cosmological parameters are $\Omega_\Lambda = 0.693$, $\Omega_{\rm b} = 0.0482519$, $\Omega_{\rm m} = 0.307$, $h = H_0/(100\ {\rm km\ s^{-1}\ Mpc^{-1}}) = 0.6777$ and $\sigma_8 = 0.8288$. These are taken from the Planck satellite data release (Planck Collaboration et al. 2014), in accordance with the EAGLE simulations.

4.2 EAGLE Simulations

Evolution and Assembly of GaLaxies and their Environment (EAGLE)[1] is a suite of hydrodynamical simulations of the formation of galaxies and other astronomical systems in a ΛCDM universe (Schaye et al. 2015; Crain et al. 2015; McAlpine et al. 2016). The EAGLE suite of simulations use a modified SPH (Smoothed Particle Hydrodynamics) version of `GADGET 3` (Springel 2005). The gravitational softening length of these particles is 2.66 comoving kpc (ckpc), limited to a maximum physical scale of 0.7 proper kpc (pkpc). The initial particle masses for baryons and dark matter are $m_{\rm b} = 1.8 \times 10^6\ {\rm M_\odot}$ and $m_{\rm dm} = 9.7 \times 10^6\ {\rm M_\odot}$, respectively (for details see Table 1 in Schaye et al. 2015; Mukherjee et al. 2018a). The resulting galaxies are overall in broad agreement with observed properties such as the star formation rate, passive fraction, Tully-Fischer relation, total stellar luminosity of galaxy cluster and colors (Schaye et al. 2015; Trayford et al. 2015), the evolution of the galaxy stellar mass function and sizes (Furlong et al. 2015, 2017), rotation curves (Schaller et al. 2015a) and the α-enhancement of ETGs (Segers et al. 2016). The sub-grid physics of EAGLE simulations include radiative cooling (Wiersma et al. 2009a), star formation (Schaye & Dalla Vecchia 2008), stellar mass loss (Wiersma et al. 2009b), energy feedback from star formation (Dalla Vecchia & Schaye 2012), black hole accretion (Rosas-Guevara et al. 2015) and AGN feedback (Schaye et al. 2015). Crain et al. (2015) presented 13 cosmological simulations that

[1] `http://icc.dur.ac.uk/Eagle/`

explore the parameter space of EAGLE by using different values for the parameters of various sub-grid models.

In this analyses, we have chosen to use the 100 and 50 cMpc Reference simulations and eight other model variations, namely FBconst, FBZ, FBσ, ViscLo, ViscHi, AGNdT8, AGNdT9 and NOAGN, each having only a 50 cMpc simulation box [Tag L050N0752] (see Table 4.1 and Mukherjee et al. 2018b). These selected simulations includes both calibrated and reference model variations (see Crain et al. 2015). We chose overall eight out of 13 model variations because the remaining EAGLE simulation model variations have a too-small box size (25 cMpc) with very few massive ETGs. An identical set of initial conditions subjected to different physical models ensures that we have similar samples of galaxies when comparing results between different model variations (Crain et al. 2015; Mukherjee et al. 2018b). For reference, we briefly describe the details of the model variations:

Table 4.1: Main subgrid parameters of the EAGLE simulations used in this work. Columns are: the comoving side length of the volume (L) and the particle number per species (i.e. gas, DM) per dimension (N), the power-law slope of the polytropic equation of state ($\gamma_{\rm eos}$), the scaling variable of the efficiency of star formation feedback ($f_{\rm th}$), the asymptotic maximum and minimum values of $f_{\rm th}$, the Ref model's density term denominator ($n_{\rm H,0}$) and exponent ($n_{\rm n}$) from equation 5 in Mukherjee et al. (2018b), the subgrid accretion disc viscosity parameter ($C_{\rm visc}$) from equation 7 in Crain et al. (2015), and the temperature increment of stochastic AGN heating ($\Delta T_{\rm AGN}$). The star formation density threshold ($n_{\rm H}^{\star}$) is implemented by equation 1 in Mukherjee et al. (2018b). The upper section comprises the four calibrated model to reproduce the $z = 0.1$ GSMF, and the lower section comprises Reference variations simulation (varied parameter highlighted in bold). All models also adopt $n_{\rm Z} = 2/\ln 10$ with the exceptions of FBσ, for which the parameter $n_{\rm Z}$ is replaced by $n_{\rm T}$ with the same numerical value (see equation 3 in Mukherjee et al. 2018b), and FBconst, for which the parameter is inapplicable. Partially reproduced from Crain et al. (2015).

Identifier	Side length [cMpc]	N	$\gamma_{\rm eos}$	$f_{\rm th}$-scaling	$f_{\rm th,max}$	$f_{\rm th,min}$	$n_{\rm H,0}$ [cm^{-3}]	$n_{\rm n}$	$C_{\rm visc}/2\pi$	$\Delta T_{\rm AGN}$ $\log_{10}$ [K]
Calibrated models										
FBconst	50	752	4/3	–	1.0	1.0	–	–	10^3	8.5
FBσ	50	752	4/3	$\sigma^2_{\rm DM}$	3.0	0.3	–	–	10^2	8.5
FBZ	50	752	4/3	Z	3.0	0.3	–	–	10^2	8.5
Ref (FBZρ)	50	752	4/3	Z, ρ	3.0	0.3	0.67	$2/\ln 10$	10^0	8.5
Ref-100 (FBZρ)	100	1504	4/3	Z, ρ	3.0	0.3	0.67	$2/\ln 10$	10^0	8.5
Reference-variations										
ViscLo	50	752	4/3	Z, ρ	3.0	0.3	0.67	$2/\ln 10$	$\mathbf{10^2}$	8.5
ViscHi	50	752	4/3	Z, ρ	3.0	0.3	0.67	$2/\ln 10$	$\mathbf{10^{-2}}$	8.5
AGNdT8	50	752	4/3	Z, ρ	3.0	0.3	0.67	$2/\ln 10$	10^0	**8.0**
AGNdT9	50	752	4/3	Z, ρ	3.0	0.3	0.67	$2/\ln 10$	10^0	**9.0**
NOAGN	50	752	4/3	Z, ρ	3.0	0.3	0.67	$2/\ln 10$	10^0	**–**

FBConst: In this model, a fixed amount of energy per unit stellar mass is injected into the interstellar medium (ISM), during star formation, independently of the local conditions. The FBConst model represents the simplest model and provides the maximum level of energy that can be injected into the ISM.

FBσ: In this model, energy injection by stellar feedback is prescribed according to local conditions, inferred from the neighboring dark-matter particles. The feedback efficiency, $f_{\rm th}$, is a function of the local dark-matter velocity dispersion, $\sigma^2_{\rm DM}$, inferred from local dark-matter particles.

FBZ: In this model, the radiative losses are modeled as a function of the metallicity of the ISM. When the metallicity is sufficient for efficient line cooling, energy losses associated with star-formation feedback are significantly larger. The transition in characteristics of outflowing gas at temperatures $10^5{\rm K} < {\rm T} < 10^7{\rm K}$, in the simulations, is expected to occur at $Z \sim 0.1 Z_{\odot}$ (Wiersma et al. 2009a).

Reference (FB$Z\rho$): The two previous feedback models (FBσ and FBZ) are numerically inefficient. In these models, a significant fraction of the star particles forms at densities exceeding the resolution-dependent critical density ($n_{\rm H,t_c}$) above which feedback energy is quickly radiated away (Dalla Vecchia & Schaye 2012). To compensate for these numerical losses, a density dependence of the feedback efficiency is introduced in this model.

ViscLo and ViscHi: The rate by which gas flows through the accretion disc and the angular-momentum scale at which gas, which is accreting onto the black hole, reaches the Bondi-limited regime, are both regulated by the viscosity parameter, $C_{\rm visc}$ (see Crain et al. 2015 for details). A lower (higher) value of the viscosity parameter $C_{\rm visc}$, corresponding to a higher (lower) sub-grid viscosity, leads to an earlier (later) onset of the dominance of AGN feedback, and a larger (smaller) energy injection rate when in the viscosity-limited regime.

AGNdT8 and AGNdT9: The AGN ISM-heating temperature is crucial for any cosmological simulation (Schaye et al. 2015). The EAGLE Reference model adopted $\Delta T_{\rm AGN} = 10^{8.5}$K. The two Reference-model variations with $\Delta T_{\rm AGN} = 10^{8}$K (AGNdT8) and $\Delta T_{\rm AGN} = 10^{9}$K (AGNdT9) are examined in this work. The peak baryon conversion efficiency is higher (lower) in the AGNdT8 (AGNdT9) model, with respect to the Reference model.

NOAGN: This model assumes the absence of AGN feedback and is the most extreme galaxy-formation model variation. All other parameters are the same as in the Reference model.

Table 4.1 briefly summarizes the most important parameter values adopted in the different EAGLE model variations used in this work. For a detailed description of the various galaxy-formation prescriptions and sub-grid physics models, we refer to Schaye et al. (2015) and Crain et al. (2015).

4.3 Methodology

In this work, we use the SEAGLE lens-simulation pipeline (see Mukherjee et al. 2018a, M18 hereafter)– which can also incorporate the `GLAMER` (Metcalf & Petkova 2014; Petkova et al. 2014) ray-tracing code and the parametric lens-modeling code (`LENSED`: Tessore et al. 2016; Bellagamba et al. 2017) – only to selected galaxies from the simulations based on their stellar mass and create their dark-matter, stellar, gas and black-hole surface mass density maps. We use these mass maps in our subsequent analyses, and we do not infer any of the quantities in this work via simulated lens systems, as was done by Mukherjee et al. 2018a and in Mukherjee et al. (2018b, in prep).

The SEAGLE pipeline automatically identifies and extracts samples of (lens) galaxies from the `Friends-Of-Friend` (`FoF`) catalogues of the EAGLE simulations. After selecting the galaxy identifiers using an initial selection function, we identify the desired `GroupNumber` and `SubGroup-Number` (numbers assigned to `FoF` group and subgroup, respectively) and select their particles (gas, DM and stars). We currently use a high total galaxy stellar-mass threshold of 10^{11}M$_{\odot}$ (see M18) and a combination of a

lower limit on the stellar velocity dispersion and the stellar half-mass radius (> 1 kpc), taken from the `SubFind` catalogues to remove blatant outliers and to select only genuinely massive galaxies. The number of galaxies with $M_\star > 10^{11} \mathrm{M}_\odot$ that are extracted for each EAGLE galaxy-formation model variation is tabulated in Table 2 of Mukherjee et al. (2018b) and ranges between 8 to 37 for the 50 cMpc boxes. After extraction of the particles of an individual galaxy, we project each galaxy along their three principle axes, producing their associated projected mass maps (see M18). This procedure triples the number of galaxies and includes sample variance due to projection effects, although they are not entirely independent.

We use the projected half-mass radius as a proxy of the stellar-light effective radius (i.e. $R_{\rm eff}$) for each projected mass maps. We calculate the central dark-matter fractions within the effective radius, i.e., $f_{\rm DM}(< R_{\rm eff})$, and within half of the effective radius, $f_{\rm DM}(< 0.5R_{\rm eff})$ for all the EAGLE strong lensing candidates, following the definition in Auger et al. (2010a) and Tortora et al. (2009):

$$f_{\rm DM} \equiv 1 - \frac{M_\star(\beta R_{\rm eff})}{M_{\rm T}(\beta R_{\rm eff})} \quad \text{with } \beta = 0.5 \text{ or } 1, \tag{4.1}$$

where $M_\star(\beta R_{\rm eff})$ is the projected stellar mass within $\beta R_{\rm eff}$ and $M_{\rm T}(\beta R_{\rm eff})$ is the total projected mass within $\beta R_{\rm eff}$. We adopt the projected dark-matter fraction inside these two radii in this work because they represent most closely the the observables. We note again that the effective radius, unlike in the observations, is not derived from the simulated galaxy brightness distribution via model fitting (e.g. with a Sérsic profile), but directly inferred from the simulations. Similarly, the stellar and total masses are not derived from lens modelling, but directly inferred from the mass maps. Although this can lead to differences between the observations and simulations, we expect these to be moderate compared to the much larger differences and scatter that are observed between these quantities (discussed further below).

Observationally, Auger et al. (2010a) found that differences in the stellar-population properties (e.g. age, metallicity, extinction, star-formation history) of very massive ETGs in the SLACS sample are not sufficiently significant to solely account for the broad trends in their inferred stellar M/L with galaxy mass, for a non-varying universal IMF. Under the latter

assumption, Auger et al. (2010a) concluded that the total mass-to-light ratio in SLACS lens galaxies increases with their total stellar mass, most likely as a result of an increasing dark-matter fraction (see also Cappellari et al. 2006; Tortora et al. 2009). The above analyses of SLACS lens galaxies were repeated twice, assuming a Chabrier as well as a Salpeter IMF, respectively. The assumption of a Chabrier IMF, however, allows us to directly compare SLACS results with the results from model variations of EAGLE galaxy-formation simulations.

In the remainder of the chapter, therefore, we assume the following: (i) a fixed universal Chabrier IMF, (ii) the projected stellar half-mass radius is a good proxy for the observed stellar-light effective radius (iii) the projected stellar and total masses are excellent proxies for those inferred from mass modelling of observed lens galaxies. We also carry out the analyses in the galaxy stellar-mass range as for SLACS lenses. The impact of assuming a non-universal IMF are investigated in a future work.

4.4 Results

In this section, we present the results obtained from our comparisons between observed and simulated galaxies. In Section 4.4.1, we first discuss the motivation for adopting $f_{\rm DM}(< 0.5R_{\rm eff})$ in strong lensing studies, which is often different from what is adopted in simulation studies (i.e. $f_{\rm DM}(< R_{\rm eff})$). In Section 4.4.2, we discusses the central dark matter fractions (inside both $0.5R_{\rm eff}$ and $R_{\rm eff}$) of EAGLE galaxy-formation model variations and compare them with strong lensing results from SLACS, under the assumptions outlined at the end the previous section.

4.4.1 Importance of $f_{\rm DM}(< 0.5R_{\rm eff})$ in strong lensing

The mass distribution within half the effective radius ($R_{\rm eff}/2$) has been chosen for SLACS because it is well-matched to the typical Einstein radius and therefore leads to relatively small errors from inter- or extrapolating the power-law mass models in the strong lensing and dynamical analyses. The density slopes can be sensitive to the scale lengths over which they are measured (Xu et al. 2017). Hence choosing $R_{\rm eff}/2$ is important for

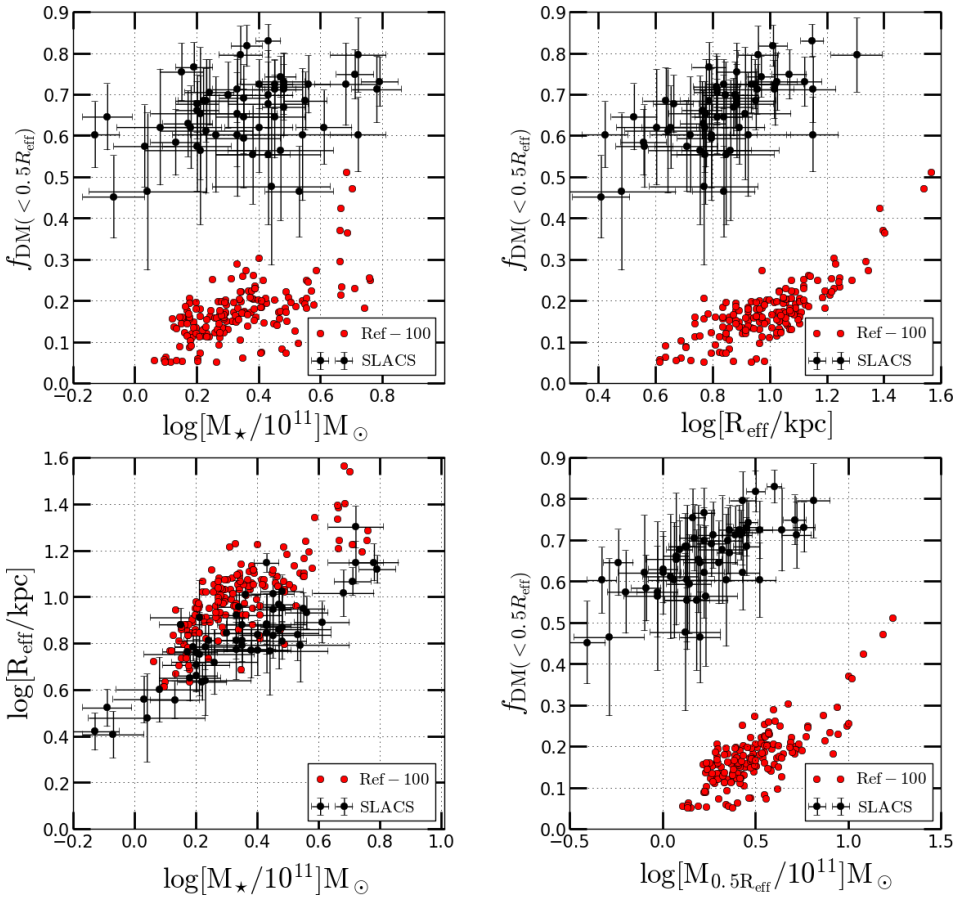

Figure 4.1: Comparison between the EAGLE-Reference 100 cMpc simulation (red dots) and SLACS (black dots) for trends in (a) $f_{\rm DM}(< 0.5R_{\rm eff})$ with stellar mass ($\rm M_\star$) (top left), (b) $f_{\rm DM}(< 0.5R_{\rm eff})$ with projected effective radius ($\rm R_{eff}$) (top right), (c) projected effective radius ($\rm R_{eff}$) with stellar mass ($\rm M_\star$) (bottom left) and (d) $f_{\rm DM}(< 0.5R_{\rm eff})$ with the half total mass ($\rm M_{0.5R_{eff}}$) (bottom right). The comparison has been done assuming a constant M/L ratio and Chabrier IMF for SLACS. We note a better agreement for galaxy mass-size, than for DM fraction.

comparison with strong lensing studies such as SLACS and SL2S (Ruff et al. 2011). Strong lensing studies have calculated and compared the scaling relations and parameter planes of the lens galaxies at this radius only (Koopmans et al. 2006; Auger et al. 2010b,a; Barnabè et al. 2011). Despite this only one recent hydrodynamic simulation (Xu et al. 2017) calculated $f_{\rm DM}(< 0.5R_{\rm eff})$ (see Figure 11 therein), although they did not compare the DM fraction trend with strong lensing results.

4.4.2 Dark matter fractions within $R_{\rm eff}/2$

We start our comparison with simulated galaxies from the largest 100 cMpc simulation box of EAGLE, in order to limit sample variance, especially for high-mass galaxies. This box size, however, has been used only for the Reference galaxy-formation model (Schaye et al. 2015). Figure 4.1 shows the mass-size relation and trends of $f_{\rm DM}(< 0.5R_{\rm eff})$ against different observables for galaxies from the EAGLE-Reference 100 cMpc box at z_l=0.271 and SLACS. Both assume a Chabrier IMF. The $f_{\rm DM}(< 0.5R_{\rm eff})$ values have a large range starting as low as ∼0.05 and increasing up to ∼0.51 with a mean of ∼0.17. The 16th and 84th percentiles are 0.11 and 0.22, respectively. We immediately observe a major discrepancy between the central dark-matter fraction values $f_{\rm DM}(< 0.5R_{\rm eff})$ found in the simulations and in the SLACS observations, when plotted against either stellar or total mass inside the same radius. We find much lower dark matter fractions in the EAGLE simulations than in the SLACS observations. This discrepancy persists in all EAGLE simulations, being a factor of 2–3 depending on the model variation (see Figures 4.2 and 4.3). We discuss the latter models in more detail in Section 4.4.3. When we plot $f_{\rm DM}(< 0.5R_{\rm eff})$ against $R_{\rm eff}$ instead of against a measure of galaxy mass, we find a tighter correlation (see upper right panel of Figure 4.1). This trend, although differing by a again a factor of 2-3 in the dark-matter fraction values, is interestingly similar to that observed in SLACS where also a tighter correlation was reported between $f_{\rm DM}(< 0.5R_{\rm eff})$ and $\rm R_{eff}$ than with $\rm M_\star$ (Auger et al. 2010a). Also other studies gave a clear correlation between the size and the central dark matter fraction (e.g. Tortora et al. 2012; Xu et al. 2017; Remus et al. 2017; Tortora et al. 2018).

Despite these significant discrepancies between simulations and observations, we find that the EAGLE-Reference-100 cMpc simulation produces

lensing galaxies with only slightly larger projected effective radii compared to SLACS, about 0.2 dex at similar stellar mass. In the bottom left panel of Figure 4.1, we see that the stellar mass-size relation of simulated EAGLE galaxies is slightly steeper than that for SLACS galaxies. So even though there is overlap between EAGLE lensing galaxies and SLACS in stellar masses, the simulated galaxies tend to have somewhat larger effective radii than SLACS at the high-mass end. This discrepancy can come from the different methodologies used for calculating the effective radii in observations, which involves modeling the light coming from the galaxies (in different bands), compared to direct inference of the stellar mass from stellar particles in the simulations. Some of the observed excess stellar mass might also be accounted for by a varying stellar M/L as function of radius (and/or galaxy mass), which currently is assumed universal. The mass-size relation difference of $\sim$0.2 dex is unlikely the explanation of the much lower dark-matter fraction in EAGLE. In fact, larger effective radii are expected to lead to larger values of $f_{\rm DM}$ in general, not smaller values. SLACS observations, on the other hand, could suffer from low signal-to-noise imaging in the outer regions of the lens galaxies leading to an underestimate of their effective radii. Differences can also arise due to systematic errors in calculating the effective radius, e.g. the choice of fitting model to obtain the light profile of the galaxy (Trayford et al. 2018).

Comparison to other simulations

Xu et al. (2017) calculated $f_{\rm DM}(< 0.5R_{\rm eff})$ and $f_{\rm DM}(< R_{\rm eff})$ for Illustris (Vogelsberger et al. 2014) at z_l=0.3, but did not compare with SLACS (see figure 11 in Xu et al. 2017). Their study also revealed lower dark-matter fractions, although they conclude that the lower dark-matter fraction within $0.5R_{\rm eff}$ is likely due to an aperture effect: baryons dominate more and more towards the center of the galaxy, and the dark matter fraction drops with decreasing radius. Remus et al. (2017) probed $f_{\rm DM}(< R_{\rm eff})$ and not $f_{\rm DM}(< 0.5R_{\rm eff})$ (see their section 4 therein) and conclude that the dark-matter fractions are similar in their simulations and observations. However, the latter authors incorrectly compare predictions of $f_{\rm DM}(< R_{\rm eff})$ in the simulations to SLACS dark-matter fractions that are calculated inside $R_{\rm eff}/2$. This measurement on different scales could lead to $\sim$30-40% differences (see Xu et al. 2017 and also Lovell et al. 2018). Although

Remus et al. (2017) did not find any clear correlation between stellar mass and central DM fractions in the Magneticum Pathfinder simulations (Hirschmann et al. 2014), even at higher redshifts, and reported only a general tendency for more massive systems to have slightly higher dark-matter fractions for the simulations from Oser et al. 2010, we find a clear correlation between those quantities in the EAGLE-Reference 100 cMpc simulation (see bottom two panels of Figure 4.1). We note that the correlation between $f_{\rm DM}(< 0.5R_{\rm eff})$ and $\rm M_\star$ does have a large scatter for the Reference-100 simulation. Hence the limited sample size and the large system to system scatter in $f_{\rm DM}$ may have prevented Remus et al. (2017) from obtaining significant trends between the dark-matter fraction and stellar mass. Finally, resolution effects in the simulations could also be affecting the dark-matter fraction inside $R_{\rm eff}/2$. We will explore and quantify the resolution effect of the simulation on our analysis in Section 4.4.4 and also in Appendix A.

In conclusion, even though the dark-matter fraction values of the EAGLE Reference-100 simulation are considerably lower than the ones obtained from strong lensing observations from SLACS, the observed trends are strikingly similar. Keeping this difference in mind, we now try to explain the trends in $f_{\rm DM}(< 0.5R_{\rm eff})$ with galaxy properties for different EAGLE model variations to assess whether the observed discrepancy is affected by changes in galaxy formation.

4.4.3 Impact of subgrid physics on $f_{\rm DM}(< 0.5R_{\rm eff})$

In the previous section we have shown that the EAGLE Reference-100 simulation yield much lower dark matter fractions than that inferred from observed SLACS galaxies, whereas the overall trend of their stellar mass versus effective radius is only mildly different. We now assess how changes in the sub-grid physics (in particular feedback and viscosity) affect the dark-matter fraction. The essential parameters of the respective model variations are found in Table 4.1. Due to the smaller box sizes of the model variations, i.e. 50 cMpc, we are limited to smaller numbers of massive galaxies than in the Reference 100 cMpc box.

The EAGLE model variations are divided into two subcategories, namely calibrated simulations and Reference variations. The calibrated simulations differ in terms of the adopted sub-grid efficiency of feedback associated with star formation, and the way in which this feedback efficiency depends upon the properties of the local environment. The simulations are calibrated to match the present galaxy stellar mass function (GSMF), although the agreement at the high-mass end is poorly constrained due to the limited box size. In the Reference variation simulations, only one parameter of the Reference model is varied. These reference variation simulations are not calibrated with the GSMF.

$f_{\rm DM}(< 0.5R_{\rm eff})$ in calibrated simulations

Figure 4.2 shows the comparison of three calibrated (FBconst, FBZ and FBσ) and one extreme Reference-variation simulations (NOAGN). We note that only EAGLE galaxies having $M_\star > 10^{11}{\rm M}_\odot$ are shown (see M18 for motivation), although all SLACS galaxies are shown. The three calibrated models have very low average DM fractions (8-12%) within half an effective radius. Although the maximum values of $f_{\rm DM}(< 0.5R_{\rm eff})$ are around 0.5, the 16th and 84th percentile values range from 0.07 to 0.14. A small fraction of galaxies have comparable stellar mass to SLACS, but they have much larger effective radii. The latter lead to higher average dark matter fractions ($f_{\rm DM}(< 0.5R_{\rm eff}) \sim 0.45$). Except for these 'outliers' on the mass-size relation, the overall trend of $f_{\rm DM}(< 0.5R_{\rm eff})$ with stellar mass is almost flat and does not match that of SLACS.

When we examine the trends of $f_{\rm DM}(< 0.5R_{\rm eff})$ versus $R_{\rm eff}$, we see a flat plateau at lower effective radii up to 8 kpc which then tends to increase non-linearly with increasing effective radius. Regardless of these uncharacteristic trends, the calibrated models produce galaxies that are more compact, i.e. have a smaller effective radius than the reference model shown in Figure 4.1. This result can be explained by the fact that all these calibrated simulations have lower feedback efficiency (see Crain et al. 2015) thus allowing the baryons to cool more efficiently and settle at the center of the halo and form stars. This effect also explains why the stellar mass fraction increases inside $R_{\rm eff}/2$ when compared to the Reference model in Figure 4.1. Crain et al. (2015) showed that galaxies with $\rm M_\star > 10^{10}M_\odot$

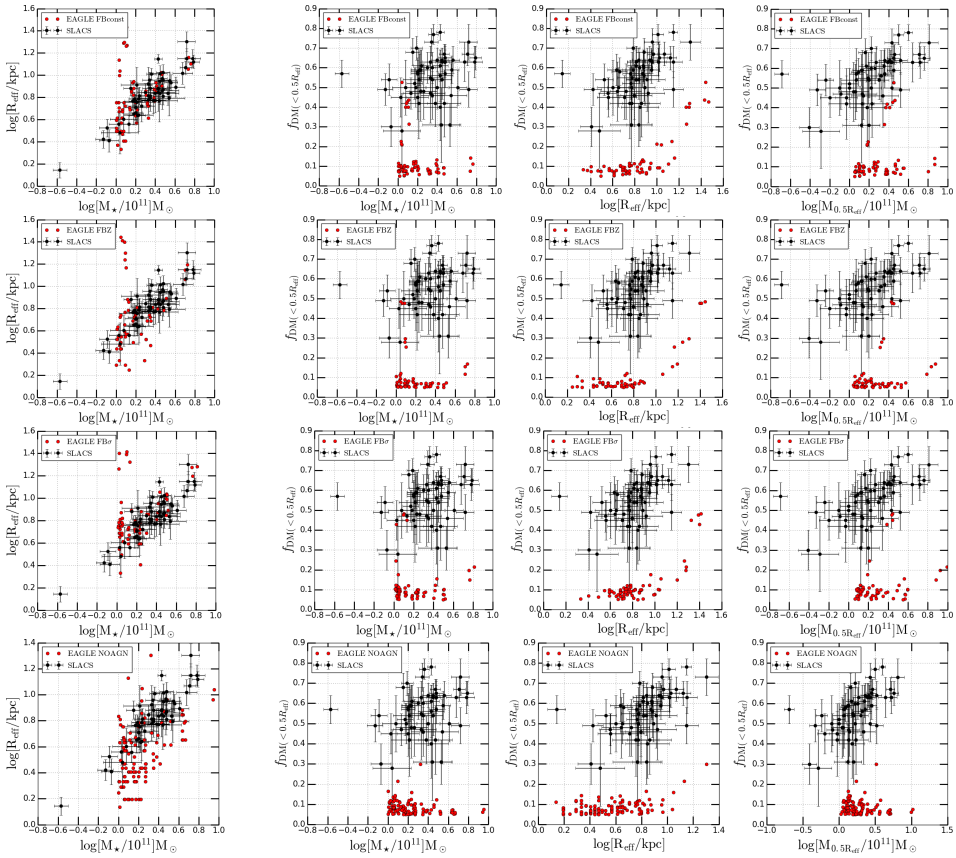

Figure 4.2: Comparison of properties of four different galaxy formation scenarios of EAGLE (red dots) with SLACS (black dots). The scenarios are shown in their respective rows as follows: FBconst in top row, FBZ in row 2, FBσ in row 3 and NOAGN in the bottom row. The properties that are compared in each of the frames are the same as in Figure 4.1 i.e. (a) projected effective radii ($\mathrm{R_{eff}}$) as a function of stellar mass ($\mathrm{M_\star}$) (first column from left), (b) $f_{\mathrm{DM}}(< 0.5R_{\mathrm{eff}})$ versus stellar mass ($\mathrm{M_\star}$) (second column from left), (c) $f_{\mathrm{DM}}(< 0.5R_{\mathrm{eff}})$ versus projected effective radii ($\mathrm{R_{eff}}$) (third column from left) and (d) $f_{\mathrm{DM}}(< 0.5R_{\mathrm{eff}})$ versus half the total mass ($\mathrm{M_{0.5R_{eff}}}$) (fourth column from left). FBconst, FBZ and FBσ are calibrated simulations and NOAGN is a Reference variation.

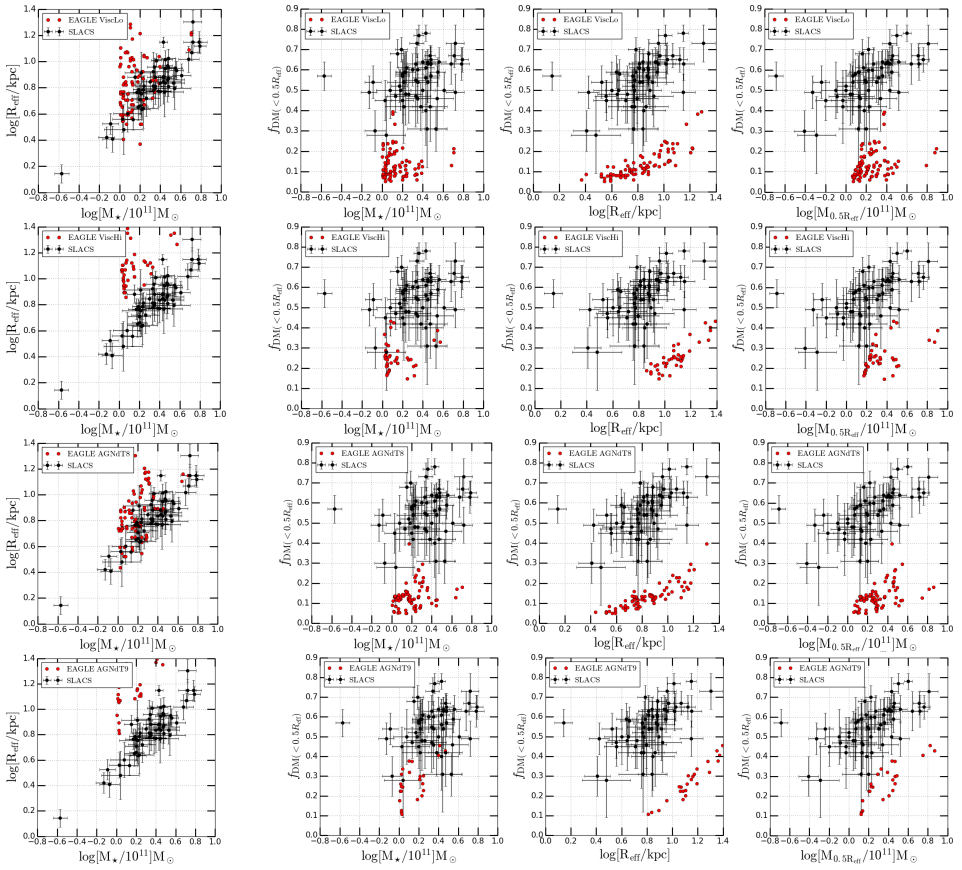

Figure 4.3: As Figure 2 but for reference model variations. EAGLE in red dots and SLACS in black dots. The scenarios are presented in their respective rows as follows: Viscosity-Lo (top row), Viscosity-Hi (row 2), AGNdT8 (row 3) and AGNdT9 (row 4).

sometimes become too compact with median sizes having an upper limit of only a few times the gravitational softening scale ($\epsilon_{\rm prop} = 0.7$ kpc). Hence lower feedback efficiency could explain the low values of $f_{\rm DM}(< 0.5R_{\rm eff})$ in the calibrated models for lower mass galaxies. The NOAGN model (a Reference-variation model) behaves similarly to the calibrated simulations showing similar trends in $f_{\rm DM}(< 0.5R_{\rm eff})$ with $M_\star$, $R_{\rm eff}$ and $M_{0.5R_{\rm eff}}$ and a similar mass-size relation. Table 4.2 summarizes the maximum, minimum, mean and median values of $f_{\rm DM}(< 0.5R_{\rm eff})$.

$f_{\rm DM}(< 0.5R_{\rm eff})$ in Reference-model variations

Figure 4.3 presents the results for the Reference-model variations: Viscosity-Lo, Viscosity-Hi, AGNdT8 and AGNdT9. The value of $f_{\rm DM}(< 0.5R_{\rm eff})$ generally have similar ranges, but there are some striking differences in their trends compared to the calibrated models. In all four scenarios, EAGLE galaxies show qualitatively similar trends as SLACS galaxies when we examine $f_{\rm DM}(< 0.5R_{\rm eff})$ versus $R_{\rm eff}$. However, we again find a discrepancy of a factor of 2–3 in the values of $f_{\rm DM}(< 0.5R_{\rm eff})$ between EAGLE and SLACS, similar to the reference model. The mass-size relations are also strongly affected by these non-calibrated model variations. We also see the signature of different feedback processes in the variation of the minimum, maximum, mean and median values of $f_{\rm DM}(< 0.5R_{\rm eff})$.

To understand these effects better from a physical point of view, we compare the $f_{\rm DM}(< 0.5R_{\rm eff})$ values in pairs: (a) ViscLo and ViscHi and (b) AGNdT8 and AGNdT9. For comparison (a) we find that the $f_{\rm DM}(< 0.5R_{\rm eff})$ values in the ViscLo model has a 16th percentile value of 0.08 compared to 0.19 for the ViscHi model, and an 84th percentile value of 0.20 compared to 0.32 for the ViscHi model. These lower dark-matter fractions are the consequence of the lower value of the viscosity parameter, which leads to a higher accretion-disc viscosity (ViscHi model) and consequently to an earlier onset of the dominance of AGN feedback. Conversely, a higher value of viscosity parameter corresponds to a value of the viscosity (ViscLo model) and lead to a later onset of AGN feedback activity. Thus in the ViscHi simulation, the AGN feedback starts earlier, and gas is more effectively ejected throughout the galaxy formation process thereby increasing their sizes and dark-matter fractions.

Similarly, for comparison (b) we find that the values of $f_{\rm DM}(< 0.5R_{\rm eff})$ in the AGNdT8 model have a 16th percentile value of 0.08 and 0.18 for the AGNdT9 model, and 84th percentile values of 0.18 and 0.38, respectively. Both the maximum and minimum values of $f_{\rm DM}(< 0.5R_{\rm eff})$ are lower (higher) for AGNdT8 (AGNdT9) than for the Reference model when measured at similar radii. These variations are the consequence of the implementation of the AGN heating temperature in the EAGLE simulations. The change in gas temperature for each AGN feedback event is $\Delta T_{\rm AGN} = 10^8$K for the AGNdT8 model and $\Delta T_{\rm AGN} = 10^9$K for the AGNdT9 model. The peak baryon conversion efficiency is higher (lower) in the AGNdT8 (AGNdT9) model, compared to the Reference model, which assumes $\Delta T_{\rm AGN} = 10^{8.5}$K. Hence the dark-matter fraction has a lower (higher) value in AGNdT8 (AGNdT9). Table 4.2 summarizes the maximum, minimum, mean and median values of $f_{\rm DM}(< 0.5R_{\rm eff})$. More details about the Reference-variations and the calibrated simulations can be found in Crain et al. (2015) and Mukherjee et al. (2018b).

We see that the discrepancy in $f_{\rm DM}(< 0.5R_{\rm eff})$ values between simulations and observations remains robustly present even when the sub-grid physics changes in EAGLE model variations. This observation could be a consequence of the dark-matter density distribution in the EAGLE simulations being more shallow than that from the SLACS observations at the very inner regions (inner $\sim$4 kpc) of the galaxies. A more shallow dark-matter density profile leads to a lower dark-matter fraction if the galaxy has a similar total projected mass inside the same effective radius. A similar effect can occur if the stellar IMF is not constant and there is a radial dependence/gradient in the stellar M/L in the observations, with an increasing number of low-mass stars toward the centers of massive galaxies (Smith & Lucey 2013; Smith et al. 2015). If a radial increase in the stellar M/L ratio occurs towards the center in observed galaxies, it could mimic a steeper dark-matter density profile. This degeneracy between low-mass stars (that contribute a tiny fraction to the total stellar galaxy luminosity) and dark matter might be hard to break observationally and can lead to the inference of too steep dark-matter density profiles in observations (Napolitano et al. 2010). We address the IMF dependence and dark-matter slope analyses in an upcoming work.

The conclusion that remains robust, however, is that observations and simulations disagree strongly in their inferred dark-matter fractions inside

$R_{\rm eff}/2$, using the same stellar IMF assumption. This discrepancy can come from the use of inexact galaxy-formation physics in the simulations, an incorrect calibration of the simulations, an incorrect assumption regarding the stellar IMF, differences in the galaxy selection, or resolution effects (see Appendix A). Currently, it is hard to distinguish which of these effects is the cause.

4.4.4 Dark matter fraction within $R_{\rm eff}$

Having found a clear discrepancy between simulations (EAGLE) and observation (SLACS) in their resulting dark-matter fractions inside half of the effective radius, we now try to determine whether this difference still exists when we calculate these quantities inside the effective radius itself, $R_{\rm eff}$. We calculate the value of $f_{\rm DM}(< R_{\rm eff})$ for SLACS galaxies assuming that the stellar M/L ratio is constant with radius (consistent with the assumption in Auger et al. 2010a). To further complement our SLACS analysis, we also compare the dark-matter fractions with those inferred from non-lensing galaxies of the SPIDER sample (Tortora et al. 2012). This comparison allows us to assess whether SLACS galaxies are a representative or a biased representation of massive early-type galaxies.

To calculate the value of $f_{\rm DM}(< R_{\rm eff})$ for SLACS galaxies, we multiply $\rm M_{0.5R_{eff}}$ taken from Auger et al. 2010a by a factor of exactly two, in order to obtain the total mass $\rm M_T(< R_{eff})$. This factor of two is exact for SIE models where the mass scales linearly with radius. Although SLACS galaxies have a scatter in their density slopes around isothermal, we ignore this deviation because its impact is far smaller than the strong offset in the dark-matter fraction that we find between SLACS and EAGLE galaxies. This extrapolation leads to a moderate increase in the scatter of the inferred dark-matter fractions, but it will not lead to a significant bias (i.e. shift up or down). We obtain the values of $\rm M_\star(< R_{eff})$ following the definition that it is half the total stellar mass given in Auger et al. (2010a). We then calculate $f_{\rm DM}(< R_{\rm eff})$ for SLACS as outlined earlier. For EAGLE galaxies we follow the same procedures as before as well and determine the dark-matter fractions directly from the mass maps.

The SPIDER dataset (La Barbera et al. 2010b) is a volume-limited sample of $\sim$ 40000 bright ETGs with and r-band rest-frame magnitude ${}^{0.1}M_r <$

Table 4.2: The maximum, minimum, mean, median, 16th and 84th percentile (PCTL) values of $f_{\rm DM}(< 0.5R_{\rm eff})$ and $f_{\rm DM}(< R_{\rm eff})$ of lensing galaxies in the EAGLE variations, SLACS and Illustris. Also $f_{\rm DM}(< R_{\rm eff})$ values for SLACS, SPIDER, Illustris, IllustrisTNG-100 and EAGLE-Reference-100.

$f_{\rm DM}(< 0.5R_{\rm eff})$

	Scenario	Max.[%]	Min.[%]	Mean[%]	Median[%]	$16^{\rm th}$ PCTL	$84^{\rm th}$ PCTL
Calibrated	Ref-100	51.3	5.1	17.2	16.7	11.4	22.3
	FBconst	52.6	5.1	12.7	8.8	6.9	13.8
	FBZ	48.4	5.0	10.5	6.9	5.4	11.8
	FBσ	48.2	5.1	11.8	9.4	6.9	12.3
Ref-variation	Visc-Lo	39.4	5.2	13.6	11.8	8.0	20.1
	Visc-Hi	43.2	14.7	25.6	24.3	19.0	32.5
	AGNdT8	39.6	5.0	13.4	12.8	7.7	18.2
	AGNdT9	45.6	10.7	27.1	26.2	18.1	37.7
	NOAGN	29.9	5.0	8.5	7.5	5.6	11.3
	SLACS	78.0	28.0	55.2	57.0	45.3	64.7
	Illustris	37.5	6.0	23.2	23.1	11.3	35.1

$f_{\rm DM}(< R_{\rm eff})$

	Sim/Obs	Max.[%]	Min.[%]	Mean[%]	Median[%]	$16^{\rm th}$ PCTL	$84^{\rm th}$ PCTL
	Ref-100	83.6	30.3	60.8	61.6	48.9	70.3
	Illustris	64.2	49.1	54.3	54.1	50.0	62.0
	TNG-100	68.1	57.6	63.0	62.7	49.5	65.5
	SLACS	83.1	45.3	65.8	67.0	57.8	73.0
	SPIDER	80.5	33.5	56.1	56.9	38.7	72.5

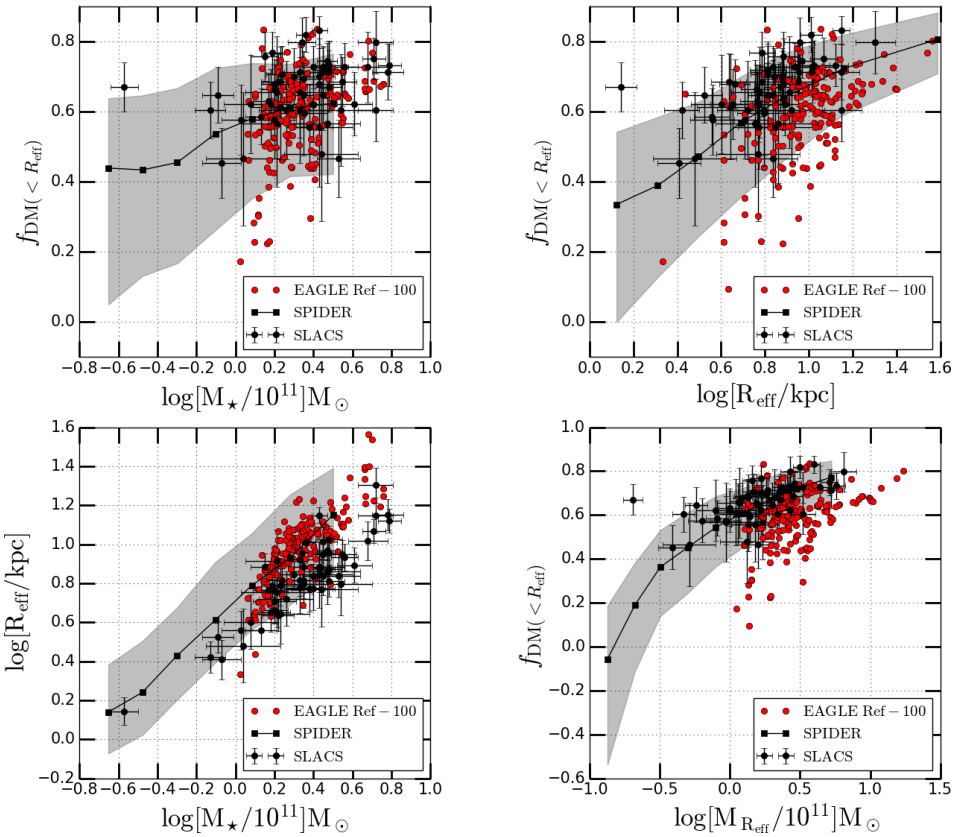

Figure 4.4: Comparison between SLACS (black dots), SPIDER (black square) and the EAGLE-Reference 100 cMpc simulation (red dots) for trends in (a) $f_{\rm DM}(< R_{\rm eff})$ with stellar mass ($\rm M_\star$) (top left), (b) $f_{\rm DM}(< R_{\rm eff})$ with projected effective radius ($R_{\rm eff}$) (top right), (c) projected effective radius ($R_{\rm eff}$) with stellar mass ($\rm M_\star$) (bottom left) and (d) $f_{\rm DM}(< R_{\rm eff})$ with half total mass ($\rm M_{R_{eff}}$) [dynamical mass for SPIDER](bottom right). Black squares (connected by a black line) and gray shaded region are medians and 16-84th percentile trends for SPIDER (determined as discussed in Tortora et al. 2012).

-20, in the redshift range $z = 0.05 - 0.095$, with available *ugriz* photometry and optical spectroscopy, where ${}^{0.1}M_r$ is the k-corrected SDSS Petrosian magnitude in r band. SPIDER ETGs are luminous bulge-dominated systems, with passive spectra in the central SDSS fiber aperture. For the present study, we use a sample of $\sim$ 4200 ETGs, with stellar masses derived from the fit of stellar population synthesis to optical+near-infrared photometry (assuming a Chabrier stellar IMF), structural parameters from g through K band, and velocity dispersions within the SDSS aperture. The velocity dispersions are modeled using the spherical isotropic Jeans equations, to determine the dynamical (total) mass, following the approach in Tortora et al. (2009). Dark-matter fraction $f_{\rm DM}(< R_{\rm eff})$ values are extracted from Tortora et al. (2012) (see therein for further details on the sample selection and the dark-matter fraction calculation). To perform a coherent comparison with the SLACS and EAGLE dark-matter fractions, we have first converted de-projected masses in Tortora et al. (2012) to projected quantities, and updated sizes and stellar masses to the cosmology adopted in this study. SPIDER DM fractions are computed within the K-band effective radius, making our estimated values less affected by metallicity and age gradients, dust extinction and (low fractions of) young stars. For these reasons, SPIDER provides a useful dataset for a direct comparison with simulations using $R_{\rm eff}$ inferred via the mass particles, and in particular, with EAGLE data.

Figure 4.4 shows the comparison of $f_{\rm DM}(< R_{\rm eff})$ from the EAGLE-Reference 100 cMpc simulation at z_l=0.271 with that of SPIDER and SLACS. We still find a large scatter ranging from $f_{\rm DM}(< R_{\rm eff})$ $\sim$0.10 at the low-mass end to $\sim$0.80 at the massive end of the stellar mass of EAGLE galaxies, consistent with other simulation studies (Wu et al. 2014; Courteau & Dutton 2015; Remus et al. 2017; Xu et al. 2017). From Figure 4.4 it is immediately self-evident that dark-matter fractions within $R_{\rm eff}$ from EAGLE simulations match the SLACS and SPIDER distributions considerably better than they do within $R_{\rm eff}/2$. This suggest that the discrepancy seen inside $R_{\rm eff}/2$ is most likely genuine and due to one of the assumptions made either in the simulations or in the observations. The exact cause remains unexplained.

Comparing EAGLE, SLACS and SPIDER

In the previous sections, we demonstrated that the dark-matter fraction dramatically increases in the EAGLE simulations when calculated inside $R_{\rm eff}$ rather than inside $R_{\rm eff}/2$). This result is consistent with other numerical simulations (e.g. Xu et al. 2017; Lovell et al. 2018) and with some observations (e.g. Napolitano et al. 2010; Tortora et al. 2012). Although part of this variation could be due to an aperture effect (see Xu et al. 2017; Peirani et al. 2018; Lovell et al. 2018), this alone can not account for the large deficiency of dark matter compared to observations inside $R_{\rm eff}/2$.

Since we find that the total mass density slopes agree well with the observations (Mukherjee et al. 2018a,b; see also Remus et al. 2017; Xu et al. 2017), there appears to be some conspiracy between the stellar and dark matter content of the galaxies in the simulations. In short, although the sum of the dark matter and stellar mass add up to almost the same mass inside the same effective radius as in the observations, their relative contributions are vastly different. Despite these differences, the inferred mass density profiles agree between simulation and observations inside $R_{\rm eff}/2$.

In Figure 4.4 we notice that value of $R_{\rm eff}$ in SLACS are biased low, especially at the high-mass end. This bias indicates that mass-selected SLACS galaxies might prefer more compact galaxies (Hezaveh et al. 2012) than the volume-limited galaxies from SPIDER. The SPIDER galaxies agree well with EAGLE in their respective mass-size relation. On the other hand, SLACS galaxies are not different from their parent-population ETGs as far as their photometric properties are concerned (Koopmans et al. 2006). Treu et al. (2006) show that the SLACS galaxies are representative of luminous red galaxies and display similar trends in galaxy properties as other ETGs. Also, despite the discrepancy seen in $f_{\rm DM}(< 0.5R_{\rm eff})$ when comparing $f_{\rm DM}(< R_{\rm eff})$ in the observation and simulation, we find that $f_{\rm DM}(< R_{\rm eff})$ in SLACS is biased only slightly higher than EAGLE. The deviation in $R_{\rm eff}$ between SLACS and SPIDER can be attributed to how the effective radius is measured in the observations. The SPIDER sample used a Sersic (1968) profile with a freely varying index (optimized with a penalty function) to calculate the $R_{\rm eff}$, whereas SLACS used a de Vaucouleurs (1948) profile. Auger et al. (2010a) demonstrated that their assumption of de Vaucouleurs (1948) profile is valid in the luminosity range covered by the SLACS sample. The systematic trends in Sérsic index n for such high-luminosity galaxies

are dominated by the intrinsic scatter in the correlation. Also Auger et al. (2010b) used HST imaging to determine the effective radius of SLACS galaxies, and employed a linear model of $R_{\rm eff}$ as a function of wavelength to infer the rest-frame V-band $R_{\rm eff}$. For SPIDER galaxies, Tortora et al. (2012) used the K-band data, which might also contribute to the slightly larger values in $R_{\rm eff}$ and consequently lower value of $f_{\rm DM}(< R_{\rm eff})$ and better agreement with EAGLE. Moreover, SLACS galaxies were selected spectroscopically from the Sloan Digital Sky Survey (SDSS) database having the galaxy spectra with multiple nebular emission lines. SLACS was optimized to select bright, massive ETGs with faint lensed sources. Contrary, the SPIDER sample is generically selected with optical ($griz$) photometry and spectroscopy from the SDSS Data Release 6 (SDSSDR6) and near-infrared ($YJHK$) photometry from the UKIRT Infrared Deep Sky Survey-Large Area Survey (UKIDSS-LAS) (DR4). So both surveys have different selection strategies that might contribute to the differences in their structural parameters. We see that a difference in observational strategy, methodology (i.e. using different fitting prescriptions), observational filters/bands used in the surveys and environment where the ETGs reside can lead to slight systematical variations in the measurements. We have used similar assumption on IMF, stellar mass range and projected quantities for our analysis. Although systematical differences are present when compared with strong lensing and non-lensing observations, the overall trends and inferences remain unaffected.

4.4.5 Comparison to Illustris and IllustrisTNG-100

Similar to EAGLE, both Illustris (Vogelsberger et al. 2014) and IllustrisTNG (Springel et al. 2018) are recent state-of-the-art hydrodynamic simulations. We compare the values of $f_{\rm DM}(< R_{\rm eff})$ from the EAGLE Reference-100 model with both the Illustris and IllutrisTNG-100 simulations in Figure 4.5. The dark-matter fraction values from the Illustris and IllustrisTNG simulations are from Lovell et al. (2018) at z=0, whereas EAGLE-Reference and other model variations are at $z_l = 0.271$. We compare these simulations assuming that the evolution in the redshift range $0 < z < 0.3$ is small. We see in Figure 4.5 that the EAGLE Reference simulation exhibits almost a very similar trend as the IllustrisTNG-100 simulation (Lovell et al. 2018) when comparing galaxies with total stellar

masses $M_\star > 10^{11} M_\odot$. As pointed out in Lovell et al. (2018), the difference in the values of $f_{\rm DM}(< R_{\rm eff})$ between Illustris and IllustrisTNG-100 galaxies is mainly due to the former galaxies being more massive and more extended than their TNG counterparts. They are in worse agreement with observational constraints although this shift is only about 0.1 in the dark-matter fraction. Hence the dark-matter fractions inferred from EAGLE simulation agree well with these independent simulations.

4.5 Discussions and Conclusions

In this chapter, we have studied the central projected dark-matter mass fraction in simulated EAGLE galaxies and compared the results to the mass-selected (strong-lens) galaxies from the SLACS survey and with volume-limited galaxies from the SPIDER survey, inside $R_{\rm eff}$ and $R_{\rm eff}/2$. We carried out this comparison for ten different EAGLE simulations that have different sub-grid physics models. We focus in particular on changes in the stellar and AGN feedback and the accretion-disk viscosity. Under the assumption of a universal Chabrier steller IMF, we find a marked discrepancy in the values of $f_{\rm DM}(< 0.5R_{\rm eff})$ between simulations and SLACS observations. We have studied the observed trends in the dark-matter fraction with galaxy mass or size for each of the EAGLE model variations but can not explain the difference in dark matter fraction based on any current galaxy formation model. Similarly, differences in the way these quantities are inferred in the simulations and observations, resolution effects in the simulation, nor selection biases seem sufficiently strong to explain this difference. The discrepancy, however, virtually disappears when the dark-matter fraction is measured inside $R_{\rm eff}$ and compared with SLACS and SPIDER galaxies. This better agreement inside $R_{\rm eff}$ could suggest that different or additional formation mechanisms play a role in massive early-type galaxies in their inner $R_{\rm eff}/2$, controlling star formation and the (re)distribution of dark matter, or a significant break down in our fundamental assumptions. One of these assumptions is the use of a universal Chabrier stellar IMF. Although changing the IMF to Salpeter would not help since it lowers the dark-matter content equally in the observations as well as the simulation, a non-universal IMF varying as a function of galaxy mass and radius might be able to mitigate these dark-matter fraction differences. The impact of the IMF will be investigated in a forthcoming

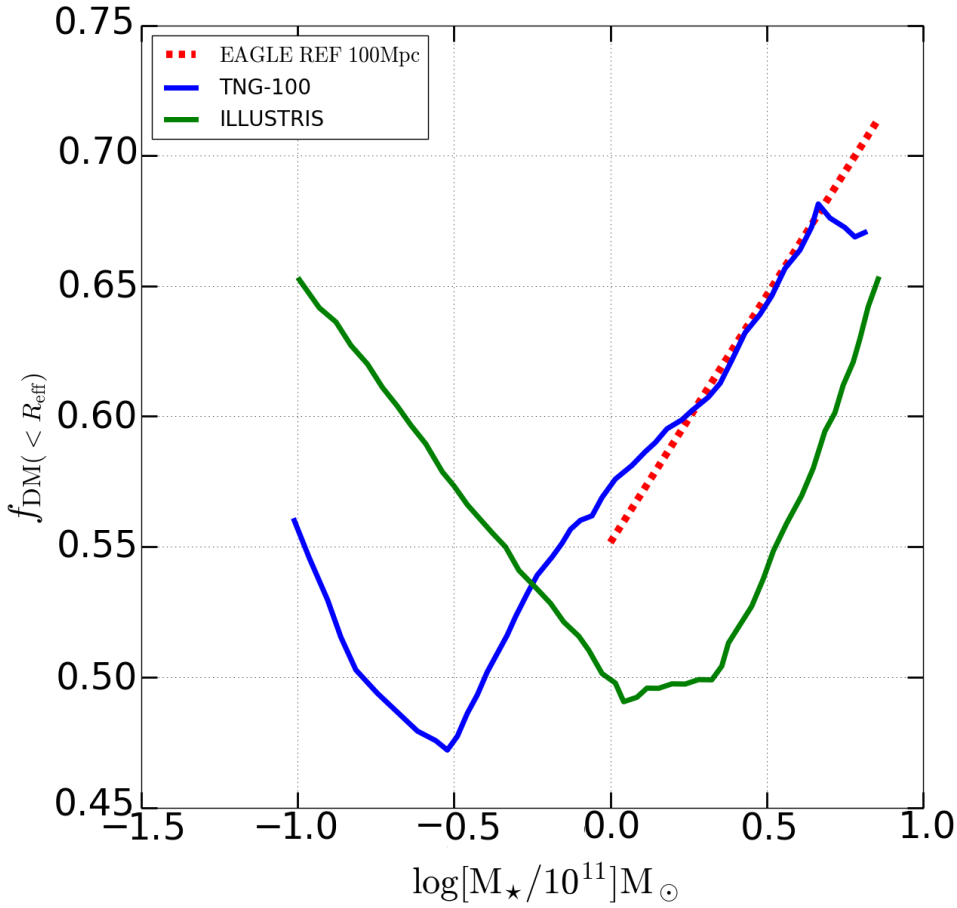

Figure 4.5: Comparison of $f_{\rm DM}(<R_{\rm eff})$ for EAGLE-Reference-100 (red dotted line), Illustris (green solid line) and IllustrisTNG-100 (blue solid line). The Illustris and IllustrisTNG-100 data were obtained from Lovell et al. (2018). Note that we restrict our analysis in this study to $\rm M_\star > 10^{11} M_\odot$.

work.

The main conclusions of this work are summarized as follows:

- There is a notable discrepancy, by a factor of 2–3, between the dark-matter fractions inside $R_{\rm eff}/2$ inferred from simulated EAGLE galaxies and those inferred from observed SLACS galaxies with stellar masses exceeding $10^{11}\,{\rm M}_{\odot}$ and under the assumption of a universal Chabrier stellar IMF. As one progresses to more massive galaxies, the dark-matter component becomes more prominent, and there is an increasing dark-matter fraction with stellar mass. This trend is similar to strong lensing observations seen in SLACS galaxies, but it has the bias as mentioned above.

- Galaxies obtained from EAGLE simulations that have limited stellar or AGN feedback, display a more compact structure (i.e. they have smaller effective radii) and appear to be closer analogues of SLACS galaxies (Mukherjee et al. 2018a,b). Although these models are preferred by the observed mass-size relation of SLACS galaxies (i.e. $R_{\rm eff}$ versus $M_{\star}$) and are in agreement with other studies (Remus et al. 2017; Peirani et al. 2018; Mukherjee et al. 2018b), they also lead to more discrepant dark-matter fractions within $R_{\rm eff}$.

- The discrepancy of the dark-matter fractions between the EAGLE simulations and SLACS observations is largely lifted when calculated within one effective radius $f_{\rm DM}(< R_{\rm eff})$. Although part of this effect might be attributed to resolution or convergence in the simulations, or differences in their inference (Bahé et al. 2017; Xu et al. 2017), we think that the difference between $R_{\rm eff}$ and $R_{\rm eff}/2$ is too large to be purely attributed to these effects. Hence either the dark-matter fraction inside $R_{\rm eff}/2$ is overestimated in observation, or it is too low in the simulations. This discrepancy must then be related to one of the fundamental assumption made in both cases, for example the assumption of a universal IMF (Smith et al. 2015).

- EAGLE galaxies are also well matched with the non-lensing galaxies of SPIDER (Tortora et al. 2012) in their $f_{\rm DM}(< R_{\rm eff})$ values when compared with ${\rm M}_{\star}$, $R_{\rm eff}$ and ${\rm M}_{\rm R_{eff}}$. The mass-size relation is also in

better agreement to SPIDER than SLACS. The mild differences in mass-size or $f_{\rm DM}$ relation of EAGLE galaxies with SLACS galaxies, especially at high mass end, may be due to systematics involved in the observations.

- Stronger stellar or AGN feedback increases both $R_{\rm eff}$ and $f_{\rm DM}$ for a fixed galaxy stellar mass, $\rm M_\star$. Although stronger feedback improves the agreement with observations for $f_{\rm DM}$, it worsens the agreement with $R_{\rm eff}$. Hence, we may not be able to get an agreement with the data for both observables simultaneously simply by changing the feedback efficiency.
- The dark-matter fraction in the central region ($<R_{\rm eff}$) of the galaxies in EAGLE and IllustrisTNG-100 hydrodynamic simulations agree well with each other. However, due to the larger sizes and higher stellar masses, Illustris galaxies shows a small (0.1) difference with EAGLE galaxies in their dark-matter fractions.

We end with the following general remark: The significant difference of inner dark-matter fraction $f_{\rm DM}(<0.5R_{\rm eff})$ between observation and simulations, although maybe partially explained by the feedback mechanisms and the minor difference in inference, raises an important question about our current understanding of galaxy formation.

In particular, we think that a wrongful assumption of a universal stellar IMF could play a dominant role in both the simulation and observations. Letting this assumption go, can lead to changes in the inferred dark matter fraction with radius and galaxy mass. For example, low-mass stars might be more prevalent at smaller radii, mimicking dark matter in observations, whereas if the dark-matter density slope is more cored inside $R_{\rm eff}$ in the simulations and more cuspy in the observations, this could quite easily account for the discrepancy in dark matter inside $R_{\rm eff}/2$ even if there is good agreement inside $R_{\rm eff}$.

Acknowledgements

SM, LVEK, CT and GV are supported through an NWO-VICI grant (project number 639.043.308). SM thanks SURFSARA network in Amsterdam. MS is supported by VENI grant 639.041.749. JS is supported by VICI grant 639.043.409. FB thanks the support from the grants ASI n.I/023/12/0 "Attività relative alla fase B2/C per la missione Euclid" and PRIN MIUR 2015 "Cosmology and Fundamental Physics: Illuminating the Dark Universe with Euclid". This work used the DiRAC Data Centric system at Durham University, operated by the Institute for Computational Cosmology on behalf of the STFC DiRAC HPC Facility (www.dirac.ac.uk). This equipment was funded by BIS National E-infrastructure capital grant ST/K00042X/1, STFC capital grant ST/H008519/1, and STFC DiRAC Operations grant ST/K003267/1 and Durham University. DiRAC is part of the National E-Infrastructure. This work was supported by the Netherlands Organisation for Scientific Research (NWO), through VICI grant 639.043.409.

References

Auger, M. W., Treu, T., Bolton, A. S., et al. 2010a, ApJ, 724, 511
Auger, M. W., Treu, T., Gavazzi, R., et al. 2010b, ApJL, 721, L163
Bahé, Y. M., Barnes, D. J., Dalla Vecchia, C., et al. 2017, MNRAS, 470, 4186
Barnabè, M., Czoske, O., Koopmans, L. V. E., Treu, T., & Bolton, A. S. 2011, MNRAS, 415, 2215
Bellagamba, F., Tessore, N., & Metcalf, R. B. 2017, MNRAS, 464, 4823
Bolton, A. S., Burles, S., Koopmans, L. V. E., et al. 2008a, ApJ, 682, 964
Bolton, A. S., Burles, S., Koopmans, L. V. E., Treu, T., & Moustakas, L. A. 2006, ApJ, 638, 703
Bolton, A. S., Treu, T., Koopmans, L. V. E., et al. 2008b, ApJ, 684, 248
Brownstein, J. R., Bolton, A. S., Schlegel, D. J., et al. 2012, ApJ, 744, 41
Cabanac, R. A., Alard, C., Dantel-Fort, M., et al. 2007, A&A, 461, 813
Cappellari, M., Bacon, R., Bureau, M., et al. 2006, MNRAS, 366, 1126
Chabrier, G. 2003, PASP, 115, 763
Cole, S., Lacey, C. G., Baugh, C. M., & Frenk, C. S. 2000, MNRAS, 319, 168
Conroy, C. 2013, ARA&A, 51, 393
Conroy, C., Gunn, J. E., & White, M. 2009, ApJ, 699, 486
Courteau, S. & Dutton, A. A. 2015, ApJL, 801, L20
Crain, R. A., Schaye, J., Bower, R. G., et al. 2015, MNRAS, 450, 1937
Daddi, E., Renzini, A., Pirzkal, N., et al. 2005, ApJ, 626, 680
Dalla Vecchia, C. & Schaye, J. 2012, MNRAS, 426, 140
de Vaucouleurs, G. 1948, Annales d'Astrophysique, 11, 247
Duffy, A. R., Schaye, J., Kay, S. T., et al. 2010, MNRAS, 405, 2161
Fontanot, F., De Lucia, G., Monaco, P., Somerville, R. S., & Santini, P. 2009, MNRAS, 397, 1776
Furlong, M., Bower, R. G., Crain, R. A., et al. 2017, MNRAS, 465, 722
Furlong, M., Bower, R. G., Theuns, T., et al. 2015, MNRAS, 450, 4486
Gavazzi, R., Treu, T., Marshall, P. J., Brault, F., & Ruff, A. 2012, ApJ, 761, 170
Hezaveh, Y. D., Marrone, D. P., & Holder, G. P. 2012, ApJ, 761, 20
Hirschmann, M., Dolag, K., Saro, A., et al. 2014, MNRAS, 442, 2304
Khochfar, S. & Burkert, A. 2003, ApJL, 597, L117
Koopmans, L. V. E., Bolton, A., Treu, T., et al. 2009, ApJL, 703, L51
Koopmans, L. V. E. & Treu, T. 2003, ApJ, 583, 606

Koopmans, L. V. E., Treu, T., Bolton, A. S., Burles, S., & Moustakas, L. A. 2006, ApJ, 649, 599
La Barbera, F., de Carvalho, R. R., de La Rosa, I. G., & Lopes, P. A. A. 2010a, MNRAS, 408, 1335
La Barbera, F., de Carvalho, R. R., de La Rosa, I. G., et al. 2010b, MNRAS, 408, 1313
La Barbera, F., Lopes, P. A. A., de Carvalho, R. R., de La Rosa, I. G., & Berlind, A. A. 2010c, MNRAS, 408, 1361
Lovell, M. R., Pillepich, A., Genel, S., et al. 2018, ArXiv e-prints
McAlpine, S., Helly, J. C., Schaller, M., et al. 2016, Astronomy and Computing, 15, 72
Metcalf, R. B. & Petkova, M. 2014, MNRAS, 445, 1942
Mukherjee, S., Koopmans, L. V. E., Metcalf, R. B., et al. 2018a, ArXiv e-prints
Mukherjee, S., Koopmans, L. V. E., Metcalf, R. B., et al. 2018b, ArXiv e-prints
Napolitano, N. R., Romanowsky, A. J., & Tortora, C. 2010, MNRAS, 405, 2351
Oser, L., Ostriker, J. P., Naab, T., Johansson, P. H., & Burkert, A. 2010, ApJ, 725, 2312
Peirani, S., Dubois, Y., Volonteri, M., et al. 2017, MNRAS, 472, 2153
Peirani, S., Sonnenfeld, A., Gavazzi, R., et al. 2018, ArXiv e-prints
Petkova, M., Metcalf, R. B., & Giocoli, C. 2014, MNRAS, 445, 1954
Planck Collaboration, Ade, P. A. R., Aghanim, N., et al. 2014, A&A, 571, A16
Pontzen, A. & Governato, F. 2014, Nature, 506, 171
Remus, R.-S., Dolag, K., Naab, T., et al. 2017, MNRAS, 464, 3742
Rosas-Guevara, Y. M., Bower, R. G., Schaye, J., et al. 2015, MNRAS, 454, 1038
Ruff, A. J., Gavazzi, R., Marshall, P. J., et al. 2011, ApJ, 727, 96
Sales, L. V., Navarro, J. F., Schaye, J., et al. 2010, MNRAS, 409, 1541
Schaller, M., Frenk, C. S., Bower, R. G., et al. 2015a, MNRAS, 451, 1247
Schaller, M., Frenk, C. S., Bower, R. G., et al. 2015b, MNRAS, 452, 343
Schaye, J., Crain, R. A., Bower, R. G., et al. 2015, MNRAS, 446, 521
Schaye, J. & Dalla Vecchia, C. 2008, MNRAS, 383, 1210
Segers, M. C., Schaye, J., Bower, R. G., et al. 2016, MNRAS, 461, L102
Sersic, J. L. 1968, Atlas de galaxias australes
Shu, Y., Bolton, A. S., Brownstein, J. R., et al. 2015, ApJ, 803, 71

Shu, Y., Brownstein, J. R., Bolton, A. S., et al. 2017, ArXiv e-prints
Smith, R. J., Alton, P., Lucey, J. R., Conroy, C., & Carter, D. 2015, MNRAS, 454, L71
Smith, R. J. & Lucey, J. R. 2013, MNRAS, 434, 1964
Sonnenfeld, A., Gavazzi, R., Suyu, S. H., Treu, T., & Marshall, P. J. 2013a, ApJ, 777, 97
Sonnenfeld, A., Treu, T., Gavazzi, R., et al. 2013b, ApJ, 777, 98
Sonnenfeld, A., Treu, T., Marshall, P. J., et al. 2015, ApJ, 800, 94
Spiniello, C., Trager, S., Koopmans, L. V. E., & Conroy, C. 2014, MNRAS, 438, 1483
Springel, V. 2005, MNRAS, 364, 1105
Springel, V., Pakmor, R., Pillepich, A., et al. 2018, Monthly Notices of the Royal Astronomical Society, 475, 676
Tessore, N., Bellagamba, F., & Metcalf, R. B. 2016, MNRAS, 463, 3115
Thomas, D., Maraston, C., Bender, R., & Mendes de Oliveira, C. 2005, ApJ, 621, 673
Toomre, A. & Toomre, J. 1972, ApJ, 178, 623
Tortora, C., La Barbera, F., Napolitano, N. R., de Carvalho, R. R., & Romanowsky, A. J. 2012, MNRAS, 425, 577
Tortora, C., Napolitano, N. R., Romanowsky, A. J., Capaccioli, M., & Covone, G. 2009, MNRAS, 396, 1132
Tortora, C., Napolitano, N. R., Romanowsky, A. J., & Jetzer, P. 2010, ApJL, 721, L1
Tortora, C., Napolitano, N. R., Roy, N., et al. 2018, MNRAS, 473, 969
Trayford, J. W., Frenk, C. S., Theuns, T., Schaye, J., & Correa, C. 2018, ArXiv e-prints
Trayford, J. W., Theuns, T., Bower, R. G., et al. 2015, MNRAS, 452, 2879
Treu, T., Koopmans, L. V., Bolton, A. S., Burles, S., & Moustakas, L. A. 2006, ApJ, 640, 662
Treu, T. & Koopmans, L. V. E. 2004, ApJ, 611, 739
van Dokkum, P. G., Franx, M., Fabricant, D., Kelson, D. D., & Illingworth, G. D. 1999, ApJL, 520, L95
Vogelsberger, M., Genel, S., Springel, V., et al. 2014, MNRAS, 444, 1518
White, S. D. M. & Frenk, C. S. 1991, ApJ, 379, 52
Wiersma, R. P. C., Schaye, J., & Smith, B. D. 2009a, MNRAS, 393, 99
Wiersma, R. P. C., Schaye, J., Theuns, T., Dalla Vecchia, C., & Tornatore, L. 2009b, MNRAS, 399, 574
Wu, X., Gerhard, O., Naab, T., et al. 2014, MNRAS, 438, 2701

Xu, D., Springel, V., Sluse, D., et al. 2017, MNRAS, 469, 1824
Zirm, A. W., van der Wel, A., Franx, M., et al. 2007, ApJ, 656, 66

Appendix 4.A

4.A.1 $f_{\rm DM}$ in High-resolution simulation

To check if our analyses is strongly dependent on the resolution of the simulation, we apply our methodology to one massive ETG ($M_\star \sim 10^{10.6}\ M_\odot$) extracted from high resolution Reference simulation of EAGLE. The high resolution run of EAGLE, identified as L025N0752, has a box size of 25 cMpc with 752^3 particles and softening length of 0.35 kpc. We find $f_{\rm DM}(< R_{\rm eff}/2) \approx 11\%$ and $f_{\rm DM}(< R_{\rm eff}) \approx 43.7\%$. So, this is in the range seen in the lower resolution boxes and the differences in $f_{\rm DM}$ values in simulation and observations are not biased by resolution effect. We believe that to solve the discrepancy between numerical predictions and observations, there has to be either energy transfer from baryons to dark matter or a proper implementation of a variable IMF.

Chapter 5

Central Dark matter fraction of early type galaxies in variable IMF scenarios

——— **Based on**

SEAGLE–IV: Impact of IMF variation on the inference of the dark matter fraction and slope in strong lenses,

Sampath Mukherjee, Cresenzo Tortora, Christopher Barber, Léon V. E. Koopmans, Joop Schaye, R. Beneton Metcalf ———

To be submitted to MNRAS

Abstract

Various studies have suggested non-universality of the initial stellar initial mass function (IMF). Systematic variations of the stellar IMF have significant consequences for observational interpretations of how galaxies form and evolve. In this work, we investigate the impact of a non-universal stellar IMF on the inference of the dark matter distribution in early-type galaxies (ETGs). We use two new cosmological, hydrodynamical simulations based on the EAGLE Reference model having either a bottom-heavy IMF (LoM) or a top-heavy IMF (HiM). We calculate the dark-matter fraction inside one and inside half of the effective radius, respectively. We find that the LoM IMF partly solves the dark-matter fraction discrepancy, previously reported, when compared to SLACS lens galaxies, and that massive ETGs are consistent with a Salpeter IMF. Finally, we observe a notable radial dependence of the IMF mismatch parameter $\left(\delta_{\rm IMF} = (M_\star/L)_{\rm IMF}/(M_\star/L)_{\rm Chab}\right)$, where $M_\star/L$ is the stellar mass to light ratio, in the LoM IMF model and a milder dependence in the HiM IMF model, similar to Barber et al. (2018a). We obtain a mean logarithmic dark-matter density slope of $t^{'}_{\rm DM}$=1.48±0.17 in the LoM IMF model, consistent with strong -lens galaxies. We caution though that the lens models are generally obtained using an assumed constant IMF model.

5.1 Introduction

The stellar IMF is an empirical relation quantifying the number of stars as a function of their stellar mass at the time when the stellar population formed. The stellar initial mass function (IMF) is a fundamental outcome of star formation. Understanding the properties and the origin of the stellar IMF is currently one of the most significant challenges in galaxy formation theory. Salpeter (1955) was the first to quantify the stellar IMF as a simple power-law function using main-sequence stars in the solar neighbourhood. Currently, various modifications have been considered at the low-mass end, and Kroupa (2001) and the Chabrier (2003) gave the most commonly used forms. The stellar IMF of a galaxy might depend on the environmental properties of the molecular clouds it originated from, such as their metallicity, temperature, density, and cosmic ray flux. Hence the IMF could, therefore, be non-universal (e.g. Padoan et al. 1997; Hennebelle & Chabrier 2008, 2009; Hopkins 2012; Hennebelle & Chabrier 2013; Hopkins 2013; Offner et al. 2014).

The stellar IMF is crucial to infer physical properties such as masses and star formation rates from observations. A non-universal stellar IMF could, therefore, have significant consequences for the interpretation of the observations of galaxy populations (Clauwens et al. 2016). Also, knowledge of the variety in IMF shapes provides insights into the role of the environment during the star formation and galaxy evolution processes.

However, observations have produced confusing constraints on the IMF shape from self-similar IMF trends across different environments within the Milky Way (see e.g. Bastian et al. 2010), to a systematically varying IMF as a function of mass or velocity dispersion (e.g. Treu et al. 2010; Cappellari et al. 2012; Conroy & van Dokkum 2012; Dutton et al. 2012; Tortora et al. 2013; Spiniello et al. 2014), but see Smith & Lucey (2013) and Clauwens et al. (2015). The IMF of early-type galaxies (ETGs) can be analyzed by modeling the total mass distribution using gravitational lensing (Treu et al. 2010; Auger et al. 2010a; Smith et al. 2015, 2018), stellar kinematics (Cappellari et al. 2013), or both methods in combination (Auger et al. 2010a; Barnabè et al. 2013; Newman et al. 2017) and absorption lines (Spiniello et al. 2012; Conroy & van Dokkum 2012; Tortora et al. 2013). This approach generally assumes that the stellar mass density follows the luminosity density (i.e. a constant stellar M/L) and that

the dark matter (DM) profile follows a parameterized form, such as a power law or an NFW density profile (Navarro-Frenk-White, Navarro et al. 1996, 1997). This model leads to an integral constraint on the IMF, i.e., $M_\star/L$. Another alternative method of evaluation of the IMF is performing a detailed analysis of stellar absorption-line spectra. This approach of using stellar population synthesis (SPS) models has revolutionized in particular the study of the chemical abundance patterns and the IMF in unresolved old stellar populations (Conroy & van Dokkum 2012; van Dokkum & Conroy 2012; La Barbera et al. 2013; Spiniello et al. 2014; Dries et al. 2016, 2018). Note that both methods are generally restricted to the centers of the ETGs where the signal to noise of the spectra is sufficiently large.

Comparing measurements of the IMF with models is complicated because present-day stellar populations are ensembles of stars formed at different epochs in a range of environments. This composite nature of the stellar population adds to the complexity of proper understanding of the IMF. For massive ETGs, it is further complicated (Smith et al. 2015, 2017, 2018) because a significant fraction of their present-day stellar mass is believed to have been accreted from other systems (e.g. van Dokkum & Conroy 2010), possibly leading to a radially varying IMF.

Strong lens galaxies provide one way to break the degeneracy between stellar and dark matter mass in galaxies. Even though systematic IMF studies have been carried out of observed strong lens galaxies (e.g. Barnabè et al. 2013; see also Auger et al. 2010a; Tortora et al. 2013; Sonnenfeld et al. 2013b; Smith et al. 2017; Newman et al. 2017), considerably fewer simulation-driven studies of the IMF have been done (Sonnenfeld et al. 2017). This lack of numerical studies is partially due to the lack of galaxy-formation simulations that incorporate a varying IMF as part of their (sub-grid) physics model.

To disentangle the impact of galaxy formation mechanisms in strong gravitational lens galaxies, using cosmological hydrodynamic simulations, Mukherjee et al. (2018a) (hereafter M18) recently introduced the simulation framework 'SEAGLE' (Simulating EAGLE LEnses). The SEAGLE simulation pipeline has been used to provide insight into observational trends such as the mass density slope (Mukherjee et al. 2018a,b) and the DM fraction (Mukherjee et al. 2018c), using the state-of-the-art EAGLE hydrodynamical simulations (Schaye et al. 2015; Crain et al. 2015). These simulated galaxies

were compared to observed strong-lens galaxies from the Sloan Lens ACS Survey (SLACS; Bolton et al. 2006; Koopmans et al. 2006; Bolton et al. 2008a,b; Koopmans et al. 2009; Auger et al. 2010b,a; Shu et al. 2015, 2017), the Strong Lensing Legacy Survey (SL2S; Cabanac et al. 2007; Ruff et al. 2011; Gavazzi et al. 2012; Sonnenfeld et al. 2013a,b, 2015) and the BOSS Emission-Line Lens Survey (BELLS Brownstein et al. 2012).

In this chapter, we address the impact of a non-universal IMF on the properties of strong-lens ETGs. We make use of the Reference-50 EAGLE simulation and a pair of new cosmological hydrodynamical simulations that incorporate two physics-motivated non-universal IMF models. All models are publicly available[1] (McAlpine et al. 2016).

Barber et al. (2018a) introduced the IMF-variations in the EAGLE simulations where the excess stellar mass-to-light (M/L) ratio, compared to a reference-model IMF, increases either due to an overabundance of low-mass dwarf stars (bottom heavy; LoM) or due to the stellar remnants (black holes, neutron stars, and white dwarfs) of massive stars (top heavy; HiM). The IMF variations in these simulations depend on the local pressure of the star-forming gas and are calibrated to reproduce the correlations between galaxy-wide mass-to-light excess and central stellar velocity dispersion, inferred by Cappellari et al. (2013). This match was achieved by increasing the contribution of either low-mass dwarf stars or stellar remnants to the stellar M/L by varying the low-mass or high-mass IMF slope, respectively, to become bottom-heavy or top-heavy in high-pressure environments on a per-particle basis. The IMF variations in these simulations are fully self-consistent in terms of the local star formation law, stellar energetic feedback, and nucleosynthetic yields. In a series of papers Barber et al. (2018a,b,c) showed that these simulations agree with the observables used to calibrate this model, namely the present-day galaxy luminosity function, half-light radii, and super-massive black hole masses, respectively. These authors explored the predictions and convergences of these simulations for the evolution of galaxy populations as well as internal gradients.

This chapter is focused on the dark-matter fractions and variation in mass-to-light-ratio excess i.e. the IMF mismatch parameter ($\delta_{\rm IMF}$), and is structured as follows: in Section 5.2 we summarize the EAGLE galaxy-formation simulations and the relevant codes that we use in this chapter.

[1] http://icc.dur.ac.uk/Eagle/database.php

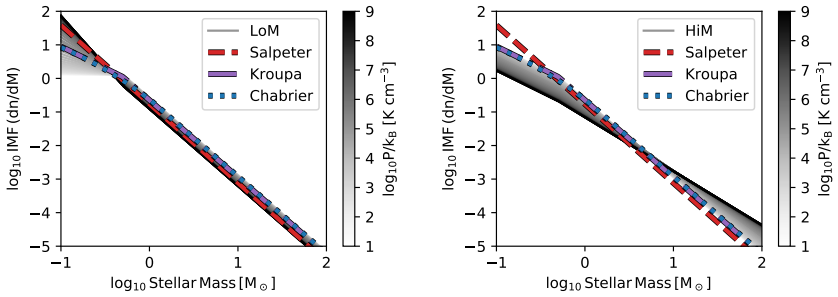

Figure 5.1: IMF variation prescriptions employed by LoM-50 (left panel) and HiM-50 (right panel). Grey lines show the IMF assigned to stellar populations for a range in birth ISM pressures (see greyscale bar). For all IMFs the integrated mass is normalized to $1M_{\odot}$. In LoM-50, the low-mass ($m < 0.5M_{\odot}$) IMF slope is varied such that the IMF transitions from bottom-light to bottom-heavy from low- to high-pressure environments. In HiM-50, the high-mass ($m > 0.5M_{\odot}$) IMF slope is instead varied to become top-heavy in high-pressure environments. Figure reproduced from Fig. 2 of Barber et al. (2018a).

Section 5.3 describes the methodology used in this work to calculate the dark-matter fraction ($f_{\rm DM}$). In Section 5.4, we present the dark-matter fractions obtained from the simulations and their comparison with SLACS galaxies. The implications of our results for galaxy formation are discussed in Section 5.5. Our main conclusions are finally presented in Section 5.6. Throughout the chapter we use EAGLE simulations that assume these values of the cosmological parameters: $\Omega_{\Lambda} = 0.693$, $\Omega_{\rm b} = 0.0482519$, $\Omega_{\rm m} = 0.307$, $h = H_0/(100\ {\rm km\ s^{-1}\ Mpc^{-1}}) = 0.6777$ and $\sigma_8 = 0.8288$. These are taken from the Planck satellite data release (Planck Collaboration et al. 2014), in accordance with the EAGLE simulations.

5.2 EAGLE-IMF variations

The set of EAGLE simulations, including stellar IMF changes, were run with a modified version of the smoothed particle hydrodynamics (SPH) code GADGET3 (Springel 2005). These changes include the use of a pressure-entropy formulation of smooth particle hydrodynamics (SPH; Hopkins

2013) and the time-step limiter of Durier & Dalla Vecchia (2012). The largest EAGLE simulation, which we will refer to as Ref-100 (Schaye et al. 2015) was run in a periodic volume of size L = 100 comoving Mpc (cMpc), containing N = 1504^3 DM particles and an equal number of baryonic particles. The gravitational softening length of these particles is 2.66 comoving kpc (ckpc), limited to a maximum physical scale of 0.7 proper kpc (pkpc). The initial particle masses for baryons and DM are $m_{\rm b} = 1.8 \times 10^6$ $\rm M_\odot$ and $m_{\rm dm} = 9.7 \times 10^6$ $\rm M_\odot$, respectively (for details see Table 1 in Schaye et al. 2015, M18). EAGLE also has several model variations (see Crain et al. 2015) which were run in periodic volumes of size L = 50 cMpc, having the same mass resolution and softening length. Halos and galaxies are identified from the simulation using the Friends-of-Friends and `SUBFIND` algorithms (Dolag et al. 2009). Radiative cooling rates are computed element-by-element (Wiersma et al. 2009a). Energy feedback from star formation and AGN is implemented by stochastically heating gas particles surrounding newly formed star particles and BH particles, respectively (Dalla Vecchia & Schaye 2012). The BHs, with which halos are seeded as in Springel et al. (2005), grow through mergers and gas accretion, where the accretion rate takes into account the angular momentum of the gas (Schaye et al. 2015; Rosas-Guevara et al. 2015). The stellar and AGN feedback have been calibrated to reproduce the observed present-day galaxy stellar mass function and galaxy sizes. In combination with a metallicity-dependent density threshold (motivated by Schaye 2004), the star formation is modeled as the pressure-dependent stochastic conversion of gas particles into star particles (Schaye & Dalla Vecchia 2008). The star particles then enrich their environment with the mass lost through stellar evolution in a time-dependent fashion (Wiersma et al. 2009b). The resulting galaxies are in overall agreement with many key observed properties such as the star formation rate, the Tully-Fischer relation and the colors (Schaye et al. 2015; Trayford et al. 2015), the evolution of the galaxy stellar mass function and sizes (Furlong et al. 2015, 2017), the rotation curves (Schaller et al. 2015) and the α-enhancement of ETGs (Segers et al. 2016).

Barber et al. (2018a) introduced two variable/non-universal IMF simulations that differ from the Reference EAGLE model in not assuming a fixed Chabrier IMF but rather self-consistently varying the IMF for individual star particles. The latter is done as a function of the pressure of the interstellar medium (ISM) in which each star particle formed. The

finite resolution of the EAGLE simulations makes this equal to the ISM pressure averaged on scales of ≈ 1 kpc. The stellar masses of the IMF is defined over the range $0.1 - 100\mathrm{M}_{\odot}$ with a mass-dependent slope $x(m)$ as $\mathrm{d}n/\mathrm{d}m \propto m^{x(m)}$. The two IMF variation prescriptions studied in this work are shown in Figure 5.1 (reproduced from Barber et al. 2018a). The left panel shows the model termed "LoM", where the IMF transitions from bottom-light to bottom-heavy, i.e. from low to high pressures, by varying the low-mass ($m < 0.5M_{\odot}$) slope of the IMF. In the LoM model, the high-mass slope fixed at the Salpeter value of $x = -2.3$. The second prescription, called "HiM", (right panel) varies the high-mass slope ($m > 0.5M_{\odot}$). The IMF transitions from Kroupa-like to top-heavy, i.e. from low to high pressures. The low-mass slope of the IMF in this model is fixed at the Kroupa value of $x = -1.3$. Both IMF variation prescriptions were calibrated to broadly match the correlation between the excess mass-to-light ratio, relative to that expected for a given fixed IMF, and the central stellar velocity dispersion, σ_e, inferred for high-mass ETGs in Cappellari et al. (2013). Stellar feedback, the star-formation law, and metal yields were all adjusted to account for the local IMF variations. Barber et al. (2018a) showed that the simulations maintain consistency with the observables that were used to calibrate the feedback in the Reference model. We refer the reader to Barber et al. (2018a) for further details of these IMF prescriptions and their calibration.

Because the simulations do not explicitly model the emission of optical light, Barber et al. (2018a,b,c) computed photometric luminosities for all stellar particles (in post-processing) using the Flexible Stellar Population Synthesis (FSPS) software package (Conroy et al. 2009; Conroy & Gunn 2010), using the Basel spectral library (Lejeune et al. 1997, 1998; Westera et al. 2002) with Padova isochrones (Marigo & Girardi 2007; Marigo et al. 2008), where the stellar population's age, metallicity, initial stellar mass, and IMF are all taken into account. They also recomputed stellar masses using FSPS and reported a larger stellar masses of up to 0.2 dex for the highest-mass ($M_{\star} > 10^{11} M_{\odot}$) galaxies. Similar to Schaye et al. (2015) and Crain et al. (2015), all the galaxies in Barber et al. (2018a) are identified in the simulations using a `Friends-Of-Friend` (`FoF`) halo finder combined with the `SUBFIND` algorithm (Springel et al. 2001; Dolag et al. 2009). The global galaxy properties such as the stellar velocity dispersion, σ_e, are computed as a Sloan Digital Sky Survey (SDSS) r-band light-weighted average overall

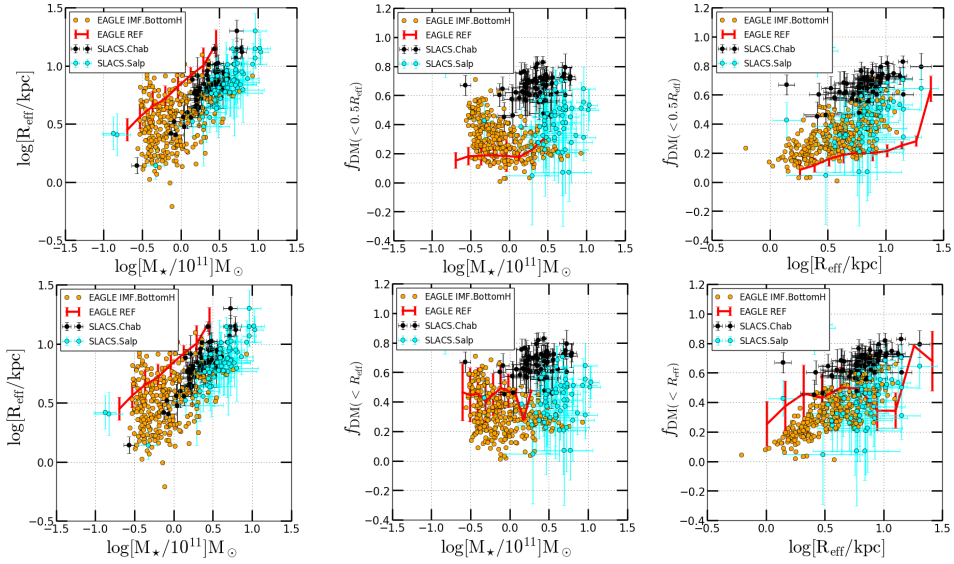

Figure 5.2: The mass-size relation and the dark matter fractions of galaxies from the EAGLE galaxy formation scenario having a bottom-heavy LoM IMF model (orange dots) compared to SLACS galaxies for a Chabrier (black dots) and Salpeter IMF (cyan dots). The EAGLE-Reference model is shown for reference, after binning the data (red line). The first row presents, from left to right, the projected effective radii ($R_{\rm eff}$) in kpc versus the total stellar mass of the galaxy ($M_\star$) in $M_\odot$, the value of $f_{\rm DM}(< 0.5R_{\rm eff})$ versus the total stellar mass ($M_\star$) in $M_\odot$ and the value of $f_{\rm DM}(< 0.5R_{\rm eff})$ versus the projected effective radius ($R_{\rm eff}$) in kpc, respectively. In the second row from the top, we present the same but for the value of $f_{\rm DM}(< R_{\rm eff})$.

bound star particles within the projected r-band half-light radius of each galaxy, where the projection is along the z-axis of the simulation.

5.3 Methodology

We use the SEAGLE (M18) pipeline that incorporates `GLAMER` (Metcalf & Petkova 2014; Petkova et al. 2014) ray tracer and a parametric GPU based modeling code (`LENSED`: Tessore et al. 2016; Bellagamba et al. 2017). SEAGLE uses a galaxy stellar mass threshold (see M18) and a combination

of a lower limit on the velocity dispersion and the effective radius to remove strong outliers and only select massive galaxies. It automatically identifies and extracts samples of galaxies from the `FoF` catalogs of the EAGLE simulations. After selecting, the galaxy indices using our selection function are used recover the desired `GroupNumber` and `SubGroupNumber` (numbers assigned to `FoF` group and subgroup, respectively) and extract all their particles from the simulation snapshot. The total number of galaxies extracted for each IMF model variation of the EAGLE are given in Section 5.4. Below we recap the methodologies of inferring the projected dark-matter fractions inside a fixed radius assuming either a universal (non-varying) IMF (see also Mukherjee et al. 2018c) or an IMF that varies with local environment and is non-universal. We note that in the analyses we use the projected mass maps of EAGLE galaxies directly and do not infer their properties via simulated lensing observations as in e.g. Mukherjee et al. (2018a,b).

5.3.1 Dark-matter fractions with a universal IMF

Each simulated galaxy is projected along its three principal axes, producing three projected mass maps (see M18). After projection, we calculate the projected stellar half-mass radius as a proxy of the effective radius ($R_{\rm eff}$) of the brightness distribution. We note that this method of calculating $R_{\rm eff}$ is only used for the constant stellar M/L models (e.g. the Reference model; Schaye et al. 2015), where the effective radius also contains half of the stellar mass. This assumption breaks down if the stellar IMF varies with radius (Smith et al. 2015; Sonnenfeld et al. 2018) and is therefore not used when we determine the inferred dark-matter mass fraction from the varying IMF models. We find that the values of $R_{\rm eff}$ calculated from the projected mass maps are in excellent agreement with those in `subfind`, to within 0.02dex, for the Reference simulation. We compute the central dark-matter fractions within the effective radius, $f_{\rm DM}(< R_{\rm eff})$, and within half of the effective radius, $f_{\rm DM}(< 0.5R_{\rm eff})$ for the selected EAGLE galaxies at a redshift of z_l=0.271, following the definition in Auger et al. (2010a):

$$f_{\rm DM} = 1 - \frac{M_\star(\beta R_{\rm eff})}{M_T(\beta R_{\rm eff})}, \quad \text{with } \beta = 0.5 \text{ or } 1, \tag{5.1}$$

where $\rm M_\star$ is the stellar mass within $\beta R_{\rm eff}$ and $\rm M_T$ is the total mass within $\beta R_{\rm eff}$. We adopt the projected (two-dimensional) dark-matter fraction

in this study, because it is the closest quantity to what is inferred from observations.

For very massive ETGs in the SLACS sample, Auger et al. (2010a) found that differences in their stellar population properties (e.g. age, metallicity, extinction and star-formation histories) are not sufficiently significant to account for the observed trends in their inferred stellar M/L with either galaxy mass or effective radius, for an assumed stellar IMF being either of the Chabrier or Salpeter form. Auger et al. (2010a) conclude that assuming a universal IMF, the central dark-matter fraction increases with the stellar mass of a galaxy. Although the total mass-to-light ratio in SLACS galaxies must increase with the total stellar mass if the IMF is fixed, conversely, the same observed trend can also be due to a varying stellar IMF for a fixed central dark-matter fraction. Because the analysis of SLACS lens galaxies was performed with a fixed Chabrier and Salpeter IMF, respectively, this allows us to compare the results on equal footing with the model variations of the EAGLE simulations that assume a fixed Chabrier IMF. In this case, by definition, $M_{\star}(< R_{\rm eff}) = 0.5 \times M_{\star}$. We calculate the value of $M_{\rm DM}(\beta R_{\rm reff})$ for SLACS galaxies from the quantities given by Auger et al. (2010a), as

$$M_{\rm DM}(< 0.5R_{\rm eff}) \equiv M_{\rm T}(< 0.5R_{\rm eff}) - M_{\star}(< 0.5R_{\rm eff}), \tag{5.2}$$

and

$$M_{\rm DM}(< R_{\rm eff}) \equiv [2 \times M_{\rm T}(< 0.5R_{\rm eff})] - M_{\star}(< R_{\rm eff}). \tag{5.3}$$

The factor of two in equation 5.3 comes from our assumption that the galaxies follow to good approximation isothermal mass models, where the enclosed mass increases linearly with radius. The assumption of (near) isothermality is supported by Koopmans et al. (2006, 2009) and several other strong lensing studies (see e.g. Treu 2010). The observed $\sim 5\%$ scatter in the logarithmic total-mass density slopes leads to a small $\sim 10\%$ increase in the scatter of the inferred (generally extrapolated) values of the total mass inside $R_{\rm eff}$.

5.3.2 Dark-matter fractions with non-universal IMFs

For both EAGLE IMF variations (i.e., LoM and HiM), we estimate $M_{\rm DM}(\beta R_{\rm reff})$ using information in the `subfind` catalogs of Barber et al.

(2018a). To make this comparison in line with the observations, we take the total light in r-band (similar to SLACS) inside $R_{\rm eff}/2$ (and $R_{\rm eff}$) for these galaxies and multiply it with the assumed stellar M/L ratio for either a Salpeter or Chabrier IMF. This approach mimics that taken for SLACS galaxies, where stellar mass is estimated by multiplying the luminosity inside the chosen aperture ($\beta R_{\rm reff}$) by the stellar M/L for the assumed and non-varying IMF. This choice might lead to the slight under-estimation of the stellar mass which we also know directly from the mass maps, but this approach recreates exactly the mass estimation procedure done in SLACS (with fixed IMF). We find systematic differences of 0.1-0.2 dex between the values of $R_{\rm eff}$ of different IMF model variations and Reference simulation calculated directly from the mass maps. On the other hand, we find an excellent agreement using half-light radius (<0.05 dex) between the LoM and Reference, whereas 0.2 dex difference, is still present between HiM and Reference (consistent with Barber et al. 2018a: see Figure 13 therein). We also calculate the ratio (R) of the DM mass in the one and half effective radius for SLACS and EAGLE IMF variations. Assuming that the dark-matter mass has a power-law radial dependence with an average surface density slope $t_{\rm DM}$, this ratio R is related to the dark-matter density slope by the equation:

$$R \equiv \frac{M_{\rm DM}(< R_{\rm eff})}{M_{\rm DM}(< 0.5 R_{\rm eff})} = 2^{(2-t_{\rm DM})}, \tag{5.4}$$

where $t_{\rm DM}$ is related to the three-dimensional dark-matter density slope $t^{'}_{\rm DM}$, as $t^{'}_{\rm DM} = t_{\rm DM} + 1$ (Kormann et al. 1994; Tortora et al. 2009). An excess M/L ratio relative to that expected from a fixed reference IMF has been adopted to parametrize the IMF observationally. We refer to this quantity as the 'mismatch parameter', $\delta_{\rm IMF}$. The value of $\delta_{\rm IMF}$ is directly related to what dynamical IMF studies measure, and is easily computed given a best-fit IMF in spectroscopic studies. We calculate the mismatch parameter in accordance with the definitions in Auger et al. (2010a) and Tortora et al. (2014):

$$\delta_{\rm IMF} = \frac{(M_\star/L_r)_{\rm IMF}}{(M_\star/L_r)_{\rm Chab}}, \tag{5.5}$$

where L_r is the r-band luminosity. Throughout the chapter, we use r-band luminosity. Note that we use a non-logarithmic definition of the mismatch parameter and compare M/L relative to a Chabrier IMF, in contrast with

for example Barber et al. (2018a) and Barber et al. (2018b), where a logarithmic, and Salpeter-relative definition is used, and also with Barber et al. (2018c), where they calculate the mismatch relative to a Kroupa IMF. Our definition facilitates the comparison with SLACS galaxies and also with other observational studies.

In the next section, we compare the results from the LoM and HiM IMF-variations of EAGLE galaxies to the analysis of SLACS galaxies, that were analysed assuming either a fixed Chabrier or Salpeter IMF. This comparison provides a primary benchmark to understand the effect of IMF variations in galaxies in simulations and how different or similar they are from observations.

5.4 Comparison of EAGLE and SLACS galaxies

Here we show the results obtained from our analysis. In Section 5.4.1 we describe the central dark-matter fractions inside $R_{\rm eff}/2$ and $R_{\rm eff}$ of the LoM IMF model. Section 5.4.2 presents details on the central dark-matter fractions of the HiM model. Both IMF models are compared with results from SLACS galaxies, assuming both a fixed Chabrier and Salpeter IMF. In Section 5.4.3, we present the radial and aperture dependence of $\delta_{\rm IMF}$. In this study, we select 252 (Reference-50), 296 (LoM-50) and 129 (HiM-50) galaxies following a total stellar mass threshold of $M_\star > 1.7 \times 10^{10}{\rm M}_\odot$ corresponding to the lowest-mass galaxy in SLACS (see M18). Given the small 50 cMpc box sizes, we use the full sample to assess the trends with IMF and other relevant galaxy properties, rather than the larger stellar mass threshold of $M_\star > 10^{11}{\rm M}_\odot$ used in earlier papers (i.e. M18, Mukherjee et al. 2018b,c).

5.4.1 The bottom-heavy (LoM) IMF model

We start our comparison with observations using the LoM simulation, using the EAGLE-Reference simulation in the 50 cMpc box at z_l=0.271 as a baseline reference. Figure 5.2 presents trends between $f_{\rm DM}(< 0.5R_{\rm eff})$ and different galaxy properties in the the LoM model. The value of $f_{\rm DM}(< 0.5R_{\rm eff})$ range from $\sim$0.01 to $\sim$0.71, with 16th and 84th PCTL

of 17 and 43 respectively. We see an overall agreement in trends between the central dark-matter fraction values $f_{\rm DM}(< 0.5R_{\rm eff})$ versus $R_{\rm eff}$ found in the LoM simulations when compared to SLACS observations, when using a Salpeter IMF for SLACS galaxies. However, due to a scarcity in the number of massive ETGs, we are unable to find any correlation between $f_{\rm DM}(< 0.5R_{\rm eff})$ and $M_\star$. We also find a much better agreement in the mass-size relation of the LoM galaxies with that of SLACS galaxies. Similarly, there is an excellent agreement in $f_{\rm DM}(< R_{\rm eff})$ and $R_{\rm eff}$ as well. Figure **??** reveals that the trends are strikingly different from the Reference simulation. This difference has two major consequences: (1) the discrepancy between the dark matter fraction inside half of the effective radius between simulated EAGLE and observed (SLACS) galaxies, reported by Mukherjee et al. 2018c, appears mostly lifted when using a non-universal varying bottom-heavy (LoM) IMF model and (2) a constant universal IMF, as assumed in the Reference model, has major shortcomings in reproducing the properties of strong-lens galaxies.

We find that the value of R in the simulations – i.e., the inferred projected dark-matter mass ratio between one and half of the effective radius – have a median value $\sim$3 with standard deviation of 0.35 and 16th and 84th PCTL of 2.57 and 3.39 for the LoM IMF model. The $f_{\rm DM}(< R_{\rm eff})$ having 16th to 84th PCTL range of 20 to 47. This is in excellent agreement with the results from SLACS galaxies (Treu et al. 2010; Auger et al. 2010a). When we use equation 5.4 to estimate the projected dark-matter slope of the galaxies, we find an average projected dark-matter surface mass density slope of $t_{\rm DM}$=0.48 with an rms spread of 0.17. Consequently, the three-dimensional density slope – following Kormann et al. (1994) and Tessore & Metcalf (2015) – becomes $t^{'}_{\rm DM}$=1.48$\pm$0.17. This is consistent with several strong lensing and non-lensing studies that probed dark-matter mass density slope (Treu & Koopmans 2004; Napolitano et al. 2010; Sonnenfeld et al. 2012; Grillo 2012; Tortora et al. 2014, 2018). This result not only confirms that a LoM IMF model gives a consistent dark-matter mass-density distribution, but that the relative stellar and dark-matter masses inside the effective radius and inside half of the effective radius are in much better agreement with SLACS lens galaxies when using a non-universal bottom-heavy (i.e. LoM) IMF model.

To recapitulate, varying the stellar IMF in simulations to produce a more bottom heavy IMF, in accordance with the LoM model prescription in

Barber et al. (2018a), appears to resolve the discrepancies noticed in earlier work (Mukherjee et al. 2018b,c) between observed and simulated galaxies, in particular improving agreement in their mass-size relation, dark-matter fraction and dark-matter density slopes when compared to SLACS (lens) galaxies (e.g. Treu & Koopmans 2004; Sonnenfeld et al. 2012; Grillo 2012).

5.4.2 The top-heavy (HiM) IMF model

Next, we assess the impact of the top-heavy (high-mass) IMF on the galaxy properties. Figure 5.3 presents trends between $f_{\rm DM}(< 0.5R_{\rm eff})$ and different galaxy properties for the HiM IMF model. We find a large scatter in the values of $f_{\rm DM}(< 0.5R_{\rm eff})$ in HiM IMF simulation, starting from $\sim$0.25 and increasing up to $\sim$ 0.91. The mean $f_{\rm DM}(< 0.5R_{\rm eff})$ (= 62.8%) in HiM is considerably larger than that of $f_{\rm DM}(< 0.5R_{\rm eff})$ (=30.0%) in the LoM IMF model. The 16th and 84th PCTL for $f_{\rm DM}(< 0.5R_{\rm eff})$ in HiM are 51 and 76 respectively. Unlike the LoM simulations, we observe an anti-correlation between the central dark-matter fraction $f_{\rm DM}(< 0.5R_{\rm eff})$ and $M_\star$ in the HiM simulations. The mass-size relation is also larger than the Reference model and SLACS by 0.2-0.3 dex, consistent with Barber et al. 2018a. This trend could be explained from the fact that when galaxies are populated with stellar remnants, the overall stellar mass increases but they do not accrete to the center of the galaxy. Thus the star particles are more dispersed than their LoM or Reference counterparts resulting in larger effective radii. The latter in turn results in larger dark-matter fractions. However, when calculating $f_{\rm DM}(< R_{\rm eff})$ i.e. at one effective radius, we find lower value of DM fraction than what obtained at half effective radius in HiM model. This result either implies that the dark-matter fraction decreases further away from the center, or the stellar density may be not decreasing rapidly enough such that $f_{\rm DM}(< R_{\rm eff}) < f_{\rm DM}(< 0.5R_{\rm eff})$ in HiM galaxies.

In short, the HiM model leads to a results that would appear in closer agreement with SLACS, under the assumption of a Chabrier IMF for the latter. Whereas observed discrepancies with SLACS are solved in the LoM model by adding more low-mass stars to the center, it is resolved in the HiM model by adding more stellar remnants over a wider range of radii. This leads to a mass-size relation for this model that does not match that of SLACS lenses, whereas it does for the LoM model. Hence the LoM model is favored over the HiM model for strong lensing.

5.4.3 Aperture and radial dependence of the mismatch parameter

Lastly, we study the effect of the aperture and radial dependence of the value of the mismatch parameter $\delta_{\rm IMF}$ (see eq 5.5) in the simulations. Figures 5.4 and 5.5 show the aforementioned correlations for the LoM and HiM IMF models, respectively. We notice that both $\delta_{\rm IMF}(R_{\rm eff}/2)$ and $\delta_{\rm IMF}(R_{\rm eff})$ correlate positively with $M_\star$. However, the effect is much stronger in the LoM IMF model than in the HiM IMF model. This difference between IMF models is partially due to the smaller number of massive galaxies in the HiM simulation box. We also notice that, on average, $\delta_{\rm IMF}(R_{\rm eff}/2) > \delta_{\rm IMF}(R_{\rm eff})$ for all of the galaxies in the LoM simulation. This result suggests that the IMF slope steepens as one goes to smaller radii in the galaxy. In the HiM IMF model, on the other hand, we find no strong evidence of a change of the values of $\delta_{\rm IMF}$ when calculated at $R_{\rm eff}/2$ and $R_{\rm eff}$, respectively. On the other hand, we do observe a negative correlation (positive correlation) between the values of $\delta_{\rm IMF}$ and $R_{\rm eff}$ for galaxies in LoM (HiM) simulations.

Whereas in general more massive galaxies have larger effective radii, we in fact find that more compact galaxies have a large mismatch parameter for the LoM IMF model. This seems in contradiction with the increasing mismatch-parameter value with increasing galaxy mass (e.g. Treu et al. 2010). In Figure 5.4 we indeed see the mismatch increase with total stellar mass, but we see it decrease with effective radius. The only way these two results can be reconciled if if there is a large spread in effective radii in each stellar mass bin.

5.5 Comparison to other studies

We find that simulated galaxies, when compared to SLACS galaxies, prefer a Salpeter-like, i.e. bottom-heavy (LoM), IMF. In particular, the trends seen in the dark-matter fractions are consistent with observations at both $R_{\rm eff}/2$ and $R_{\rm eff}$, resolving the significant discrepancy that we found when assuming a constant IMF (Mukherjee et al. 2018c). The mass-size relation is also in better agreement with SLACS observations. On the other hand, simulated galaxies with a top-heavy (HiM) IMF, with more stellar

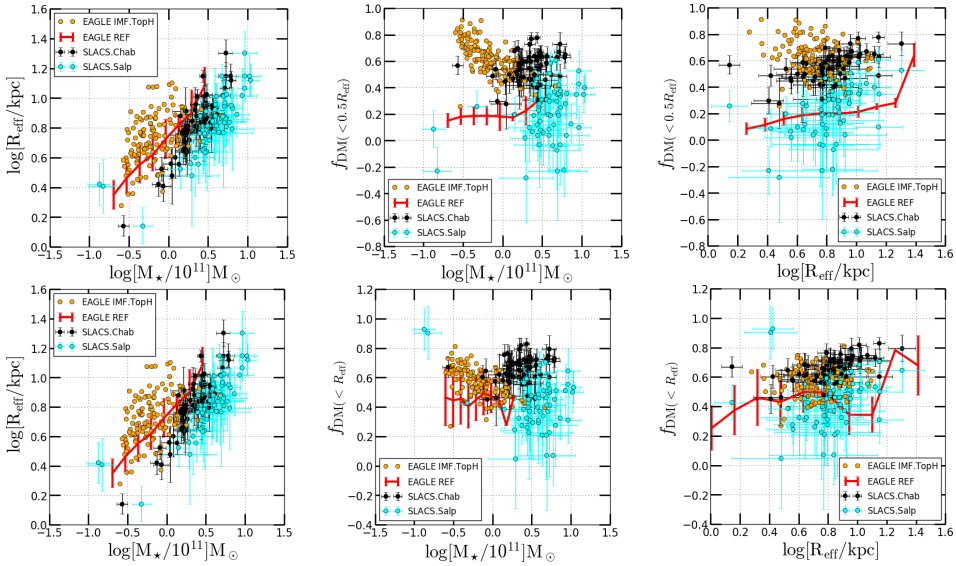

Figure 5.3: Idem to Figure 5.2 for the HiM IMF model.

remnants, cannot replicate the trends seen in SLACS galaxies. Below we place out results in the context of other studies.

Sonnenfeld et al. (2012) ruled out a Chabrier IMF at the 95% confidence level in the lens system SDSSJ0946+1006. Barnabè et al. (2013) inferred an IMF close to Salpeter for two SLACS galaxies, and Barnabè et al. (2015) studied two massive ellipticals from the XLENS Survey, for which both high-resolution HST imaging and X-Shooter spectroscopic observations were available, and again concluded that a Salpeter-like IMF characterises both galaxies. Spiniello et al. (2012) found a preference for a Salpeter IMF over a Chabrier IMF when investigating very massive lens galaxy in a group-scale halo. These results are all consistent with our conclusions from the LoM IMF simulations. Using hierarchical Bayesian inference to constrain the IMF normalization, Sonnenfeld et al. (2015) found that the stellar IMF normalization is close to a Salpeter IMF at $\log M_\star = 11.5 M_\odot$ and scales strongly with increasing stellar mass (see also Grillo 2012 on scaling relations). Dutton et al. (2012) analyzed ∼4000 non-starforming ETGs (regardless of their morphology or structure) and reported a Salpeter IMF in them while ruling out more bottom-heavy IMFs, and standard Milky Way IMFs, consistent with the LoM IMF model studied in this

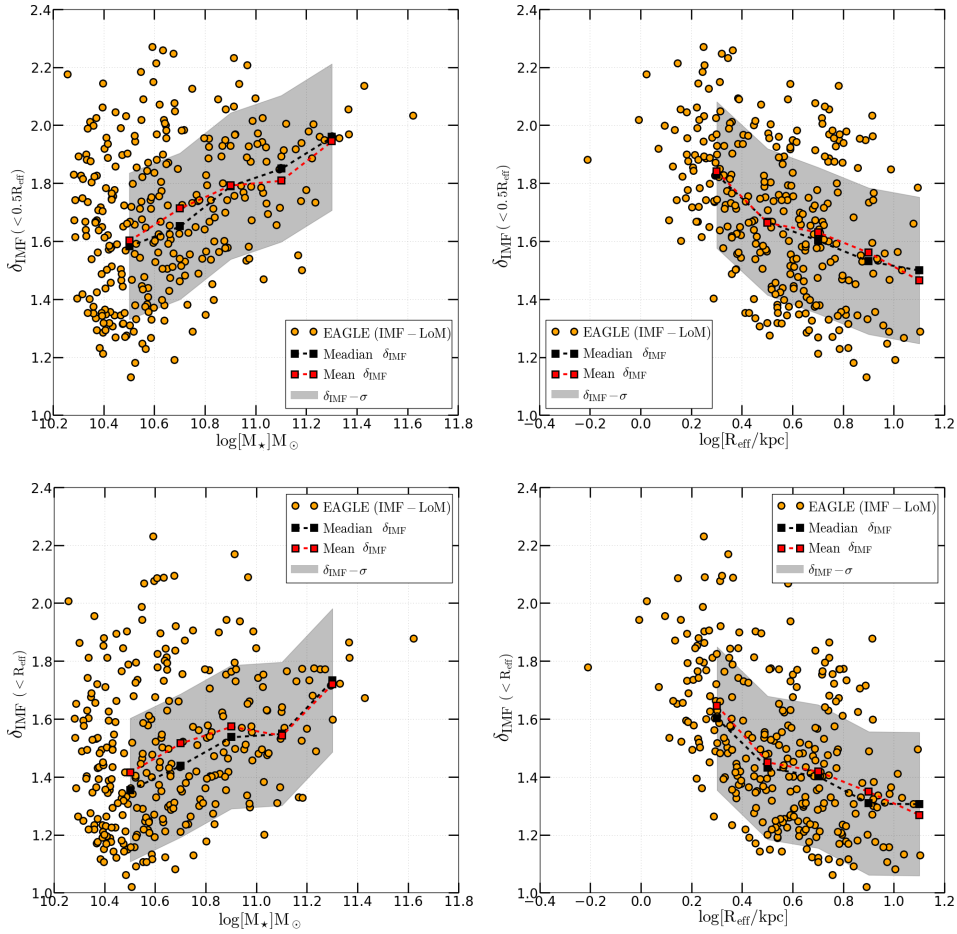

Figure 5.4: The aperture dependence and radial variation of the mismatch parameter ($\delta_{\rm IMF}$) for a bottom-heavy IMF (LoM) [orange dots], with their binned-median (black squares) and binned-mean (red squares). The variation of the $\delta_{\rm IMF}(0.5R_{\rm eff})$ with the stellar mass calculated within 30kpc aperture, $M_\star$, (Top left) and the projected effective radius, $R_{\rm eff}$, (Top right). Bottom panel shows the variation of $\delta_{\rm IMF}(R_{\rm eff})$ with $M_\star$ (bottom left) and $R_{\rm eff}$ (bottom right). The shaded region shows the standard deviation (1σ) value.

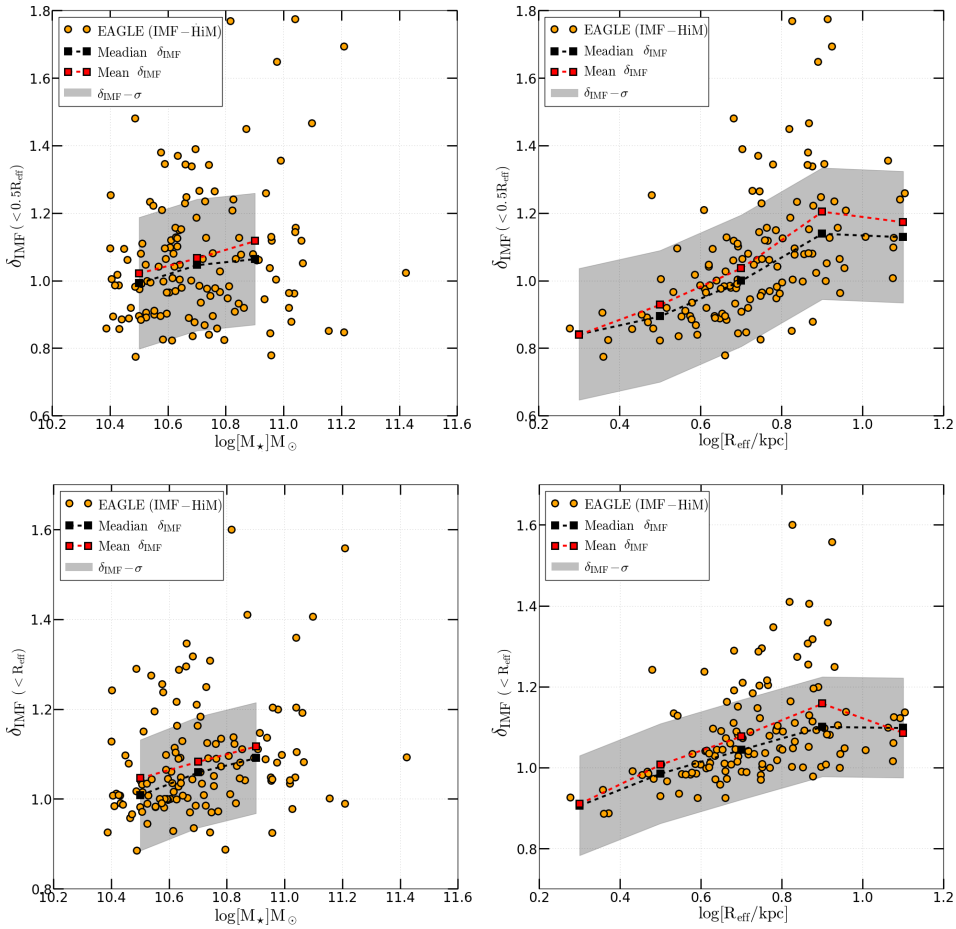

Figure 5.5: Idem to Figure 5.4 for the HiM IMF model.

work. Brewer et al. (2014), on the other hand, investigated the IMF normalization of the population of lower-mass spiral-galaxy bulges, finding that the average IMF normalization must be smaller than that of a Salpeter IMF. Bershady et al. (2011) suggested the existence of a truncated IMF to explain the stellar mass-to-light ratio in disk galaxies in DiskMass Survey. Shu et al. (2015) performed a similar IMF analysis for ETGs with $\log M_\star < 10.8\mathrm{M}_\odot$ and found that an IMF slope more shallow than that of Salpeter is favored. Dutton & Treu (2014) find that ETGs of the mass range $\log M_\star \sim 11.5\mathrm{M}_\odot$ favor a slightly heavier than Salpeter IMF. Oguri et al. (2014) analysed the average mass density profile of ETG lenses in a similar way to Grillo (2012), but using a larger sample of lens galaxies and including the constraints from gravitational microlensing data. They measured a dark-matter slope of $t'_{\rm DM} = 1.60^{+0.18}_{-0.13}$, a dark-matter fraction of$\sim$0.30, and an IMF normalization slightly lower than a Salpeter IMF. Alternatively, microlensing observations of lensed quasars can provide an independent way to determine the absolute value of the stellar mass-to-light ratio and therefore the IMF mismatch parameter ($\delta_{\rm IMF}$) and the DM fraction. Using this technique, Oguri et al. (2014) and Schechter et al. (2014), for example, showed that the Salpeter IMF is consistent with the IMF of massive ETGs. Our findings of LoM dark-matter mass fractions are consistent with their results as well. Napolitano et al. (2010) and Tortora et al. (2010) constructed composite profiles of dark-matter density with radius of ETGs, finding that they are on average cuspy, with an average density slope $t'_{\rm DM} = 1.6 \pm 0.2$. Also, Sonnenfeld et al. (2012) measured $t'_{\rm DM} = 1.7 \pm 0.2$ for the gravitational lens SDSSJ0946+1006, a z = 0.222 ETG from the SLACS sample. Independently, Grillo (2012) found $t'_{\rm DM} = 1.7 \pm 0.5$ for the average of the SLACS lenses assuming a Salpeter IMF. But Dutton & Treu (2014) showed that $t'_{\rm DM}$ measured in Grillo (2012) and Sonnenfeld et al. (2012) should be corrected to $t'_{\rm DM} = 1.40^{+0.15}_{-0.26}$.

Table 5.1: The maximum, minimum, mean, median, 16th and 84th percentile (PCTL) of $f_{\rm DM}(< 0.5R_{\rm eff})$ and $f_{\rm DM}(< R_{\rm eff})$ of lensing galaxies in the variable EAGLE-IMF scenarios and SLACS (with Chabrier and Salpeter IMF).

	$f_{\rm DM}(< 0.5R_{\rm eff})$						$f_{\rm DM}(< R_{\rm eff})$					
Scenarios	Max [%]	Min [%]	Mean [%]	Median [%]	16th PCTL	84th PCTL	Max [%]	Min [%]	Mean [%]	Median [%]	16th PCTL	84th PCTL
LoM-50	71.1	1.0	30.0	28.2	17.2	43.2	71.1	1.2	32.8	31.6	20.0	47.3
HiM-50	91.0	25.8	62.8	62.4	51.1	76.3	81.0	27.0	56.3	57.3	45.2	66.1
Reference-50	62.5	5.2	17.8	15.9	12.6	24.0	78.6	25.6	46.9	44.9	27.2	62.5
SLACS-Chab	78.0	28.0	55.2	57.0	45.3	64.7	83.1	45.0	65.8	67.0	57.8	73.0
SLACS-Salp	62.4	-28.0	20.9	23.0	4.0	37.7	62.5	48.5	42.3	42.7	27.9	55.0

5.5.1 Comparison with SNELLS galaxies

On the other hand, Smith et al. (2015) found IMF results from strong-lens galaxies – obtained from SNELLS (SINFONI Nearby Elliptical Lens Locator Survey: Eisenhauer et al. 2003) – consistent with a Kroupa IMF (Kroupa 2001) and disfavoring a Salpeter IMF. This result is inconsistent with the IMF trends reported by Cappellari et al. (2013), even after accounting for intrinsic scatter and selection bias. This result contradicts the analysis of the SLACS lens galaxy sample by Treu et al. (2010); Auger et al. (2010b). The SNELLS results also differ from the bottom-heavy IMFs inferred from spectroscopic studies by Conroy & van Dokkum (2012). In a separate study Smith et al. (2017) analyzed the stellar kinematics of the $z = 0.169$ brightest cluster galaxy in Abell 1201 and found the inner slope of the DM profile to be $t'_{\rm DM} = 1.0 \pm 0.1$, more shallow than in previous studies. They also report the presence of a $> 10^{10}{\rm M}_{\odot}$ compact central mass and hypothesize that this central mass could either be due to a massive black hole or a strongly non-uniform stellar mass-to-light ratio, e.g. from a very bottom-heavy IMF with a large stellar M/L ratio.

The apparent contrast of these lens-galaxy results between SLACS and SNELLS could be due to a selection bias or reflect the way these systems are analysed inside a fixed aperture. For example, the galaxies analyzed by Smith et al. (2015, 2018) are very low-redshift galaxies with high stellar-velocity dispersions, whereas SLACS galaxies are spread over a larger and higher redshift range. Recently Sonnenfeld et al. (2018) showed that a model with a radial gradient in the stellar mass-to-light ratio is required to simultaneously describe a galaxy sample of 45 strong-lens galaxies from SLACS and 1,700 massive quiescent galaxies from SDSS. Models with no gradient result in a too small dark-matter fraction when fitted to the strong-lens galaxy sample (similar to Mukherjee et al. 2018c). However, their measurements are unable to determine whether these $M_{\star}/L$ gradients are due to variations in stellar population parameters (e.g. age, metalicity) for a fixed shape of the IMF, or due to gradients in the IMF itself.

Despite the disagreement with SNELLS galaxies, the correlations of the dark-matter fractions and values of $\delta_{\rm IMF}$ with $M_{\star}$ reported in this work are in agreement with most strong-lens galaxy and non-lens galaxy studies (Treu et al. 2010; Conroy & van Dokkum 2012; Spiniello et al. 2012; Cappellari et al. 2013; Tortora et al. 2013, 2014; Shu et al. 2015) for

both the LoM and HiM IMF models. However, only the trend of $\delta_{\rm IMF}$ with $R_{\rm eff}$ obtained from the HiM IMF model seems consistent with the result by Tortora et al. (2014) (see Figure 1 therein). For the LoM IMF model, the trend is anti-correlated and, hence, is at odds with Tortora et al. (2014).This results agrees with Cappellari et al. (2013) who also found a mild anti-correlation in $\delta_{\rm IMF}$ with $R_{\rm eff}$. However, since EAGLE IMF-variations Barber et al. (2018a) are calibrated with the results from Cappellari et al. (2013), this trend is understandably similar.

5.6 Conclusions

We have studied the impact of a non-universal varying stellar IMF (either bottom or top-heavy), in the EAGLE galaxy-formation simulations presented by Barber et al. (2018a), on the dark-matter fraction and the IMF mismatch parameter inside one and one-half effective radius of massive early-type galaxies (ETGs). Generally, the significant discrepancy in the predicted dark-matter fractions between these simulated and observed SLACS lens galaxies inside half of the effective radius, reported by Mukherjee et al. (2018c), have mostly been mitigated by the inclusion of such a variable IMF in the simulations, and we find the best overall agreement with the non-universal bottom-heavy (EAGLE-LoM) IMF model.

The main conclusions that we draw are summarized below:

(1) The trends of the dark-matter fraction inside $R_{\rm eff}/2$ and $R_{\rm eff}$ are in good agreement between those calculated from the EAGLE bottom-heavy IMF-variation simulations (LoM: Barber et al. 2018a) and those determined from SLACS lens galaxies with a Salpeter IMF. The dark-matter fractions grow with increasing effective radius and galaxy mass. Although the simulated massive ETGs seem to prefer a Salpeter-type IMF, we found no overall trend between the dark-matter fraction from the LoM IMF model and $M_\star$ due to the small number of massive galaxies in the 50 cMpc box. The agreement is not entirely surprising, because the simulations were calibrated on the mass-to-light ratio relations found by Cappellari et al. (2013). However, the non-universal bottom-heavy (LoM) IMF model does resolve the apparent discrepancy previously found in the uncalibrated dark-

matter fraction (Mukherjee et al. 2018c) .

(2) The trend of the dark-matter fraction inside $R_{\rm eff}/2$, calculated from the EAGLE top-heavy IMF-variation simulations (HiM; Barber et al. 2018a) shows an anti-correlation with the total stellar mass of galaxies, $M_{\star}$, and is in overall disagreement with SLACS galaxies. However, the trend of the dark-matter fractions inside $R_{\rm eff}$ from the HiM IMF model agrees with SLACS galaxies.

(3) The mass-size ($M_{\star}$-$R_{\rm eff}$) relation in the LoM IMF model resembles that seen in SLACS galaxies better than in the HiM IMF model. In the HiM IMF model, the mass-size relations are offset by 0.2 dex from the SLACS-Chabrier relation and 0.3 dex from SLACS-Salpeter relation.

(4) The average projected logarithmic dark-matter density slope ($t_{\rm DM}$) inthe LoM IMF model is $t_{\rm DM}$ =0.48±0.17, corresponding to a 3D dark-matter density slope of $t^{'}_{\rm DM} \sim 1.48$. These results are consistent with other studies such as Treu & Koopmans (2004), Napolitano et al. (2010), Tortora et al. (2010), Grillo (2012), Dutton & Treu (2014), Oguri et al. (2014), and Sonnenfeld et al. (2015). However, most of these model assume a fixed stellar M/L, hence we caution that the inferred dark-matter slopes from these studies might be affected by this assumption.

(5) The mismatch parameter ($\delta_{\rm IMF}$) has a radial and aperture dependence for both the LoM and HiM IMF-model simulations. For the LoM (HiM) model there is a decreasing (increasing) trend in $\delta_{\rm IMF}$, calculated at a fixed aperture, with effective radii. The $\delta_{\rm IMF}$ is increasing with the $M_{\star}$. All of the trends are consistent with several strong lensing studies, such as Treu et al. (2010) and Sonnenfeld et al. (2015). The overall $\delta_{\rm IMF}$ value for galaxies in the LoM IMF simulation is higher by ~ 0.3 when calculated within $R_{\rm eff}/2$ than within $R_{\rm eff}$. There is only a mild, if any, increase in the value of $\delta_{\rm IMF}$ for galaxies in the HiM IMF simulation.

In summary, we have shown that the LoM IMF model (a bottom-heavy IMF) appears to alleviate many of the issues previously found between simulated galaxies and observed (strong-lens) galaxies, although

counterexamples (Smith et al. 2015, 2017) are still there. It could be that the Smith et al. (2015, 2017) lenses transition from bottom-light to bottom-heavy IMF only at smaller radii. However, for a fair comparison and better understanding, more of such lens galaxies are still needed. Ongoing surveys, such as KiDS (de Jong et al. 2015) and DES (The Dark Energy Survey Collaboration 2005), are expected to find hundreds of strong-lens galaxies and will likely also increase the number of lens systems similar to those found by Smith et al. (2017). Moreover, the availability of velocity dispersion profiles of bright (z<0.5) ETGs (e.g. with IFU such as MUSE with Adaptive Optics), out to 2-3 $R_{\rm eff}$, could significantly help in alleviating degeneracies when inferring the DM inner fraction from strong lens modeling. In a nutshell, observational data from future strong lensing survey will be crucial to draw proper conclusions on the nature of central matter distribution of ETGs.

Acknowledgements

SM, LVEK, and CT are supported through an NWO-VICI grant (project number 639.043.308). SM thanks SURFSARA network in Amsterdam. CB and JS is supported by VICI grant 639.043.409. RAC is a Royal Society University Research Fellow. This work used the DiRAC Data Centric system at Durham University, operated by the Institute for Computational Cosmology on behalf of the STFC DiRAC HPC Facility (www.dirac.ac.uk). This equipment was funded by BIS National E-infrastructure capital grant ST/K00042X/1, STFC capital grant ST/H008519/1, and STFC DiRAC Operations grant ST/K003267/1 and Durham University. DiRAC is part of the National E-Infrastructure.

References

Auger, M. W., Treu, T., Bolton, A. S., et al. 2010a, ApJ, 724, 511
Auger, M. W., Treu, T., Gavazzi, R., et al. 2010b, ApJL, 721, L163
Barber, C., Crain, R. A., & Schaye, J. 2018a, MNRAS
Barber, C., Schaye, J., & Crain, R. A. 2018b, ArXiv e-prints
Barber, C., Schaye, J., & Crain, R. A. 2018c, ArXiv e-prints
Barnabè, M., Spiniello, C., & Koopmans, L. V. E. 2015, in IAU Symposium, Vol. 309, Galaxies in 3D across the Universe, ed. B. L. Ziegler, F. Combes, H. Dannerbauer, & M. Verdugo, 77–80
Barnabè, M., Spiniello, C., Koopmans, L. V. E., et al. 2013, MNRAS, 436, 253
Bastian, N., Covey, K. R., & Meyer, M. R. 2010, ARA&A, 48, 339
Bellagamba, F., Tessore, N., & Metcalf, R. B. 2017, MNRAS, 464, 4823
Bershady, M. A., Martinsson, T. P. K., Verheijen, M. A. W., et al. 2011, The Astrophysical Journal Letters, 739, L47
Bolton, A. S., Burles, S., Koopmans, L. V. E., et al. 2008a, ApJ, 682, 964
Bolton, A. S., Burles, S., Koopmans, L. V. E., Treu, T., & Moustakas, L. A. 2006, ApJ, 638, 703
Bolton, A. S., Treu, T., Koopmans, L. V. E., et al. 2008b, ApJ, 684, 248
Brewer, B. J., Marshall, P. J., Auger, M. W., et al. 2014, MNRAS, 437, 1950
Brownstein, J. R., Bolton, A. S., Schlegel, D. J., et al. 2012, ApJ, 744, 41
Cabanac, R. A., Alard, C., Dantel-Fort, M., et al. 2007, A&A, 461, 813
Cappellari, M., McDermid, R. M., Alatalo, K., et al. 2012, Nature, 484, 485
Cappellari, M., McDermid, R. M., Alatalo, K., et al. 2013, MNRAS, 432, 1862
Chabrier, G. 2003, PASP, 115, 763
Clauwens, B., Schaye, J., & Franx, M. 2015, MNRAS, 449, 4091
Clauwens, B., Schaye, J., & Franx, M. 2016, MNRAS, 462, 2832
Conroy, C. & Gunn, J. E. 2010, ApJ, 712, 833
Conroy, C., Gunn, J. E., & White, M. 2009, ApJ, 699, 486
Conroy, C. & van Dokkum, P. G. 2012, ApJ, 760, 71
Crain, R. A., Schaye, J., Bower, R. G., et al. 2015, MNRAS, 450, 1937
Dalla Vecchia, C. & Schaye, J. 2012, MNRAS, 426, 140
de Jong, J. T. A., Verdoes Kleijn, G. A., Boxhoorn, D. R., et al. 2015, A&A, 582, A62

Dolag, K., Borgani, S., Murante, G., & Springel, V. 2009, MNRAS, 399, 497
Dries, M., Trager, S. C., & Koopmans, L. V. E. 2016, MNRAS, 463, 886
Dries, M., Trager, S. C., Koopmans, L. V. E., Popping, G., & Somerville, R. S. 2018, MNRAS, 474, 3500
Durier, F. & Dalla Vecchia, C. 2012, MNRAS, 419, 465
Dutton, A. A., Mendel, J. T., & Simard, L. 2012, MNRAS, 422, L33
Dutton, A. A. & Treu, T. 2014, MNRAS, 438, 3594
Eisenhauer, F., Abuter, R., Bickert, K., et al. 2003, in Instrument Design and Performance for Optical/Infrared Ground-based Telescopes, ed. M. Iye & A. F. M. Moorwood, Vol. 4841, 1548–1561
Furlong, M., Bower, R. G., Crain, R. A., et al. 2017, MNRAS, 465, 722
Furlong, M., Bower, R. G., Theuns, T., et al. 2015, MNRAS, 450, 4486
Gavazzi, R., Treu, T., Marshall, P. J., Brault, F., & Ruff, A. 2012, ApJ, 761, 170
Grillo, C. 2012, ApJL, 747, L15
Hennebelle, P. & Chabrier, G. 2008, ApJ, 684, 395
Hennebelle, P. & Chabrier, G. 2009, ApJ, 702, 1428
Hennebelle, P. & Chabrier, G. 2013, ApJ, 770, 150
Hopkins, P. F. 2012, MNRAS, 423, 2037
Hopkins, P. F. 2013, MNRAS, 433, 170
Koopmans, L. V. E., Bolton, A., Treu, T., et al. 2009, ApJL, 703, L51
Koopmans, L. V. E., Treu, T., Bolton, A. S., Burles, S., & Moustakas, L. A. 2006, ApJ, 649, 599
Kormann, R., Schneider, P., & Bartelmann, M. 1994, A&A, 284, 285
Kroupa, P. 2001, MNRAS, 322, 231
La Barbera, F., Ferreras, I., Vazdekis, A., et al. 2013, MNRAS, 433, 3017
Lejeune, T., Cuisinier, F., & Buser, R. 1997, A&AS, 125, 229
Lejeune, T., Cuisinier, F., & Buser, R. 1998, A&AS, 130, 65
Marigo, P. & Girardi, L. 2007, A&A, 469, 239
Marigo, P., Girardi, L., Bressan, A., et al. 2008, A&A, 482, 883
McAlpine, S., Helly, J. C., Schaller, M., et al. 2016, Astronomy and Computing, 15, 72
Metcalf, R. B. & Petkova, M. 2014, MNRAS, 445, 1942
Mukherjee, S., Koopmans, L. V. E., Metcalf, R. B., et al. 2018a, ArXiv e-prints
Mukherjee, S., Koopmans, L. V. E., Metcalf, R. B., et al. 2018b, ArXiv e-prints

Mukherjee, S., Koopmans, L. V. E., Metcalf, R. B., et al. 2018c, ArXiv e-prints
Napolitano, N. R., Romanowsky, A. J., & Tortora, C. 2010, MNRAS, 405, 2351
Navarro, J. F., Frenk, C. S., & White, S. D. M. 1996, ApJ, 462, 563
Navarro, J. F., Frenk, C. S., & White, S. D. M. 1997, ApJ, 490, 493
Newman, A. B., Smith, R. J., Conroy, C., Villaume, A., & van Dokkum, P. 2017, ApJ, 845, 157
Offner, S. S. R., Clark, P. C., Hennebelle, P., et al. 2014, Protostars and Planets VI, 53
Oguri, M., Rusu, C. E., & Falco, E. E. 2014, MNRAS, 439, 2494
Padoan, P., Nordlund, A., & Jones, B. J. T. 1997, MNRAS, 288, 145
Petkova, M., Metcalf, R. B., & Giocoli, C. 2014, MNRAS, 445, 1954
Planck Collaboration, Ade, P. A. R., Aghanim, N., et al. 2014, A&A, 571, A16
Rosas-Guevara, Y. M., Bower, R. G., Schaye, J., et al. 2015, MNRAS, 454, 1038
Ruff, A. J., Gavazzi, R., Marshall, P. J., et al. 2011, ApJ, 727, 96
Salpeter, E. E. 1955, ApJ, 121, 161
Schaller, M., Frenk, C. S., Bower, R. G., et al. 2015, MNRAS, 451, 1247
Schaye, J. 2004, ApJ, 609, 667
Schaye, J., Crain, R. A., Bower, R. G., et al. 2015, MNRAS, 446, 521
Schaye, J. & Dalla Vecchia, C. 2008, MNRAS, 383, 1210
Schechter, P. L., Pooley, D., Blackburne, J. A., & Wambsganss, J. 2014, The Astrophysical Journal, 793, 96
Segers, M. C., Schaye, J., Bower, R. G., et al. 2016, MNRAS, 461, L102
Shu, Y., Bolton, A. S., Brownstein, J. R., et al. 2015, ApJ, 803, 71
Shu, Y., Brownstein, J. R., Bolton, A. S., et al. 2017, ArXiv e-prints
Smith, R. J., Alton, P., Lucey, J. R., Conroy, C., & Carter, D. 2015, MNRAS, 454, L71
Smith, R. J. & Lucey, J. R. 2013, MNRAS, 434, 1964
Smith, R. J., Lucey, J. R., & Collier, W. P. 2018, ArXiv e-prints
Smith, R. J., Lucey, J. R., & Edge, A. C. 2017, MNRAS, 471, 383
Sonnenfeld, A., Gavazzi, R., Suyu, S. H., Treu, T., & Marshall, P. J. 2013a, ApJ, 777, 97
Sonnenfeld, A., Leauthaud, A., Auger, M. W., et al. 2018, MNRAS, 481, 164
Sonnenfeld, A., Nipoti, C., & Treu, T. 2017, MNRAS, 465, 2397

Sonnenfeld, A., Treu, T., Gavazzi, R., et al. 2012, ApJ, 752, 163
Sonnenfeld, A., Treu, T., Gavazzi, R., et al. 2013b, ApJ, 777, 98
Sonnenfeld, A., Treu, T., Marshall, P. J., et al. 2015, ApJ, 800, 94
Spiniello, C., Trager, S., Koopmans, L. V. E., & Conroy, C. 2014, MNRAS, 438, 1483
Spiniello, C., Trager, S. C., Koopmans, L. V. E., & Chen, Y. P. 2012, ApJL, 753, L32
Springel, V. 2005, MNRAS, 364, 1105
Springel, V., Di Matteo, T., & Hernquist, L. 2005, MNRAS, 361, 776
Springel, V., Yoshida, N., & White, S. D. M. 2001, New Astronomy, 6, 79
Tessore, N., Bellagamba, F., & Metcalf, R. B. 2016, MNRAS, 463, 3115
Tessore, N. & Metcalf, R. B. 2015, A&A, 580, A79
The Dark Energy Survey Collaboration. 2005, ArXiv Astrophysics e-prints
Tortora, C., La Barbera, F., Napolitano, N. R., et al. 2014, MNRAS, 445, 115
Tortora, C., Napolitano, N. R., Romanowsky, A. J., Capaccioli, M., & Covone, G. 2009, MNRAS, 396, 1132
Tortora, C., Napolitano, N. R., Romanowsky, A. J., & Jetzer, P. 2010, ApJL, 721, L1
Tortora, C., Napolitano, N. R., Roy, N., et al. 2018, MNRAS, 473, 969
Tortora, C., Romanowsky, A. J., & Napolitano, N. R. 2013, ApJ, 765, 8
Trayford, J. W., Theuns, T., Bower, R. G., et al. 2015, MNRAS, 452, 2879
Treu, T. 2010, ARA&A, 48, 87
Treu, T., Auger, M. W., Koopmans, L. V. E., et al. 2010, ApJ, 709, 1195
Treu, T. & Koopmans, L. V. E. 2004, ApJ, 611, 739
van Dokkum, P. G. & Conroy, C. 2010, Nature, 468, 940
van Dokkum, P. G. & Conroy, C. 2012, ApJ, 760, 70
Westera, P., Lejeune, T., Buser, R., Cuisinier, F., & Bruzual, G. 2002, A&A, 381, 524
Wiersma, R. P. C., Schaye, J., & Smith, B. D. 2009a, MNRAS, 393, 99
Wiersma, R. P. C., Schaye, J., Theuns, T., Dalla Vecchia, C., & Tornatore, L. 2009b, MNRAS, 399, 574

Chapter 6

Conclusions and Future Prospects

6.1 Conclusions

In this thesis, I have investigated some of the key open questions related to galaxy formation that yielded into some important conclusions but also opened up some thought-provoking questions. In the following sections, I summarize the main results obtained in each chapter. I start with some general conclusions and then move on to chapter-wise conclusions. I end this chapter with future prospects.

6.1.1 Chapter 2: A novel pipeline for simulating and modeling strong gravitational lenses

This chapter is based on Paper-I of SEAGLE series. In this chapter, I introduced the strong-lens simulation and modeling pipeline, SEAGLE. I showed the effectiveness of this setup by assessing the systematics between different mass-model parameters (e.g., density slope, complex ellipticity) inferred from lens modeling and from direct fitting to the simulations, using the same mass-model family. For this work, I chose the EAGLE (Reference-L050N0752) hydrodynamical galaxy simulations, the `GLAMER` ray-tracing package, and the `LENSED` lens-modeling code. All the simulated lenses were modeled with a power-law elliptical mass model or singular isothermal ellipsoid mass model with external shear. An observationally motivated stellar mass cut was made when selecting lensing galaxies from EAGLE. Then I made a stellar mass cut in EAGLE at $> 10^{11}\mathrm{M}_{\odot}$ and re-weighted the EAGLE stellar mass function $\mathrm{dN/dM}_{\star}$ by a simple estimator of the lens cross-section. The simulated EAGLE lenses have a broadly similar stellar mass function and also strikingly similar visual appearance to SLACS and SL2S.

When comparing the results from lens modeling and direct fitting of the mass surface density of lenses in the simulations, I found a correlation between the external shear (γ) and the complex ellipticity (ϵ), with $\gamma \sim \epsilon/4$. This result suggests a degeneracy in the mass model, where the shear compensates for a mismatch between the model and the real mass distribution. *I gave an empirical relation for the first time, between shear and complex ellipticity angles and showed that they are correlated.* I found that there could be 20% (2σ) scatter in calculating the Einstein radii from

the lens modeling and direct fits which was later observationally confirmed indirectly from mass calculations performed by Li et al. 2018. We attribute this surprisingly large scatter because lens modeling only fits the density profile (more precisely that of the potential) near the lensed images, whereas the direct fit is mostly fitting the higher density regions inside the mask, which might lead to a larger scatter when inferring the Einstein radius. I found that the mass density slope of galaxies inferred from lens-modeling generally agrees well. However the average total density slope, $t = 2.26$, is higher than SL2S, $t = 2.16$ or SLACS, $t = 2.08$. This slight difference within rms can be due to the feedback mechanisms and sub-grid physics adopted in simulations, and also due to systematics. When comparing the complex ellipticity between EAGLE and SLACS lenses, it was seen that three-quarters of the modeled EAGLE lenses agree quite well with the distribution of SLACS lenses and much more within the SL2S lens domains. Although a degeneracy exists between q and ϕ but for massive ETGs in EAGLE, there is a broad agreement with SLACS and SL2S lenses.

In this work, I have extended previous studies in the literature by incorporating the aspects of lens modeling and by comparing the inputs to quantify systematic effects in lens modeling focusing for full automation of simulated lens creation, modeling, and comparison with observations which will be needed when future surveys start discovering 1000s of strong lenses.

6.1.2 Chapter 3: Strong lens galaxies prefer a weaker AGN feedback or constant star-formation feedback

In this chapter (based on Paper-II of SEAGLE series) I have explored the impact of different galaxy formation process on the strong-lens simulation analysis with SEAGLE pipeline (Paper-I), allowing us to constrain and explain the (dis)agreement between mass-model parameters (e.g., density slope) inferred from lens modeling and from direct fitting to the simulations, using the same mass-model family. In the current implementation, I used ten EAGLE simulation boxes having the same initial conditions in this simulations. All lenses having $M_\star > 10^{11} M_\odot$ are modeled as power-law elliptical mass models and singular isothermal ellipsoid mass models with external shear. When making a stellar mass cut in EAGLE at $> 10^{11} M_\odot$ and after re-weighting the EAGLE stellar mass function $dN/dM_\star$ by a

simple estimator of the lens cross-section, we find that the simulated lenses have a broadly similar stellar mass function to SLACS, SL2S, and BELLS.

I found changing the subgrid physics and feedback mechanisms in simulations has an impact on the number density of lensing galaxies at a given redshift (here z_l=0.271). ViscHi produces the lowest number of strong lensing galaxies and NOAGN and FBZ resulted in the most number of lensing galaxies. Galaxy formation models where the stellar feedback is relatively inefficient produces very compact systems which thereby reduces the area of caustic. Thus the strong lenses formed from them have mostly ring and arc-like systems. This is important since the feedback mechanism then controls not only the morphology of the galaxy but also the strong lenses. This result will be of great value to constrain the morphology of the lens systems from their Einstein rings when 1000s of lenses are found in future surveys. *Strong lensing galaxies tend to favor model variation with weaker AGN activity and less efficient stellar feedback. AGN model variation with* $\Delta T = 10^8$K *shows relatively better agreement with observations (SLACS) than other model variations.* The mean total mass density slope of galaxies from AGNdT8 simulation is t=2.01 and of FBconst t=2.07. This is very close to isothermal (t=2) and the one obtained from observed lenses t =2.08 for SLACS, t=2.11 for BELLS and t=2.18 for SL2S. Thus FBconst and AGNdT8 emerged as the optimal simulations to have produced lensing galaxies that have total mass density slope which are closest to isothermal and most analogous to observations. Even though FBconst produces very compact systems, comparison to observations shows that strong lenses might have generically compact nature.

This work extensively studied the inner structure of early-type galaxies and the impact of the subgrid physics on their strong lensing properties. This present study particularly demonstrates that the total inner density profiles of lensing galaxies are very sensitive to sub-grid physics and especially to AGN and stellar feedback. This work for the first time (to our knowledge) compiled **ten** simulations for studying the total mass density slopes via strong lensing making it the first study till date to explore so many galaxies be probed from strong lensing perspective.

6.1.3 Chapter 4: Fixed Chabrier IMF simulations produce ETGs with lower DM fraction at $R_{\rm eff}/2$ than observations

In this Chapter, based on paper-III of SEAGLE series, I have investigated the central matter distribution (both dark and luminous) and presented the results in the light of strong lensing observations of SLACS. *I found a serious discrepancy in the* $f_{\rm DM}(< 0.5R_{\rm eff})$ *between simulations and observations. For the first time (to our knowledge) this discrepancy/difference has been explained in the literature from strong lensing point of view. I explicitly studied the trends of various model variations on the basis of their type of stellar and AGN feedback processes. The discrepancy is of a factor 2-3 between the* $f_{\rm DM}(<0.5R_{\rm eff})$ *calculated from EAGLE simulations and observations, with EAGLE simulations' values being lower than SLACS.* This suggests that the inner central regions ($<0.5R_{\rm eff}$ and $<R_{\rm eff}$) of the galaxies in all EAGLE model variation simulations have very dominant stellar component. As I progressed to more massive systems, the DM becomes more dominant. Hence there is an increasing trend of DM fraction with the stellar mass ($f_{\rm DM}(< 0.5R_{\rm eff})$ versus $\rm M_\star$. This trend is similar to strong lensing observations. Galaxies obtained from simulations with limited (or NO) stellar or AGN feedback have a more compact structure (i.e., smaller effective radii) and seems to be a closer analog of the observed strong lenses. This trend potentially indicates weaker stellar and AGN feedback are preferred in the observed strong lensing galaxies. This trend is also in agreement with other comparison simulation studies.

Massive galaxies in EAGLE-Reference simulations and Reference variations (ViscLo, ViscHi, AGNdT8 and AGNdT9) having larger average DM fraction than the calibrated models, i.e. FBconst, FBZ and FBσ shows that they have undergone mostly minor merger events and the latter with major merger events. NOAGN even though being a reference-variation has lower DM fraction due its lack of feedback mechanism to blow out star particles during evolution. EAGLE galaxies are well matched with SPIDER observations in their $f_{\rm DM}(< R_{\rm eff})$ values when compared with $\rm M_\star$, $R_{\rm eff}$ and $\rm M_{R_{eff}}$. The mass-size relation is also similar to SPIDER. The DM fraction in the central region ($<R_{\rm eff}$) of the galaxies in EAGLE and IllustrisTNG-100 hydrodynamic simulations agree well with each other. However, due to the larger sizes and higher stellar masses, Illustris shows

differences with EAGLE in their DM fractions. The difference of inner DM fraction $f_{\rm DM}(<0.5R_{\rm eff})$ between observation and simulations although partially explained by the feedback mechanisms, raises a fundamental issue of the limitations and importance of various sub-grid recipes implemented in simulations. Further, it poses a big question on our understanding of galaxy evolution. We believe IMF has a major role in explaining this major discrepancy.

6.1.4 Chapter 5: DM fraction and DM slope in ETGs are consistent with lensing observations in variable IMF simulations

This chapter is based on Paper-IV of SEAGLE series, where I studied the impact of IMF variation in the EAGLE simulations on the strong lensing properties, e.g. DM fraction. I show that the significant difference in predicted DM fractions between simulated and observed lenses in SEAGLE-III can be solved by the inclusion of a bottom-heavy IMF in the simulations. The trend of DM fractions inside $R_{\rm eff}/2$ and $R_{\rm eff}$ calculated from EAGLE bottom-heavy IMF-variation simulations (LoM) are consistent with strong lensing observations in SLACS, having a Salpeter like IMF. The mass-size ($M_\star$-$R_{\rm eff}$) relation in LoM is also much closer to the one seen in SLACS suggesting dwarf stars rather than stellar remnants dominate SLACS lenses. In a top-heavy IMF (HiM) the mass-size trends are offset by 0.2 dex from the SLACS-Chabrier and 0.3 dex from SLACS-Salpeter trends. The average projected DM slope ($t_{\rm DM}$) for massive galaxies in LoM simulation is $t_{\rm DM}$ $=0.48\pm0.17$ which in 3D DM density slope is $t^{'}_{\rm DM} \sim 1.48$, consistent with several other independent studies. The mismatch parameter ($\delta_{\rm IMF}$) has a radial and aperture dependence for both LoM and HiM IMF-variation simulations. For LoM (HiM) there is a decreasing (increasing) trend in $\delta_{\rm IMF}$, calculated at a fixed aperture, with effective radii and an increasing trend for $\delta_{\rm IMF}$ in both LoM and HiM versus the $M_\star$. All of the trends are consistent with several strong lensing studies. The overall $\delta_{\rm IMF}$ for galaxies in LoM simulation is higher by ~ 0.3 when calculated within $R_{\rm eff}/2$ than $R_{\rm eff}$. However, there is only a mild to no increase in $\delta_{\rm IMF}$ for galaxies in HiM simulation.

In this work, I have shown that the LoM model (a bottom-heavy IMF) alleviates many of the issues previously found between simulations and lens

observations, although counterexamples are still there. It could be that the lenses have a transition from bottom-light to bottom-heavy IMF only at smaller radii in those lens systems. However, for a fair comparison and better understanding, we have to wait for the upcoming survey to discover $\sim$1000s of strong lenses.

6.2 Some Future Prospects

This thesis presents a coherent strong lensing study, aimed at providing answers to some of the open questions of galaxy formation and evolution via strong lensing simulations. However, it also opened up new questions and opportunities for future research in strong lens simulations and galaxy formation. I conclude this thesis by highlighting some of the key aspects of future research where SEAGLE can make a useful contribution to our understanding of strong lensing and in turn galaxy formation mechanism.

6.2.1 Redshift evolution study

This thesis deals with the galaxy formation questions at only redshift z=0.271. However, lens or source can be at a range of redshifts. A full-scale study of the effect of redshift evolution on key observables distributions will be a great future work complementing this thesis. Especially from the context of mass density slope and dark matter fraction, a coherent study at different redshift will reveal the evolution trends of the before-mentioned properties.

6.2.2 Improvements in SEAGLE pipeline

Necessary assumptions and simplifications in current work can be improved in the coming years. Improvement can be made in the following sections:
(i) Instead of ray tracing with a single lens plane, a light cone can be constructed to mimic the reality of strong lensing deflections more closely.
(ii) We assumed a simple model for magnification and lens selection biases which can be improved with more complicated but realistic prescriptions.
(iii) Using more realistic sources (e.g., extracted from HST deep fields, quasars from KiDS, etc.) than parametric (Sérsic) models in SEAGLE to produce lensed images, will make the analysis more realistic and robust when compared to the observations.
Both of these aspects will improve the present theoretical framework of the pipeline and make a significant contribution to the understanding of galaxy-formation physics and systematics therein.

6.2.3 SEAGLE with next generation simulations

There are new, upcoming next generations of hydrodynamic simulations. SEAGLE being fully capable of handling data coming from any `Gadget` based simulations, it will be fascinating to see the effects of modified and state of the art sub-grid recipes and improved implementation of baryonic physics on the simulations of strong lenses. The future work on this will be relatively less time-consuming regarding software development since SEAGLE is fully automated.

Samenvatting

Al vanaf het begin van de mensheid is men geïnteresseerd in de eeuwigheid en in wat daaraan voorbij gaat. De eerste mens ontwikkelde al snel interesse in astronomie, met als doel de oorsprong van het heelal te ontdekken. Sinds die tijd is er heel veel kennis vergaard over het ontstaan en de evolutie van sterrenstelsels. Desalniettemin resten er nog vele onopgeloste kernvragen op dit gebied. In deze samenvatting beschrijf ik de belangrijkste resultaten van mijn werk in de context van ons algeheel begrip van de geschiedenis van het heelal.

Het verhaal over het ontstaan van het heelal

In de loop van de twintigste eeuw zijn vele theorieën ontstaan over het ontstaan en de evolutie van ons heelal. Geen enkele van deze theorieën kan de grote variëteit aan structuur om ons heen precies verklaren. Van alle bestaande theorieën is die van de Oerknal het meest succesvol in het beschrijven van het heelal.

De theorie van de Oerknal beschrijft hoe het heelal vele malen heter en compacter was in haar eerste beginfase. Op jonge leeftijd was het heelal zo heet dat protonen en neutronen niet konden worden gevormd. Ongeveer een half miljoen jaar na de Oerknal (zie 'Dark ages' in Figuur 1), terwijl het zich uitzet, koelt het heelal adiabatisch af. Doordat de

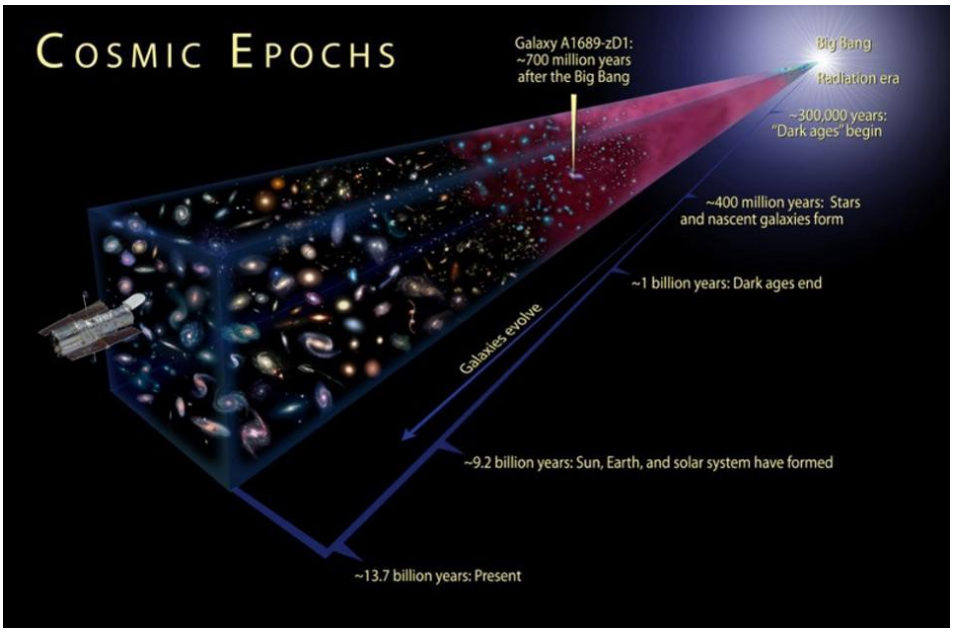

Figuur 1: Een samenvatting van de bijna 14 miljard jarige geschiedenis van het heelal. In de beginfase was het heelal vrijwel uniform verdeeld, op enkele kleine fluctuaties na. Deze fluctuaties veranderden langzamerhand in een rijke variëteit van kosmische structuur die we vandaag de dag kunnen observeren: vanaf de kleinste sterren en planeten tot aan de grootste groepen van sterrenstelsels. Beeld met dank aan: NASA/STScI/A. Feild.

energie van de fotonen afnam met de steeds sneller verlopende expansie van het heelal konden neutrale waterstof, helium en sporen van lithium zich vormen. Tijdens het afkoelen begon de zwaartekracht de overhand te krijgen, waardoor materie op grote en kleine schaal begon samen te trekken. De allereerste dichtheidsfluctuaties, die ontzettend klein waren ten tijde van de Oerknal, begonnen te groeien tot steeds grotere rimpelingen. Daar waar de rimpelingen zich ophoopten vormden ze gebieden met hoge dichtheid. Dit veroorzaakte een hoge druk die in staat was om het nabije gas aan te zetten tot de vormen van sterren. Dit alles gebeurde ongeveer 400 miljoen jaar na de Oerknal (zie Figuur 1). Kleine verstoringen in ruimtetijd zorgden ervoor dat het heelal zich vormde tot het huidige spinnenwebachtige. Dit kosmische web groeit door sterrenstelsels aan te trekken, vergelijkbaar met kralen aan een ketting. Het enige verschil is dat de ketting voor altijd zal blijven evolueren, terwijl de sterrenstelsels als balletdansers in hun eigen zwaartekrachtsveld tollen.

Nabootsen van het heelal

Aan het begin van de twintigste eeuw probeerden theoretisch natuurkundigen met pen en papier uit te rekenen hoe het heelal is ontstaan. Tegelijkertijd waren astronomen bezig met het ontwikkelen van nieuwe observatietechnieken en ze ontdekten astronomische objecten die de mysteries van het heelal konden blootleggen. Echter, het bleek onmogelijk om één allesomvattende analytische theorie te ontwikkelen om het ontstaan van de structuur op alle kosmische schalen te verklaren. In deze tijd werden berekeningen steeds sneller, waarbij de opkomst van nieuwe technologie het mogelijk maakte om duizenden berekeningen relatief snel uit te voeren. Wetenschappers zagen vele toepassingen voor het gebruik van snelle berekeningen en begonnen met het implementeren van algoritmes voor het vinden van numerieke oplossingen voor complexe vergelijkingen. Zo begonnen simulaties waarin de verdeling van deeltjes zich evolueert aan de hand van zwaartekrachtsvergelijkingen invloed te krijgen op de theoretische aspecten van de kosmologie en studies van de evolutie van sterrenstelsels. Met de vooruitgang van de technologie en rekenkracht richtten wetenschappers zich op numerieke simulaties in hun zoektocht naar antwoorden. Een veelzeggende definitie van numerieke simulaties wordt gegeven in het blad Nature: *“Een numerieke simulatie is een*

berekening die wordt uitgevoerd door een computer door middel van een programma dat een wiskundig model hanteert voor een fysisch systeem. Numerieke simulaties zijn nodig voor het bestuderen van systemen waarvoor de wiskundige modellen te complex zijn om analytisch op te lossen, zoals in de meeste niet-lineaire systemen."

Het laten evolueren van een groep fictieve deeltjes met behulp van computers wordt een N-deeltjes simulatie genoemd. Dit concept werd als eerste getest met slechts 16 deeltjes door von Hoerner (1960) en daarna uitgebreid tot 100 deeltjes door Aarseth (1963). Hoe dan ook, was er baat bij het vergroten van het aantal deeltjes naar meer dan 500 om een dichtbevolkte cluster van sterrenstelsels te kunnen modelleren zonder dat het nodig is om de simulatie te herschalen. De eerste simulatie op grote schaal werd uitgevoerd in Cambridge in 1970 door White (1976), waarin 700 deeltjes ("sterrenstelsels") willekeurig werden verdeeld in een bol die uniform uitzette, maar die gebonden was door de zwaartekracht zoals in het heelal.

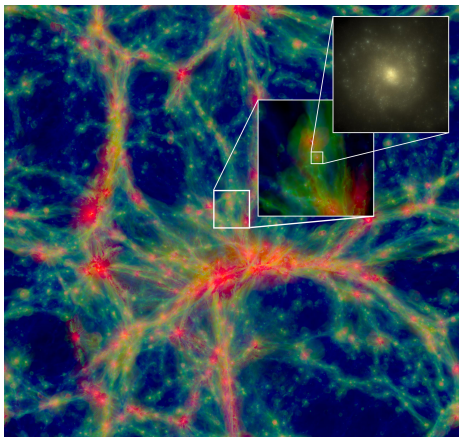

Figure 2: $100 \times 100 \times 20$ cMpc snede van EAGLE Reference-L100N1504 op $z = 0.0$. Beeld met dank aan: Schaye et al. (2015).

Sindsdien hebben kosmologen geprobeerd de gehele 14 miljard jaar aan geschiedenis te simuleren met behulp van supercomputers. Hiermee probeerden ze de evolutie na bootsen die heeft geleid to het huidige heelal. Simulaties werden een laboratorium voor het bestuderen van de echte kosmos. Bijna dertig jaar aan weergaloze verbeteringen in rekenkracht en vooruitgang in algoritmes voor het integreren resulteerden in de creatie van de Millennium Simulatie (MS; Springel et al. 2005) door onderzoekers. In deze simulatie worden 10 miljard deeltjes in een kubus gevolgd om zo de groei van de structuur van donkere materie te kunnen bestuderen en nauwkeurig de observaties te reproduceren. Daarna

hebben verscheiden groepen wetenschappers hun eigen versie van de simulaties gemaakt, versies met verschillende massa's en ruimtelijke schalen.

Later begonnen hydrodynamische simulaties hun opmars doordat ze de co-evolutie van donkere materie en baryonen op een realistischere wijze kunnen hanteren. De meest recentelijk uitgevoerde simulaties zijn Illustris (Vogelsberger et al. 2014) en EAGLE (zie Figuur 2; Schaye et al. 2015). Beide simulaties hebben geresulteerd in vele doorbraken op het gebied van het ontstaan en de evolutie van sterrenstelsels. EAGLE (Evolution and Assembly of GaLaxies and their Environments), omvat echter allerlei simulaties met verschillende combinaties van parameters. Dit maakt het mogelijk om de scenarios voor de formatie van sterrenstelsels te bestuderen in verschillende omgevingen. Onderzoekers hebben de eigenschappen van deze simulaties getest tegen de waarneembare eigenschappen van sterrenstelsels. In mijn onderzoek gebruik ik sterke zwaartekrachtslenzen (ook wel bekend als de natuurlijke telescopen van het heelal) om zware sterrenstelsels te bestuderen in een jong universum met behulp van de EAGLE modellen. Mijn onderzoek combineert simulaties en sterke zwaartekrachtslenzen op een unieke manier om zo de verdeling van massa te bepalen in systemen van zware sterrenstelsels uit simulaties. Hierbij worden de gesimuleerde systemen vergeleken met vergelijkbare systemen die zijn waargenomen in het heelal.

De schoonheid van sterke zwaartekrachtlenzen

Licht bestaat uit fotonen (de kleinste pakketjes van elektromagnetische straling) en een lichtstraal is een bundel van deze deeltjes die samen reizen. De beelden die we zien met de telescopen en detectoren zijn het licht dat is uitgestraald door verre bronnen die door het heelal zijn gereisd om ons te bereiken. De banen van lichtstralen kunnen worden afgebogen door de ongelijke verdeling van materie langs de. Hierdoor kan het lijken alsof de lichtstralen zijn vervormd en vanuit een andere richting komen. Soms kan de verbuiging veroorzaakt door objecten met hoge dichtheid in de voorgrond, zoals sterrenstelsels, groepen en clusters, meerdere beelden creëren van verre lichtbronnen. Dit fenomeen wordt een sterke zwaartekrachtslens genoemd (zie Figuur 3).

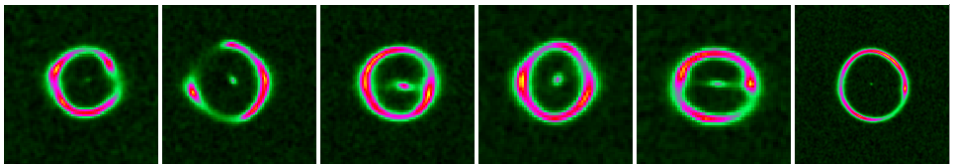

Figuur 3: Enkele voorbeelden van gesimuleerde sterke zwaartekrachtslenzen uit EAGLE. De ring-achtige structuur is wereldwijd bekend als een Einstein Ring.

De eerste sterke zwaartekrachtslens is meer dan dertig jaar geleden ontdekt. In het begin van de jaren '80 waren er niet veel sterke lenzen geobserveerd, voornamelijk omdat de instrumenten niet nauwkeurig genoeg waren om deze objecten waar te nemen. Bovendien waren de waargenomen systemen intrinsiek erg bijzonder en ze vinden was vergelijkbaar met het vinden van een naald in een hooiberg. In de laatste twintig jaar is het aantal bekende lenzen drastisch toegenomen en de kwaliteit van de data drastisch verbeterd. Het aantal bekende lenzen op de schaal van sterrenstelsels is gerezen van $\sim$ 10 in 1990, naar $\sim$ 200 in het jaar 2000, tot ongeveer 500 bevestigde lenzen op dit moment. Met deze aantallen sterk gelensde systemen is een statistische analyse mogelijk geworden. De discrete en zelfstandige natuur van de analyses van sterke lenssystemen is langzaam veranderd tot een onafhankelijke niche binnen de sterrenkunde. Zwaartekrachtslenzen veranderden zo in belangrijke instrumenten voor de kosmologie die interessant zijn in het algemeen, maar ook statistisch vele toepassingen kennen. Sterke zwaartekrachtslenzen werden steeds meer beschouwd als het meest robuuste intstrument om de inhoud van de materie in het heelal te meten en bestuderen. De waarneembare eigenschappen van sterke lenzen zijn afhankelijk van de zwaartekrachtspotentiaal van het sterrenstelsel op de voorgrond (de lens of deflector) en zijn afgeleiden, maar ook van de algehele geometrie van het heelal. Dit maakte het dus mogelijk om de geldigheid van verscheidene kosmologische modellen testen. Zo biedt het dus ook een krachtige manier om de daadwerkelijke oorsprong van ons huidige heelal en de verdeling van massa te achterhalen.

Een bijkomstig voordeel voor de observeerder van zwaartekrachtslenzen is dat de helderheid van de bron in de achtergrond door de lens wordt vergroot (meer dan een orde van grootte). Zo kunnen zwaartekrachtslenzen helpen om een antwoord te geven op belangrijke hoofdvragen in de astrofysica,

zoals de natuur van baryonen en hun interacties met donkere materie op de ruimtelijke schaal van kiloparsecs (kpc) en kleiner. Dit maakt het voor ons ook mogelijk om sterrenstelsels, zwarte gaten en de kernen van actieve sterrenstelsels te bestuderen die voor de huidige instrumenten te klein of te zwak zijn om te worden waargenomen. Spectroscopische observaties (bijv. SLACS en BELLS) werden de meest gunstige studies voor het vinden van sterke lenzen omdat de roodverschuiving en informatie over de snelheidsdispersie nodig zijn voor de astrofysische toepassingen. Later werden ze bijgestaan door fotometrische studies zoals SL2S. Vele duizenden sterk gelensde systemen van elk van deze zoektechnieken worden verwacht te worden ontdekt door aankomende observaties zoals KiDS, DES en toekomstige missies, zoals Euclid. Het is dus duidelijk dat een revisie nodig is van de methodes relevant voor de analyse van deze systemen om zo klaar te zijn voor de aankomende instroom van duizenden lenzen.

Dit proefschrift

In dit proefschrift heb ik kader van simulaties gemaakt dat gesimuleerde en geobserveerde lenzen met elkaar verbindt. SEAGLE is ontwikkeld als een manier om hydronamische simulaties te gebruiken de studie van sterke lenzen. Ik heb gebruik gemaakt van de moderne EAGLE simulaties en de bijbehorende variaties in modellen om de formatie van sterrenstelsels te onderzoeken door middel van sterke zwaartekrachtslenzen.

In hoofdstuk 2 presenteerde ik de simulatie- en analysepijplijn van SEAGLE (zie figuur 4). Ik heb een verzameling van karakteristieke massieve vroege type sterrenstelsels (ETGs; van het Engelse Early Type Galaxies) uit EAGLE Reference-simulaties gehaald en heb sterke gravitationeel gelensde systemen gemaakt door een analytische bron achter hen te plaatsen en de lichtstralen te traceren door het volume van de simulatie. Vervolgens werden deze lenzen gemodelleerd met parametrische modelleringssoftware om de observeerbare variabelen van de lens te verkrijgen. Over het algemeen vertegenwoordigden ze de waargenomen sterke lenzen zeer goed in hun morfologie en andere eigenschappen. Ik vond een iets hogere totale massa-dichtheid richtingscoëfficient ($t = 2{,}26 \pm 0{,}25$) dan in de waarnemingen van SLACS ($t = 2{,}08$) en SL2S ($t = 2{,}16$). Ik rapporteerde ook een degeneratie

in de positiehoek en asverhouding van de gemodelleerde parameters, niet alleen in EAGLE-simulaties maar ook in SLACS- en SL2S-waarnemingen.

In Hoofdstuk 3 heb ik laten zien hoe verschillende fysische effecten van baryonen kunnen bijdragen aan verschillen in de totale massadichtheidsrelatie en massa-grootteverhouding. Door een elliptische machtsfunctie op de gesimuleerde lenzen toe te passen, ontdekte ik dat simulaties met zwakkere feedback door actieve sterrenstelsels of een constante feedback resulteren in de productie van sterrenstelsels met een isothermisch massaprofiel. Deze sterrenstelsels hebben bovendien een zeer vergelijkbare massa-grootte relatie ten opzichte van waargenomen sterke lenzen. Efficiëntere feedback levert daarentegen steilere hellingen op. Hoofdstuk 4 beschreef een afwijking in de fractie van donkere materie (DM) bij een halve effectieve straal tussen simulaties en waarnemingen. Het verschil in de DM-fractie bij een halve effectieve straal verdwijnt wanneer deze wordt berekend bij een hele effectieve straal, wat mogelijk aangeeft dat een fysisch fenomeen op die schaal niet op de juiste manier wordt vertegenwoordigd. Het veranderen van de feedback doet de DM-fractie toenemen bij een halve effectieve straal, maar het verhoogt ook de algehele grootte van het sterrenstelsel. Het antwoord op deze tegenstrijdigheid bevindt zich dus niet in het model voor de vorming van sterrenstelsels zelf.

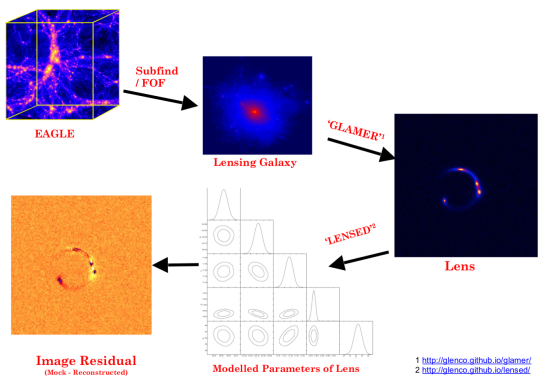

Figuur 4: Een grafische beschrijving van de `SEAGLE` pijplijn.

In hoofdstuk 5 beantwoord ik de vraag die in het vorige hoofdstuk naar voren is gekomen en laat zien een variabele initiële massafunctie (IMF) dit schijnbare DM-fractie op halve effectieve straal oplost. Ik toonde ook aan dat het verschil in de DM-dichtheidsprofiel in een model met variabele IMF met een grotere fractie van lage massa sterren nauw overeenkomt met de voorspelling van verschillende observationele studies. In dit hoofdstuk wordt vastgesteld dat een variabele IMF vereist

is om te voldoen aan alle bekende correlaties van eigenschappen in sterke lenzen.

Dit proefschrift heeft geresulteerd in meerdere verbazingwekkende resultaten die ontzettend veel hebben bijgedragen aan het huidige begrip van de vorming van sterrenstelsels in ETGs. De resultaten in dit proefschrift introduceren niet alleen een nieuwe methode van simuleren en modelleren van sterke lenzen, maar ze verzamelen ook het, op dit moment, grootste aantal simulaties dat gebruikt kan worden voor elke studie van sterke zwaartekrachtslenzen. Tegelijkertijd met het ontdekken van minder donkere materie op de half effectieve radius en degeneraties in de modellen van lenzen heeft dit proefschrift ook geresulteerd in belangrijke inzichten in de niet-universele aard van het IMF en de rol ervan rol in de formatie van sterrenstelsels.

Meer systematische vervolgstudies zullen nodig zijn, samen met verdere inspanningen om nieuwe sterk gelensde systemen to ontdekken. Door de grote instroom van informatie zal het van cruciaal belang zijn om het process te automatiseren waarbij de parameters van een lenssysteem worden bepaald.

Dit proefschrift biedt een enorme stap richting het overwinnen van serieuze beperkingen bij het vergaren van informatie over het lens-sterrenstelsel en betrouwbare lensmodellen. Het theoretische kader van SEAGLE zal het mogelijk maken om lensinformatie te verkrijgen en om hun fysische kenmerken te interpreteren wanneer tienduizenden van deze systemen zullen worden ontdekt.

Referenties

Aarseth, S. J. 1963, MNRAS, 126, 223
Schaye, J., Crain, R. A., Bower, R. G., et al. 2015, MNRAS, 446, 521
Springel, V., White, S. D. M., Jenkins, A., et al. 2005, Nature, 435, 629
Vogelsberger, M., Genel, S., Springel, V., et al. 2014, MNRAS, 444, 1518
von Hoerner, S. 1960, Z. Astrophys, 50
White, S. D. M. 1976, MNRAS, 177, 717

Summary

Since the beginning of civilization, we have been interested in the eternity and the beyond. Soon we started to gain interest in astronomy to find the origin of the Universe. There has been significant increase in the understanding of the formation and evolution of the galaxies but many key questions remain unsolved. In my thesis I unravel some of the mysticism of the most massive galaxies of the Universe with simulations of strong gravitational lenses. In this summary I present a very brief compilation of the important contribution of my work in the perspective of overall understanding of the history of the Universe.

The story of the creation of the Universe

Many theories of the formation and evolution of the Universe were placed throughout the last century. But none could explain all the varied characteristic of the present day Universe. Ultimately the theory of the Big Bang could explain formation and evolution of the Universe more successfully than any other theories.

The Big Bang theory portrays a hot, dense, smaller and more uniform picture of the Universe at very early stage. At a young age the Universe was so hot that protons and neutrons could not be formed. About a half a million years after the Big Bang (see 'Dark ages' in Figure 1), as

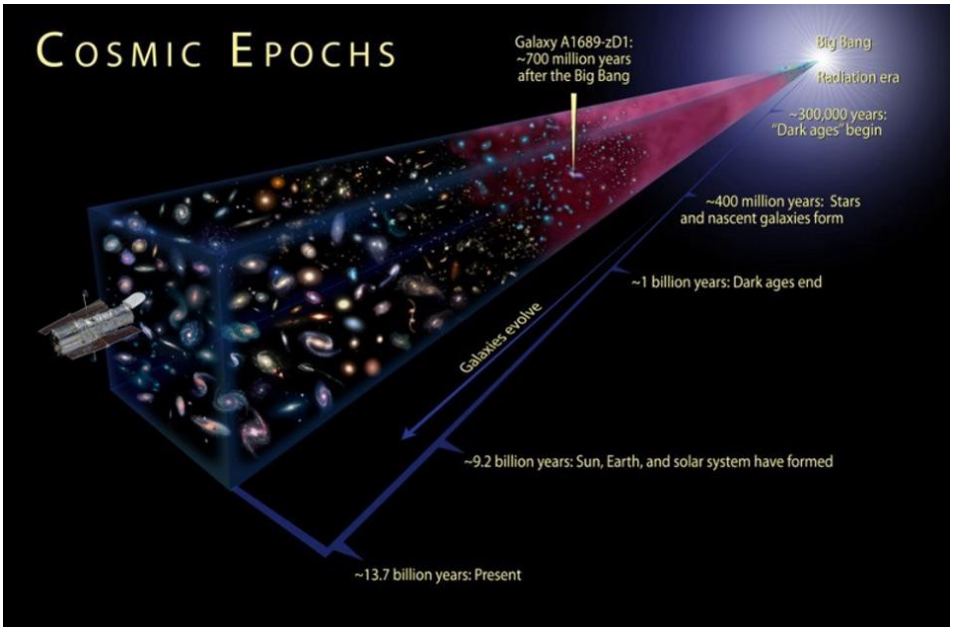

Figure 1: A summary of the almost 14 billion year history of the Universe. The initial phase of the Universe was almost uniform and had only small scale fluctuations which slowly evolved into a rich variety of cosmic structure ranging from stars and planets to galaxies and galaxy clusters that we observe today. Image credit: NASA/STScI/A. Feild.

the Universe expanded, it cooled adiabatically. As the energy of photons dropped neutral hydrogen, helium and traces of lithium started to form. All the while the Universe was expanding at an accelerated rate.

While it cooled, it started to experience gravitation and gravitational collapse on small and large scales. The primordial density fluctuations which were very small at the time of the Big Bang, started to grow with time, creating ripples in the Universe. Where the ripples coincided they formed overdense regions, thereby creating sufficient pressure on the enclosed gas and triggering the formation of first stars. This was almost 400 million years after the Big Bang (see Figure 1). From small disturbances embedded into space-time, the Universe became like a web that started collecting galaxies and giving the cosmos its present form, like beads on a string. The only difference was that the 'string' is ever evolving, and the galaxies perform a ballet within their gravitational fields.

Simulating the Universe

In the early 20th century theoretical physics were trying to unfold the formation history of the Universe with pen and paper calculations; at the same time, astronomers were devising new ways to observe and discover astronomical objects that could reveal the mysteries of the Universe. However, it become clear that one complete analytic theory explaining the formation of structures over the vast cosmological scales was impossible to develop. During this time computing was becoming faster and the advent of new technologies could made thousands of calculations possible at relatively high speed. Scientists saw great potential in using faster computation and started implementing algorithms to find numerical solutions to complex equations. Thus numerical simulations with fictitious particles evolving with gravitational equations, started to influence the theoretical aspects of cosmology and galaxy evolution studies. With the advancement in technology and computing power, the researchers thus turned towards numerical simulations in their quest to find answers. An eloquent definition of numerical simulation is given in the journal of Nature: *"A numerical simulation is a calculation that is run on a computer following a program that implements a mathematical model for a physical system. Numerical simulations are required to study the behaviour of systems whose*

mathematical models are too complex to provide analytical solutions, as in most nonlinear systems."

The concept of evolving fictitious particles in computers came to be known as N-body simulation. This concept was first tested with a maximum of 16 particles by von Hoerner (1960) and later increased to 100 particle by Aarseth (1963). However there was a need to increase the number beyond 500 to make the calculations with sufficient number of particles to model a rich galaxy cluster without any need for scaling assumptions. The first large scale simulation was performed in Cambridge in the 1970s by White (1976) with 700 particles ("galaxies") placed at random within a sphere that uniformly expanded but was gravitationally bound like the Universe.

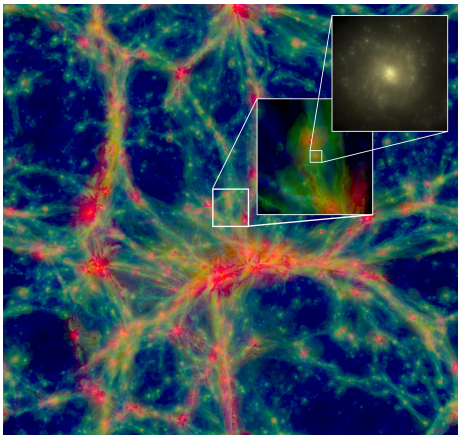

Figure 2: $100 \times 100 \times 20$ cMpc slice of EAGLE Reference-L100N1504 at $z = 0.0$. Image courtesy: Schaye et al. (2015).

Cosmologists since then have tried to simulate the 14-billion-year history of the Universe on supercomputers, in an attempt to mimic the evolution that led to the present-day Universe. Simulations became like a laboratory for studying the real cosmos. Almost over three decades of unprecedented improvements in computer power and advancement in integration algorithms saw researchers built the Millennium Simulation (MS; Springel et al. 2005) which follows 10 billion particles in a cube and simulated the growth of dark matter structure in order to accurately reproduce the observations. Since then, many different groups of scientists made their own versions of the simulations at various mass and spatial scales.

Later hydrodynamic simulations started to gain even more popularity due to its more realistic treatment of co-evolution of dark matter and baryons. Most recently two state-of-the-art simulations Illustris (Vogelsberger et al. 2014) and EAGLE (see Figure 2; Schaye et al. 2015) came

into existence, both resulting in many breakthroughs in galaxy formation and evolution. The EAGLE (Evolution and Assembly of GaLaxies and their Environments), however, has simulation runs with different settings of parameters enabling researchers to study galaxy formation scenarios in different galaxy formation environments. Within these simulations researchers used different probes to test against the observational properties of galaxies. In my research, I use gravitational lenses (nicknamed to the Universe's natural telescopes) to study massive galaxies in the early universe with EAGLE models.

My research uniquely combines simulations and strong gravitational lenses to determine the mass distribution within massive galaxy systems in simulations by comparing them to similar systems found in the Universe.

The beauty of strong gravitational lensing

Light is composed of photons (the tiniest packets of the electromagnetic radiation) and a light ray is a bundle of those particles travelling together. The images we see with the telescopes and detectors are the light emitted from distant sources that have travelled across the Universe to reach us. The trajectories of light rays can get deflected by the inhomogeneous distribution of matter along the line of sight and thus can appear to us slightly displaced and distorted in comparison with the way they would appear in a perfectly homogeneous and isotropic universe. Sometimes the deflection caused by overdense foreground objects such as galaxies, groups, and clusters can create multiple images of the distant light source. This phenomenon is called strong gravitational lensing (examples in Figure 3).

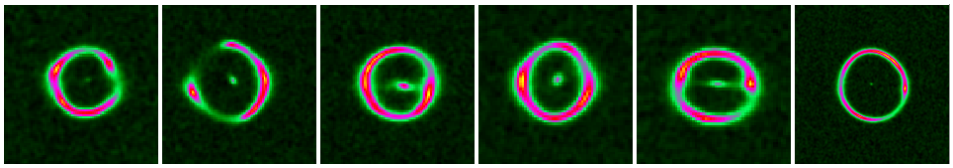

Figure 3: Some examples of simulated strong gravitational lenses from EAGLE. The ring like structure is famously known as the Einstein Ring.

More than thirty years ago, the first strong gravitational lens system was discovered. In the early 1980's not many strong lenses were observed mostly because the instruments were not sensitive enough to resolve these objects. Moreover these systems are intrinsically very rare and literally finding them was similar to finding a needle in a haystack. The last twenty years have seen a dramatic increase in the number of known lenses and in the quality of the data. The number of known galaxy-scale lenses rose from $\sim$ 10 in 1990's to $\sim$ 200 in 2000's and roughly 500 confirmed lenses presently. Hence a statistical analysis became possible with strong lensed systems. The discrete and standalone nature of the analyses of strong lens systems has slowly changed to an independent niche field. This started producing major breakthroughs in cosmology via gravitational lensing, thus making it a powerful tool of general interest and statistical power. Strong gravitational lensing started to be considered the most robust tool to measure and understand matter content of the Universe. The observables in strong lensing depend on the gravitational potential of the foreground galaxy (lens or deflector) and its derivatives, as well as on the overall geometry of the Universe. Thus it could test the validity of various cosmological models. That in turn provides a robust inference of the actual theoretical framework for the origin of our present Universe and its mass distribution. An additional advantage of gravitational lensing is the magnification (more than an order of magnitude) of the background source to the observer. It makes gravitational lensing a very important tool for addressing major key questions in astrophysics such as the nature of baryons and their interaction with dark matter on the spatial scales of kilo parsec (kpc) and sub-kpc. This also allows us to study galaxies, black holes and active nuclei that are too small or too faint to be resolved or detected with current instrumentation. Spectroscopic surveys (e.g. SLACS and BELLS) became the most advantageous surveys for finding strong lenses since the astrophysical applications requires redshift and velocity dispersions information. Later they were complemented by photometric surveys such as SL2S. Several thousand strong lens systems from each of these search techniques are expected to be discovered from the ongoing surveys like KiDS, DES and future surveys such as Euclid. Thus it is obvious that an overhaul of the methodologies involved in the analysis of these systems is needed in order to withstand the inflow of thousands of lenses.

This thesis

In this thesis, I have built a simulation framework which connects simulated to observed lenses. SEAGLE is developed as a tool to use hydrodynamic simulations for strong lensing. I have used state-of-the-art EAGLE simulations with its various model variations to probe galaxy formation via strong gravitational lensing. In Chapter 2, I presented the simulation and analysis pipeline of SEAGLE (see Figure 4). I extracted an ensemble of typical massive early type galaxies (ETGs) from EAGLE Reference simulations and created strong gravitational lensed systems by placing an analytic source behind them and ray-tracing through the simulation box. Then these lenses were modelled with a parametric modelling software to get the lensing observables. Overall, they represented the observed strong lenses very well in their morphology and other properties. I found a slightly higher total mass density slope (t=2.26 $\pm$ 0.25) than the observations of SLACS (t=2.08) and SL2S (t=2.16). I also reported a degeneracy in the position angle and axis ratio of the modelled parameters not only in EAGLE simulations but also in SLACS and SL2S observations.

In Chapter 3, I showed how different baryonic physics can contribute to differences in the total mass density slope and mass-size relation. Fitting an elliptical power law model to the simulated lenses, I found that simulations with weaker AGN feedback or a constant feedback produces galaxies having an isothermal mass profile and also very similar mass-size relation to observed strong lenses. Whereas more efficient feedback produces steeper slopes. Chapter 4 described a discrepancy in the dark matter (DM) fraction at half effective radius between simulations and observations. The difference in DM fraction at half effective radius disappears when calculated at one effective radius, potentially indicating that some physical phenomenon is not accounted properly at that scale. Changing the feedback do increases the DM fraction at half effective radius but it also increases the overall galaxy size. Thus the answer to the discrepancy does not reside in the galaxy formation model itself.

In chapter 5, I answer the question raised in the previous chapter and show that having a variable IMF lift s this apparent DM fraction difference at half effective radius. I also showed that the DM density profile in a bottom heavy variable IMF model is very close to one predicted in several observational

studies. This chapter establishes the fact that a variable IMF is required to comply all the know correlations of properties in strong lenses.

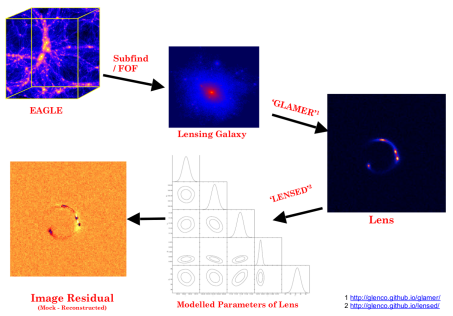

Figure 4: A graphical description of the `SEAGLE` pipeline.

This thesis has resulted in quite a few new results and contributed to the present understanding of galaxy formation in ETGs. The results in this thesis not only introduce a novel method of simulating and modelling strong lenses but also compiles the *largest* number of simulations to date used for any strong lensing related study. In parallel with the finding of lower dark matter fraction at half effective radius and lens modeling degeneracies, this thesis also has resulted in providing important insight on the non-Universality of the IMF and its role in galaxy formation.

More systematic follow-ups will be required in parallel with the discovery efforts of new strong lensed systems. Due to the large influx of information, automatisation of extracting lensing parameters is of paramount importance. This thesis provides a step towards overcoming serious limitation towards obtaining lens galaxy information and reliable lens modelling. The theoretical framework of SEAGLE will make it possible to retrieve lensing information and interpret their physical feature when tens of thousands of systems will be discovered.

References

Aarseth, S. J. 1963, MNRAS, 126, 223
Schaye, J., Crain, R. A., Bower, R. G., et al. 2015, MNRAS, 446, 521
Springel, V., White, S. D. M., Jenkins, A., et al. 2005, Nature, 435, 629
Vogelsberger, M., Genel, S., Springel, V., et al. 2014, MNRAS, 444, 1518
von Hoerner, S. 1960, Z. Astrophys, 50
White, S. D. M. 1976, MNRAS, 177, 717

Acknowledgements

This section summarizes the people responsible to make me go through the four years of my doctoral study and beyond

I still remember the day when I walked roughly 9 km from Mooiland (meaning 'Beautiful Land') to enter the Kapteyn Astronomical Institute for the very first time. It was a walk with mixed feelings of hope, anxiety, and wonder. Now, after four years I am leaving Kapteyn and somehow, I have many of the same feelings as I write this part of my thesis. Time flies, and good time flies even faster. In this four years I have changed a lot both personally and professionally. I will try my best to name the people who have contributed to these changes.

Léon, it is impossible to summarize your contributions both to my thesis and to my life in this short paragraph. Thank you very much for your continuous support of my Ph.D research, and for your patience, motivation, enthusiasm, and immense knowledge. Over the years you have been not only my doctoral advisor, but now have become a part of my family. Your guidance helped me in all the time of research, writing of this thesis and dealing with tricky situations in life. I could not have imagined having a better advisor and mentor. You helped me learn how and what to do in research and connect the dots to see the big picture. I really wonder

how you manage so many students. You give plenty of freedom to all your students and very little pressure. Yet you get all the work done in time. I find your humbleness and humility towards research and your students unparallel.

Joop, I never ever thought I would be able to meet you, let alone to work with you. From my masters studies in India, I learnt about your work in simulations. It has been a fantastic experience to work with you especially in the last 1.5 years. Contrary to many people's belief you are an amazing person. I think your humorous side is hidden from the most. Your intriguing questions, crucial suggestions and eye for details have given this thesis the sharpness that it needed. I look forward to many more joint works with your upcoming simulations.

Ben, you have been a tremendous influence in my research. Although we have met only few times, I personally find you and your personality, in many aspects, very much similar to mine. Your technical expertise has been one of the main pillars of my thesis.

Crescenzo, this thesis would not have been this thicker if not for you. I learned many things about IMF and how observations work. Thanks for teaching me how to think like an observer.

My heartfelt thanks to the entire SEAGLE team, especially **Matthieu**, **Fabio** and **Rob**. You guys patiently heard my babbling in the initial (also later) stages of my PhD years. Our discussions and email conversations have been a valuable source of knowledge for me. **Chris**, it was amazing to work with you on IMFs.

Thanks to all the people of my extended strong lensing family: **Saikat, Cristiana, Enrico, Dorota, Hannah, Giorgos, Gijs, John, Simona, Chris, Matt, Elisa, Adriano, Carlo** and **Gulia**. It has been stimulating to discuss, argue, share and appreciate many strong lensing and non-lensing results. Especially during the Lensing Happy Hours.

My sincere thanks to the rest of my thesis committee: **Prof. Piero Rosati**, **Prof. Mark Vogelsberger** and **Prof. Amina Helmi** for their encouragement, insightful comments, and suggestions that improved the thesis to its present form.

Thanks **Lucia, Christa, Martina, Ramona, Hennie** and **Gineke** for dealing with the bureaucratical and financial matter. **Christa**, I don't know if you remember or not, you were the first person I met in Kapteyn. It feels like yesterday.

A big thank you to all the past and present members of computer group, especially **Martin, Eite, Wim, Leon** and **Valentin**. It would have been impossible without you guys. In the same line of thought, thanks to "**Hawking**", my workstation and "**Argo**" my best computing pal. Both of you were awesome. I will 'remotely' be in touch with both of you.

This acknowledgement would be incomplete if I don't mention **Prof. Somnath Bharadwaj** from whom I got introduced to N-body simulations and cosmology and got the motivation to pursue a PhD. A big thanks to **Prof. Sayan Kar** for his exceptional GR course and unparallel passion of teaching. A special thanks to **Prof. Sugata Pratik Khastgir** for all the numerous interesting discussions about a variety of topic outside the usual classroom hours. Those experiences hugely shaped my approach to life and contributed to the person of what I am.

A heartfelt thanks to **Prof. Sudipta Sasmal** for accepting me as a project student during my Bachelors degree. And a super special thanks to **Prof. Amit Kumar Patra** for hosting and mentoring me in NARL during the summer of 2013 that eventually led to my first paper and eventually a long standing connection. To **Dr. Rabindranath Chattopadhyay** and **Santimoy Chattopadhyay** (Shanti-babu), thanks a lot for all your support and help during my formative period of school days and later in my life. Both of you have been an integral part of my growing up to the person I have become.

Mallika, thanks a lot for being there for me always. Thanks for the countless hours that you have been on Skype, phone and messenger. Even-though we could not live together due to our PhD institutes being in different countries, I knew you were always beside me. Visiting you was a good excuse to go away from cold dutch weather to warm and sunny Barcelona. Groningen also felt much nicer when you visited. Our spontaneous trips were the best part. I look forward to many more trips in the future.

Thanks to my **parents, brother** and **family**. My parents had the greatest contribution in making me come this far. From a tiny village in India, they made me dream about going abroad for studies. If not for their sacrifices, I would be having a different life. I give my humble pranaams to my parents for what they have done for me. Also thanks to my **grandfather** who had a great influence on my character from my very childhood days.

Groningen would have been a different place without the amazing individuals that I have spent countless lunches, dinners, movies, coffee breaks, and happy hours. **Saikat**, thanks for your constant philosophical talks. I remember the first day when you didn't come to Groningen station to receive me, I knew we will become great buddies. After all who else could make you rational. It has been a long, interesting, patience-testing, enjoyable, and 'mf'-ing four years. **Abhik-da**, **Pulastya**, **Aditya** and **Shankha-da**, I will not forget the bangali-addas that were a constant source of refreshment in my first couple of years in Groningen. **Khan-da** thanks a lot for sharing your perspective in life. It was great to know your philosophical ideas and your effort to make science accessible to all via your popular articles in bengali. Hopefully we will meet again. **Katya** and **Enrico** both of you have been great persons to talk to. The fact that you will be staying in Groningen for the next years, gives me additional motivation to visit Groningen.

My current and former officemates: **Eva**, it was great to share office with you. I was like a kid during my first year, asking you all sorts of questions. You always answered my questions and I learned a lot from you about dutch culture and habits. **Marlies**, even-though you would be very busy with organizing the public nights, we still would have interesting conversations about life. Thanks very much for the dinners at your place. I really enjoyed them. **Julia**, thanks for all your English, Python and bakfiets expertise. Also being Star Wars and Tesla fan. Thanks for all the help when I needed the most. **Nika**, you have been amazing. Thanks for great conversations about life. **Helmer**, I really liked your humours. And also your python expertise. Thanks for the interesting conversations and naming the pet animals (spiders) in our office. A special thanks for your help in writing the dutch summary. The office dinners were awesome. It has been an absolute pleasure to share office 178 with you all. I nominate **Laurent** (my worthy successor) to take over my desk. I hope office 178 will remain awesome until I return.

Thanks **Will, Olmo, Smaran, Giorgos, Laura, Jack, Cresenzo, Teymoor, Dimitris, Vaggelis, Emilliano, Andrea, Laurent, Lorenzo, Evandro, Liang, Simon, Davide** and many others for the football matches those were indeed refreshing.

Kapteyn has been a special place where I felt at home all the time. Regardless of the age, people interact so enthusiastically is truly an important part of Kapteyn family. **Avanti, Bharat, Pooja, Punya, Suma, Pandey-ji, Sweta-ji** and **Tirna**, thanks a lot for so many group dinners and activities. You have been great over the four years. **Smaran, Nika** and **Olmo** you are the '*three musketeers*' of Kapteyn. **Robin, Alesandro, Tadeja, Giulio, Kostas, Anstasia, Francesco, Veronica, Jonnas, Davide (Massari & Punzo), Marta, Antonino, Elahe, Syda, Kostas, Aku, Jorrit, Kristina (& Karlis), Umit, Kyle, Kelly** and **Kiril**, Kapteyn would have been incomplete without you all. **Julia** and **Tadeja** a big thanks for your useful comments on the Summary and Introduction and making it better. Thanks **Robin** for your useful and timely comments on the Dutch summary. The International Dinners were great to know you all outside Kapteyn environments. Also thanks to **SIRIUS-A** team who are doing an excellent job and for having me as one of the speakers for STAR Talks.

To my I(ndian & talian)MFs, Kapteyn would not be such a awesome place without you all. A big round of applause for all the activities that you all have organised and thus increased the awesomeness of Kapteyn.

And not to forget, thanks to **NWO**, specifically **VICI** grants (639.043.308 & 639.043.409) and **LKBF** for providing the funding for this thesis.

There has been more than one occasion when my eyes would get moist with memories when I was writing this acknowledgement. I will definitely try to return to Kapteyn, someday, with a different role.